Electronic Scientific Notebook # 354E:
Theoretical Model Development for Flow on
Rough Surfaces of Unsaturated Fractures
(06/30/1999 through 09/22/2000)

Dani Or
Utah State University
Scientific Notebook #354

**Dani Or
Utah State University
Scientific Notebook #354**

**Volume 1 – Unsaturated Flow in Fractures
Volume 2 - Dripping in Subterranean Cavities**

June 30, 1999

<u>Volume 1:</u> Flow in Unsaturated Fractured Porous Media - Hydraulic Conductivity of Rough Surfaces

Dani Or   1/09/99

Thermal Effects - Key Technical Issue

Account Number: 20-1402-661
Collaborators: Markus Tuller (USU), Randall Fedors, Ron Green (CNWRA)
Directories: C:\SCI_NOTE_FRACTURE\

Objectives: Documentation of theoretical model development for flow on rough surfaces of unsaturated fractures based on hydrostatic liquid configuration governed by adsorptive and capillary forces, and model comparisons with available measurements. The documentation includes: (1) development of a unit roughness element to represent fracture surface geometry; (2) basic considerations for calculating equilibrium liquid-vapor interfaces in the proposed unit element dependent on chemical potential (water potential); (3) introduction of flow phenomena in thin adsorbed films and in liquid filled corners/grooves bounded by liquid-vapor interface; (4) development of different averaging procedures for surface hydraulic conductivity of a unit roughness element; (5) introduction of a statistical scheme representing rough fracture surfaces by a statistical distribution of geometric attributes of roughness elements and derivation of ensemble surface hydraulic conductivity; (6) tests of model performance by matching the resulting expressions for single and distribution of roughness elements to measurements.

1/09/99

Initial entry

New insights into modeling of equilibrium liquid-vapor interfaces in angular pore systems of porous media [Tuller et al., 1999; Or and Tuller, 1999], the underestimation or ignorance of flow phenomena in adsorbed liquid films in most models, and recent observations of the importance of water film flow along fracture surfaces of porous rock [Tokunaga and Wan, 1997] provide the motivation for the study. A physically-based model for flow on rough surfaces of unsaturated fractures is proposed based on hydrostatic liquid configuration due to adsorptive and capillary forces. The model is considered as a first step towards developing a comprehensive framework for liquid retention and hydraulic conductivity in partially saturated fractured porous media that combines realistic models for matrix and fracture pore space geometry and explicitly consider the roles of adsorption, capillarity, and hydrodynamic processes in such dual porosity system.

To ensure the practical applicability of the model, surface geometrical features are kept simple enough to obtain closed-form expressions for hydraulic conductivity programmable into conventional spreadsheet software (e.g., Excel, Quattro Pro).

The proposed model is to be based on appropriate thermodynamically and physically considerations. Simplifications should be kept at a minimum and are highlighted and explained at the appropriate level of the development process.

Representation of fracture surface geometry

A single unit element (roughness element) with cross-sectional geometry as depicted in Figure 1 is chosen to represent the cross-sectional profile of a rough fracture surface with relatively wide aperture. Each roughness element contains a groove or an isolated pit attached to a flat surface segment. Pit geometry is defined by its depth L, an angle γ, and by pit spacing βL. The nondimensional parameter β defines the pit/groove density per unit fracture surface - assumed to be proportional to pit depth L.
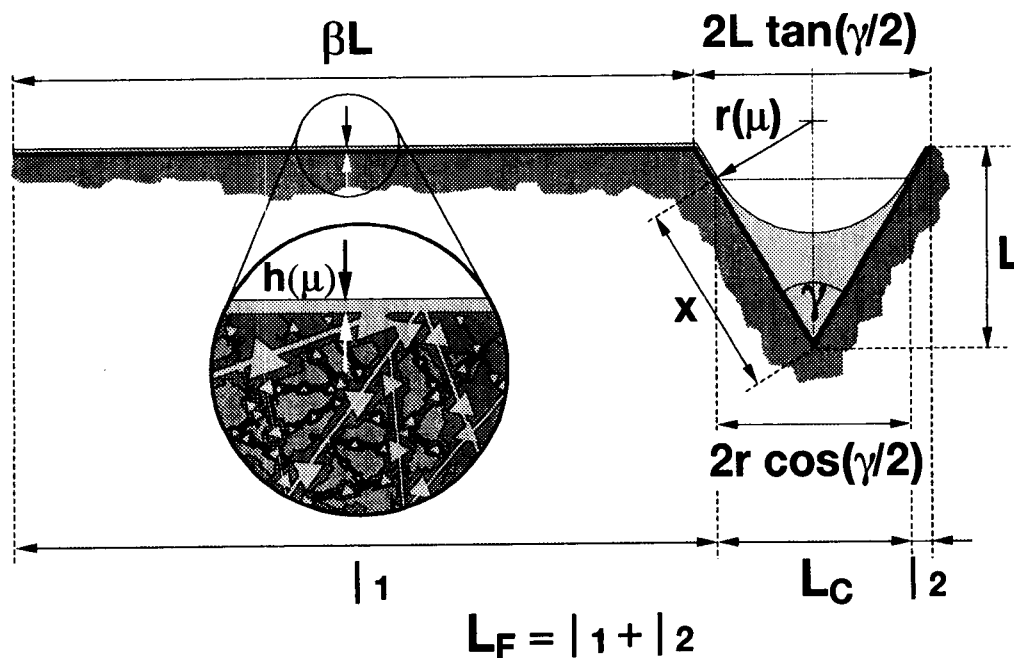

Fig.1 Definition sketch for a unit element representing unsaturated fracture surface with a single pit of depth L and angle γ. Liquid-vapor interfaces are functions of the chemical potential μ, which determines the radius of curvature in the pit r(μ), and film thickness h(μ). The inset represents the partially saturated porous rock matrix forming the fracture; water in the rock matrix pore space is in equilibrium with water on the fracture surface.

The fracture aperture is assumed to be sufficiently wide to preclude fracture snap-off (spontaneous filling of the gap or the entire aperture) at all chemical potentials and flow rates under consideration. The extension of the analysis to fully saturated fractures is

simple for a known aperture size (or a distribution of aperture sizes). In assembling the unsaturated hydraulic conductivity for the rough surface, we consider the individual contributions of film and groove (corner) flows to the total flow on the fracture surface. This enables clear separation and identification of flow regimes for different scenarios (fracture surface properties and chemical potentials). If fracture surface roughness is primarily in the form of isolated pits, the dominating hydraulic regime is expected to be in the form of liquid film flow. In the presence of an appreciable number of continuous grooves, most of the flow is expected to be conducted as "corner" flow [Ransohoff and Radke, 1988; Dullien et al., 1986]. Under most realistic conditions, flow on unsaturated fracture surfaces is likely to be a result of these two processes.

1/16/99

$\boxed{Dani\ Or}$

Chemical potential dependent equilibrium liquid-vapor interfaces in the proposed unit element.

Two elements are considered to assemble the equilibrium liquid-vapor interfacial configuration in the proposed unit element: (1) adsorbed liquid films covering the flat section and dependent on chemical potential part of the groove surface (Fig.1); (2) the liquid held due to capillary forces in the groove (pit). These equilibrium interfaces should be used for subsequent calculations of hydraulic conductivity.

The thickness (h) of a liquid film adsorbed on a planar surface and confined by a vapor phase is calculated as a function of chemical potential (μ) as [Iwamatsu and Horii, 1996]:

$$h(\mu) = \sqrt[3]{\frac{A_{svl}}{6\pi\rho\mu}} \tag{1}$$

where A_{svl} is the Hamaker constant for solid-vapor interactions through the intervening liquid, and ρ is the density of the liquid. The total amount of liquid associated with films is determined not only by the area of the film of the flat segment: $\beta L \cdot h(\mu)$, but also by films exposed on the pit/groove surfaces as the radius of curvature decreases and liquid recedes deeper into the groove (Fig.1). To calculate these additional film surfaces, we first need to know the interface of the liquid retained in the groove (pit) by capillary forces.

The radius of liquid-vapor interface curvature (r) for unsaturated conditions is dependent on chemical potential (μ) according to the Young-Laplace relationship:

$$r(\mu) = -\frac{\sigma}{\rho\mu} \qquad (2)$$

where σ is the surface tension of the liquid. An interesting feature of this uniform capillary radius of curvature is that all grooves with an angle γ retain the same amount of liquid-filled cross-sectional area regardless of the groove's depth (L). The amount of liquid retained in a corner A_C (expressed in this analysis as cross-sectional area) is given by (Fig.2):

$$A_C(\mu) = r(\mu)^2 F(\gamma) \qquad (3)$$

where $F(\gamma)$ is pit angularity factor defined as [Tuller et al., 1999]:

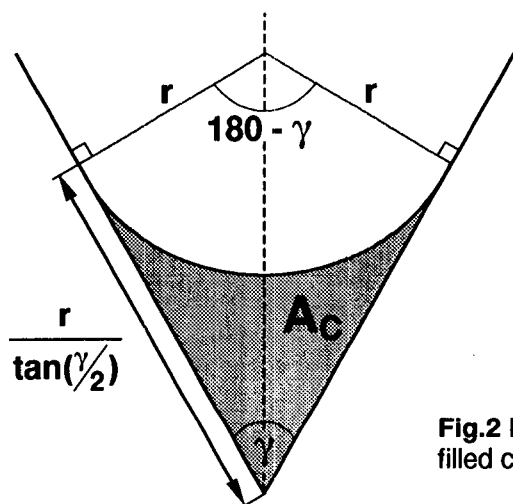$$F(\gamma) = \frac{1}{\tan(\gamma/2)} - \frac{\pi(180 - \gamma)}{360} \qquad (4)$$

Fig.2 Liquid vapor interfacial configuration and liquid-filled cross sectional area in a corner.

With the liquid cross-sectional area associated with capillarity defined, we may now calculate the cross-sectional film area A_F as (see Fig.1):

$$A_F(\mu) = h(\mu)\left(\beta L + 2\left[\frac{L}{\cos(\gamma/2)} - \frac{r(\mu)}{\tan(\gamma/2)} \right] \right) \qquad (5)$$

where $h(\mu)$ is the thickness of the adsorbed film (Eq.1).

When the curved liquid-vapor interface reaches the pit edge, the pit is considered completely filled and no further increase of interface curvature is possible (i.e., we

assume "jump" to a flat liquid-vapor interface). The relationships between pit geometry and the critical chemical potential μ_c at this point is defined by:

$$-\frac{\sigma}{\rho\mu_c\tan(\gamma/2)} = \frac{L}{\cos(\gamma/2)} \qquad \Rightarrow \qquad \mu_c = -\frac{\sigma\cos(\gamma/2)}{\rho L\tan(\gamma/2)} \qquad (6)$$

The interface curvature $r(\mu)$ expressed as $-\sigma/(\rho\mu)$ (Eq.2) at the pit edge (left hand term) is linked with pit geometry (right hand term) (see also Fig.1).

The critical radius of curvature is simply: $\qquad r_c(\mu_c) = \frac{L\tan(\gamma/2)}{\cos(\gamma/2)}$.

Remarks:

(1) Chemical potential is chosen as the measure for the potential energy status of liquid in fractured porous media. The chemical potential is expressed in terms of energy per unit mass [J/kg] and may be converted to pressure (energy/volume) [Pa] by multiplication with water density (ρ).

(2) The spontaneous filling of the pit at the chemical potential where the interface reaches the pit edge (μ_c) may be explained in analogy to processes in (rhombic) pores. In pores the formation of an inscribed circle by the liquid vapor interface marks an unstable configuration leading to snap-off (spontaneous pore fill-up). The reason is the diminishing influence of surface forces that "anchor" the interface. A similar process is likely to occur in the pit when the interface reaches the pit edge. The presence of residual "depressions" on the otherwise flat surface of the fracture is highly unlikely (from energetic considerations), hence conceptually we treat these pits/grooves as completely full with flat interfaces (matching the film interface).

2/06/99
Average liquid velocity in thin adsorbed films

The flow velocity distribution normal to film cross-section is obtained from a solution of the following Navier-Stokes equation [Spurk, 1997]:

$$-\frac{dP}{dz} = \eta_0\frac{d^2v}{dy^2} \qquad (7)$$

where v is the velocity, y is the distance taken normal to the solid surface, dP/dz is the pressure gradient in flow direction z, and η_0 is the viscosity of bulk liquid. Double integration of Eq.7 yields the velocity profile normal to the solid surface:

$$v(y) = \frac{y^2-2hy}{2\eta_0}\left(-\frac{dP}{dz}\right) \qquad (8)$$

The velocity profile (Eq.8) may be integrated again and divided by film thickness (h) to yield an average liquid velocity for a given chemical potential:

$$\overline{v} = \frac{h^2(\mu)}{3\eta_0}\left(-\frac{dP}{dz}\right) \tag{9}$$

This expression relates the film thickness h (Eq.1) as a function of the chemical potential μ and the mean velocity, and is valid only when the liquid viscosity is constant throughout the film. Experimental and theoretical evidence shows a presence of a thin layer with modified viscosity close to the solid surface. Liquid viscosity is elevated relative to bulk liquid due to short- and long-range interfacial forces [Low, 1976, 1979; Derjaguin et al., 1987; McBride and Baveye, 1995]. Expressions derived by Low [1979] for viscosity profiles of water altered by interfacial forces were recently modified by Or and Wraith [1999] to represent viscosity in terms of distance from the solid surface:

$$\eta(y, T) = \eta_0 \exp\left(\frac{a}{yT}\right) \tag{10}$$

where y is the distance from the solid surface (Å), T is temperature (K), and a = 1621 (Å K) is a constant modified from Low [1979]. Substituting Eq.10 into Eq.7, and performing the integration yields an expression for average velocity considering effects of modified liquid viscosity near solid surfaces:

$$\overline{v} = \frac{A}{12\eta_0\, h(\mu)}\left(-\frac{dP}{dz}\right) \tag{11}$$

with the constant A for a given film thickness h(μ):

$$A = \left(a^2 h(\mu) + 5a h(\mu)^2 - 4h(\mu)^3\right)\exp\left(-\frac{a}{h(\mu)}\right) + \left(a^3 + 6a^2 h(\mu)\right)Ei\left[-\frac{a}{h(\mu)}\right]$$

where $Ei[x] = \displaystyle\int_{-\infty}^{x}\frac{e^t}{t}dt$ is the exponential integral [Abramowitz and Stegun, 1964].

The resulting average velocities for constant (Eq.9) and variable viscosity (Eq.11) become indistinguishable for liquid films greater than about 10 nm. We therefore use the simpler expression in Eq.9 for flow in films thicker than 10nm, and the more complex Eq.11 for flow in very thin films.

Remark: Mathematica Version 3.0 was used to perform and check the integrations yielding Eqs.8, 9, and 11.

2/15/99

Average liquid velocity in corners bounded by a vapor phase

Mathematical expressions for average liquid velocity in corners bounded by liquid-vapor interfaces were derived by Ransohoff and Radke [1988]. They used a detailed numerical scheme to solve the Navier-Stokes equations for the assumed geometry and boundary conditions. Their results were reduced to the general form:

$$\bar{v} = \frac{r(\mu)^2}{\varepsilon \eta_0}\left(-\frac{dP}{dz}\right)$$

(12)

where ε is a dimensionless flow resistance parameter dependent on the corner angle γ [Ransohoff and Radke, 1988]. The tabulated values of Ransohoff and Radke [1988] for ε for different corner angles and for zero surface shear stress (i.e., liquid-vapor interface) were fitted with the following parametric expression (Fig.3):

$$\varepsilon(\gamma) = \exp\left(\frac{b+d\gamma}{1+c\gamma}\right)$$

(13)

with b=2.124, c=-0.00415, and d=0.00783 (r^2 =0.995) for γ values in the range of $10^0 < \gamma < 150^0$ (Fig. 3).
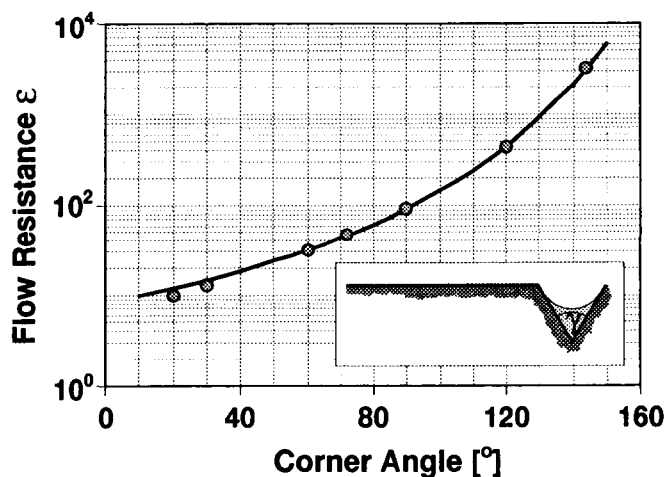
Fig.3 Nondimensional corner resistance to flow as a function of corner angle γ calculated from tabulated values of Ransohoff and Radke, [1988].

Remark: MS-Excel 97 was used to fit a parametric expression (Eq.13) to the tabulated values of Ransohoff and Radke [1988].

Unsaturated hydraulic conductivity for films and corners

Analogy between average velocity calculated from the Navier-Stokes solutions (Eqs.9, 11, and 12) and Darcy's law representation of the liquid flux was used to obtain the hydraulic conductivity for films and corners. Darcy's law is given as:

$$\bar{v} = \frac{Q}{A} = \frac{K}{\rho g}\left(-\frac{dP}{dz}\right) \qquad \textbf{(14)}$$

where Q is the volumetric discharge rate, A is the cross-sectional area occupied by the liquid, K is the hydraulic conductivity, and g is the acceleration of gravity. Assuming a unit pressure gradient, rearranging Eq.14, and inserting the solution in Eqs.9, 11, and 12, yield the following expressions for $K(\mu)$:

Flow in films with constant liquid viscosity

$$K_F(\mu) = \frac{\rho g}{3\eta_0}h^2(\mu) \qquad \textbf{(15)}$$

Flow in films with variable liquid viscosity

$$K_F(\mu) = \frac{\rho g}{3\eta_0}\frac{A}{4h(\mu)} \qquad \textbf{(16)}$$

Corner flow [Ransohoff and Radke, 1988]

$$K_C(\mu) = \frac{\rho g}{3\eta_0}\frac{3r^2(\mu)}{\varepsilon} \qquad \textbf{(17)}$$

Remarks:

(1) In the derivation of Eqs. 15 to 17 we implicitly assume that fracture surfaces are vertical. The results may be extended to tilted fracture surfaces by simply multiplying the terms on the RHS of Eqs.15 to17 by the cosine of the tilt angle.

(2) Effects of gravity on the liquid vapor interfaces are neglected.

(3) The definition of unsaturated hydraulic conductivity in the derivations above (and subsequently) is slightly different than the commonly accepted definition requiring knowledge of a cross-sectional area of the porous medium. For known fracture aperture size and average spacing between adjacent fractures these two definitions could be reconciled by redefinition of A in Eq. 14. For lack of a better term, for simplicity, and to maintain the usual form of Darcy's law, we use "surface hydraulic conductivity" to describe and characterize the inverse of "surface hydraulic resistivity".

2/22/99

Development of different averaging procedures to obtain surface hydraulic conductivity for a unit element

Two averaging methods are applied to derive the effective, unsaturated, hydraulic conductivity for fracture surface roughness elements from their respective film (Eqs.15 and 16) and corner (Eq.17) conductivities. One method involves averaging over liquid cross-sectional area in the films and occupying the corner. The other approach averages over the projected lengths of film and partially-filled corner segments transverse to flow direction as depicted in Fig.1. The latter method appears advantageous from a practical point of view because quantities can be measured directly. In other words, experimental information on the average hydraulic conductivity per fracture length (transverse to flow) is likely to be more observable than total liquid cross sectional area. However, for the sake of completeness and to facilitate comparisons, both methods will be developed and discussed.

Liquid Area Averaged Hydraulic Conductivity – $K_A(\mu)$

To obtain expressions for individual roughness element liquid area averaged hydraulic conductivity as a function of chemical potential we must distinguish between two stages of pit filling (completely full and partially filled pits). These two states are separated by the critical chemical potential μ_c (Eq.6). The average hydraulic conductivity for chemical potentials, which are more negative than the critical chemical potential ($\mu < \mu_c$; where pits are partially filled), is given as:

$$K_{A1}(\mu) = \frac{K_F(\mu)A_{F1} + K_C(\mu)A_{C1}\delta}{A_{F1} + A_{C1}} \tag{18}$$

where A_{F1} and A_{C1} are the liquid-filled cross-sectional areas of the film and the corner/pit (prior to pit filling), respectively, and δ is a connectivity factor ($0.0<\delta<1.0$). The factor δ accounts for partial connectivity among neighboring pits or grooves in the direction of flow (i.e., the fraction of pits and grooves in the cross-section that participate in corner flow). When observing adjacent cross-sections, not all pits on the fracture wall are likely to be connected to form continuous grooves (see Fig.4). These "isolated" pits are not contributing to corner flow, and thus are not considered as part of the K_C contribution (see Eq.18). This spatial connectivity factor is required even at the individual roughness element level for: (1) proper introduction of connectivity issues operating at the fracture surface scale; and (2) to facilitate the use of a single roughness element for representation of the entire fracture surface roughness behavior. The individual contributions of film $K_{AF1}(\mu)$ and corner flows $K_{AC1}(\mu)$ from Eq.18 are given as:

$$K_{AF1}(\mu) = \frac{K_F(\mu)A_{F1}}{A_{F1}+A_{C1}} \qquad K_{AC1}(\mu) = \frac{K_C(\mu)A_{C1}\delta}{A_{F1}+A_{C1}} \qquad (19)$$

For chemical potentials greater than or equal to μ_c, the liquid-area averaged hydraulic conductivity is given as:

$$K_{A2}(\mu) = \frac{K_F(\mu)A_{F2}+K_C(\mu)A_{C2}\,\delta}{A_{F2}+A_{C2}} \qquad (20)$$

where A_{F2} and A_{C2} are the liquid filled cross-sectional areas after a complete filling of the pit. The individual contributions of film and corner flows for this case are derived in the same fashion as for partially filled pits:

$$K_{AF2}(\mu) = \frac{K_F(\mu)A_{F2}}{A_{F2}+A_{C2}} \qquad K_{AC2}(\mu) = \frac{K_C(\mu)A_{C2}\,\delta}{A_{F2}+A_{C2}} \qquad (21)$$

The liquid-filled cross-sectional areas associated with films and corners A_{F1}, A_{C1}, A_{F2}, and A_{C2} are derived as follows:

The derivations for liquid filled cross-sectional areas prior to pit filling ($\mu<\mu_c$) were already introduced previously. The liquid filled cross-sectional area in corners A_{C1} is calculated according to Eq.3, and the film Area A_{F1} according to Eq.5.

The cross-sectional area of liquid retained in the corner after pit filling ($\mu<\mu_c$) is given as:

$$A_{C2} = L^2 \tan(\gamma/2) \qquad (22)$$

The cross-sectional area of the liquid film after pit filling ($\mu \geq \mu_c$) is defined as:

$$A_{F2}(\mu) = h(\mu)\big(L\beta + 2(1-\delta)L\tan(\gamma/2)\big) \qquad (23)$$

Remark:
It seems reasonable to ignore the contribution of the film forming over a flowing groove area due to surface perturbations introduced by the hydrodynamic regime within the groove below. The situation must be rectified for non-flowing pits where local depressions in the liquid-vapor interface (after pit filling) are not likely to be sustainable (from surface energy considerations). Thus, we propose to base the correction on the fraction of connected and flowing pits $(1-\delta)$ where δ is a "pit connectivity" factor.

Length Averaged Hydraulic Conductivity – $K_L(\mu)$

Expressions for averaging hydraulic conductivity by the roughness element projected length transverse to flow are derived in the same fashion considering two pit-filling stages. The fracture length-averaged hydraulic conductivity as a function of chemical potential prior to pit filling ($\mu < \mu_c$) is given as:

$$K_{L1}(\mu) = \frac{K_F(\mu)L_{F1} + K_C(\mu)L_{C1}}{L_{F1} + L_{C1}} \qquad (24)$$

and the average hydraulic conductivity after pit-filling is defined as:

$$K_{L2}(\mu) = \frac{K_F(\mu)L_{F2} + K_C(\mu)L_{C2}}{L_{F2} + L_{C2}} \qquad (25)$$

with film and corner contributions calculated in the same fashion as for area averaged conductivity, and with L_{F1}, L_{C1}, L_{F2}, and L_{C2} as the projected lengths derived as follows:

The average surface conductivity K_L (Eqs.24 and 25) is related to the projected lengths (transverse to flow direction) of the regions with film and corner flow as shown in Fig.1. The projected length of film and corner covered surface area prior to pit filling ($\mu < \mu_c$) is given as:

$$L_{F1}(\mu) = L(\beta + 2\tan(\gamma/2)) - 2\delta r(\mu)\cos(\gamma/2) \qquad (26)$$

$$L_{C1}(\mu) = 2\delta r(\mu)\cos(\gamma/2)) \qquad (27)$$

The projected lengths after pit filling ($\mu \geq \mu_c$) are defined as:

$$L_{F2} = L(\beta + 2(1-\delta)\tan(\gamma/2)) \qquad (28)$$

$$L_{C2} = 2L\delta\tan(\gamma/2)) \qquad (29)$$

3/1/99

Statistical scheme to represent the fracture surface as a distribution of geometric attributes of the unit element

A more realistic representation of natural fracture surfaces requires a distribution of roughness element geometric attributes (pit sizes, angles, and associated "flat" segments). A conceptual sketch for a distribution of surface roughness elements on a fracture surface is depicted in Fig. 4.
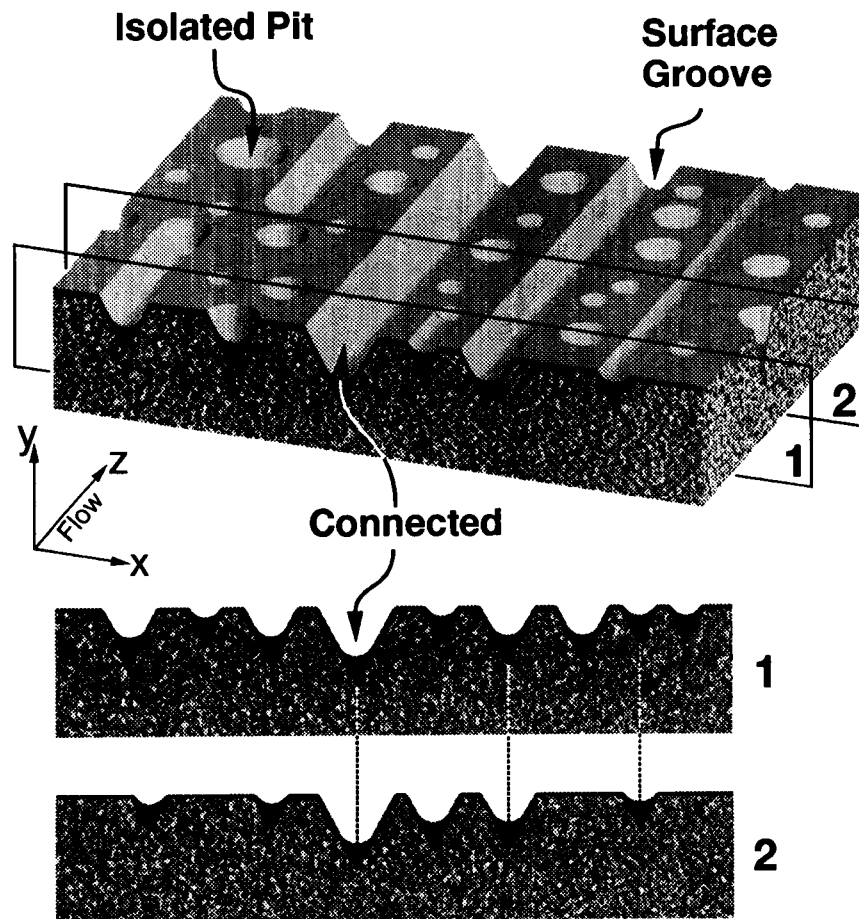
Fig.4 A conceptual sketch for a distribution of roughness elements forming a rough fracture surface, and illustration of pit/groove connectivity between two adjacent cross sections transverse to flow direction.

Statistical Distribution of Pit/Groove Depths

Fracture surface roughness is represented by a statistical Gamma distribution of pit depths (L). The pit angle (γ) is kept constant in subsequent derivations to retain mathematical tractability. The Gamma distribution [Rice, 1995] facilitates derivation of closed-form expressions for the expected value of the fracture surface unsaturated

hydraulic conductivity. The Gamma density function for the pit depth, f(L), is dependent on two parameters, ξ and ω:

$$f(L) = \frac{L^{\xi}}{\xi! \omega^{\xi+1}} \exp\left(-\frac{L}{\omega}\right) \qquad L \geq 0 \qquad\qquad (30)$$

The parameter ξ is limited to integer values only. The cumulative Gamma distribution is expressed as:

$$F(L) = \int_{0}^{L} \frac{t^2}{2\omega^3} \exp\left(-\frac{t}{\omega}\right) dt \qquad t \geq 0 \qquad\qquad (31)$$

The range of admissible L values for the assumed gamma distribution was limited to values between L_{min} and L_{max}, representing the smallest and largest pit depths. To ensure that the integration of Eq.30 within the limits L_{min} and L_{max} is as close to unity as possible, or to truncate the distribution tail effect at L_{max}, we minimize the expression

$$\text{minimize} \qquad \left(\int_{L_{min}}^{L_{max}} f(L) dL - 1\right) \qquad\qquad (32)$$

(i.e., the deviation between the cumulative Gamma distribution and unity) by adjusting ω for a given L_{max}.

The Expected Value of Unsaturated Surface Hydraulic Conductivity

Analogous to hydraulic conductivity calculations for individual elements, both averaging methods, projected lengths average and liquid cross-sectional area average are derived to determine unsaturated hydraulic conductivity for an assemblage of elements. In the following we first focus on developing expressions for length-averaged hydraulic conductivity because of the more realistic application to observable quantities.

Length-averaged hydraulic conductivity

The average hydraulic conductivity K_L is related to the projected lengths of film and corner flow regions as shown in Fig.1. Closed-form expressions for projected length conductivity K_L as a function of chemical potential μ are derived considering two filling stages – partially liquid-filled pits, and completely filled pits.

Pits are considered completely full when the curved liquid-vapor interface reaches the pit edge (contact point with the flat segment). The critical pit depth L_1 separating full and

partially filled pits varies with the chemical potential μ, and is calculated from the radius of liquid-vapor interface curvature $r(\mu)$, and pit depth L by rearranging Eq.6:

$$-\frac{\sigma}{\rho\mu\tan(\gamma/2)} = \frac{L_1(\mu)}{\cos(\gamma/2)} \quad \Rightarrow \quad L_1(\mu) = -\frac{\sigma\cos(\gamma/2)}{\rho\mu\tan(\gamma/2)} \tag{33}$$

The expected value of averaged surface hydraulic conductivity as a function of chemical potential $< K_L(\mu) >$ is thus expressed as the sum of two terms related to the pit filling stages:

$$< K_L(\mu) > = < K_{L1}(\mu) > + < K_{L2}(\mu) > \tag{34}$$

with:

$$< K_{L1}(\mu) > = \int_{L_1}^{L_{max}} \frac{K_F(\mu)L_{F1} + K_C(\mu)L_{C1}}{L_{F1} + L_{C1}} f(L)dL \tag{34a}$$

$$< K_{L2}(\mu) > = \int_{L_{min}}^{L_1} \frac{K_F(\mu)L_{F2} + K_C(\mu)L_{C2}}{L_{F2} + L_{C2}} f(L)dL \tag{34b}$$

The first term in Eq.34 is the expected value of surface conductivity for partially filled pits obtained by integrating from L_1 (Eq.33) to the maximum pit depth L_{max}. Equations 15, 16, and 17 are used to calculate corner and film conductivities.

The second term $K_{L1}(\mu)$ covers all full pits/grooves. The lower limit of integration is the smallest pit depth L_{min} (L_{min} was set to an arbitrary value of 10 µm in this study), and the upper integration limit is calculated according to Eq.33. To observe the limiting condition for pit filling (the radius of curvature used in the estimation of K_C (Eq.17) touches pit edge), we relate the curvature to pit geometry by solving Eq.33 for $r(\mu)$ ($r = \sigma/\rho\mu$) and substitute the resulting expression into Eq.17. The resulting equation for corner hydraulic conductivity $K_C(\mu)$ for full pits is given as:

Substitution of $r(\mu) = -\sigma/\rho\mu$ into Eq.33 and solving for $r(\mu)$

$$L = r(\mu)\frac{\cos(\gamma/2)}{\tan(\gamma/2)} \quad \Rightarrow \quad r(\mu) = L\frac{\tan(\gamma/2)}{\cos(\gamma/2)}$$

Substitution of $r(\mu)$ into Eq.17

$$K_C(\mu) = \frac{\rho g}{\eta_0}\frac{r^2(\mu)}{\varepsilon} \quad \Rightarrow \quad K_C(\mu) = L^2\frac{\tan^2(\gamma/2)\rho g}{\cos^2(\gamma/2)\varepsilon\eta_0}$$

$$\tag{35}$$

The film conductivity $K_F(\mu)$ is independent of fracture geometry and is calculated according to Eqs.15 and 16, taking into consideration variable liquid viscosity for films thinner than 10 nm. The projected lengths L_{F1}, L_{C1}, L_{F2}, and L_{C2} were defined previously for single unit elements.

Detailed closed-form expressions for the integrals in Eq.34 are derived using Mathematica Version 3.0.

Remark:

ω and ξ are shape parameters of the Gamma distribution. The parameter ξ is limited to integer values by definition of the Gamma distribution. A value of $\xi=2$ was chosen in this study to obtain closed form expressions for hydraulic conductivity (higher values prevent closed form expressions for Eq.34 and Eq.36). By increasing ξ the skewness of the distribution changes from right to left.

The solution for fracture elements with partially filled pits (Eq.34a) is given as:

$$< K_{L1}(\mu) > = \frac{1}{2(2C_1+\beta)\omega^2}\left(V_1(\mu)\left(V_2(\mu)(K_C(\mu)-K_F(\mu))(L_1(\mu)+\omega)+K_F(\mu)(2C_1+\beta)\left(L_1(\mu)^2+2L_1(\mu)\omega+2\omega^2\right)\right)-\right.$$

$$\left. C_2\left(V_2(\mu)(K_C(\mu)-K_F(\mu))(L_{max}+\omega)+K_F(\mu)(2C_1+\beta)\left(L_{max}^2+2L_{max}\omega+2\omega^2\right)\right)\right)$$

with the constants:

$$C_1 = \tan(\gamma/2)$$

$$C_2 = \text{Exp}\left(-\frac{L_{max}}{\omega}\right)$$

and the variables:

$$V_1(\mu) = \text{Exp}\left(-\frac{L_1(\mu)}{\omega}\right)$$

$$V_2(\mu) = 2\,\delta\,r(\mu)\cos(\gamma/2)$$

The contribution of the films in fracture elements with partially filled pits is calculated as:

$$< K_{L1F}(\mu) > = \int_{L_1}^{L_{max}} \frac{K_F(\mu)L_{F1}}{L_{F1}+L_{C1}}f(L)dL$$

$$< K_{L1F}(\mu) > = \frac{K_F(\mu)}{2(2C_1 + \beta)\omega^2}\left(V_1(\mu)\left(-V_2(\mu)\left(L_1(\mu)+\omega\right)+(2C_1+\beta)\left(L_1(\mu)^2+2L_1(\mu)\omega+2\omega^2\right)\right)\right)-$$

$$C_2\left(-V_2(\mu)\left(L_{max}+\omega\right)+(2C_1+\beta)\left(L_{max}^2+2L_{max}\,\omega+2\omega^2\right)\right)\Big)$$

The contribution of corners is given as:

$$< K_{L1C}(\mu) > = \int_{L_1}^{L_{max}} \frac{K_C(\mu)L_{C1}}{L_{F1}+L_{C1}}f(L)dL$$

$$< K_{L1C}(\mu) > = \frac{V_2(\mu)K_C(\mu)}{2(2C_1+\beta)\omega^2}\left(V_1(\mu)\left(L_1(\mu)+\omega\right)-C_2\left(L_{max}+\omega\right)\right)$$

The solution for the second term (Eq. 34b) is given as:

$$< K_{L2}(\mu) > = \left(2(C_4+C_5)\omega^2\right)^{-1}\left(-V_1(\mu)\left(C_4 K_F(\mu)\left(L_1(\mu)^2+2L_1(\mu)\omega+2\omega^2\right)+C_3 C_5\left(L_1(\mu)^4+4L_1(\mu)^3\omega+\right.\right.\right.$$

$$\left.12L_1(\mu)^2\omega^2+24L_1\omega^3+24\omega^4\right)\Big)+C_6\left(C_4 K_F(\mu)\left(L_{min}^2+2L_{min}\,\omega+2\omega^2\right)+C_3 C_5\left(L_{min}^4+4L_{min}^3\omega+\right.\right.$$

$$\left.12L_{min}^2\omega^2+24L_{min}\,\omega^3+24\omega^4\right)\Big)\Big)$$

with the constants:

$$C_3 = \frac{C_1^2\,\rho g}{\cos^2(\gamma/2)\varepsilon\,\eta_0}$$

$$C_4 = \beta+2(1-\delta)C_1$$

$$C_5 = 2\delta C_1$$

$$C_6 = Exp\left(-\frac{L_{min}}{\omega}\right)$$

The contribution of the films in fracture elements with full pits is calculated as:

$$< K_{L2F}(\mu) > = \int_{L_{min}}^{L_1} \frac{K_F(\mu)L_{F2}}{L_{F2}+L_{C2}}f(L)dL$$

$$< K_{L2F}(\mu) > = \frac{C_4 K_F(\mu)}{2(C_4+C_5)\omega^2}\left(-V_1(\mu)\left(L_1(\mu)^2+2L_1(\mu)\omega+2\omega^2\right)+C_6\left(L_{min}^2+2L_{min}\,\omega+2\omega^2\right)\right)$$

The contribution of corners is given as:

$$< K_{L2C}(\mu) > = \int_{L_{min}}^{L_1} \frac{K_C(\mu)L_{C2}}{L_{F2}+L_{C2}}f(L)dL$$

$$< K_{L2C}(\mu) > = \frac{C_3 C_5}{2(C_4+C_5)\omega^2}\left(-V_1(\mu)\left(L_1(\mu)^4+4L_1(\mu)^3\omega+12L_1(\mu)^2\omega^2+24L_1(\mu)\omega^3+24\omega^4\right)+\right.$$

$$\left.C_6\left(L_{min}^4+4L_{min}^3\omega+12L_{min}^2\omega^2+24L_{min}\,\omega^3+24\omega^4\right)\right)$$

Liquid area-averaged hydraulic conductivity

Analytical expressions for the expected value of liquid area averaged hydraulic conductivity $< K_A(\mu) >$ are derived in the same fashion as for length-averaged conductivity, and are subjected to identical limits of integration:

$$< K_A(\mu) >=< K_{A1}(\mu) > + < K_{A2}(\mu) > \tag{36}$$

with:

$$< K_{A1}(\mu) >= \int_{L_1}^{L_{max}} \frac{K_F(\mu) A_{F1} + K_C(\mu) A_{C1} \delta}{A_{F1} + A_{C1}} f(L)dL \tag{36a}$$

$$< K_{A2}(\mu) >= \int_{L_{min}}^{L_1} \frac{K_F(\mu) A_{F2} + K_C(\mu) A_{C2} \delta}{A_{F2} + A_{C2}} f(L)dL \tag{36b}$$

Closed-form expressions for liquid cross-sectional area averaged hydraulic conductivity are somewhat more complicated involving exponential integrals. The analytical solution for Eq. 36a is given as:

$$< K_{A1} >= \frac{1}{2 V_3(\mu)^2 \omega^2} \Big(V_1(\mu) \big(V_4(\mu)(V_5(\mu)\delta K_C(\mu) - V_5(\mu) K_F(\mu)) + V_5(\mu)\delta K_C(\mu)(- V_5(\mu) + V_3(\mu)(L_1(\mu) + \omega)) +$$

$$K_F(\mu)\big(V_5(\mu)^2 - V_3(\mu) V_5(\mu)(L_1(\mu) + \omega) + V_3(\mu)^2 (L_1(\mu)^2 + 2L_1(\mu)\omega + 2\omega^2)\big)\big) - C_6(V_4(\mu)(V_5(\mu)\delta K_C(\mu) -$$

$$V_5(\mu) K_F(\mu)) + V_5(\mu)\delta K_C(\mu)(- V_5(\mu) + V_3(\mu)(L_{max} + \omega)) + K_F(\mu)\big(V_5(\mu)^2 - V_3(\mu) V_5(\mu)(L_{max} + \omega) +$$

$$V_3(\mu)^2 (L_{max}^2 + 2L_{max}\omega + 2\omega^2)\big)\big) + \frac{(V_4(\mu) - V_5(\mu))^2 V_6(\mu)(- V_5(\mu)\delta K_C(\mu) + V_5(\mu) K_F(\mu))(- E_1[U_1(\mu)] + E_1[U_2(\mu)])}{2 V_3(\mu)^3 \omega^3}$$

with the variables:

$$V_3(\mu) = h(\mu)\left(\beta + \frac{2}{\cos\left(\frac{\gamma}{2}\right)}\right)$$

$$V_4(\mu) = \frac{2h(\mu)r(\mu)}{C_1}$$

$$V_5(\mu) = r(\mu)^2 F$$

$$V_6(\mu) = Exp\left(\frac{- V_4(\mu) + V_5(\mu)}{V_3(\mu)\omega}\right)$$

and the arguments of the exponential integrals $E_1[U]$:

$$U_1(\mu) = \frac{-V_4(\mu) + V_5(\mu) + V_3(\mu)L_1(\mu)}{V_3(\mu)\omega}$$

$$U_2(\mu) = \frac{-V_4(\mu) + V_5(\mu) + V_3(\mu)L_{max}}{V_3(\mu)\omega}$$

> *Remark:*
>
> The exponential integral $E_1[U]$ is defined as:
>
> $$E_1[U] = \int_U^\infty \frac{e^{-t}}{t}\, dt$$
>
> and is evaluated numerically using Mathematica 3.0 (Wolfram Res., Inc.). For arguments in the range $0 < U \leq 15$ the following series expansion may be applied for the evaluation:
>
> $$E_1[U] = -\gamma - \ln[U] - \sum_{n=1}^{150} \frac{(-1)^n U^n}{n\, n!}$$

The contribution of films is given as:

$$<K_{A1F}(\mu)> = \int_{L_1}^{L_{max}} \frac{K_F(\mu)A_{F1}}{A_{F1} + A_{C1}} f(L)dL$$

$$<K_{A1F}> = \frac{K_F(\mu)}{2 V_3(\mu)^3 \omega^3}\left(V_3(\mu)\omega\left(C_6\left(V_4(\mu)V_5(\mu) - V_5(\mu)^2 + V_3(\mu)V_5(\mu)L_{max} - V_3(\mu)^2 L_{max}^2 + \right.\right.\right.$$

$$V_3(\mu)\omega(V_5(\mu) - 2V_3(\mu)L_{max}) - 2V_3(\mu)^2\omega^2 \Big) + V_1(\mu)\Big(-V_4(\mu)V_5(\mu) + V_5(\mu)^2 - V_3(\mu)V_5(\mu)(L_1(\mu) + \omega) +$$

$$V_3(\mu)^2\left(L_1(\mu)^2 + 2L_1(\mu)\omega + 2\omega^2\right)\Big)\Big) + (V_4(\mu) - V_5(\mu))^2 V_5(\mu)V_6(\mu)\left(-E_1[U_1(\mu)] + E_1[U_2(\mu)]\right)\Big)$$

The contribution of corners is given as:

$$<K_{A1C}(\mu)> = \int_{L_1}^{L_{max}} \frac{K_C(\mu)A_{C1}\delta}{A_{F1} + A_{C1}} f(L)dL$$

$$<K_{A1C}> = \frac{V_5(\mu)\delta K_C(\mu)}{2 V_3(\mu)^3 \omega^3}\left(V_3(\mu)\omega\left(V_1(\mu)\left(V_4(\mu) - V_5(\mu) + V_3(\mu)(L_1(\mu) + \omega)\right)\right) - C_6\left(V_4(\mu) - V_5(\mu) + \right.\right.$$

$$V_3(\mu)(L_{max} + \omega)\Big)\Big) - (V_4(\mu) - V_5(\mu))^2 V_6(\mu)\left(-E_1[U_1(\mu)] + E_1[U_2(\mu)]\right)\Big)$$

The analytical solution for Eq. 36b representing full pits is given as:

$$< K_{A2}(\mu) >= \frac{1}{2C_1{}^6\omega^3}\left(C_1\,\omega\left(-V_1(\mu)\left(C_1{}^3V_7(\mu)K_F(\mu)(-V_7(\mu)+C_1(L_1(\mu)+\omega))+C_2\frac{C_4}{2}\left(V_7(\mu)^4-C_1V_7(\mu)^3\right.\right.\right.\right.$$

$$\left.(L_1(\mu)+\omega)+C_1{}^2V_7(\mu)^2\left(L_1(\mu)^2+2L_1(\mu)\omega+2\omega^2\right)-C_1{}^3V_7(\mu)\left(L_1(\mu)^3+3L_1(\mu)^2\omega+6L_1(\mu)\omega^2+6\omega^3\right)+\right.$$

$$\left. C_1{}^4\left(L_1(\mu)^4+4L_1(\mu)^3\omega+12L_1(\mu)^2\omega^2+24L_1(\mu)\omega^3+24\omega^4\right)\right)\right)+C_5\left(C_1{}^3V_7(\mu)K_F(\mu)(-V_7(\mu)+C_1(L_{min}+\omega))+\right.$$

$$C_2\frac{C_4}{2}\left(V_7(\mu)^4-C_1V_7(\mu)^3(L_{min}+\omega)+C_1{}^2V_7(\mu)^2\left(L_{min}{}^2+2L_{min}\omega+2\omega^2\right)-C_1{}^3V_7(\mu)\left(L_{min}{}^3+3L_{min}{}^2\omega+\right.\right.$$

$$\left.\left.6L_{min}\omega^2+6\omega^3\right)+C_1{}^4\left(L_{min}{}^4+4L_{min}{}^3\omega+12L_{min}{}^2\omega^2+24L_{min}\omega^3+24\omega^4\right)\right)\right)-V_7(\mu)^3V_8(\mu)$$

$$\left(C_2V_7(\mu)^2\frac{C_4}{2}-C_1{}^3K_F(\mu)\right)(-E_1[U_3(\mu)]+E_1[U_4(\mu)])\right)$$

with the variables:

$$V_7(\mu)=h(\mu)C_3$$

$$V_8(\mu)=Exp\left(\frac{V_7(\mu)}{C_1\omega}\right)$$

and the arguments of the exponential integrals $E_1[U]$:

$$U_3(\mu)=\frac{V_7(\mu)+C_1L_1(\mu)}{C_1\omega}$$

$$U_4(\mu)=\frac{V_7(\mu)+C_1L_{min}}{C_1\omega}$$

The contribution of films to Eq.36b is given as:

$$< K_{A2F}(\mu) >= \int_{L_{min}}^{L_1}\frac{K_F(\mu)A_{F2}}{A_{F2}+A_{C2}}f(L)dL$$

$$< K_{A2F} >= \frac{V_7(\mu)K_F(\mu)}{2C_1{}^3\omega^3}(C_1V_1(\mu)\omega(V_7(\mu)-C_1(L_1(\mu)+\omega))+C_1C_5\,\omega(-V_7(\mu)+C_1(L_{min}+\omega))+$$

$$V_7(\mu)^2V_8(\mu)(-E_1[U_3(\mu)+E_1[U_4(\mu)]])$$

The corner contribution is given as:

$$<K_{A2C}(\mu)> = \int_{L_{min}}^{L_1} \frac{K_C(\mu)A_{C2}\,\delta}{A_{F2}+A_{C2}} f(L)dL$$

$$<K_{A2C}> = \frac{C_2 C_4}{4 C_1{}^6 \omega^3}\Big(C_1\omega\big(-V_1(\mu)\big(V_7(\mu)^4 - C_1 V_7(\mu)^3 (L_1(\mu)+\omega)+C_1{}^2 V_7(\mu)^2 \big(L_1(\mu)^2 + 2L_1(\mu)\omega + 2\omega^2\big)-$$

$$C_1{}^3 V_7(\mu)\big(L_1(\mu)^3 + 3L_1(\mu)^2\,\omega + 6L_1(\mu)\omega^2 + 6\omega^3\big)+C_1{}^4\big(L_1(\mu)^4 + 4L_1(\mu)^3\,\omega + 12L_1(\mu)^2\,\omega^2 +$$

$$24L_1(\mu)\omega^3 + 24\,\omega^4\big)\big)+C_5\big(V_7(\mu)^4 - C_1 V_7(\mu)^3 (L_{min}+\omega)+C_1{}^2 V_7(\mu)^2 \big(L_{min}{}^2 + 2L_{min}\,\omega + 2\omega^2\big)-$$

$$C_1{}^3 V_7(\mu)\big(L_{min}{}^3 + 3L_{min}{}^2\,\omega + 6L_{min}\,\omega^2 + 6\omega^3\big)+C_1{}^4\big(L_{min}{}^4 + 4L_{min}{}^3\,\omega + 12L_{min}{}^2\,\omega^2 +$$

$$24L_{min}\,\omega^3 + 24\,\omega^4\big)\big)\big)-V_7(\mu)^5 V_8(\mu)\big(-E_1[U_3(\mu)]+E_1[U_4(\mu)]\big)\Big)$$

3/14/99

Test of model performance by fitting the resulting closed-form expressions for a unit element and a distribution of elements to measurements.

The resulting closed-form expressions for individual roughness elements and the statistical distribution of a population of roughness elements are programmed in Microsoft Excel and fitted to the measurements reported by Tokunaga and Wan [1997] (measurements were digitized from their published figures).

Data digitized from Tokunaga and Wan [1997]
File: C:\SCI_NOTE_FRACTURE\Tetsu_02-02-99.xls

Film Thickness

Tokunaga and Wan - data

Pa	micron	J/kg	m
15	70	0.015	0.00007
30	30	0.03	0.00003
45	20	0.045	0.00002
68	8	0.068	0.000008
92	7	0.092	0.000007
117	5	0.117	0.000005
160	3	0.16	0.000003
215	2	0.215	0.000002
320	0.5	0.32	0.0000005

Pa	Transmissivity [m²/s]			Pa	vbar [m/d]	J/kg	m/s
30	1.00E-08	0.03	0.000333333	20	700	0.02	0.008102
50	3.80E-09	0.05	0.00019	50	76	0.05	0.00088
70	1.80E-09	0.07	0.000225	100	7	0.1	8.1E-05
100	8.00E-10	0.1	0.000114286	150	1.8	0.15	2.08E-05
150	3.70E-10	0.15	0.000123333	200	0.8	0.2	9.26E-06
180	2.40E-10	0.18	0.00008	250	0.4	0.25	4.63E-06
200	1.80E-10	0.2	0.00009				
250	8.00E-11	0.25	0.00004				

We proceed with illustrative examples first for an individual surface roughness element, and then we discuss ensemble of elements forming rough fracture surfaces. Both the projected surface length (transverse to flow) and the liquid-area-averaging methods are presented. We consider the effects of different groove angles (γ), spacing (βL), and connectivity factors (δ) on calculated surface hydraulic conductivity. These model calculations are compared with experimental results reported by Tokunaga and Wan [1997]. All physical constants used in the calculations are listed in Table 1.

Table 1. Physical constants and dimensions used in the sample calculations

Property	Symbol		Unit
Acceleration of Gravity	g	9.81	[m s^{-2}]
Density of Water (20°C)	ρ	998.23	[kg m^{-3}]
Hamaker Constant (solid-vapor through liquid)	A_{svl}	-1.9E-19	[J]
Surface Tension Water-vapor (20°C)	σ	0.07275	[N m^{-1}]
Viscosity Constant	τ	5.53E-10	[m]
Viscosity of Water (20°C)	η_0	0.001002	[kg m^{-1} s^{-1}]

Remarks:

(1) The Hamaker constant represents interactions between macro-objects such as mineral surfaces and liquid due to short-range (<100Å) van der Waals forces [Ackler et al., 1996; Bergström, 1997].

(2) The potential range for the Gamma distributed pith depth (L) was constrained to observed values reported by Tokunaga and Wan [1997] where most of the variations in surface "elevation" were between 0.5 and 2 mm.

Sample worksheet of calculations for a single roughness element

File: C:\SCI_NOTE_FRACTURE\Tetsu_02-02-99.xls

FLOW ON A ROUGH FRACTURE SURFACE - SINGLE ELEMENT

CONSTANTS			
Liquid viscosity	η	0.001002	[kg/m s]
Liquid density	ρ	998.23	[kg/m3]
Liquid surface tension	σ	0.07275	[N/m]
Acceleration of gravity	g	9.81	[m/s2]
Hamaker constant	Asvl	-1.9E-19	[J]
Viscosity constant	a	5.5324E-10	[m]
Gas constant	R	461.5	[J/kg K]
Temperature	T	293	[K]
Flow resistance triangle	β_T	443.965704	
Flow resistance square	β_s	93.93	
		0.89399666	
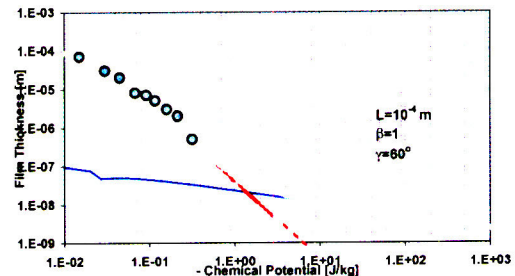
PIT DIMENSIONS

		0.0005	
Pit depth	L	0.001	[m]
Pit angle - degree	γ (deg)	120	
Pit angle - rad	γ (rad)	2.0944	
Roughness factor	β	4	
Number of segments	α	1	
Length of flat element	βL	4.0000E-03	[m]
Chem. pot. for pit filling	μ_p	-0.0210	[J/kg]
Radius of interface curvature at μ_p		0.0034641	[m]
Angularity factor	F(γ)	0.05375149	
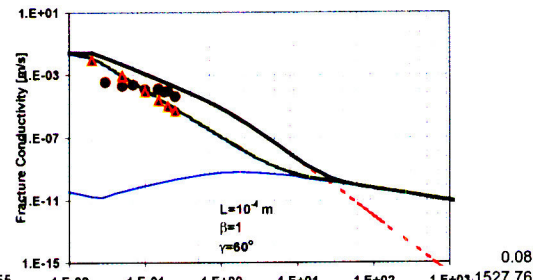
		0.01	0.02						0.08
Relative vapor pressure	p/psat	0.01	0.02						0.08
Chemical Potential	μ	-622708.81	-528981.795	-474155					1527.76
Chemical Potential *(-1)	−μ	622708.81	528981.795	474155.000					1527.764
Film thickness	h	2.53E-10	2.67E-10	2.77E-10	2.85E-10	2.92E-10	2.98E-10	3.04E-10	3.09E-10
Radius interface curvature	r	1.2E-10	1.4E-10	1.5E-10	1.7E-10	1.8E-10	1.9E-10	2.0E-10	2.1E-10
Resistance Parameters									
a	0.96589232								
b	0.051039418								
c	7.886603279								

Film Conductivity   FILMTHICKNESS < 10nm (variable viscosity) -------------------->

a/h			2.19E+00	2.07E+00	2.00E+00	1.94E+00	1.89E+00	1.85E+00	1.82E+00	1.79E+00
-E1[a/h]			-3.79E-02	-4.44E-02	-4.92E-02	-5.32E-02	-5.67E-02	-5.99E-02	-6.29E-02	-6.57E-02
exp[-a/h]			0.11239192	0.12617495	0.1358854	0.1437333	0.15048476	0.15650528	0.1620008	0.16709983
A			-2.7E-30	-3.7E-30	-4.5E-30	-5.3E-30	-6.0E-30	-6.8E-30	-7.5E-30	-8.2E-30
Viscosity			variable	variable	variable	variable	variable	variable	variable	variable
Average velocity (-dP/dz = 1)			8.9E-19	1.1E-18	1.4E-18	1.5E-18	1.7E-18	1.9E-18	2.0E-18	2.2E-18
Film conductivity	K_F	[m/s]	8.7E-15	1.1E-14	1.3E-14	1.5E-14	1.7E-14	1.8E-14	2.0E-14	2.2E-14
Area film	A_F	[m²]	2.025E-12	2.138E-12	2.217E-12	2.282E-12	2.337E-12	2.386E-12	2.432E-12	2.474E-12
$K_F * A_F$			1.77E-26	2.41E-26	2.95E-26	3.45E-26	3.93E-26	4.41E-26	4.87E-26	5.34E-26

Effective corner conductivity - connectivity (closed pits vs. continous grooves)   **1.00E-01**

Corner Conductivity

Average velocity (-dP/dz = 1)			3.079E-20	4.267E-20	5.311E-20	6.302E-20	7.276E-20	8.250E-20	9.234E-20	1.024E-19
Corner conductivity	K_c	[m/s]	3.02E-16	4.18E-16	5.20E-16	6.17E-16	7.13E-16	8.08E-16	9.04E-16	1.00E-15
Area corner	A_c	[m²]	7.36E-22	1.02E-21	1.27E-21	1.51E-21	1.74E-21	1.97E-21	2.21E-21	2.45E-21
$K_c * A_c$			2.22E-38	4.26E-38	6.60E-38	9.30E-38	1.24E-37	1.59E-37	2.00E-37	2.45E-37

Average Conductivity - Fracture Segment   **Area Average**

Total liquid occupied area $A_T=A_F+A_C$	[m²]	2.02E-12	2.14E-12	2.22E-12	2.28E-12	2.34E-12	2.39E-12	2.43E-12	2.47E-12
Average conductivity	K	8.72E-15	1.13E-14	1.33E-14	1.51E-14	1.68E-14	1.85E-14	2.00E-14	2.16E-14
Film contribution		8.72E-15	1.13E-14	1.33E-14	1.51E-14	1.68E-14	1.85E-14	2.00E-14	2.16E-14
Corner contribution		1.10E-26	1.99E-26	2.98E-26	4.08E-26	5.30E-26	6.68E-26	8.21E-26	9.92E-26

Average Conductivity - Fracture Segment   **Surface Average**

Projected length of the fracture segment M*	[m]	7.46E-03							
Projected length of the corner interface M_c	[m]	1.17E-10	1.38E-10	1.54E-10	1.67E-10	1.80E-10	1.92E-10	2.03E-10	2.13E-10
Projected length of the film interface M_F	[m]	7.46E-03	7.46E-03	7.46E-03	7.46E-03	7.46E-03	7.46E-03	7.46E-03	7.46E-03
Total length film L_F	[m]	8.00E-03	8.00E-03	8.00E-03	8.00E-03	8.00E-03	8.00E-03	8.00E-03	8.00E-03

Fit of unit element expressions to Tokunaga and Wan's measurements

Liquid retention on the rock surface as a function of chemical potential was calculated and compared with experimental results expressed as a uniform "effective" film thickness. Representative geometrical parameters (L, β, and γ) were fitted to yield the best match fit between model calculations and measurements (Fig.5a). The modeled "effective" film thickness as a function of μ was calculated by dividing the liquid filled cross-sectional area with the projected roughness element length ($\beta L+2L\tan(\gamma/2)$, see Fig.1). The individual contributions of capillarity and adsorption to liquid storage are illustrated and show a crossover for chemical potential values of $\mu=-1$ to -2 J/kg.

Fracture length-averaged unsaturated hydraulic conductivity $K_L(\mu)$ (Eq.34) was calculated for the same element geometry as used for "effective film" calculations (i.e., $L=10^{-3}$ m; $\beta=4$; and $\gamma=120^{0}$). The average film velocity reported by Tokunaga and Wan [1997] (see their Fig. 8) were obtained by two methods: (1) by using the average film thickness in smooth film equation (Eq.15, denoted as v-bar), and (2) by dividing their estimated transmissivity by the effective film thickness (denoted as T). The connectivity factor δ is an additional parameter required for matching calculated and experimental surface hydraulic conductivity. The results with $\delta=0.1$ are depicted in Fig.5b showing a reasonable agreement between calculated $K_L(\mu)$ and Tokunaga and Wan's [1997] average film velocities that were measured under unit pressure gradient conditions. The contributions of corners (K_{LC}) and films (K_{LF}) to the overall value of $K_L(\mu)$ are shown. Similar to liquid storage behavior, a crossover from corner-domination to film-domination is observed near chemical potential values of $\mu<-6$ J/kg. The simultaneous agreement with average film thickness and film velocity (which for a unit gradient equals surface conductivity) is remarkable considering the use of only one surface roughness element for both processes. These results illustrate the potential usefulness of the proposed approach for modeling liquid retention and conductivity on rough rock surfaces.
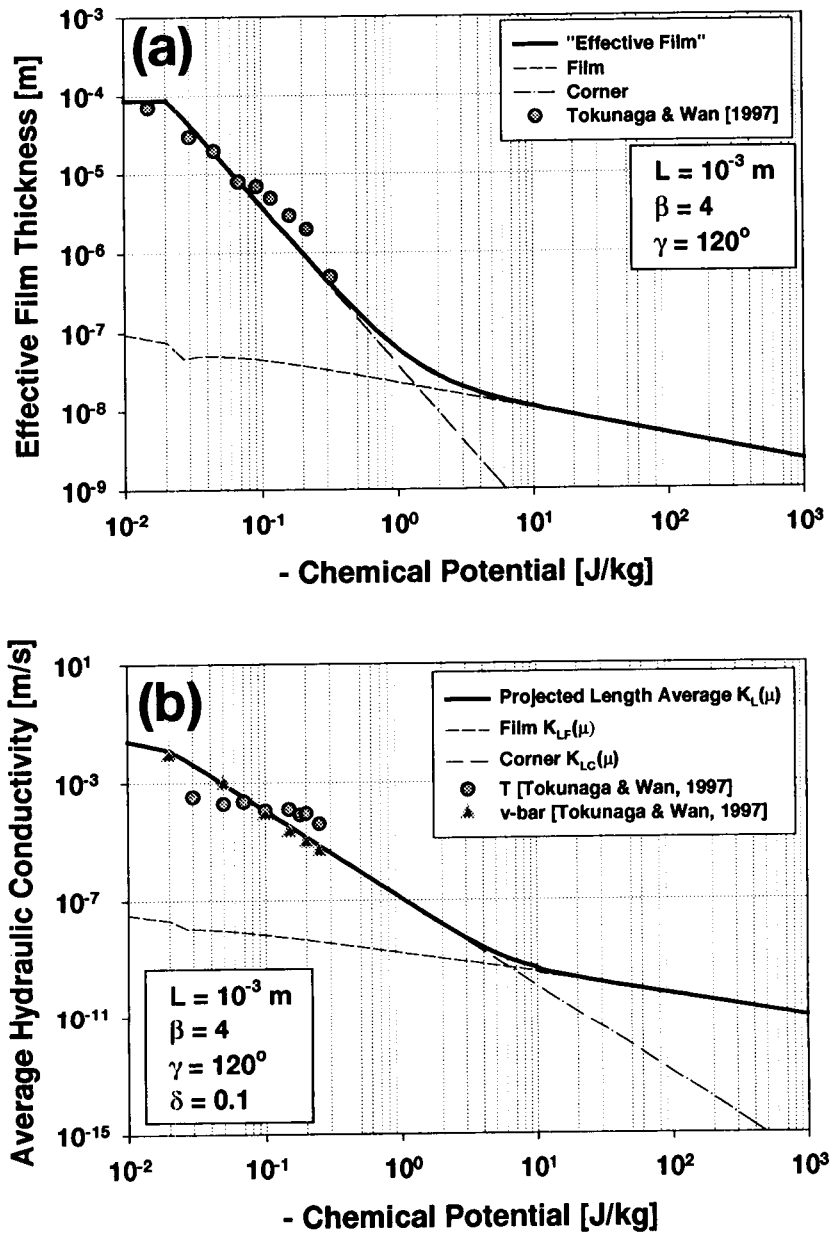
Fig.5 Comparison of model calculations for an individual fracture element with experimental data of Tokunaga and Wan [1997]. T denotes transmissivity divided by the average film thickness; v-bar denotes average film velocity evaluated with the smooth film equation [Tokunaga and Wan, 1997].

Additional sample calculations for unit roughness elements

We also investigated effects of surface roughness on liquid storage and surface hydraulic conductivity for $\delta=1$ (100% connectivity) by comparing two different groove densities characterized by the spacing parameter β. The results for a surface represented by an individual element are depicted in Fig.6a for $\beta=1$ (small spacing = rough surface), and in Fig. 6b for $\beta=100$ (large spacing = smooth surface). As expected, surface liquid retention (expressed as effective film thickness) for a given chemical potential was larger for the rough surface relative to the smooth surface. The storage difference diminishes with decreasing chemical potential (more negative), and the amount of liquid storage for $\mu<-100$ J/kg is very similar (dominated by thin liquid films). The crossover between capillary- and film-dominant storage occurs at lower potential values for the rough surface.

Significant differences were found in the behavior of $K_L(\mu)$ and $K_A(\mu)$, especially for the smooth surface (Fig.6b bottom). The $K_L(\mu)$ value for a rough surface is approximately in the same range as that of $K_A(\mu)$ at high potentials, whereas for smooth surfaces a difference of about two orders of magnitude exists $[K_A(\mu),>K_L(\mu)]$. These differences diminish with decreasing chemical potential (as it becomes more negative), until they practically vanish when film flow becomes dominant. These differences are attributed to the large carrying capacity of corner flow over similar liquid cross-section in a film configuration. The transition from corner to film dominated flow regimes for a smooth surface occurs at higher potentials than for the rough surface (similar to the liquid storage behavior).

An interesting transitional behavior in film contribution (K_{AF}) to $K_A(\mu)$ as a function of μ is observed for the two surfaces (more pronounced in the rough surface). The increase and later a decrease in film contribution represent an interplay between the reduction of film thickness with decreasing potential, and the creation of new film surfaces with the receding menisci into the grooves and pits. The total response is dependent on the proportions of these two opposing processes as shown in Fig. 6.
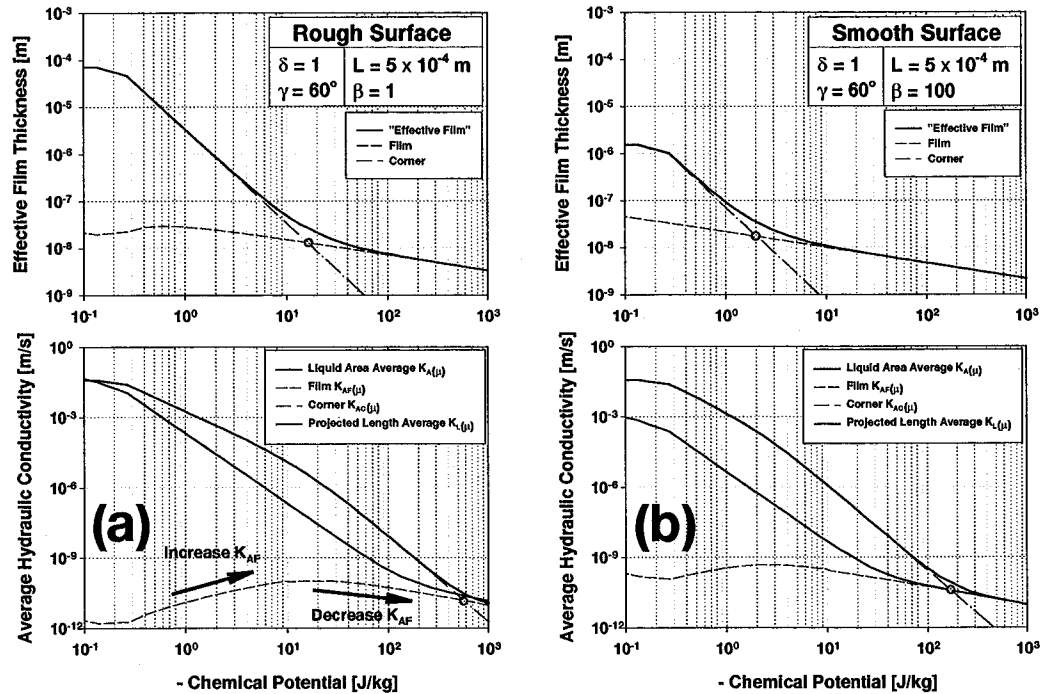
Fig. 6 Model calculations of individual element's effective film thickness and unsaturated hydraulic conductivity for (a) small β (rough surface) and (b) high β (smooth surface). Note the increase in film contribution to hydraulic conductivity.

Matching a distribution of roughness elements to Tokunaga and Wan's measurements

The statistical representation of pit depth (L) yields analytical expressions for the expected values of "effective" film thickness, liquid-area averaged hydraulic conductivity $<K_A(\mu)>$ (where square brackets denote expected value operation), and fracture length-weighted unsaturated hydraulic conductivity $<K_L(\mu)>$. To test the analytical solutions, we again used the experimental data of Tokunaga and Wan [1997] in the same fashion as for the representative (individual) roughness element. The maximum pit depth for the Gamma distributed L was set to 3 mm, and the pit angle was fixed at 120^0. The other parameters that provided the best fit to the data were $\beta=8$, and $\delta=0.1$. Surprisingly there was little difference in model performance between the individual representative element and the statistical representation (Fig.7). The only difference was smoother transitions in the hydraulic conductivity curve (and slightly different fitting parameters). The results of this limited test reinforce our conclusion that a representative surface roughness element is capable of modeling effective film thickness and unsaturated conductivity of rough fracture surfaces.
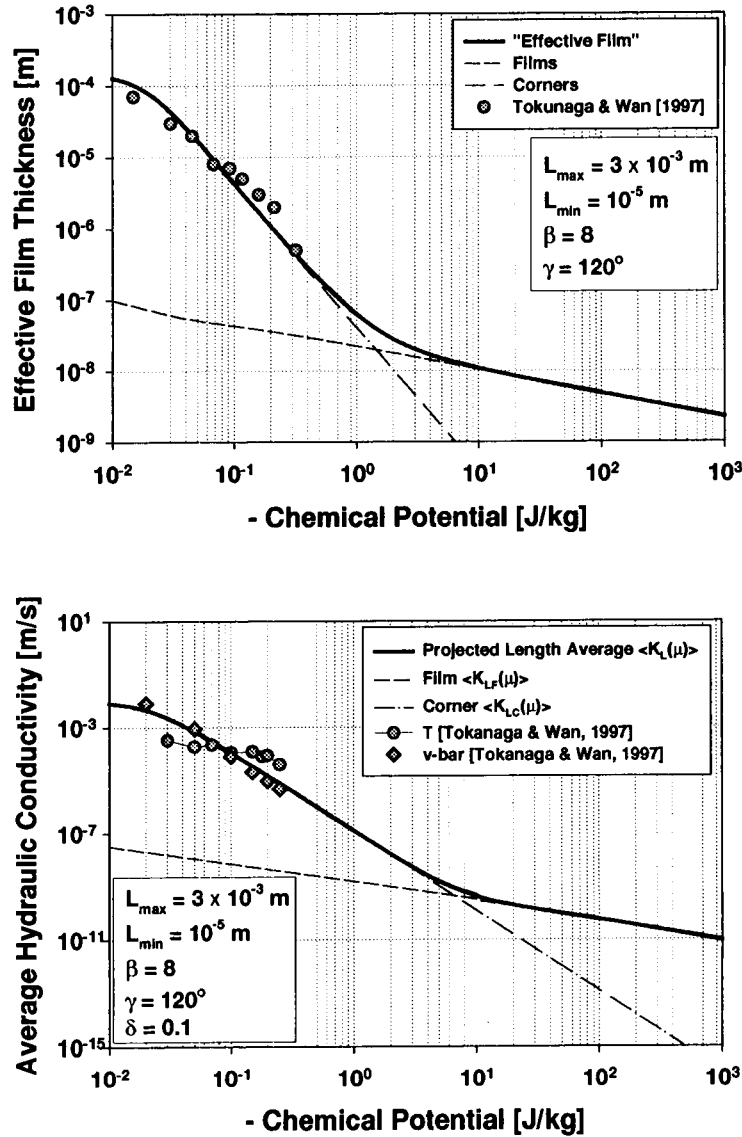
Fig.7 Comparison of model calculations for a statistical distribution of surface roughness elements with experimental data of Tokunaga and Wan [1997].

Additional sample calculations

The relationships between surface length–weighted hydraulic conductivity, $<K_L(\mu)>$, and liquid-area averaged hydraulic conductivity $<K_A(\mu)>$ for two different pit angles ($\gamma=30^0$ and 120^0) are depicted in Fig.8. Liquid area averaged hydraulic conductivity $<K_A(\mu)>$ was higher than the projected length averaged conductivity $<KL(\mu)>$ (for the assumed geometry) over the entire range of chemical potentials considered (-0.001 $< \mu < -$ 400000 J/kg). While calculations for $\gamma=30^0$ are reasonably close to the 1:1 line, large differences at midrange of chemical potential values are observed for $\gamma=120^0$. These

differences may be attributed to the relatively large carrying capacity of corner flow for $\gamma=120^0$ that tends to be underestimated by length averaging. Note that the cross-sectional area of grooves with a larger angle ($\gamma=120^0$) tend to be larger than that for a smaller angle ($\gamma=30^0$).
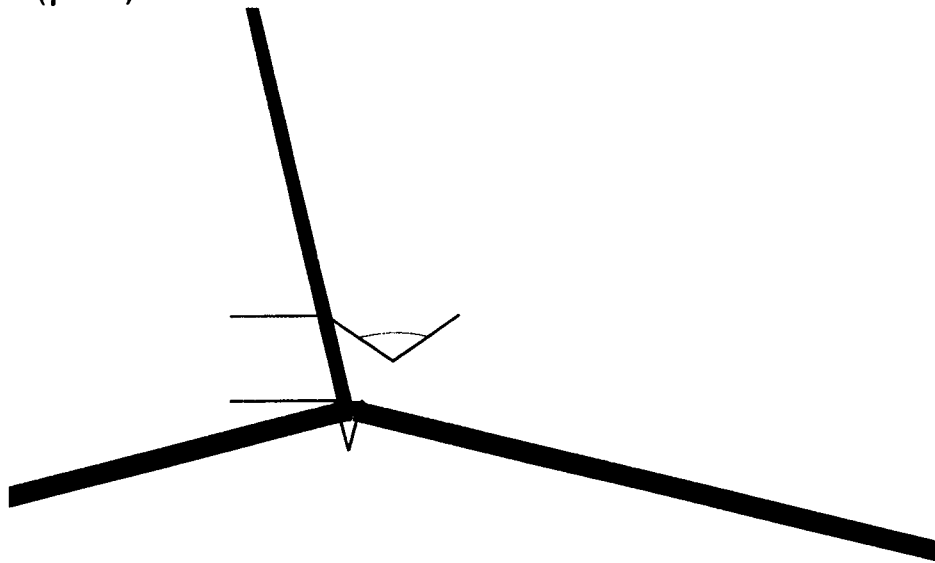

Fig.8 The relationships between the expected values (statistical representation) of unsaturated hydraulic conductivity for liquid cross-sectional area average $<K_A>$ versus fracture length averaged $<K_L>$ for groove angles of 30^0 and 120^0.

## Sample worksheet for a statistical distribution of roughness elements

File: C:\SCI_NOTE_FRACTURE\Fracture_Flow_Stat._Consid. _02-19-99.xls

FLOW ON A ROUGH FRACTURE SURFACE - STATISTICAL CONSIDERATIONS

CONSTANTS		
Liquid viscosity	η	0.001002 [kg/m s]
Liquid density	ρ	998.21 [kg/m3]
Liquid surface tension	σ	0.0728 [N/m]
Acceleration of gravity	g	9.81 [m/s2]
Hamaker constant	Asvl	-6E-20 [J]
Viscosity constant	a	5.5324E-10 [m]
Gas constant	R	461.5 [J/kg K]
Temperature	T	293 [K]
Flow resistance triangle	β_T	443.9657044
Resistance Parameters	a	2.12370
	b	-0.00414
	c	0.00784

	-1.9E-19
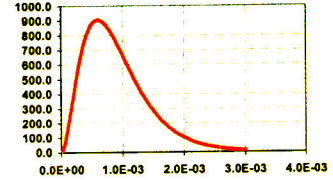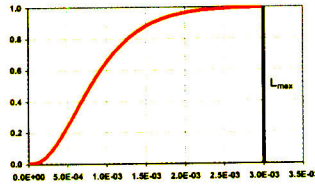
Gamma distribution parameter	ω	3.00E-04
Maximum pit depth	L_{max}	3.0000E-03 [m]
Minimum pit depth	L_{min}	1.0000E-05 [m]
Roughness factor	β	8
Pit angle - degree	γ (deg)	120
Pit angle - rad	γ (rad)	2.0944
Pit connectivity factor	δ	0.1000
Angularity factor	$F(\gamma)$	0.053751494
Solutioncell ω		2.77E-03 [m]
Mean L	L*	0.0009
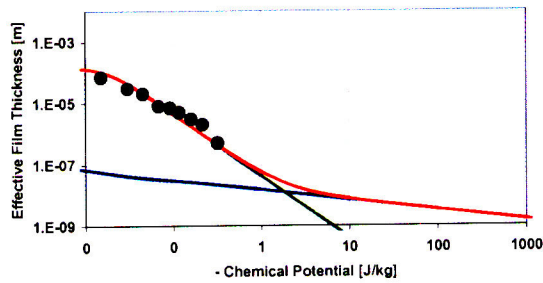
Variance	0.00000027
L*	0.010317691

	L [m]	density	cumulative
1	0.00E+00	0.00E+00	0.00E+00
2	3.03E-05	1.54E+01	1.59E-04
3	6.06E-05	5.56E+01	1.18E-03
4	9.09E-05	1.13E+02	3.70E-03
5	1.21E-04	1.82E+02	8.14E-03
6	1.52E-04	2.57E+02	1.48E-02
7	1.82E-04	3.34E+02	2.37E-02
8	2.12E-04	4.11E+02	3.50E-02
9	2.42E-04	4.85E+02	4.86E-02
10	2.73E-04	5.55E+02	6.44E-02
11	3.03E-04	6.19E+02	8.22E-02
12	3.33E-04	6.77E+02	1.02E-01
13	3.64E-04	7.29E+02	1.23E-01
14	3.94E-04	7.73E+02	1.46E-01
15	4.24E-04	8.10E+02	1.70E-01
16	4.55E-04	8.41E+02	1.95E-01
17	4.85E-04	8.65E+02	2.21E-01
18	5.15E-04	8.83E+02	2.47E-01
19	5.45E-04	8.94E+02	2.74E-01
20	5.76E-04	9.01E+02	3.01E-01
21	6.06E-04	9.02E+02	3.29E-01
22	6.36E-04	8.99E+02	3.56E-01
23	6.67E-04	8.92E+02	3.83E-01
24	6.97E-04	8.81E+02	4.10E-01
25	7.27E-04	8.67E+02	4.37E-01
26	7.58E-04	8.51E+02	4.63E-01
27	7.88E-04	8.32E+02	4.88E-01

Dani Or
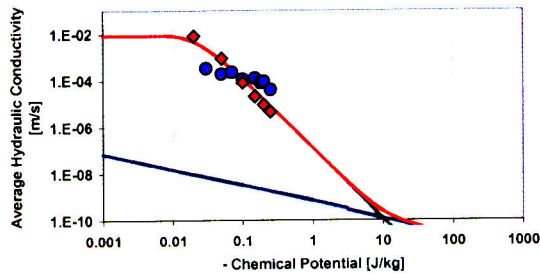
03/24/99 – Status

A paper was written for journal submission (Water Resource Research) and started on the CNWRA technical and programmatic process. Hence, it is a good idea to re-assess at this point the status of the work and where it may be heading.

Open issues (pertaining to the TEF-KTI) for future model improvement

- The assumed roughness geometry does not consider asperities and similar elements rising above mean fracture surface plane. Introduction of such elements should add realism to the model and capture some of the intermittent flow behavior observed. For inclusion of these elements we need to consider liquid build-up around conical objects (see "edge" in Appendix B of Tuller et al., 1999).

- The developments in this portion of the work coupled with additional studies on liquid configuration in porous media provide a sound basis for consistent representation of liquid retention and hydraulic conductivity in fractured porous media. First, we will expand the liquid retention model to include two pore space populations (rock matrix pores, and fractures). The disparity in pore size distribution should not present a problem for their joint modeling.

- The dynamics matrix-fracture interactions were not treated in this work – some of the rates of such interactions would be useful to capture the essence of potential bypass flow through these fracture surfaces (e.g., as liquid flux encounter low porosity/permeability layer such as the PTN).

References

Abramowitz, M., and I.E. Stegun, Handbook of mathematical functions with formulas, graphs, and mathematical tables, National Bureau of Standards Applied Mathematics, Series 55, 1964.

Ackler, H.D., R.H. French, and Y-T Chiang. Comparisons of Hamaker constants for ceramic systems with intervening vacuum or water: From force laws and physical properties. *J. Colloid Interface Sci., 179*, 460-469, 1996.

Bergström, L., Hamaker constants of inorganic materials, *Advances in Colloid and Interface Science, 70*, 125-169, 1997.

Derjaguin, B.V., N.V. Churaev, and V.M. Muller, Surface Forces, Plenum Publishing Corporation, Consultants Bureau, New York, 1987.

Dullien, F. A. L. , F. S. Y. Francis and I. F. MacDonald, Hydraulic continuity of residual wetting phase in porous media, *Journal of Colloid and Interface Science, 109* (1), 201-218, 1986.

Iwamatsu, M., and K. Horii, Capillary condensation and adhesion of two wetter surfaces, *Journal of Colloid and Interface Science, 182*, 400-406, 1996.

Low, P.F., Viscosity of interlayer water in montmorillonite, *Soil Sci. Soc. Am. J., 40*, 500-505, 1976.

Low, P.F., Nature and properties of water in montmorillonite-water systems, *Soil Sci. Soc. Am. J., 43*, 651-658, 1979.

McBride, M. B., and P. Baveye, Mobility of anion spin probes in hectorite gels: Viscosity of surficial water, *Soil Sci. Soc. Am. J., 59*, 388-394, 1995.

Or, D., and J. M. Wraith, Temperature effects on soil bulk dielectric permittivity measured by time domain reflectometry: A physical model, *Water Resour. Res., 35*(2), 371-383, 1999.

Or, D., and M. Tuller, Liquid retention and interfacial area in variably saturated porous media: Upscaling from pore to sample scale model, *Water Resour. Res.* (in review).

Ransohoff, T. C., and C. J. Radke, Laminar flow of a wetting liquid along the corners of a predominantly gas-occupied noncircular pore, *Journal of Colloid and Interface Science, 121*(2), 392-401, 1988.

Rice, J.A., Mathematical Statistics and Data Analysis, 2nd ed., Duxbury Press, Belmont, California, 1995.

Spurk, J.H., Fluid mechanics. Springer-Verlag, Berlin, Heidelberg, 1997.

Tokunaga, T. K., and J. Wan, Water film flow along fracture surfaces of porous rock, *Water Resour. Res., 33*(6), 1287-1295, 1997.

Tuller, M., D. Or, and L.M. Dudley, Adsorption and capillary condensation in porous media - Liquid retention and interfacial configurations in angular pores. *Water Resour. Res.* (in press), 1999.

SCIENTIFIC NOTEBOOK #354

DANI OR
Utah State University

TEF KTI

Volume I -- Flow in Unsaturated Fractured Porous Media,
Hydraulic Conductivity of Rough Surfaces (cont.)

Feb 1, 2000 notebook submission
Volume I Pages 33-62 plus appendices

Volume 1: Flow in Unsaturated Fractured Porous Media - Hydraulic Conductivity of Rough Surfaces (Continuation)

Thermal Effects - Key Technical Issue

Account Number: 20-1402-661
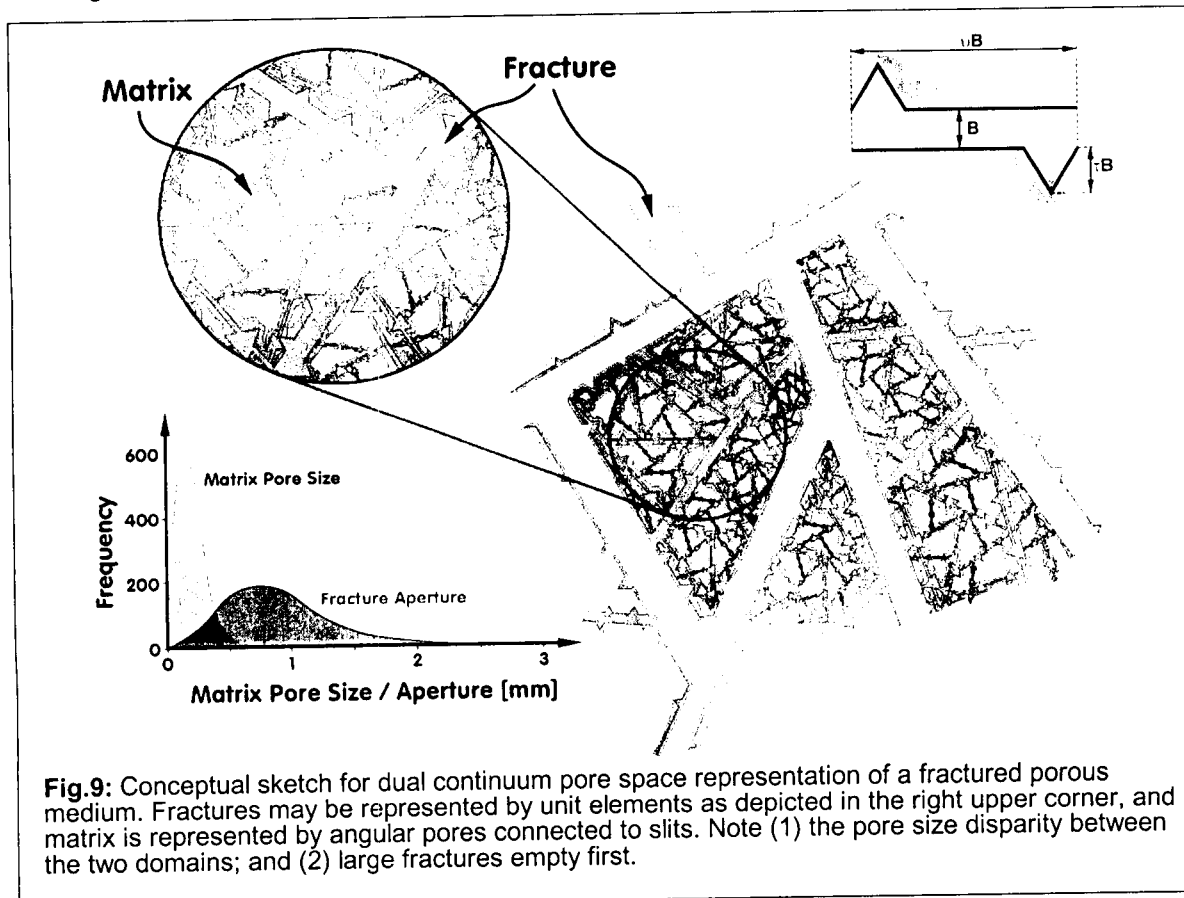Collaborators: Markus Tuller (USU), Randall Fedors, Ron Green (CNWRA)
Directories: C:\SCI_NOTE_FRACTURE\

Objectives: Documentation of theoretical model development for flow in unsaturated fractured porous media based on dual-continuum modeling of matrix and fracture pore spaces unified by equilibrium chemical potential. The documentation includes: (1) brief review of development of unsaturated hydraulic conductivity relationships in the matrix based on the Tuller et al. (1999) and Or and Tuller (1999) models of pore space and liquid configuration governed by adsorptive and capillary forces; (2) development of a unit fracture element including roughness elements; (3) Flow phenomena in a unit fracture; (4) flow and a sample of FPM consisting of Gamma distribution of matrix pore size and fracture apertures; (5) comparison with measurements reported by Wang and Narasimhan (1993); (6) potential applications to general porous media with large structural pore space (e.g., macropores in soils, etc.).

11/15/99 – Initial entry (notebook continuation)

Models for equilibrium liquid-vapor interfacial configurations in fractured porous media enable detailed liquid retention modeling and provide approximate boundary conditions for introduction of hydrodynamic considerations. In the following we will represent media pore space by a bimodal distribution of pores reflecting the two disparate populations of matrix pores and fracture apertures (Fig.9).

Fig.9: Conceptual sketch for dual continuum pore space representation of a fractured porous medium. Fractures may be represented by unit elements as depicted in the right upper corner, and matrix is represented by angular pores connected to slits. Note (1) the pore size disparity between the two domains; and (2) large fractures empty first.

Additionally, fracture surface roughness (previous notebook) is incorporated and represented by a distribution of angular pits and grooves. Three flow regimes will be considered: (1) flow in completely filled pore spaces (primarily near saturation); (2) corner flow in partially filled pores and grooves; and (3) film flow on surfaces. The Navier-Stokes equation for plane flow is solved to obtain average cross-sectional film velocities for different chemical (matric) potentials. The chemical potential and pore (and pit) geometry determine liquid-vapor interfacial configuration and position thereby defining the shape of the moving liquid in such geometries. The assumption that these interfaces are stable under slow laminar flow conditions enables derivation of average "corner" flow equations for different pore and pit sizes and angularities. Liquid saturation degree is calculated first according to Tuller et al. (1999) in the assumed geometry, and then used to derive sample-scale unsaturated conductivity for various potentials by combining the velocity expressions (for a unit gradient) over the appropriate liquid-occupied cross sectional areas (neglecting 3-D network effects). Sample calculations of unsaturated constitutive relations for different pore spaces and fracture characteristics will be shown and comparisons with available data of Wang and Narasimhan (1993) will be discussed.

To ensure the practical applicability of the model, surface geometrical features are kept simple enough to obtain closed-form expressions for hydraulic conductivity programmable into conventional spreadsheet software (e.g., Excel, Quattro Pro).

The proposed model is to be based on appropriate thermodynamically and physically considerations. Simplifications should be kept at a minimum and are highlighted and explained at the appropriate level of the development process.

Remark:

- The assumed fracture element and its roughness geometry do not consider asperities and similar elements rising above mean fracture surface plane. Introduction of such elements should add realism to the model and capture some of the intermittent flow behavior observed. For inclusion of these elements we need to consider liquid build-up around conical objects. These elements lead to intermittent rivulet flows and are treated separately.

- The dynamics matrix-fracture interactions are not treated in this work. Rates of such interactions would be useful to capture the role of fracture surfaces as potential bypass flow pathways at boundaries of formations with two contrasting porosities (e.g., what happens when a large pulse of matrix liquid flux encounters a low porosity/permeability layer such as the PTN?).

21/11/99 - Matrix unsaturated hydraulic conductivity relationships

Hydrostatic Considerations – Review of the Tuller et al. (1999) and Or and Tuller (1999) model

Tuller et al. (1999) (see *Appendix VI*) developed a model for liquid configuration and liquid retention in partially saturated porous media that serves as the basis for hydrodynamic considerations. This novel framework includes two complementary elements: (1) a unitary approach for explicit consideration of the individual contributions of adsorptive and capillary forces to the matric (chemical) potential; and (2) its implementation within a new pore space geometry (unit cell) comprising an angular central pore for capillary processes attached to slit-shaped spaces with surface area for adsorptive processes. Interface science formalism and the concept of the disjoining pressure (Derjaguin et al., 1987) provided the physicochemical basis for incorporation of adsorption phenomena into the augmented Young-Laplace (AYL) equation (Derjaguin, 1957; Philip, 1977; Novy et al., 1989; Blunt et al., 1995). Simplifications of the rigorous AYL equation have been instrumental in the development of practical closed-form expressions for both saturation and interfacial area as a function of chemical potential at the pore scale.

In a subsequent study, Or and Tuller (1999) (see *Appendix VII*) used the pore-scale model to develop a statistical framework for upscaling from a pore to a sample of variably saturated porous medium. The statistical distribution of pore sizes was modeled as a gamma distribution with the expected values of liquid configuration in pores calculated (in a closed form) from geometrical and chemical potential considerations. One of the advantages of Or and Tuller's (1999) framework is the use of measurable media properties to estimate upscaling parameters. This is accomplished by matching predicted and measured retention data subject to measured porosity and surface area constraints.

Unitary Approach to Adsorption and Capillary Condensation

The pioneering work of Edlefsen and Anderson (1943) on mechanisms of water distribution on soil particles provided the qualitative basis for Philip's (1977) development of a quantitative unitary approach to capillary condensation and adsorption in porous media. The liquid-vapor interface is considered as a surface of constant partial specific Gibbs free energy (or chemical potential μ (Nitao and Bear, 1996)) made up of an adsorptive component (A) and a capillary component (C):

$$\mu = A(h) + C(\kappa) \tag{37}$$

with κ as the mean curvature of the liquid-vapor interface, and h as the distance from the solid to the liquid-vapor interface, taken normal to the solid surface (thickness of the adsorbed film). Tuller et al. (1999) extended and updated Philip's (1977a) unitary approach by (1) establishing a linkage with modern interface science concepts (Derjaguin et al, 1987; Iwamatsu and Horii, 1996); and (2) applying the updated theory to an entire pore space model rather than to individual geometrical features (e.g., corners, wedges, etc.). An important component in the updated unitary approach is the application of more general and versatile adsorption terms based on Derjaguin's disjoining pressure concept (Derjaguin et al. 1987; Iwamatsu and Horii 1996):

$$\mu = \frac{A_{svl}}{6\pi\rho h^3} - \frac{2\sigma\kappa}{\rho} \tag{38}$$

where A_{svl} is the Hamaker constant in Joules for solid-vapor interactions through the intervening liquid. Such refinements are important at very low water contents when films on adjacent surfaces are completely separated by a vapor phase. They also allow for direct incorporation of various surface electrochemical properties that, in turn, affect flow in thin liquid films.

Pore Space Geometry

Inspection of thin sections or micrographs of rocks and soils reveal that natural pore spaces do not resemble cylindrical capillaries (Fig.10). Because many types of porous media are formed by aggregation of primary particles and various mineral surfaces, the resulting pore space is more realistically described by angular or slit-shaped pore cross sections rather than by cylindrical capillaries (Li and Wardlaw, 1986; Mason and Morrow, 1991). Tuller et al. (1999) proposed a pore space representation capable of accommodating adsorptive processes in an internal surface area in addition to capillarity. The proposed elementary unit cell (Fig.11 is comprised of a polygon-shaped (e.g., triangle, square, other regular polygons) large central pore for capillary processes connected to slit-shaped spaces representing internal surface area.

Different soil textural and structural classes may be represented by adjusting pore width (L) and the proportions of exposed surfaces (determined by the slit-width αL and the slit-length βL), or even modifying the pore shape and angularity according to scanning electron micrographs.

Information potentially subject to copyright protection was redacted from this location. The redacted material (Fig. 10, Devonian Sandstone) is from the following reference:

Roberts and Schwartz, 1985 is the only information available.

Fig.11: Unit cell for pore space representation comprising an angular central pore attached to slit-shaped spaces.

Pore-Scale Liquid-Vapor Interfacial Configurations

The complex augmented Young-Laplace (AYL) solutions for interface configurations in the proposed pore geometrical model were greatly simplified by calculating capillary (menisci) and adsorptive (films) contributions separately and superimposing the resulting liquid-vapor interfaces. This simplified treatment, termed shifted Young-Laplace equation (SYL) was shown to give nearly identical values for liquid saturation and interfacial area as the rigorous AYL solution (Tuller et al., 1999).

Relatively simple closed-form expressions for pore-scale liquid saturation and interfacial area were derived taking into consideration two major snap-off mechanisms (spontaneous redistribution of liquid) within the unit cell. The transition from capillary-dominated to adsorption-dominated drainage is illustrated in Fig.12 for a triangular central pore. When we start with a completely saturated unit cell and lower the chemical potential gradually we reach a critical potential where liquid is spontaneously redistributed from the center of the pore (pore snap-off). The radius of interface curvature at pore snap-off is dependent on geometrical aspects of the central pore and is calculated according to Mason and Morrow (1991) and Tuller et al. (1999):
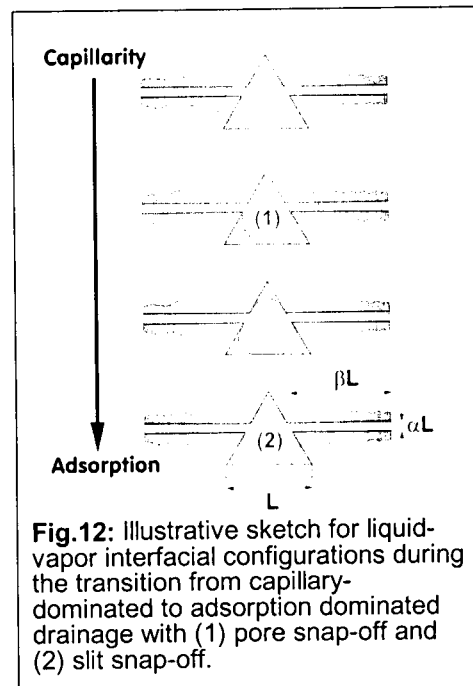

Fig.12: Illustrative sketch for liquid-vapor interfacial configurations during the transition from capillary-dominated to adsorption dominated drainage with (1) pore snap-off and (2) slit snap-off.

$$r_d = \frac{P}{2\left[(F_n + \pi) + \sqrt{\pi(F_n + \pi)}\right]} \qquad (39)$$

where P is the perimeter of the central pore and F_n is a pore angularity factor dependent on pore shape (Tuller et al. 1999). A further decrease in chemical potential results in recession of capillary menisci into the corners of the central pore, and at a certain potential in spontaneous redistribution of liquid from the slits. Slit snap-off occurs when the thickness of the adsorbed films is about one third of the slit spacing αL (Iwamatsu and Horii, 1996). Pore and slit snap-off are hysteretic phenomena. Critical potentials and related interface curvature and film thickness are discussed in Tuller et al. (1999).

Sample-Scale Liquid-Vapor Interfacial Configurations

The representation of liquid configuration in variably saturated porous media invariably involves consideration of a range of pore sizes (unit cells). Or and Tuller (1999a) employed a statistical upscaling scheme (Fig.4) based on gamma distributed pore sizes (L) to derive closed-form expressions for sample-scale saturation and liquid-vapor interfacial area.

> *Remark:*
> - The upscaling scheme is similar to the scheme developed for fracture surface roughness (see previous notebook vol.1 p.13). A detailed description is given in Or and Tuller (WRR 35(12):3591-3605, 1999). *Appendix VI*

Or and Tuller's (1999) physical model was fitted to measured SWC data using the slit length parameter β, the shape parameter ω of the gamma distribution, the potential at the air entry point, and a parameter λ controlling the overlap between pore and slit spacing distributions, as free model parameters. Constraints were imposed to ensure that the modeled pore space geometry preserved measured properties, namely, porosity and specific surface area.

> *Remark:*
> - The Or and Tuller (1999) model was programmed in MS-Excel 2000. A sample work sheet is archived under C:\SCI_NOTE_FRACTURE\Or-Tuller99.xls

Model calculations were in excellent agreement with measured liquid retention data over a wide range of soil textural classes. An important feature of the Or and Tuller (1999) pore scale model is the ability to separate capillary (C) and adsorptive (A) contributions as depicted in Fig.13.

The best-fit parameters were also used to calculate liquid-vapor interfacial area at different potentials (Fig.13b). Detailed information about liquid-filled spaces and liquid-vapor interface configurations in partially saturated porous media may clarify relationships between chemical potential, microbial habitats, and related interfacial exchange processes (e.g., oxygen transport).
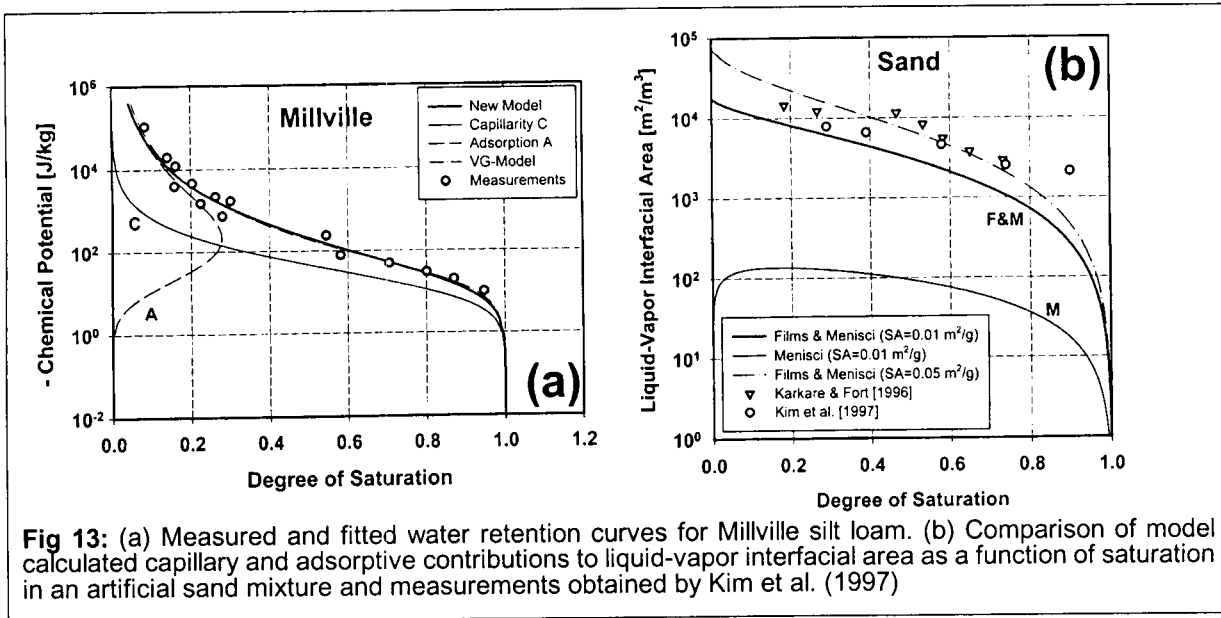
Fig 13: (a) Measured and fitted water retention curves for Millville silt loam. (b) Comparison of model calculated capillary and adsorptive contributions to liquid-vapor interfacial area as a function of saturation in an artificial sand mixture and measurements obtained by Kim et al. (1997)

11/29/99 - Hydrodynamic Considerations – Rock Matrix

The underlying assumption for introduction of hydrodynamic considerations is that equilibrium liquid configurations and interfaces remain relatively stable under slow laminar flow conditions. Ignoring network effects and assuming flow direction perpendicular to the medium cross-section only we propose to use equilibrium liquid-vapor interfaces as fixed boundaries defining different laminar flow regimes. Based on cell filling stage (determined by chemical potential and geometrical attributes) we can identify average flow velocities for four primary flow regimes (Fig.14a). For complete saturation, liquid flows in full ducts (central pore) and between parallel plates (slits). For partial saturation, and after pore and slit snap-off, flow occurs in thin adsorbed films lining all flat parts of the cell, and in the corners of the central pore. The onset and contribution of each flow regime is dependent on the filling stage of the unit cell as determined by chemical potential. Solutions of the Navier-Stokes equation for different geometry and boundary conditions are used to obtain the average velocities in films, corners, ducts, and parallel plates.
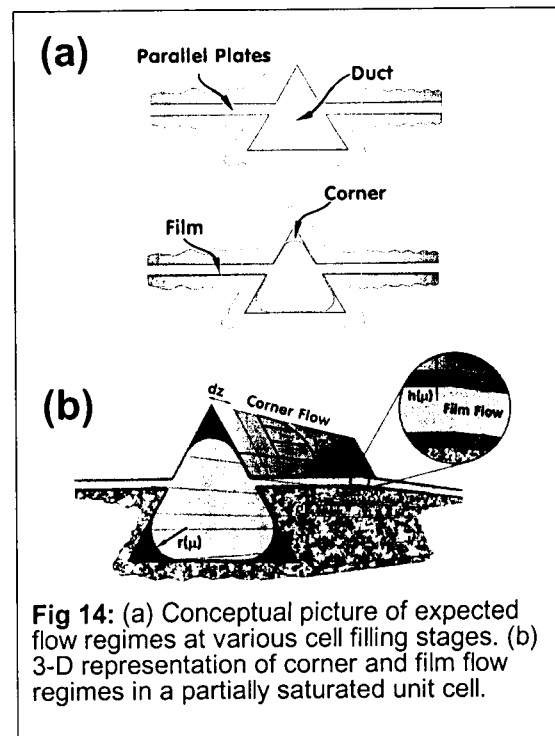

Fig 14: (a) Conceptual picture of expected flow regimes at various cell filling stages. (b) 3-D representation of corner and film flow regimes in a partially saturated unit cell.

Average Flow Velocities in Ducts and Between Parallel Plates

Analytical solutions for average flow velocities in ducts and between parallel plates are extensively discussed in fluid mechanics literature (e.g., Spurk, 1997).

For laminar flow between parallel plates relationships between viscosity, geometry, pressure gradient and mean flow velocity are given as:

$$\overline{v} = \frac{(\alpha L)^2}{12\eta_0}\left(-\frac{dP}{dz}\right) \tag{40}$$

where η_0 is the viscosity of bulk liquid, αL is the spacing between the plates (i.e., slit spacing), and $-dP/dz$ is the pressure gradient in flow direction z.

In this study we consider flow through ducts with triangular, square-shaped, and higher order polygonal cross-sections. For simplicity we employ the circular duct solution to approximate average velocities in higher order polygons (n > 4).

The average velocity in a full rectangular duct (of dimensions $L_1 \times L_2$ with $L_1 > L_2$) is given by:

$$\overline{v} = \frac{L_2^2 B_S}{4\eta_0}\left(-\frac{dP}{dz}\right) \tag{41}$$

with

$$B_S = \frac{1}{3} - \frac{L_2}{L_1}\frac{64}{\pi^5}\sum_{n=1}^{\infty}\frac{\tanh\left(\frac{L_1}{L_2}\frac{\pi(2n-1)}{2}\right)}{(2n-1)^5}$$

For a square-shaped duct the solution simplifies as $L_2/L_1 = 1$.

The solution for an equilateral triangular duct is given as (Spurk, 1997):

$$\overline{v} = \frac{L^2}{80\eta_0}\left(-\frac{dP}{dz}\right) \tag{42}$$

The circular duct solution related to a polygon with the same cross-sectional area is given as (Spurk, 1997):

$$\overline{v} = \frac{L^2 A_n}{8\eta_0\pi}\left(-\frac{dP}{dz}\right) \tag{43}$$

where L is the side-length of the polygon, and A_n is the area factor defined in **Appendix I**.

Average Flow Velocities in Thin Films

Analytical solutions for average flow velocities in thin films, considering modification of liquid viscosity near solid surfaces are derived and extensively discussed in the previous notebook (p.6-7). The resulting velocity functions are given as:

Film thickness > 10 nm
$$\overline{v} = \frac{h^2(\mu)}{3\eta_0}\left(-\frac{dP}{dz}\right) \tag{44}$$

Film thickness ≤ 10 nm
$$\overline{v} = \frac{A(\mu)}{12\eta_0\,h(\mu)}\left(-\frac{dP}{dz}\right) \tag{45}$$

with the function $A(\mu)$ for a given film thickness $h(\mu)$:

$$A(\mu) = \left(a^2 h(\mu) + 5ah(\mu)^2 - 4h(\mu)^3\right)\exp\left(-\frac{a}{h(\mu)}\right) + \left(a^3 + 6a^2 h(\mu)\right)Ei\left[-\frac{a}{h(\mu)}\right]$$

Average Flow Velocities in Corners of Angular Pores

Average velocities for corner flow regimes are obtained from expressions derived by Ransohoff and Radke (1988). They used a numerical scheme to solve the Navier-Stokes equations for corner flow bounded by a liquid-vapor interface. Their results were reduced to the general form:

$$\bar{v} = \frac{r(\mu)^2}{\varepsilon \eta_0}\left(-\frac{dP}{dz}\right) \tag{46}$$

where ε is a dimensionless flow resistance parameter dependent on the corner angle γ (Ransohoff and Radke, 1988), and r is the radius of interface curvature (Eq.2) of the capillary meniscus at a given chemical potential. For a detailed discussion see previous notebook page 8.

Average Hydraulic Conductivities of the Pore-Scale Flow Regimes

With average velocities for various flow regimes known we now seek analogy with Darcy's law to obtain the proportionality coefficient between flux and hydraulic gradient that represents the average hydraulic conductivity. This approach was instrumental for prediction of unsaturated hydraulic conductivity in studies by Childs and Collis-George (1950), Burdine (1953), Gardner (1958), Mualem (1976), and others. Darcy's law is given as:

$$\bar{v} = \frac{Q}{A} = \frac{K}{\rho g}\left(-\frac{dP}{dz}\right) \tag{47}$$

where Q is the volumetric discharge rate, A is the cross-sectional area occupied by the liquid, K is the hydraulic conductivity, and g is the acceleration of gravity. Assuming a unit pressure gradient, rearranging, and substituting the Navier-Stokes solutions for average flow velocity into Eq.47 we obtain expressions for average hydraulic conductivities of various flow regimes as demonstrated for corner flow:

$$\frac{K}{\rho g}\left(-\frac{dP}{dz}\right) = \frac{r(\mu)^2}{\varepsilon \eta_0}\left(-\frac{dP}{dz}\right) \quad \Rightarrow \quad KC(\mu) = \frac{\rho g}{\eta_0}\frac{r(\mu)^2}{\varepsilon} \tag{48}$$

Parallel plates (slits)
$$KS = Ks\, L^2 = \frac{\rho g \alpha^2}{12\eta_0}L^2 \tag{49}$$

Triangular duct
$$KD_T = Kd_T\, L^2 = \frac{\rho g}{80\eta_0}L^2 \tag{50}$$

Square-shaped duct
$$KD_S = Kd_S\, L^2 = \frac{\rho g B_s}{4\eta_0}L^2 \tag{51}$$

Circular duct
$$KD_C = Kd_C\, L^2 = \frac{\rho g A_n}{8\pi\eta_0}L^2 \tag{52}$$

Thick film (h $\geq$ 10 nm)
$$KF(\mu) = \frac{\rho g}{\eta_0}\frac{h(\mu)^2}{3} \tag{53}$$

Thin film (h < 10 nm)

$$KF(\mu) = \frac{\rho g}{\eta_0} \frac{A(\mu)}{12\,h(\mu)}$$

(54)

Corner

$$KC(\mu) = \frac{\rho g}{\eta_0} \frac{r(\mu)^2}{\varepsilon}$$

(55)

The thickness of the adsorbed film $h(\mu)$ and the radius of interface curvature $r(\mu)$ are calculated according to Eqs.1 and 2.

Unit Cell Hydraulic Conductivity

The hydraulic conductivity for the entire unit cell can be constructed by weighting conductivities of various elements by their liquid occupied cross-sectional areas and divide by the total cross-sectional cell area (pore + solid shell). The total cross-sectional area A_T is obtained by dividing pore cross-sectional area by the porosity ϕ of the porous medium:

$$A_T = \frac{(2\alpha\beta + A_n)L^2}{\phi}$$

(56)

where A_n is an area factor of the central pore (see **_Appendix I_**). Taking into consideration different cell filling stages determined by chemical potential and cell snap-off mechanisms we can derive relatively simple expressions for pore scale hydraulic conductivities <u>for the unit cell</u>:

Complete Saturation

$$K_{sat} = \frac{2\alpha\beta L^2\,KS + A_n L^2\,KD}{A_T}$$

(57)

After Pore Snap-off

$$K(\mu) = \frac{2\alpha\beta L^2\,KS + h(\mu)n\left(L - \dfrac{2r(\mu)}{\tan(\gamma/2)}\right)KF(\mu) + r(\mu)^2\,F_n\,KC(\mu)}{A_T}$$

(58)

After Slit Snap-off

$$K(\mu) = \frac{h(\mu)\left(4\beta L + n\left(L - \dfrac{2r(\mu)}{\tan(\gamma/2)}\right)\right)KF(\mu) + r(\mu)^2\,F_n\,KC(\mu)}{A_T}$$

(59)

with $KF(\mu)$ and $KC(\mu)$ as the hydraulic conductivities for films and KS and KD as the parallel plate and duct hydraulic conductivities.

Results showed that even these simple algebraic expressions for a <u>single</u> cell were capable of predicting unsaturated hydraulic conductivities for porous media with very narrow pore size distributions. For example, the liquid retention model (Tuller et al., 1999) was fitted to measured retention data (Fig.15a) for Hygiene sandstone (van Genuchten, 1980) by varying unit cell dimensions L, α, and β (Fig.11). The resulting best-fit cell dimensions were used to predict unsaturated hydraulic conductivity (Fig.15b).
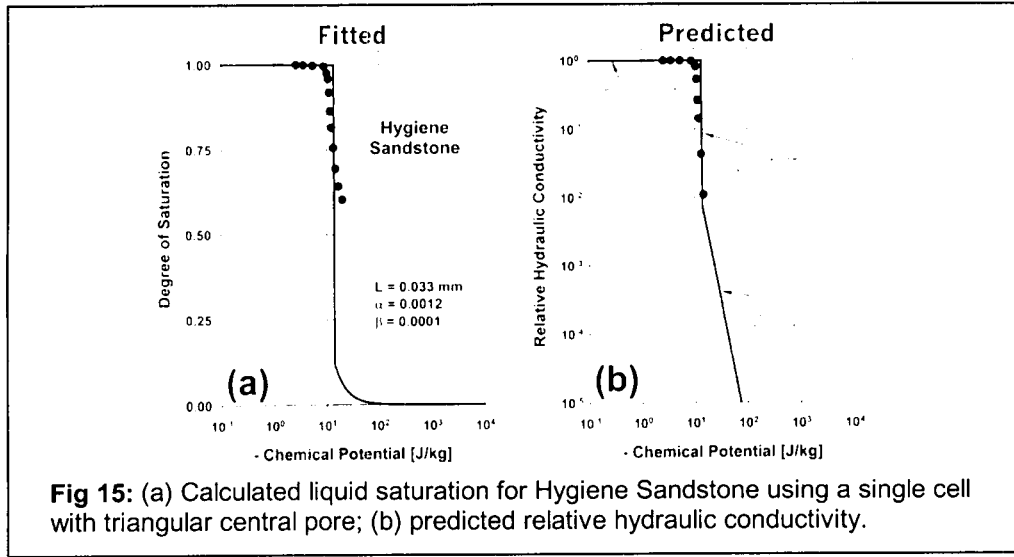
Fig 15: (a) Calculated liquid saturation for Hygiene Sandstone using a single cell with triangular central pore; (b) predicted relative hydraulic conductivity.

12/5/99 - Sample-Scale Hydraulic Conductivity

Before we proceed with a detailed discussion of the upscaling scheme we give a brief outline of the parameter estimation scheme for sample-scale hydraulic conductivity (Fig.16)
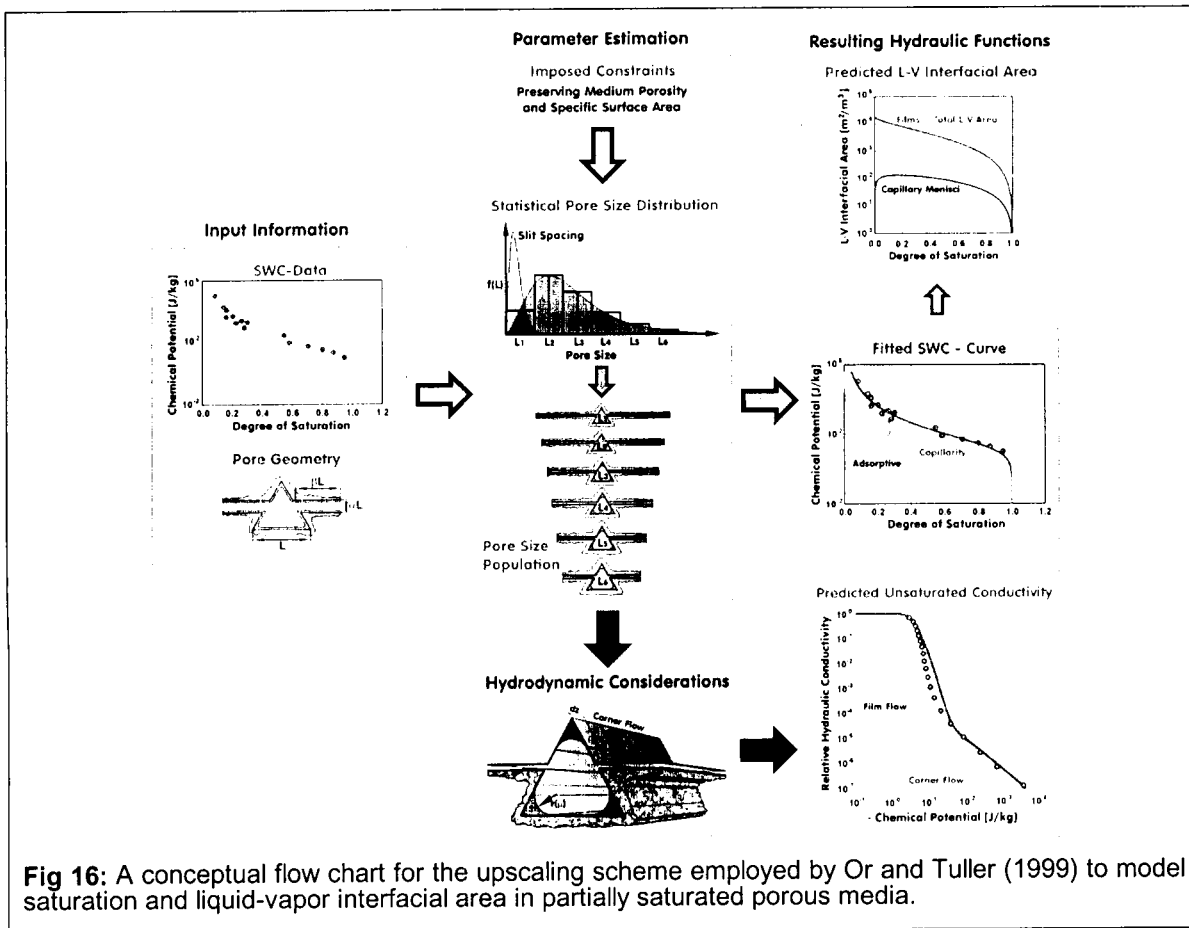

Fig 16: A conceptual flow chart for the upscaling scheme employed by Or and Tuller (1999) to model saturation and liquid-vapor interfacial area in partially saturated porous media.

Measured liquid retention data and assumed pore geometry serve as input data to obtain a set of best-fit parameters for the Or and Tuller (1999) sample-scale liquid retention model. Specific surface area and porosity constraints (measured media specific surface area and porosity is preserved) are imposed when fitting the analytical solutions for sample-scale liquid retention. The resulting fitting parameters (see Or and Tuller (1999)) are then used to predict (1) liquid-vapor interfacial area as a function of chemical potential, and (2) to predict sample-scale unsaturated hydraulic conductivity (red arrows).

Using the pore-scale relationships for unsaturated hydraulic conductivity and employing a similar statistical upscaling scheme (Fig.17) as introduced on page 13 for rough fracture surfaces (instead of the pit depth we now employ a gamma distribution for the central pore length L to represent a population of unit cell elements) we obtain closed-form expressions for the sample scale hydraulic conductivity.

A population of gamma-distributed square pores (Fig.17a) is represented for illustrative purposes by 6 bins (L_1 to L_6). The fixed relationship between central pore length L and slit spacing αL results in adjoin Gamma distributed slit spacing as depicted in Fig.17a. The physical model predicts the shapes of liquid-vapor interfaces for each pore size and chemical potential μ, leading to different stages of pore filling according to chemical potential and pore geometry (Fig.17b) The fraction of pores at each of the several filling stages is determined from the statistical distribution of pore length, f(L), and is expressed as the expected value of a certain range of pore spaces to be completely or partially liquid filled. The total sample scale saturation is calculated as the weighted sum of different pore filling stages.
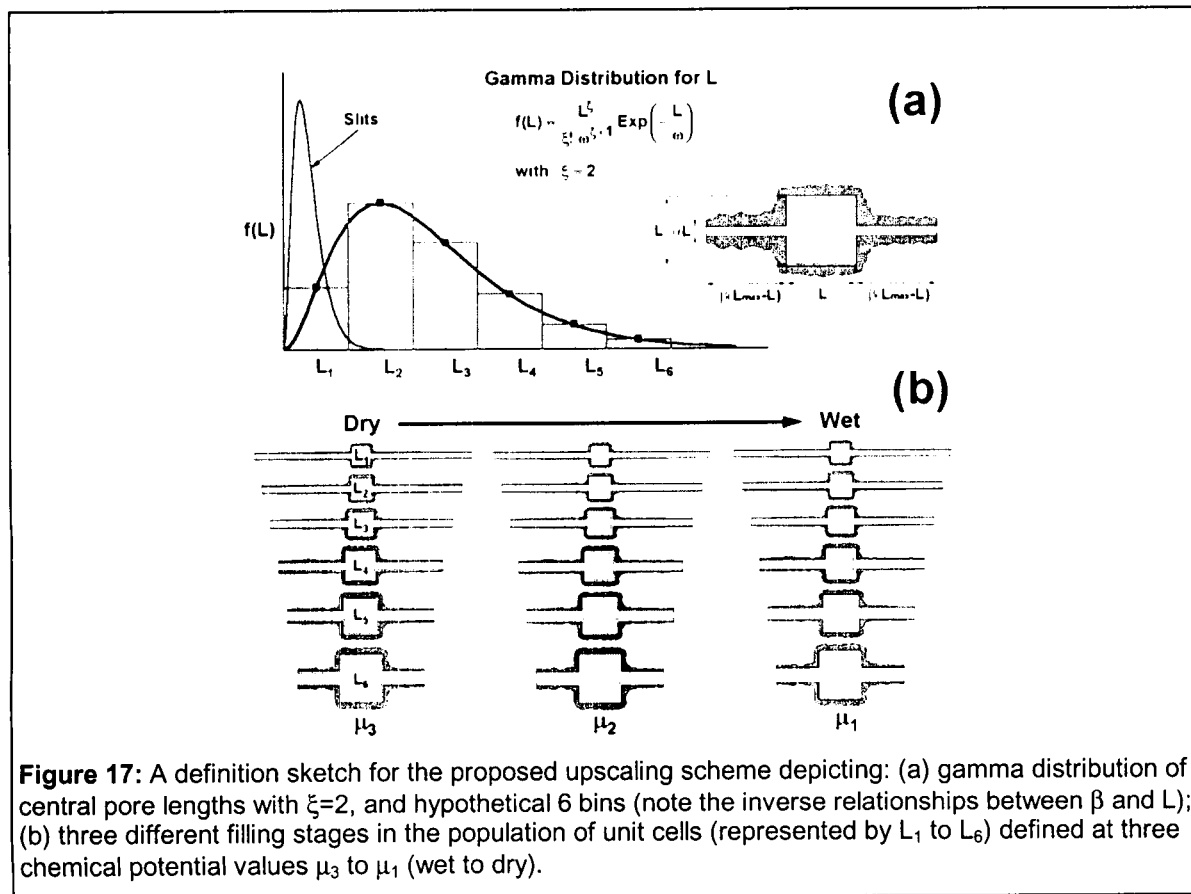

Figure 17: A definition sketch for the proposed upscaling scheme depicting: (a) gamma distribution of central pore lengths with ξ=2, and hypothetical 6 bins (note the inverse relationships between β and L); (b) three different filling stages in the population of unit cells (represented by L_1 to L_6) defined at three chemical potential values μ_3 to μ_1 (wet to dry).

This statistical approach has been instrumental in representing the distribution for the pore radii in the bundle of cylindrical capillaries model as illustrated in the studies of Laroussi and de Backer [1979] or more recently by Kosugi [1994, 1996] who assumed log-normal distribution of pore radii. In the proposed upscaling scheme outlined in this study we represent the statistical distribution of central pore length (L)

by a gamma distribution [Rice, 1995]. The gamma distribution resembles the commonly used lognormal distribution with its positive skewness, and also facilitates derivation of closed-form expressions for liquid retention and interfacial area. Several other probability laws including the incomplete gamma distribution [Brutsaert, 1966] or the Weibull distribution [Assouline et al., 1998] may also be considered in future studies.

The gamma density function for the central pore length, f(L), is dependent on two parameters, ξ and ω:

$$f(L) = \frac{L^{\xi}}{\xi! \, \omega^{\xi+1}} \exp\left(-\frac{L}{\omega}\right) \qquad L \geq 0 \qquad\qquad (60)$$

The parameter ξ is limited to integer values. Calculations involving expectations of f(L) are greatly simplified by the choice of ξ=2 which provides a balance between flexibility and tractability (ξ=2 was used for this study). The moment-generating function of the gamma distribution [Rice, 1995] is used to obtain expressions for the mean m(L) and variance v(L) of L given as:

$$m(L) = \omega(\xi + 1) \qquad\qquad (61a)$$

$$v(L) = \omega^2(\xi + 1) \qquad\qquad (61b)$$

We also limit the range of admissible L values for the assumed gamma distribution to values between L_{min} and L_{max}, representing the smallest and largest central pore lengths, respectively. The relationships between slit length and central pore length distribution is expressed as $\beta(L_{max}-L)$. Such inverse relationships facilitate the representation of clayey soils by unit cells with relatively small central pores and large slits (on average), whereas sandy soils would be represented by larger central pores attached to shorter slits (i.e., less internal surface area). The relationships between pore length distribution and slit spacing is expressed as αL. Constraints on the values of α, β, and f(L) are imposed based on measurable medium properties such as porosity, and specific surface area (for details see Or and Tuller (1999)).

Our calculations yield K(μ) expressed as the sum of five terms representing expected hydraulic conductivity values for different filling stages as determined by chemical potential, pore geometry, and pore size distribution:

$$K(\mu) = K_1(\mu) + K_2(\mu) + K_3(\mu) + K_4(\mu) + K_5(\mu) \qquad\qquad (62)$$

The separation into five terms provides a means to distinguish between flow contributed by films and by corners and full ducts. The integrals for all five terms can be cast in the same general form:

$$K_i(\mu) = \int_{L_L}^{L_U} \frac{AL^4 + BL^3 + CL + D}{EL^2 + FL} f(L) \, dL \qquad\qquad (63)$$

where f(L) is any pore size statistical distribution function (gamma density function with ξ=2 in this case), L_L and L_U are the lower and upper integration limits determined by snap-off mechanisms and A, B, C, D, E, and F are constants and variables comprising geometrical cell attributes and average hydraulic conductivities of the flow regimes involved. All constants for saturated and unsaturated conditions are listed in *Appendix II*. The analytical solution for the integral in Eq.63 is derived in *Appendix III*.

The first term $K_1(\mu)$ is the expected value of unsaturated hydraulic conductivity for completely filled central pores integrated between the minimum pore dimension L_{min} (L_L) and the upper limit L_1 (L_U), which is determined from the radius of curvature at the onset of drainage in the central pore:

$$r_d = \frac{L}{C_n} \tag{64}$$

The particular value $L=L_1$ is obtained by the substitution $r_d = -\sigma/\rho\mu$ (the standard Young-Laplace equation) using the proper value of the coefficient C_n which defines drainage curvature for different shaped central pores (as listed in *Appendix I*) to yield for a given potential:

$$L_1(\mu) = -\frac{\sigma}{\rho\mu} C_n \tag{65}$$

The limit of integration (L_1) indicates that all unit cells with pore lengths L smaller than L_1 will remain completely full at the given potential μ.

The second term describes the fraction of unit cells having full slits with integration limits L_{min} and L_2. The upper limit L_2 is determined from the chemical potential at slit snap-off. It is implicitly assumed that slits remain full for all slit spacing smaller than αL_2 which defines slit spacing for the onset of spontaneous slit snap-off at the chemical potential μ. Spontaneous slit filling occurs when film thickness $h(\mu)$ is approximately one third of the slit-spacing αL:

$$h(\mu) = \frac{\alpha L}{3} \tag{66}$$

Rearranging Eq.64 and substituting Eq.1 for $h(\mu)$ yields the required upper limit of integration L_2:

$$L_2(\mu) = \frac{3}{\alpha} \sqrt[3]{\frac{A_{svl}}{6\pi\rho\mu}} \tag{67}$$

Although it is unclear whether slit snap-off during drainage occurs at the same chemical potential as for imbibition, we have adopted a similar expression for simplicity. In any case, we expect effects of slits emptying at lower chemical potentials to have a minor influence on the upscaling scheme due to the presence of a distribution of slit spacing in a sample. The integration limits are illustrated in Fig.17.

Flow in films adsorbed on slit walls is accounted for in $K_3(\mu)$ with the integration limits L_2 and the maximum pore dimension L_{max}. The chemical potential at the onset of drainage μ_d (air entry value) is often attributed to the largest pore size present in the porous medium, which we denote as L_{max}. Equation 2 is used to obtain the appropriate pore dimension $L_1(\mu_d)$. A small correction is introduced by calculating film thickness $h(\mu_d)$ lining the pore walls according to Eq.1. The resulting maximum pore size is given as:

$$L_{max} = L_1(\mu_d) + 2h(\mu_d) \tag{68}$$

The fourth term represents the contribution of films aligning the flat parts of the central pore (between the curved corner menisci). The limits of integration are defined between L_1 and L_{max}. Finally $K_5(\mu)$ calculates the contribution of corner flow within the central pore from pore snap-off (L_1) to L_{max}. The contribution of film flow to the overall unsaturated hydraulic conductivity is represented by the sum of terms $K_2(\mu)$, $K_3(\mu)$, and $K_4(\mu)$.

The expected value of sample-scale saturated hydraulic conductivity K_{sat} is obtained by integrating Eq.63 with variables and constants listed in *Appendix II* between L_{min} and L_{max} (full saturation). The relative hydraulic conductivity is simply the quotient of $K(\mu)$ and K_{sat}.
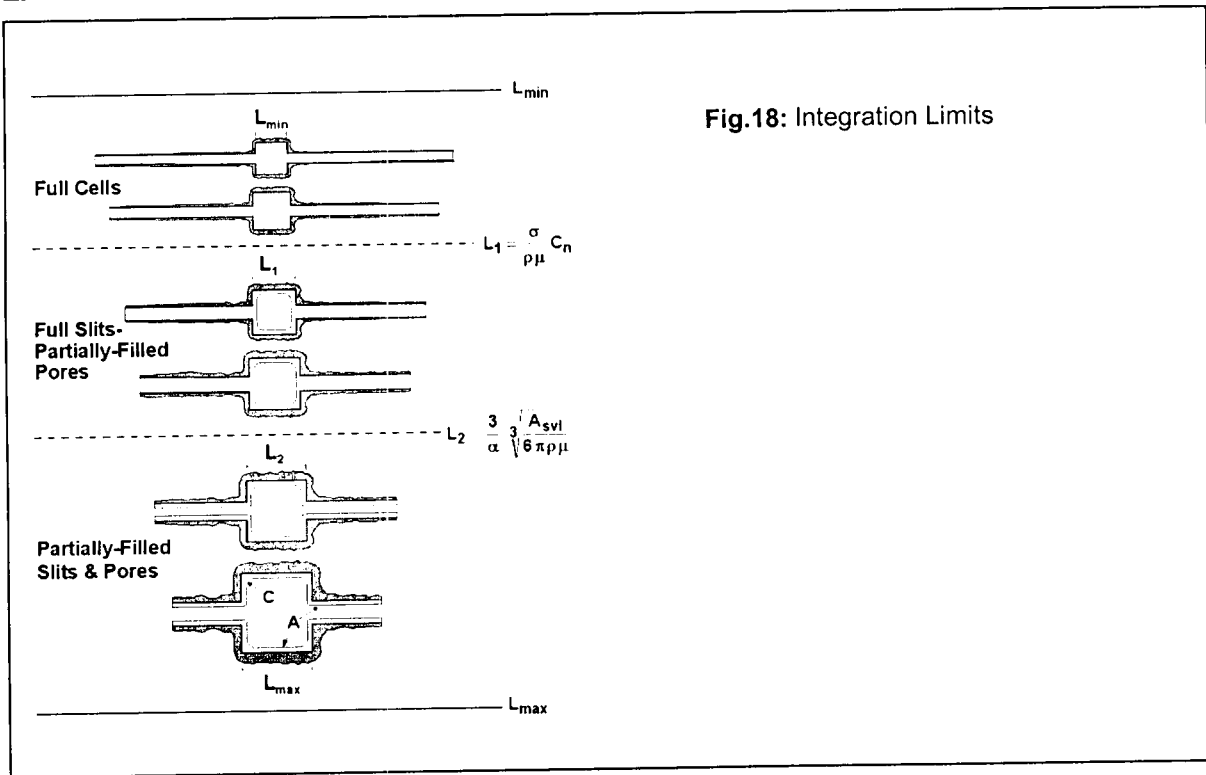
Fig.18: Integration Limits

The upscaling scheme was tested for a variety of different textured soils. An example for Gilat loam data (van Genuchten, 1980) is depicted in Fig.18. The predicted relative hydraulic conductivity curve (Fig.8b) is in excellent agreement with measured data. The dash-dotted line represents film flow contribution to the overall hydraulic conductivity. Figure 8b also illustrates the important role of film flow, whose contribution begins to dominate the contribution of corners and full ducts at relatively high chemical potentials in the range of -70 J/kg. Such film contributions are often discounted in pore scale models (e.g., Ransohoff and Radke, 1988; Dullien et al., 1986). Another interesting feature of the proposed model is ability to reproduce the "tail" of the $K(\mu)$ curve as evidenced by measurements. Common parametric models (e.g., Van Genuchten, 1980) rely entirely on capillarity and thus are incapable of capturing film flow contribution which alters the slope of $K(\mu)$ significantly.
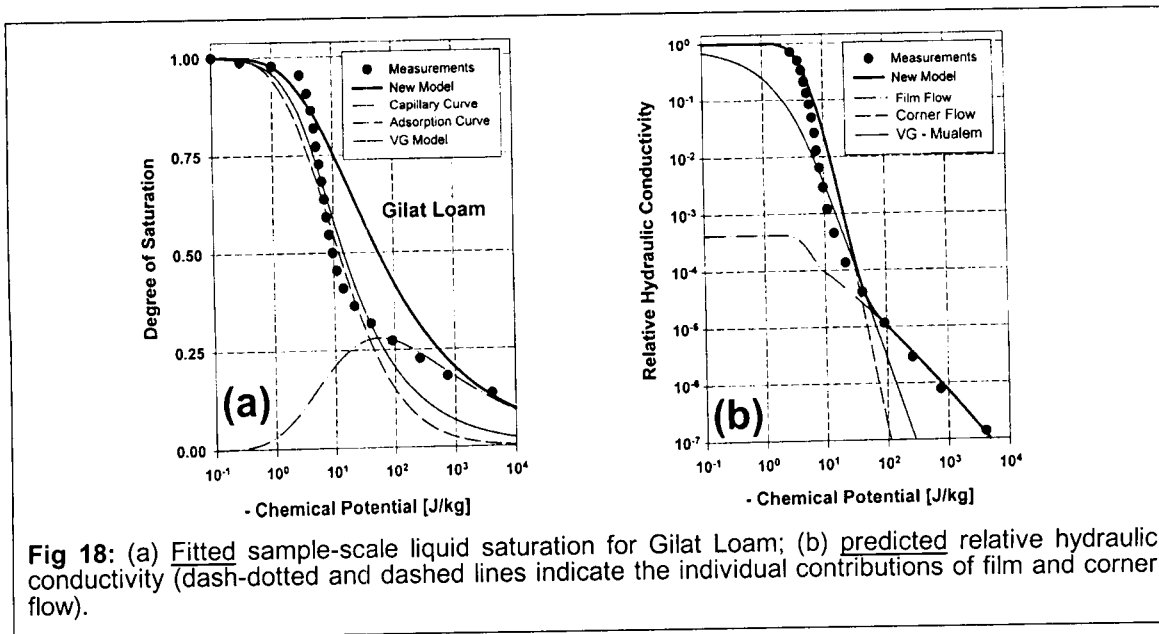

Fig 18: (a) Fitted sample-scale liquid saturation for Gilat Loam; (b) predicted relative hydraulic conductivity (dash-dotted and dashed lines indicate the individual contributions of film and corner flow).

> *Remark:*
>
> ● The closed-form expressions for sample-scale hydraulic conductivity were programmed in MS-Excel 2000. A sample work sheet is archived under C:\SCI_NOTE_FRACTURE\Tuller-Or2000.xls

12/15/99 - Dual Continuum Approach (DCA) for Fractured Porous Media

Fractured porous media pore geometry is represented by a bimodal distribution for pore lengths and fracture apertures to account for the two disparate pore scales and porosity of matrix and fractures (Fig.19).

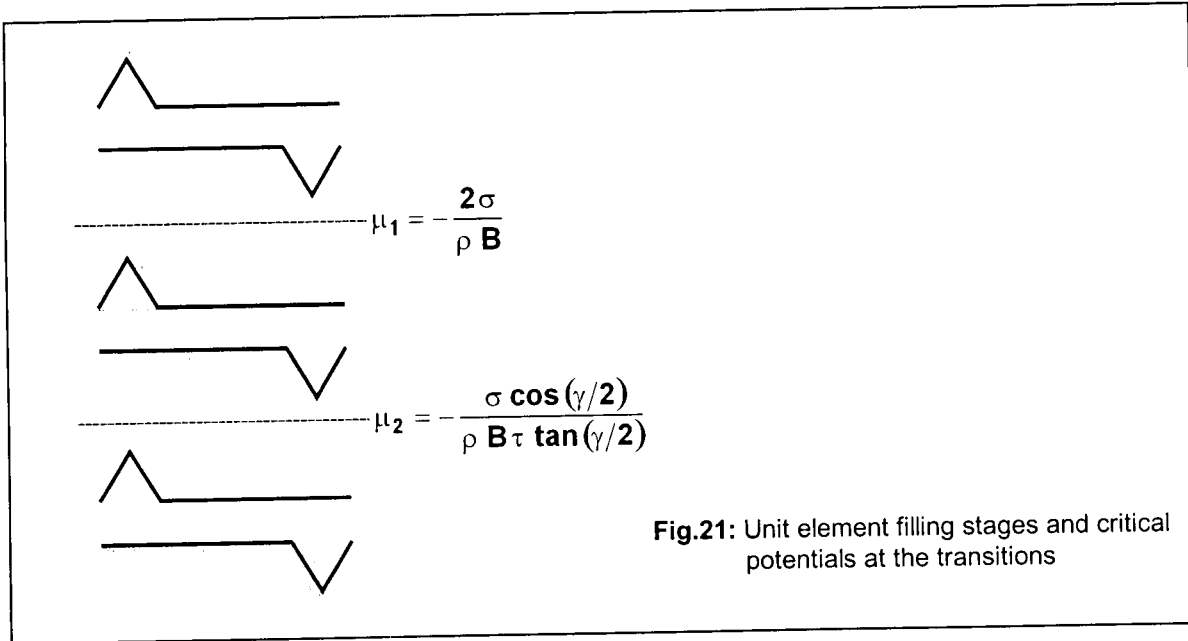**Fig.19:** Bimodal distribution of pore lengths and apertures to represent fractured medium pore space.
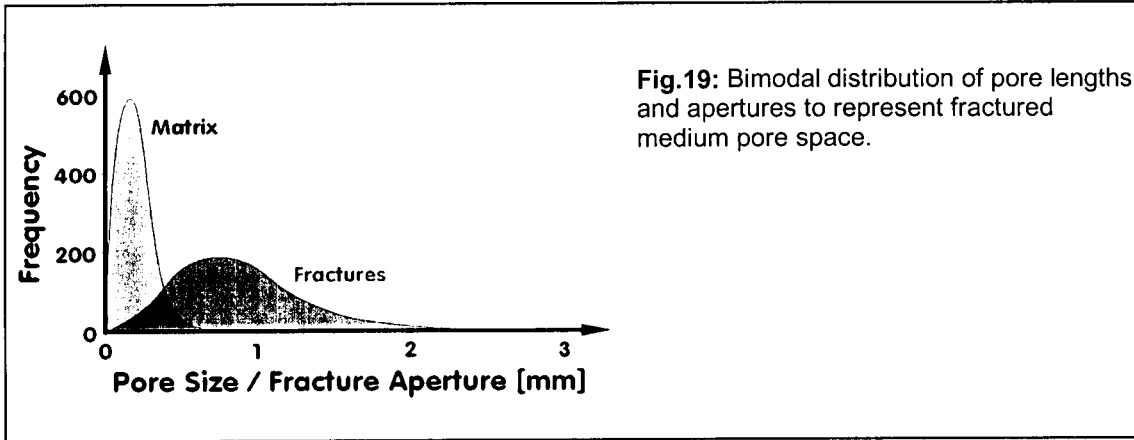
Matrix retention and unsaturated hydraulic conductivity is obtained by applying the model introduced in the previous sections of this notebook. For retention and flow phenomena in the fracture pore space we use a similar physically based approach starting with a single fracture element comprised of two facing surfaces separated by a certain aperture (B). Each surface contains a single pit for surface roughness representation, with all geometrical length attributes related to the aperture B (Fig.20).

Fig.20: Geometry of a single fracture element
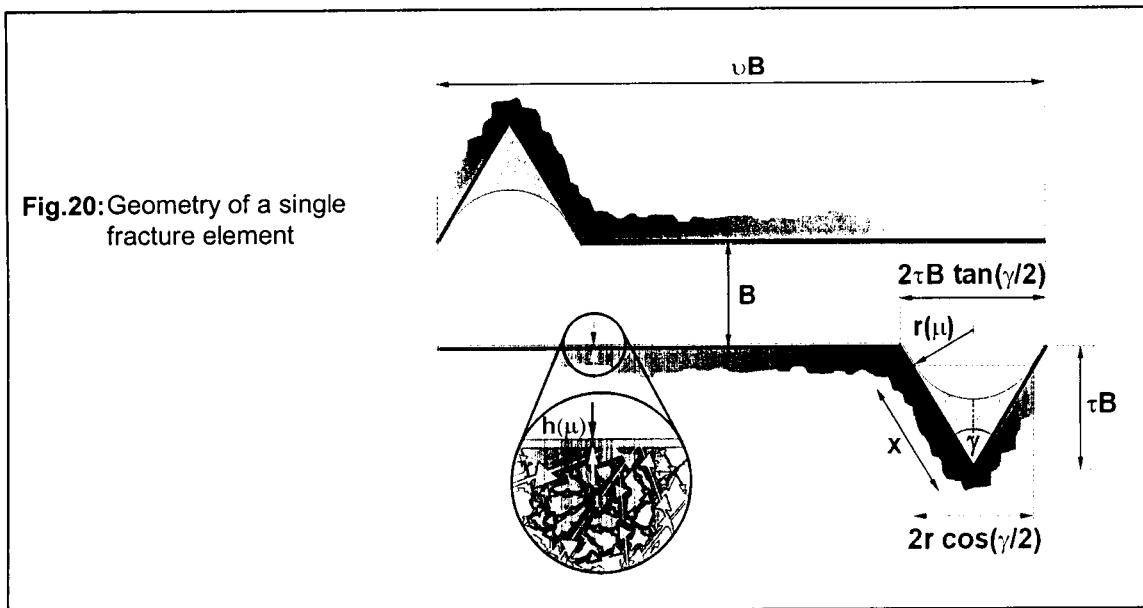
DCA- Hydrostatic Considerations

First we derive expressions for liquid saturation, considering different filling stages of the unit fracture element (Fig.21).

$$\mu_1 = -\frac{2\sigma}{\rho B}$$

$$\mu_2 = -\frac{\sigma \cos(\gamma/2)}{\rho B\tau \tan(\gamma/2)}$$

Fig.21: Unit element filling stages and critical potentials at the transitions

In the transition from complete saturation (high matric potential) to dry conditions (low matric potential) and vice versa we have to distinguish between 3 filling stages of the unit fracture element as determined by matric potential, element geometry, and mathematical considerations. Starting with a completely saturated unit fracture element and lowering matric potential gradually will lead to a certain potential threshold μ_1, where liquid is redistributed (drained) spontaneously from the center of unit element and two separate liquid-vapor interfaces develop on the facing fracture surfaces. The critical potential μ_1 at the point of separation is may be derived from the capillary force balance considerations:

$$\mu_1 = -\frac{2\sigma}{\rho B} \tag{69}$$

where σ is the surface tension of the liquid, ρ is the density of the liquid, and B is the fracture aperture. To facilitate mathematical tractability and to enable derivation of closed form expressions for liquid retention we assume that the pits remain completely filled till a circle with the radius of interface curvature obtained from the Young-Laplace equation (Eq.2) tangents the pit surfaces. This simplification, necessary for mathematical tractability, leads to a minor overestimation of retained liquid in the matric potential range from μ_1 to μ_2. The critical potential μ_2, where the radius of interface curvature starts touching the pit surfaces may be obtained from simple geometrical considerations. The side-length of the triangular pit in Fig.20 can be derived from the radius of interface curvature and the pit angle as well as from the pit depth τB and the pit angle. Equating the two expressions leads to an expression for μ_2 separating completely and partially filled surface pits:

$$x = \frac{\tau B}{\cos(\gamma/2)} = \frac{r(\mu)}{\tan(\gamma/2)} \tag{70}$$

Substitution of $r(\mu)=-\sigma/\rho\mu$ and rearranging Eq.70 gives:

$$\mu_2 = \frac{-\sigma\cos(\gamma/2)}{\tau B\rho\tan(\gamma/2)} \tag{71}$$

When matric potentials is gradually lowered below μ_2 liquid reseeds into the pit corners and the thickness of films adsorbed on all flat parts of the unit fracture element decreases according to Eq.1.

A relative saturation curve for a given unit element geometry is obtained by first calculating the critical potentials separating the filling stages of a unit element and applying the appropriate expressions for relative liquid saturation for the matric potential value under consideration (relative saturation is obtained by dividing the liquid occupied cross-sectional area by the total cross-sectional unit element area (disregarding the associated solid shell):

Complete Saturation $\mu > \mu_1$

$$S_1 = \frac{B^2(\upsilon + 2\tau^2 \tan(\gamma/2))}{B^2(\upsilon + 2\tau^2 \tan(\gamma/2))} = 1 \tag{72}$$

Seperated interfaces / full pits $\mu_1 \geq \mu > \mu_2$

$$S_2 = \frac{2h(\mu)B(\upsilon - 2\tau \tan(\gamma/2)\delta) + B^2 2\tau^2 \tan(\gamma/2)}{B^2(\upsilon + 2\tau^2 \tan(\gamma/2))} \tag{73}$$

Seperated interfaces / partially filled pits $\mu \leq \mu_2$

$$S_3 = \frac{2h(\mu)\left(\upsilon B - 2\tau B \tan(\gamma/2) + \frac{2\tau B}{\cos(\gamma/2)} - \frac{2r(\mu)}{\tan(\gamma/2)}\right) + 2r(\mu)^2\left(\frac{1}{\tan(\gamma/2)} - \frac{\pi(180-\gamma)}{360}\right)}{B^2(\upsilon + 2\tau^2 \tan(\gamma/2))} \tag{74}$$

With υ and τ as dimensionless scaling parameters for fracture element length and pit depth respectively (Fig.20), γ as the pit angle, B as the fracture aperture, δ as the pit connectivity factor (see discussion on page 10 of the previous notebook), $h(\mu)$ as the thickness of adsorbed films (Eq.1), and $r(\mu)$ as the radius of interface curvature (Eq.2).

DCA - Hydrodynamic Considerations

Dependent on the filling stage of the unit element, as determined by matric potential and geometry, we have to distinguish between four laminar flow regimes (similar to the matrix domain). For completely saturated fracture elements we consider flow between parallel plates, and flow in triangular ducts (at this point we limit our calculations to equilateral triangles $\gamma = 60°$, a solution for average liquid velocities in isosceles triangular ducts is under investigation). For partially filled elements we consider flow in equilateral triangular ducts, flow in adsorbed films lining all flat parts of the element, and flow in the pit corner.

Solutions for average flow velocities of these flow regimes (defined by the equilibrium liquid-vapor interfaces) were already discussed under hydrodynamic considerations for matrix flow. For completeness we list the average hydraulic conductivities for all flow regimes under consideration that were obtained by equating the solutions of the Navier-Stokes equations with Darcy's law assuming unit pressure gradient in flow direction:

Parallel plates

$$KS = Ks\,B^2 = \frac{\rho g}{12\eta_0}\,B^2 \qquad (75)$$

Triangular duct (equilateral)

$$KD = Kd\,B^2 = \frac{\rho g \tau^2}{60\eta_0}\,B^2 \qquad (76)$$

Thick film (h ≥ 10 nm)

$$KF(\mu) = \frac{\rho g}{\eta_0}\,\frac{h(\mu)^2}{3} \qquad (77)$$

Thin film (h < 10 nm)

$$KF(\mu) = \frac{\rho g}{\eta_0}\,\frac{A(\mu)}{12h(\mu)} \qquad (78)$$

Corner

$$KC(\mu) = \frac{\rho g}{\eta_0}\,\frac{r(\mu)^2}{\varepsilon} \qquad (79)$$

With ρ as the liquid density, g as the acceleration of gravity, η_0 as the viscosity of bulk liquid, B as the fracture aperture, τ as the dimensionless pit depth scaling parameter, $A(\mu)$ as a function for thin films (see page 39), $h(\mu)$ as the thickness of the adsorbed film (Eq.1), $r(\mu)$ as the radius of interface curvature (Eq.2), and ε as a dimensionless flow resistance parameter (see discussion on page 39).

Average hydraulic conductivity for the entire unit fracture element is obtained by weighting the individual contributions of each flow regime over the associated liquid occupied cross-sectional area, and dividing the resulting expression by the total cross-sectional area including the matrix shell. The total cross-sectional fracture area A_T is obtained by dividing the fracture area with the porosity of the fracture domain:

$$A_T = \frac{B^2\,(\upsilon + 2\tau^2\,\tan(\gamma/2))}{\phi_F} \qquad (80)$$

Where ϕ_F is the fracture porosity. For equilateral pits ($\gamma = 60°$) Eq.80 simplifies to:

$$A_T = \frac{B^2\,(\upsilon + 2\tau^2/\sqrt{3})}{\phi_F} \qquad (81)$$

Taking into consideration different filling stages of the unit fracture element, as determined by chemical potential, average hydraulic conductivities for fracture elements with equilateral pits are given as:

$K_{SAT}\ \mu > \mu_1$

$$K_{SAT} = \frac{\upsilon B^2\dfrac{\rho g}{\eta_0}\dfrac{B^2}{12} + \dfrac{2\tau^2\delta}{\sqrt{3}}B^2\dfrac{\rho g}{\eta_0}\dfrac{\tau^2 B^2}{60}}{B^2(\upsilon + 2\tau^2/\sqrt{3})}\phi_F$$

$$K_{SAT} = \frac{\dfrac{\rho g}{\eta_0}\left(\dfrac{\upsilon}{12} + \dfrac{\tau^4\,\delta}{30\sqrt{3}}\right)\phi_F\,B^2}{\upsilon + 2\tau^2/\sqrt{3}} \qquad (82)$$

$K_1(\mu)$ - seperated interfaces / full pits $\mu_1 \geq \mu > \mu_2$

$$K_1(\mu) = \frac{2h(\mu)\left(\upsilon - \frac{2\tau\delta}{\sqrt{3}}\right)B\ K_F(\mu) + \frac{2\tau^2\delta}{\sqrt{3}}B^2\ \frac{\rho g}{\eta_0}\frac{\tau^2}{60}B^2}{B^2(\upsilon + 2\tau^2/\sqrt{3})}\phi_F$$

(83)

$$K_1(\mu) = \frac{\frac{\rho g}{\eta_0}\frac{\tau^4\delta}{30\sqrt{3}}\phi_F B^3 + 2h(\mu)\left(\upsilon - \frac{2\tau\delta}{\sqrt{3}}\right)K_F(\mu)\phi_F}{(\upsilon + 2\tau^2/\sqrt{3})B}$$

$K_2(\mu)$ - seperated interfaces / partially filled pits $\mu \leq \mu_2$

$$K_2(\mu) = \frac{2h(\mu)\left(\upsilon + \frac{2\tau}{\sqrt{3}}\right)K_F(\mu)\phi_F\ B - 4\sqrt{3}\,h(\mu)r(\mu)K_F(\mu)\phi_F + 2\left(\sqrt{3} - \frac{\pi}{3}\right)r(\mu)^2\ \delta K_C(\mu)\phi_F}{(\upsilon + 2\tau^2/\sqrt{3})B^2}$$

(84)

With ρ as the liquid density, g as the acceleration of gravity, η_0 as the viscosity of bulk liquid, B as the fracture aperture, τ and υ as the dimensionless pit depth and fracture length scaling parameters, $h(\mu)$ as the thickness of the adsorbed film (Eq.1), $r(\mu)$ as the radius of interface curvature (Eq.2), and $K_F(\mu)$ and $K_C(\mu)$ as the average hydraulic conductivities for film and corner flow (Eqs.77 to 79).

DCA - Upscaling Considerations

To represent liquid retention and hydraulic conductivities in the fracture domain of a sample of fractured porous medium we consider a statistical aperture distribution. The gamma distribution with $\xi = 2$ is instrumental to derive closed-form expressions for the sample scale (Fig.22).

$$f(L) = \frac{B^\xi}{\xi!\,\omega^{\xi+1}}Exp\left[\frac{-B}{\omega}\right]$$

with :

$$\xi = 2$$

Fig.22: Gamma distribution for fracture aperture
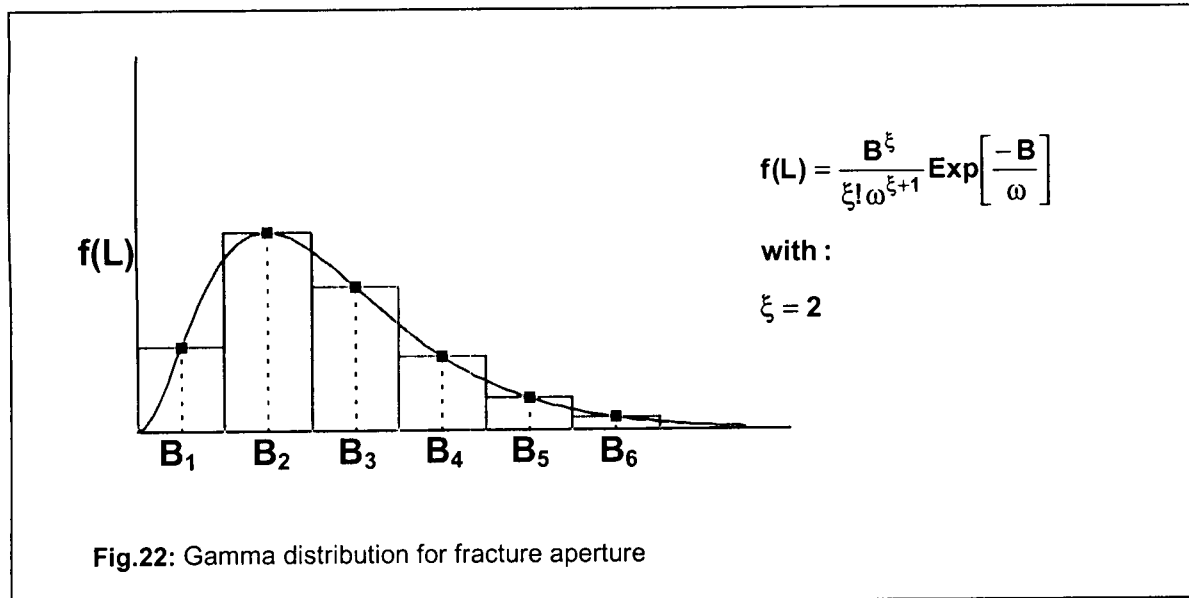
When we choose 6 representative pins for fracture aperture from the gamma distribution in Fig.22 and draw the associated unit fracture elements under "dry" (low matric potential) and under "wet" (high matric potential) we may observe that at the dry end only elements with small aperture are completely saturated. As we move to wetter conditions more and more elements are completely saturated (Fig.23a). The critical fracture apertures B_1 and B_2 separating completely filled, partially filled with full pits, and partially filled with partially filled pits for a certain matric potential are obtained by rearranging Eqs.69 and 71 to solve for B (Fig.23b). Note that all expressions are derived for equilateral pits (γ=60°). Maximum B_{max} and minimum B_{min} fracture apertures may be obtained from measured aperture distributions.
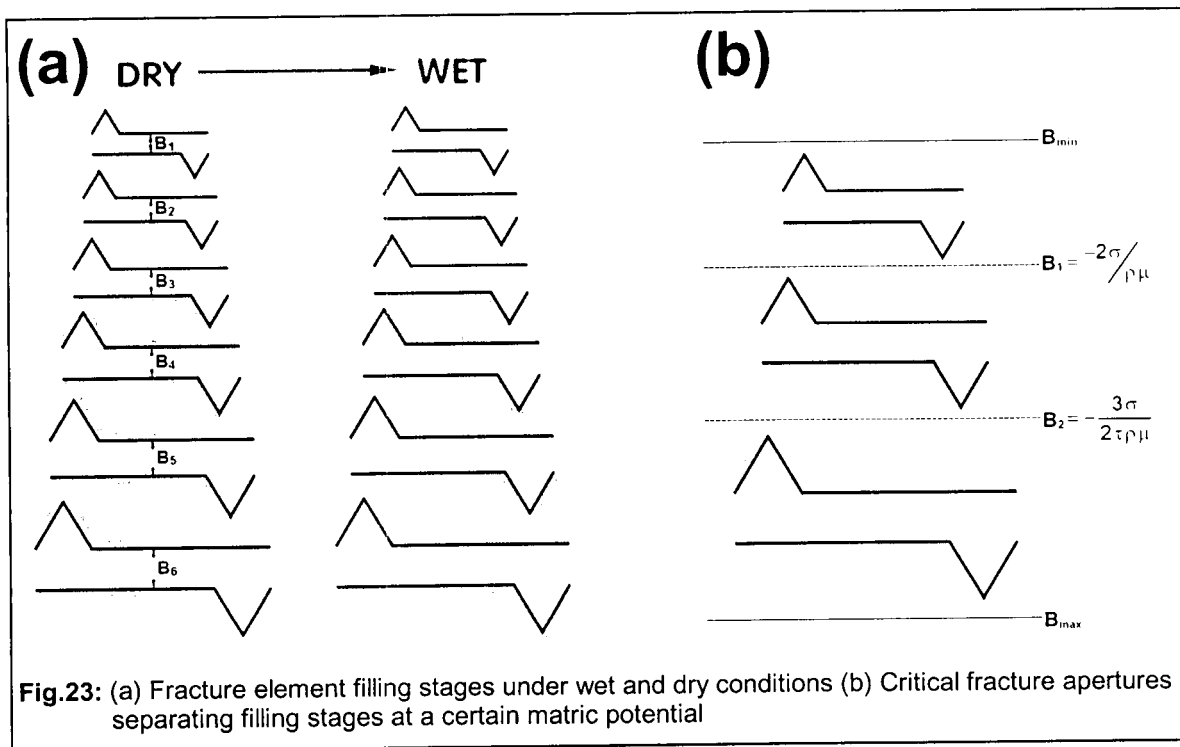

Fig.23: (a) Fracture element filling stages under wet and dry conditions (b) Critical fracture apertures separating filling stages at a certain matric potential

Expressions for sample scale fracture saturation and hydraulic conductivity are obtained by multiplying expressions derived for a single unit fracture element (Eqs.72, 73, and 74 for liquid saturation and Eqs.82, 83, and 84 for hydraulic conductivity) with the gamma distribution for fracture apertures and integrating the resulting expressions over the range of apertures related to certain filling stages, as determined by the matric potential. A sample calculation is shown for saturated hydraulic conductivity.

$$K_{SAT} = \int_{B_{min}}^{B_{max}} \frac{\frac{\rho g}{\eta_0}\left(\frac{\upsilon}{12} + \frac{\tau^4 \delta}{30\sqrt{3}}\right)\phi_F B^4}{(\upsilon + 2\tau^2/\sqrt{3})B^2} \frac{B^2}{2\omega^3}Exp\left[\frac{-B}{\omega}\right]dB \qquad (85)$$

Since all fractures are completely saturated with liquid we have to integrate between the smallest (B_{min}) and largest (B_{max}) apertures under consideration. The integrals for liquid saturation and hydraulic conductivity may be represented by one general integral given as:

$$\int_{B_L}^{BU}\left(\frac{aB^4 + bB^2 + cB + d}{eB^2}\right)\left(\frac{B^2}{2\omega^3}Exp\left[\frac{-B}{\omega}\right]\right)dB \qquad (86)$$

Where B_L and B_U are the limits of integration (see Fig.23b), and a, b, c, d, e are constants containing expressions for liquid occupied cross-sectional area and average hydraulic conductivities of the flow regimes under consideration (Eqs.75, 76, 77, 78, and 79). The analytical solution for Eq.86 is given in *Appendix IV*, all constants for liquid saturation and hydraulic conductivity are listed in *Appendix V*.

Combining Matrix and Fracture Contributions

Liquid saturation and hydraulic conductivity of a fractured porous medium is obtained by weighing the individual contributions of the matrix and fracture domain by their porosities as already included in the derived equations.

Model Application – Illustrative Example

A preliminary test of the proposed model was performed using data for the Tiva Canyon Tuff section reported by Wang and Narasimhan (1993). Available input data are listed in Tab.2; physical constants used in the sample calculations are listed in Tab.1 (page 22, previous notebook).

Tab.2. Model input parameters and measured and calculated saturated permeabilities
(from Wang and Narasimhan, 1993)

Property	Matrix	Fracture
Porosity	0.114	0.00058
Effective Aperture	NA	0.109 [mm]
VG-Model Parameters	$\alpha = 8.21 \times 10^{-3}$ [m^{-1}] n = 1.558 $\theta_r = 0.002$ [m^3 m^{-3}]	NA
Saturated Permeability *measured*	2.55×10^{-18} [m^2]	1.18×10^{-12} [m^2]
Saturated Permeability *calculated*	2.45×10^{-18} [m^2]	* 1.19×10^{-12} [m^2]

* was preserved during model application

The model for matrix saturation was fitted to the VG-saturation curve to obtain a set of best-fit parameters that was consecutively used to predict saturated und unsaturated matrix permeability. Fracture saturation and unsaturated permeability was derived by matching the mean of the aperture distribution (gamma distribution with $\zeta=2$) to the effective aperture and preserving the measured saturated fracture permeability. The maximum and minimum aperture was set to arbitrary values of 10^{-3} m and 10^{-9} m respectively. The resulting saturation and K(μ) curves are depicted in Fig.24; showing the typical double-hump curve for permeability, with a fast (preferential) flow domain associated to the fractures. In lack of measured saturation and unsaturated permeability data we preserved measured saturated fracture permeability. Saturation and permeability curves for matrix are in good agreement with the VG-saturation curves reported by Wang and Narasimhan (1993). The predicted matrix permeability of 2.45×10^{-18} m^2 is almost identical with the reported value of 2.55×10^{-18} m^2. This preliminary test shows the potential of the proposed approach for modeling liquid configuration and transport in fractured porous media, however refinements and tests with more complete datasets, including more detailed information for the fracture domain are necessary.
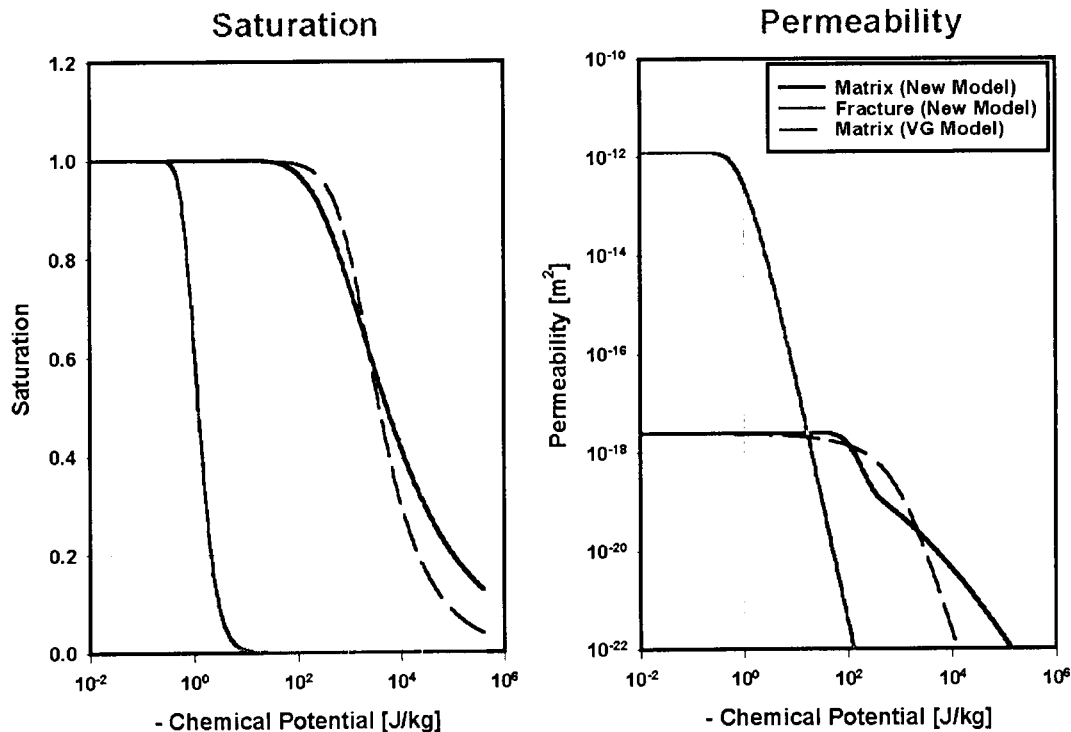
Tiva Canyon Welded Tuff Unit

Fig.24: Calculated saturation and permeability curves for Tiva Canyon Tuff

12/21/99 – Status

A paper on constitutive relationships for matrix-fracture hydraulic conductivity is in preparation for journal submission (Water Resource Research) and started on the CNWRA technical and programmatic process. Hence, it is a good idea to re-assess at this point the status of the work and where it may be heading.

Open issues (pertaining to the TEF-KTI) for future model improvement

- The assumed roughness geometry does not consider asperities and similar elements rising above mean fracture surface plane. Introduction of such elements should add realism to the model and capture some of the intermittent flow behavior observed. For inclusion of these elements we need to consider liquid build-up around conical objects (see "edge" in Appendix B of Tuller et al., 1999).

- The dynamics matrix-fracture interactions were not treated in this work – some of the rates of such interactions would be useful to capture the essence of potential bypass flow through these fracture surfaces (e.g., as liquid flux encounter low porosity/permeability layer such as the PTN).

References

Abramowitz, M., and I.E. Stegun, Handbook of mathematical functions with formulas, graphs, and mathematical tables, National Bureau of Standards Applied Mathematics, Series 55, 1964.

Assouline S., D. Tessier, and A. Bruand 1998. A conceptual model of the soil water retention curve. Water Resour. Res. 34:223-231.

Blunt, M., D. Zhou, and D. Fenwick, Three-phase flow and gravity drainage in porous media, Transport in porous media, 20, 77-103, 1995.

Brutsaert, W. 1966. Probability laws for pore-size distributions. Soil Science, 101(2):85-92.

Burdine, N.T., Relative permeability calculation size distribution data. Pet. Trans. Am. Inst. Min. Metal. Pet. Eng. 198: 71-78, 1953.

Childs, E.C., and G.N. Collis-George, The permeability of porous materials. R. Soc. London, Proc., A 201: 392-405, 1950.

Derjaguin, B.V., Correct form of the equation of capillary condensation in porous bodies, Proc. 2nd int. Congr. Surf. Action, 2, 153-159, 1957.

Derjaguin, B.V., N.V. Churaev, and V.M. Muller, Surface Forces, Plenum Publishing Corporation, Consultants Bureau, New York, 1987.

Dullien, F. A. L. , F. S. Y. Francis and I. F. MacDonald, Hydraulic continuity of residual wetting phase in porous media, Journal of Colloid and Interface Science, 109 (1), 201-218, 1986.

Edlefsen, N.E., and A.B.C. Anderson, Thermodynamics of soil moisture, Hilgardia, 15, 31-298, 1943.

Gardner, W.R., Some steady state solutions of the unsaturated moisture flow equation with application to evaporation from a water table, Soil Sci., 85: 228-232, 1958.

Iwamatsu, M., and K. Horii, Capillary condensation and adhesion of two wetter surfaces, Journal of Colloid and Interface Science, 182, 400-406, 1996.

Kim, H., P. Suresh, and C. Rao, Determination of effective air-water interfacial area in partially saturated porous media using surfactant adsorption, Water Resour. Res., 32(12), 2705-2711, 1997.

Kosugi, K. 1994. Three-parameter lognormal distribution model for soil water retention. Water Resour. Res. 30(4):891-901.

Kosugi, K. 1996. Lognormal distribution model for unsaturated soil hydraulic properties. Water Resour. Res. 32(9):2697-2703.

Laroussi, C., and L.W. De Backer 1979. Relations between properties of glass beads media and their main $\psi(\theta)$ hysteresis loops. Soil Sci. Soc. Am. J. 43:646-650.

Li, Y., and N.C. Wardlaw. Mechanisms of nonwetting phase trapping during imbibition at slow rates. J. Colloid Interface Sci. 109, 473-486, 1986.

Mason, G., and N.R. Morrow, Capillary behavior of a perfectly wetting liquid in irregular triangular tubes, J. Colloid Interface Sci., 141(1), 262-274, 1991.

Mualem, Y., A new model for predicting the hydraulic conductivity of unsaturated porous media, Water Resour. Res., 12(3), 513-522, 1976.

Nitao, J.J., and J. Bear, Potentials and their role in transport in porous media, Water Resour. Res., 32(2), 225-250, 1996.

Novy, R.A., P.G. Toledo, H.T. Davis, and L.E. Scriven, Capillary dispersion in porous media at low wetting phase saturations, Chem. Eng. Sci., 44(9), 1785-1797, 1989.

Or, D., and M. Tuller, Liquid retention and interfacial area in variably saturated porous media: Upscaling from pore to sample scale model, Water Resour. Res, 35(12), 3591-3606, 1999.

Philip, J.R., Unitary approach to capillary condensation and adsorption, The Journal of Chemical Physics, 66(11), 5069-5075, 1977.

Ransohoff, T. C., and C. J. Radke, Laminar flow of a wetting liquid along the corners of a predominantly gas-occupied noncircular pore, *Journal of Colloid and Interface Science, 121*(2), 392-401, 1988.

Rice, J.A., Mathematical Statistics and Data Analysis, 2nd ed., Duxbury Press, Belmont, California, 1995.

Spurk, J.H., Fluid mechanics. Springer-Verlag, Berlin, Heidelberg, 1997.

Tuller, M., D. Or, and L.M. Dudley, Adsorption and capillary condensation in porous media - Liquid retention and interfacial configurations in angular pores. *Water Resour. Res., 35*(7), 1949-1964, 1999.

van Genuchten, M.Th., A closed-form equation for predicting the hydraulic conductivity of unsaturated soils, *Soil Sci. Soc. Am. J., 44*, 892-898, 1980.

Wang, J.S.Y., and T.N. Narasimhan, Unsaturated flow in fractured porous media, In: Bear, J., Ch-F. Tsang, and G. De Marsily (Editors), Flow and contaminant transport in fractured rock, *Academic Press Inc.*, 325-394, 1993.

APPENDIX I

Angularity factor, area factor, and drainage radius of curvature [1] coefficient C_n (used to determine maximum pore length L1 for completely full unit cells) for different polygon-shaped central pores.

Corners	Angle	Angularity Factor F_n	Area factor A_n	Coefficient C_n defining drainage curvature	Pore Shapes
n	γ	$F_n = \sum\limits_{i=1}^{n}\left(\dfrac{1}{\tan\left(\frac{\gamma_i}{2}\right)} - \dfrac{\pi(180-\gamma_i)}{360} \right)$	$A_n = \dfrac{n}{4}\cot\left(\dfrac{\pi}{n}\right)$	$C_n = \dfrac{1}{n}\left(2(F_n+\pi)+2\sqrt{\pi\,(F_n+\pi)}\right)$	
3	60	$3\sqrt{3}-\pi$	$\dfrac{\sqrt{3}}{4}$	$\dfrac{2\left(3+\sqrt[4]{3}\sqrt{\pi}\right)}{\sqrt{3}}$	
4	90	$4-\pi$	1	$2+\sqrt{\pi}$	
12	150	$\dfrac{12}{2+\sqrt{3}}-\pi$	$3\left(2+\sqrt{3}\right)$	$\dfrac{6+\sqrt{3}\,\sqrt{(2+\sqrt{3})\pi}}{3(2+\sqrt{3})}$	

[1] The radius of curvature for imbibition, r_{imb}, is related to r_d by: $r_{imb} = r_d\left(1+\sqrt{\dfrac{\pi}{F_n+\pi}}\right)$

APPENDIX II

Integration limits, constants, and variables used in the hydraulic conductivity calculations (Eq.56)

Conductivity Term (Integration Limits[†])	A[‡]	B[‡]	C[‡]	D[‡]	E	F
Ksat (L_{min}, L_{max})	$(A_n Kd - 2\alpha\beta Ks)\phi$	$2\alpha\beta L_{max} Ks\phi$	0	0	$A_n - 2\alpha\beta$	$2\alpha\beta L_{max}$
K(μ)₁ (L_{min}, L_1)	$A_n Kd\phi$	0	0	0	$A_n - 2\alpha\beta$	$2\alpha\beta L_{max}$
K(μ)₂ (L_{min}, L_1)	$-2\alpha\beta Ks\phi$	$2\alpha\beta L_{max} Ks\phi$	0	0	$A_n - 2\alpha\beta$	$2\alpha\beta L_{max}$
K(μ)₃ (L_2, L_{max})	0	0	$-4\beta h(\mu)KF(\mu)\phi$	$4\beta L_{max} h(\mu)KF(\mu)\phi$	$A_n - 2\alpha\beta$	$2\alpha\beta L_{max}$
K(μ)₄ (L_1, L_{max})	0	0	$n\, h(\mu)KF(\mu)\phi$	$-nh(\mu)\dfrac{2r(\mu)}{\tan(\gamma/2)}KF(\mu)\phi$	$A_n - 2\alpha\beta$	$2\alpha\beta L_{max}$
K(μ)₅ (L_1, L_{max})	0	0	0	$r(\mu)^2 F_n KC(\mu)\phi$	$A_n - 2\alpha\beta$	$2\alpha\beta L_{max}$

[†] $L_{min}=10^{-9}$ m; L_{max}, L_1, and L_2 are given in Eqs.31, 25, and 27.

[‡] For Ks, Kd, KF(μ), and KC(μ) see Eqs.44-50.

APPENDIX III - Analytical Solution for Sample-Scale Matrix Hydraulic Conductivity (Eq.63)

The general integral in Eq.63 was solved using Mathematica Version 3.0.

$$K_i(\mu) = \int_{L_L}^{L_U} \frac{AL^4 + BL^3 + CL + D}{EL^2 + FL} f(L)\,dL$$

with the gamma distribution for L given as:

$$f(L) = \frac{L^\xi}{\xi!\,\omega^{\xi+1}} \exp\left(-\frac{L}{\omega}\right) \qquad L \geq 0 \qquad \{\xi \text{ was set to 2 to facilitate a closed-form solution}\}$$

$$
\begin{aligned}
K_i(\mu) = \frac{1}{2E^6\,\omega^3}\Bigg\{ & E\,\omega\Bigg[\exp\left(-\frac{L_L}{\omega}\right)\Big(DE^4 - BEF^3 + AF^4 + BE^2F^2L_L - AEF^3L_L - BE^3FL_L{}^2 + AE^2F^2L_L{}^2 \\
& + BE^4L_L{}^3 - AE^3FL_L{}^3 + AE^4L_L{}^4 + E\big(F^2(BE-AF) - 2EF(BE-AF)L_L + 3E^2(BE-AF)L_L{}^2 + 4AE^3L_L{}^3\big)\omega \\
& + 2E^2\big(BE(-F+3EL_L) + A\,(F^2 - 3EFL_L + 6E^2L_L{}^2)\big)\omega^2 + 6E^3(BE-AF+4AEL_L)\omega^3 + 24AE^4\omega^4 \\
& + CE^3(-F+E(L_L+\omega))\Big) - \exp\left(-\frac{L_U}{\omega}\right)\Big(DE^4 - BEF^3 + AF^4 + BE^2F^2L_U - AEF^3L_U - BE^3FL_U{}^2 + AE^2F^2L_U{}^2 \\
& + BE^4L_U{}^3 - AE^3FL_U{}^3 + AE^4L_U{}^4 + E\big(F^2(BE-AF) - 2EF(BE-AF)L_U + 3E^2(BE-AF)L_U{}^2 + 4AE^3L_U{}^3\big)\omega \\
& + 2E^2\big(BE(-F+3EL_U) + A\,(F^2 - 3EFL_U + 6E^2L_U{}^2)\big)\omega^2 + 6E^3(BE-AF+4AEL_U)\omega^3 + 24AE^4\omega^4 \\
& + CE^3(-F+E(L_L+\omega))\Big)\Bigg] \\
& + \exp\left(\frac{F}{E\omega}\right)F\big(DE^4 - CE^3F + F^3(-BE+AF)\big)\left(\mathrm{Ei}\left(-\frac{F+EL_L}{E\omega}\right) - \mathrm{Ei}\left(-\frac{F+EL_U}{E\omega}\right)\right)\Bigg\}
\end{aligned}
$$

The exponential integral Ei[U] is solved using the series expansion [Abramowitz and Stegun, 1964]:

$$\mathrm{Ei}[U] = \gamma_1 + \ln U + \sum_{n=1}^{\infty} \frac{U^n}{n\,n!} \qquad (0 < U < 20)$$

where γ_1 is Euler's constant ($\gamma_1 = 0.5772156649\ldots$). The series must be expanded at least to n=100 to reach the required accuracy. For $-20 < U < 0$ Ei[-U] may be expressed as $-E_1[U]$ and solved with [Abramowitz and Stegun, 1964]:

$$E_1[U] = \gamma_1 + \ln[-U] + \sum_{n=1}^{\infty} \frac{(-1)^n(-U)^n}{n\,n!} \qquad (-20 < U < 0)$$

APPENDIX IV – Analytical Solution for Sample-Scale Fracture Liquid Saturation and Hydraulic Conductivity (Eq.86)

The general integral in Eq.86 was solved using Mathematica Version 3.0.

$$\int_{B_L}^{B_U} \left(\frac{aB^4 + bB^2 + cB + d}{eB^2} \right) \left(\frac{B^2}{2\omega^3} Exp\left[\frac{-B}{\omega} \right] \right) dB =$$

$$\frac{1}{2e\omega^2} \left(Exp\left[-\frac{B_L}{\omega} \right] \left(B_L\, c + d + c\,\omega + b\left(B_L^2 + 2B_L\,\omega + 2\omega^2 \right) + a\left(B_L^4 + 4B_L^3\omega + 12B_L^2\omega^2 + 24B_L^3\omega^3 + 24\omega^4 \right) \right) \right) -$$

$$\frac{1}{2e\omega^2} \left(Exp\left[-\frac{B_U}{\omega} \right] \left(B_U\, c + d + c\,\omega + b\left(B_U^2 + 2B_U\,\omega + 2\omega^2 \right) + a\left(B_U^4 + 4B_U^3\omega + 12B_U^2\omega^2 + 24B_U^3\omega^3 + 24\omega^4 \right) \right) \right)$$

APPENDIX V – Constants for Eq.86

$$\int_{B_1}^{B_u}\left(\frac{aB^4+bB^2+cB+d}{eB^2}\right)\left(\frac{B^2}{2\omega^3}Exp\left[-\frac{B}{\omega}\right]\right)dB$$

	a	b	c	d	e
Degree of Saturation					
(1) Full Fracture (S_w=1) Integration of the gamma distribution from B_{min} to B_1	$\int_{B_{min}}^{B_1}\left(\frac{B^2}{2\omega^3}Exp\left[-\frac{B}{\omega}\right]\right)dB$				
(2) Separated Interfaces - Full Grooves Films and Grooves Integration from B_1 to B_2	0	$\dfrac{2\tau^2\delta}{\sqrt{3}}$	$2h(\mu)\left(\upsilon-\dfrac{2\tau\delta}{\sqrt{3}}\right)$	0	$\upsilon+\dfrac{2\tau^2}{\sqrt{3}}$
(2a) Separated Interfaces - Full Grooves Films Integration from B_1 to B_2	0	0	$2h(\mu)\left(\upsilon-\dfrac{2\tau\delta}{\sqrt{3}}\right)$	0	$\upsilon+\dfrac{2\tau^2}{\sqrt{3}}$
(2b) Separated Interfaces - Full Grooves Grooves Integration from B_1 to B_2	0	$\dfrac{2\tau^2\delta}{\sqrt{3}}$	0	0	$\upsilon+\dfrac{2\tau^2}{\sqrt{3}}$
(3) Separated Interfaces - Partially Filled Grooves Films and Grooves Integration from B_2 to B_{max}	0	0	$2h(\mu)\left(\upsilon+\dfrac{2\tau}{\sqrt{3}}\right)$	$2r(\mu)^2\left(\sqrt{3}-\dfrac{\pi}{3}\right)-4\sqrt{3}\,h(\mu)r(\mu)$	$\upsilon+\dfrac{2\tau^2}{\sqrt{3}}$
(3a) Separated Interfaces - Partially Filled Grooves Films Integration from B_2 to B_{max}	0	0	$2h(\mu)\left(\upsilon+\dfrac{2\tau}{\sqrt{3}}\right)$	$-4\sqrt{3}\,h(\mu)r(\mu)$	$\upsilon+\dfrac{2\tau^2}{\sqrt{3}}$
(3b) Separated Interfaces - Partially Filled Grooves Grooves Integration from B_2 to B_{max}	0	0	0	$2r(\mu)^2\left(\sqrt{3}-\dfrac{\pi}{3}\right)$	$\upsilon+\dfrac{2\tau^2}{\sqrt{3}}$

	a	b	c	d	e
Hydraulic Conductivity Ksat and K(μ)					
(1) Ksat and Full Fracture Parallel Plates and Ducts B_{min} to B_{max} (Ksat) and B_{min} to B_1 (K(μ))	$\frac{\rho g}{\eta_0}\left(\frac{\upsilon}{12}+\frac{\tau^4\delta}{30\sqrt{3}}\right)\phi_F$	0	0	0	$\upsilon+\frac{2\tau^2}{\sqrt{3}}$
(1a) Ksat and Full Fracture Parallel Plates B_{min} to B_{max} (Ksat) and B_{min} to B_1 (K(μ))	$\frac{\rho g}{\eta_0}\frac{\upsilon}{12}\phi_F$	0	0	0	$\upsilon+\frac{2\tau^2}{\sqrt{3}}$
(1b) Ksat and Full Fracture Ducts B_{min} to B_{max} (Ksat) and B_{min} to B_1 (K(μ))	$\frac{\rho g}{\eta_0}\frac{\tau^4\delta}{30\sqrt{3}}\phi_F$	0	0	0	$\upsilon+\frac{2\tau^2}{\sqrt{3}}$
(2) Separated Interfaces - Full Grooves Films and Grooves Integration from B_1 to B_2	$\frac{\rho g}{\eta_0}\frac{\tau^4\delta}{30\sqrt{3}}\phi_F$	0	$2h(\mu)\left(\upsilon-\frac{2\tau\delta}{\sqrt{3}}\right)KF(\mu)\phi_F$	0	$\upsilon+\frac{2\tau^2}{\sqrt{3}}$
(2a) Separated Interfaces - Full Grooves Films Integration from B_1 to B_2	0	0	$2h(\mu)\left(\upsilon-\frac{2\tau\delta}{\sqrt{3}}\right)KF(\mu)\phi_F$	0	$\upsilon+\frac{2\tau^2}{\sqrt{3}}$
(2b) Separated Interfaces - Full Grooves Grooves Integration from B_1 to B_2	$\frac{\rho g}{\eta_0}\frac{\tau^4\delta}{30\sqrt{3}}\phi_F$	0	0	0	$\upsilon+\frac{2\tau^2}{\sqrt{3}}$
(3) Separated Interfaces - Partially Filled Grooves Films and Grooves Integration from B_2 to B_{max}	0	0	$2h(\mu)\left(\upsilon+\frac{2\tau}{\sqrt{3}}\right)KF(\mu)\phi_F$	$2r(\mu)^2\left(\sqrt{3}-\frac{\pi}{3}\right)KC(\mu)\phi_F-4\sqrt{3}h(\mu)r(\mu)KF(\mu)\phi_F$	$\upsilon+\frac{2\tau^2}{\sqrt{3}}$
(3a) Separated Interfaces - Partially Filled Grooves Films Integration from B_2 to B_{max}	0	0	$2h(\mu)\left(\upsilon+\frac{2\tau}{\sqrt{3}}\right)KF(\mu)\phi_F$	$-4\sqrt{3}h(\mu)r(\mu)KF(\mu)\phi_F$	$\upsilon+\frac{2\tau^2}{\sqrt{3}}$
(3b) Separated Interfaces - Partially Filled Grooves Grooves Integration from B_2 to B_{max}	0	0	0	$2r(\mu)^2\left(\sqrt{3}-\frac{\pi}{3}\right)KC(\mu)\phi_F$	$\upsilon+\frac{2\tau^2}{\sqrt{3}}$

With:

δ .... Groove Connectivity Factor

η_0 .... Liquid Viscosity [kg m^{-1} s^{-1}]

ρ .... Liquid Density [kg m^{-3}]

τ .... Dimensionless Groove Depth Scaling Parameter

υ .... Dimensionless Fracture Length Scaling Parameter

ϕ_F .... Fracture Porosity

B_1, B_2 .... Integration Limits [m]

B_{min} .... Minimum Aperture [m]

B_{max} .... Maximum Aperture [m]

g .... Acceleration of Gravity [m s^{-2}]

$h(\mu)$ .... Film Thickness as a Function of Chemical Potential [m]

$KC(\mu)$ .... Corner Conductivity [m s^{-1}]

$KF(\mu)$ .... Viscosity dependent Film Conductivity [m s^{-1}]

$r(\mu)$ .... Radius of Interface Curvature as a Function of Chemical Potential [m]

Thick film (h ≥ 10 nm) $\qquad KF(\mu) = \dfrac{\rho g}{\eta_0} \dfrac{h(\mu)^2}{3}$ $\qquad\qquad B_1 = \dfrac{-2\sigma}{\rho\mu}$

Thin film (h < 10 nm) $\qquad KF(\mu) = \dfrac{\rho g}{\eta_0} \dfrac{A(\mu)}{12\,h(\mu)}$ $\qquad\qquad B_2 = \dfrac{-3\sigma}{2\tau\rho\mu}$

Corner $\qquad\qquad\qquad KC(\mu) = \dfrac{\rho g}{\eta_0} \dfrac{r(\mu)^2}{\varepsilon}$ $\qquad\qquad h(\mu) = \sqrt[3]{\dfrac{A_{svl}}{6\pi\rho\mu}}$

$$A(\mu) = \left(a^2 h(\mu) + 5a\,h(\mu)^2 - 4h(\mu)^3\right)\exp\left(-\frac{a}{h(\mu)}\right) + \left(a^3 + 6a^2 h(\mu)\right)Ei\left[-\frac{a}{h(\mu)}\right] \qquad r(\mu) = -\frac{\sigma}{\rho\mu}$$

APPENDIX VI

**Adsorption and capillary condensation in porous media:
Liquid retention and interfacial configurations in angular pores**

Markus Tuller, Dani Or, and Lynn M. Dudley
Department of Plants, Soils, and Biometeorology, Utah State University, Logan

APPENDIX VII

Liquid retention and interfacial area in variably saturated porous media: Upscaling from single-pore to sample-scale model

Dani Or and Markus Tuller
Department of Plants, Soils, and Biometeorology, Utah State University, Logan

Volume 1: Hydraulic Conductivity of Unsaturated Fractured Porous Media: Flow in a Cross-Section *(Continuation)*

Thermal Effects/USFIC - Key Technical Issues

Account Number: 20-1402-**661/861**
Collaborators: Markus Tuller (USU) and Randall Fedors (CNWRA)
Directories: C:\SCI_NOTE_FRACTURE\

Objectives: Modifications and updates for the theoretical model for flow in unsaturated fractured porous that was developed in the previous notebook. Primary modifications are related to the fracture domain. To avoid duplication, for the matrix domain we refer to the previous notebook whenever appropriate and repeat crucial derivations only. This documentation includes: (1) Change of dimensions for the unit fracture element. (2) Derivation of pore scale expressions for liquid saturation and unsaturated hydraulic conductivity taking into consideration of pore scale flow phenomena. (3) Upscaling of the pore-scale hydraulic functions to represent sample-scale response of the fracture domain. (4) Derivation of a general analytical solution for sample-scale hydraulic functions. (5) Combining matrix and fracture domain calculations to calculate the total response of the fractured porous medium. (6) Model application to measured data reported by *Wang and Narasimhan* [1993], and *Fischer et al.* [1998]. (7) Discussion of the hydraulic conductivity function for non-equilibrium conditions. (8) Introduction of potential strategies to approximate 3D network effects.

[signature: Dani Or]

03/10/01 – Initial entry (notebook continuation)

The preliminary results of the theoretical model for flow in unsaturated fractured porous media based on dual-continuum modeling of matrix and fracture pore spaces unified by equilibrium chemical potential developed in the previous notebook revealed great potential to calculate the continuous liquid saturation curve and to predict the unsaturated hydraulic conductivity function for fractured rock. In this notebook we will introduce some minor modifications to the fracture domain calculations, and develop potential concepts for incorporation of 3D network effects. Furthermore we will introduce considerations of non-equilibrium conditions and present comparison with measured datasets.

To ensure the practical applicability of the model, surface geometrical features are kept simple enough to obtain closed-form expressions for hydraulic conductivity programmable into conventional spreadsheet software (e.g., Excel, Quattro Pro).

The proposed model is to be based on appropriate thermodynamically and physically considerations. Simplifications should be kept at a minimum and are highlighted and explained at the appropriate level of the development process.

Remark:

- The assumed fracture element and its roughness geometry do not consider asperities and similar elements rising above mean fracture surface plane. Introduction of such elements should add realism to the model and capture some of the intermittent flow behavior observed. For inclusion of these elements we need to consider liquid build-up around conical objects. These elements lead to intermittent rivulet flows and are treated separately.

04/15/01 – Unit Fracture Element

The 2-D fracture network is represented as an assembly of basic fracture elements; each is comprised of two parallel surfaces separated by a certain aperture size (B). Each surface contains a single groove (or pit) representing surface roughness [*Or and Tuller*, 2000]. The fracture element length (vB), and groove depth (τB), are assumed to be proportional to fracture aperture size (B), as depicted in Fig.25a. Although such geometrical scaling imposes constraints on the nature of surface roughness, it simplifies the model and facilitates derivation of closed-form expressions for FPM hydraulic conductivity. Nevertheless, the proposed geometry shows reasonable versatility as illustrated in Figs.25b-e, using several combinations of scale parameters for mated and unmated fracture surfaces. Moreover, scaling constraints can be relaxed as more information on surface roughness becomes available (at the expense of requiring a numerical scheme for evaluation of the hydraulic functions).
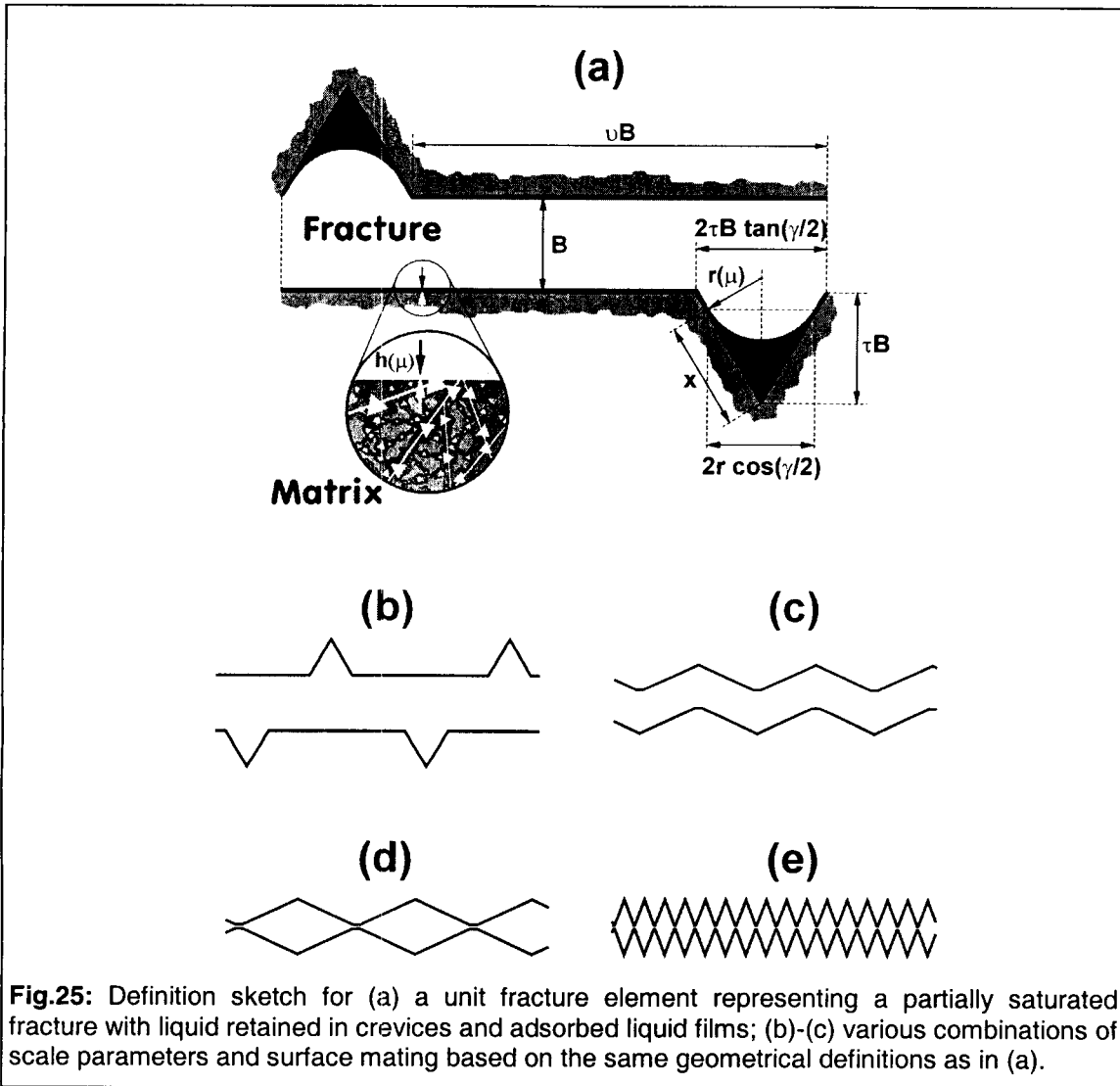

Fig.25: Definition sketch for (a) a unit fracture element representing a partially saturated fracture with liquid retained in crevices and adsorbed liquid films; (b)-(c) various combinations of scale parameters and surface mating based on the same geometrical definitions as in (a).

Remark:

- The fracture element length was changed from υB to υb+2τBtan(γ/2) to add more flexibility (see also previous notebook figure 20 page 46).

Equilibrium Liquid Configuration within a Unit Fracture Element

Both here and in subsequent derivations, we assume thermodynamic equilibrium between fracture and matrix domains (an assumption that was verified experimentally in some systems [*Wang and Narasimhan*, 1993]). Equilibrium liquid-vapor interfacial configurations evolve with changes in matric potential and determine the liquid-occupied cross-sectional areas within a unit fracture element (i.e., saturation). The desaturation of an initially saturated fracture element by a gradual decrease of matric potential is not a continuous process, but rather involves spontaneous liquid displacement (formation of separated interfaces) at certain critical potentials as determined by liquid properties and geometry. Before proceeding with identification of these critical potentials at the transition between various fracture filling stages, we first address a few basic relationships between adsorbed liquid film thickness and liquid-vapor interfacial curvature as functions of matric potential. As shown in *Tuller et al.* [1999] and *Or and Tuller* [2000], equilibrium liquid configuration can be determined by a superposition of adsorbed liquid films and liquid retained in surface pits and grooves (Fig.25) due to capillary forces. The thickness h(μ) of adsorbed films at a given potential μ is calculated as:

$$h(\mu) = \sqrt[3]{\frac{A_{svl}}{6\pi \rho \mu}} \tag{87}$$

where A_{svl} is the Hamaker constant (a parameter that combines solid-vapor interactions through intervening liquid), and ρ is liquid density. The radius of interface curvature of a capillary meniscus r(μ) is calculated for a given potential according to the Young-Laplace equation:

$$r(\mu) = -\frac{\sigma}{\rho\mu} \tag{88}$$

where σ is the liquid-vapor surface tension. Liquid films are assumed to cover all solid surfaces within the unit fracture element; we thus shift the radius of curvature r(μ) by film thickness h(μ) to obtain the composite liquid-filled cross-sectional area. In the transition from complete saturation (high matric potential) to dry conditions (low matric potential), we distinguish between three filling stages as depicted in Fig.26. We consider a completely saturated unit fracture element and lower the matric potential gradually to a certain threshold value μ_1, where the fracture spontaneously empties and two separate liquid-vapor interfaces are formed on the opposite faces of a fracture. The critical potential μ_1 at the point of separation is derived from capillarity considerations:

$$\mu_1 = -\frac{2\sigma}{\rho B} \tag{89}$$

where B is the fracture aperture. The presence of roughness on the fracture surface ensures that some liquid is retained (by capillary forces) in pits and grooves. The radius of interface curvature of a meniscus anchored at the edges of the pit is simply B/2 (or $-\sigma/\rho\mu_1$) at the separation potential. For certain pit depths (parameterized by τ) such as,

$$\tau \geq \frac{\cos(\gamma/2)}{2\tan(\gamma/2)} \tag{90}$$

the radius of interface curvature at fracture evacuation (r=B/2) results in menisci that are tangent to the surfaces of the pit which greatly simplify subsequent calculations. In cases where the inequality in Eq.90 is not satisfied, we introduce a second potential threshold (μ_2) that marks the starting point for recession of capillary menisci into the surface pit. The critical potential μ_2 is obtained from simple geometrical considerations:

$$\mu_2 = -\frac{\sigma \cos(\gamma/2)}{\tau B \rho \tan(\gamma/2)} \tag{91}$$

where γ is the pit angle (Fig.25). Hence, for a given geometry, we first evaluate Eq.90 and calculate the relevant critical potentials.
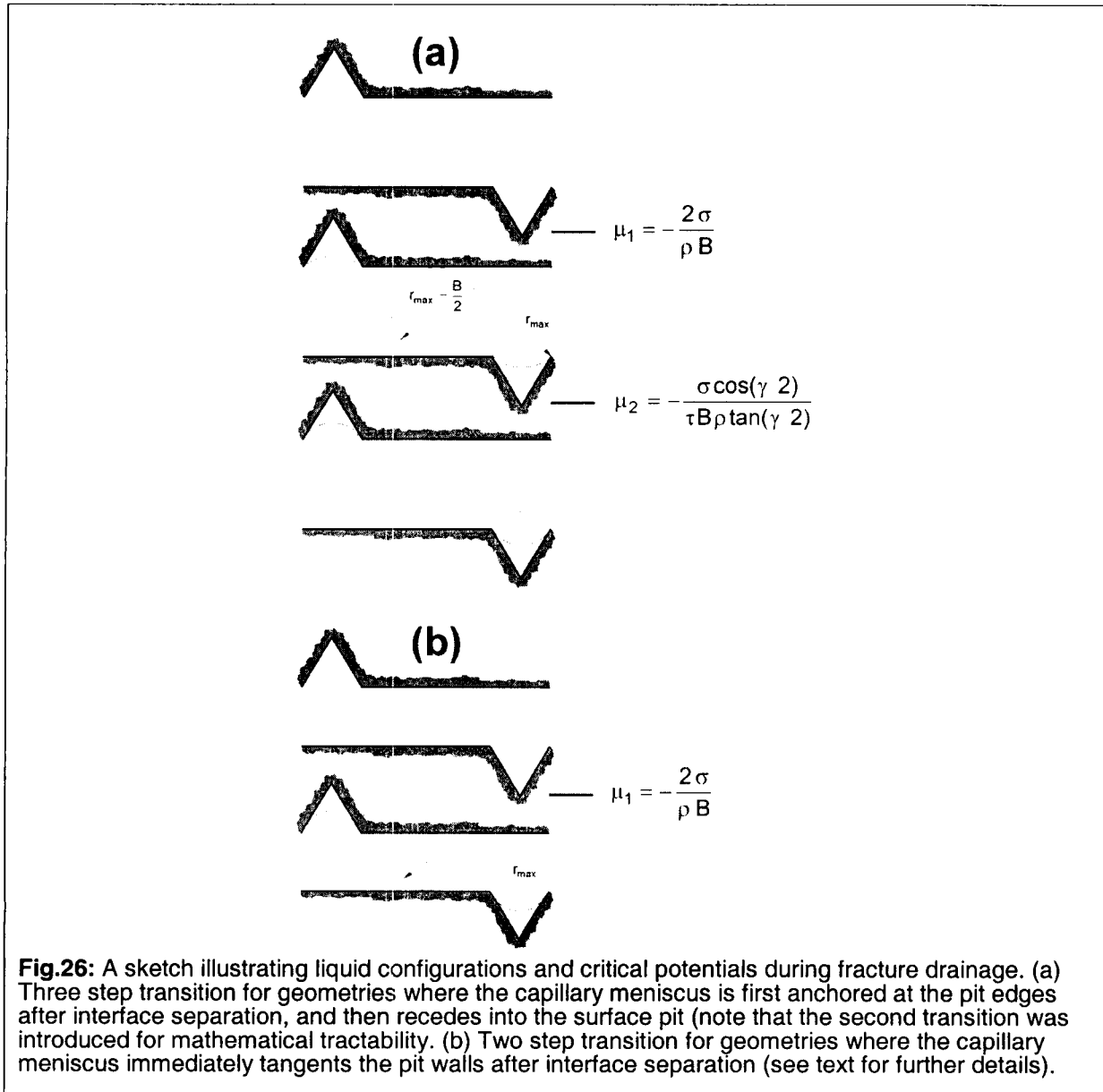

Fig.26: A sketch illustrating liquid configurations and critical potentials during fracture drainage. (a) Three step transition for geometries where the capillary meniscus is first anchored at the pit edges after interface separation, and then recedes into the surface pit (note that the second transition was introduced for mathematical tractability. (b) Two step transition for geometries where the capillary meniscus immediately tangents the pit walls after interface separation (see text for further details).

If the geometry requires introduction of μ_2 the relative saturation curve is obtained by employing the following expressions. For all potentials $\mu > \mu_1$ the unit element is completely saturated and the relative saturation is simply 1.

$$S_1 = 1 \qquad (92)$$

Note that relative saturation is obtained by dividing the liquid occupied cross-sectional area at a certain potential by the total cross-sectional unit element area disregarding the associated solid shell (i.e., calculating the fraction of liquid-filled pore space only). For all potentials $\mu_1 \geq \mu > \mu_2$ where adsorbed films

cover the flat parts of the element and the capillary menisci are anchored at the pit edges, relative saturation is given as:

$$S_2(\mu) = \frac{2\left[B\,h(\mu)\nu - r(\mu)^2 \arcsin\left(\frac{B\tau\tan\left(\frac{\gamma}{2}\right)}{r(\mu)}\right) + B\tau\tan\left(\frac{\gamma}{2}\right)\left(B\tau + \sqrt{r(\mu)^2 - \left(B\tau\tan\left(\frac{\gamma}{2}\right)\right)^2}\right) \right]}{B^2\left(\nu + 2\tau(1+\tau)\tan\left(\frac{\gamma}{2}\right)\right)} \tag{93}$$

where ν is a dimensionless fracture length scaling parameter. Note that the denominator in Eq.93 is the cross-sectional area of the unit fracture element without solid shell. Finally, for all potentials $\mu \le \mu_2$ where menisci start receding into the pit corners and additional film covered area is exposed, relative saturation is calculated as:

$$S_3(\mu) = \frac{2h(\mu)\left(B\nu + \frac{2\tau B}{\cos\left(\frac{\gamma}{2}\right)} - \frac{2r(\mu)}{\tan\left(\frac{\gamma}{2}\right)} \right) + 2r(\mu)^2 F_\gamma}{B^2\left(\nu + 2\tau(1+\tau)\tan\left(\frac{\gamma}{2}\right)\right)} \tag{94}$$

where F_γ is an angularity factor defined as:

$$F_\gamma = \frac{1}{\tan(\gamma/2)} - \frac{\pi(180-\gamma)}{360} \tag{95}$$

For all cases where capillary menisci are tangent to the pit surfaces immediately after interface separation (i.e., where [Eq.90] is satisfied), we use Eq.92 for $\mu > \mu_1$, and Eq.94 for all potentials $\mu \le \mu_1$. The equilibrium liquid configurations in a unit element cross-section provide the basis for introduction of hydrodynamic considerations within the unit element geometry.

04/20/01 – Hydrodynamic Considerations within a Unit Fracture Element

A key assumption for introduction of hydrodynamic considerations for partially filled fractures is that equilibrium liquid-vapor interfaces remain stable under slow laminar flow conditions. Hence, in view of the various liquid filling stages of a unit fracture element discussed in the previous section, we consider four laminar flow regimes. For a completely saturated fracture element, we consider parallel plate flow, and flow in isosceles triangular ducts. For partially filled elements we invoke the interfacial stability assumption and consider laminar flow in corners bounded by a liquid-vapor interface, and flow in adsorbed films lining flat solid surfaces. For the derivation of macroscopic hydraulic conductivity it is not necessary to describe details of the velocity fields; instead, we seek solutions for average flow velocities associated with these flow regimes. Solutions of the relevant Navier-Stokes equations for all flow regimes (except flow in an isosceles triangle) are discussed in *Tuller and Or* [2001].

A solution for average flow velocity in isosceles triangular ducts with a solid-liquid (no-slip) boundary at the legs of the triangle and a liquid-liquid boundary at the triangle base was derived using a finite difference-based numerical scheme. The results were generalized and expressed as:

$$\bar{v} = \zeta \frac{\tau^2 B^2}{\eta_0} \left(-\frac{dP}{dz} \right) \tag{96}$$

where ζ is a dimensionless flow resistance parameter dependent on the vertex angle (pit angle), η_0 is the liquid viscosity, and dP/dz is the hydraulic head gradient in flow direction z. The relationship between flow resistance parameter ζ and pit angle γ may be parameterized as:

$$\zeta = 3.324 \times 10^{-4} + 6.057 \times 10^{-6} \gamma^2 - 1.963 \times 10^{-8} \gamma^3 \tag{97}$$

with γ in degree (r^2=0.99998). The validity of Eq.97 and the solution for flow in corners bounded by a liquid-vapor interface [*Ransohoff and Radke*, 1988; *Or and Tuller*, 2000; *Tuller and Or*, 2001] are limited to a range of pit angles of $30° \leq \gamma \leq 150°$, because of errors at very small and very large pit angles emerging from the applied numerical evaluation schemes.

Remark:

- The Fortran code for numerical evaluation of the average flow velocity in isosceles triangular ducts is stored in Notebook/Poisson3/Poisson3.f90

The parallel plate, film, and corner flow solutions are discussed in detail in the previous notebook. Further information may be obtained from *Tuller and Or* [2001]. For completeness, we list the hydraulic conductivities for all flow regimes under study derived by equating the average velocity obtained from solution of the Navier-Stokes equations with Darcy's law, assuming a unit pressure gradient along the flow path (see also Eqs.47 and 48 page 39 of the previous notebook):

Parallel plates

$$KS = K_s \; B^2 = \frac{\rho g}{\eta_0} \frac{1}{12} B^2 \tag{98}$$

Isosceles triangular ducts

$$KD = K_d \; B^2 = \frac{\rho g}{\eta_0} \zeta \tau^2 B^2 \tag{99}$$

Thick film (h ≥ 10 nm)

$$KF(\mu) = \frac{\rho g}{\eta_0} \frac{h(\mu)^2}{3} \tag{100}$$

Thin film (h < 10 nm)

$$KF(\mu) = \frac{\rho g}{\eta_0} \frac{A(\mu)}{12 h(\mu)} \tag{101}$$

Corner

$$KC(\mu) = \frac{\rho g}{\eta_0} \frac{r(\mu)^2}{\varepsilon} \tag{102}$$

where ζ and ε are dimensionless flow resistance parameters, ρ is the density of the liquid, g as the acceleration of gravity, and $A(\mu)$ is a function for thin films (previous notebook, page 39). Note that in derivation of expressions for film hydraulic conductivities (Eqs.100 and 101) modification of liquid viscosity close to solid surfaces was considered [*Or and Tuller*, 2000; *Tuller and Or*, 2001].

With known average hydraulic conductivity for each flow regime, we now proceed to derive expressions for an entire unit fracture element by weighting the individual contributions by their associated liquid

---

occupied cross-sectional areas, and dividing the resulting expression by the total cross-sectional area, including the matrix shell. The total cross-sectional fracture area A_T is obtained by dividing the fracture area by the porosity of the fracture domain ϕ_F:

$$A_T = \frac{B^2\left(v + 2\tau(1+\tau)\tan\left(\frac{\gamma}{2}\right)\right)}{\phi_F} \tag{103}$$

The resulting expressions for hydraulic conductivity corresponding to various unit element-filling stages are given as:

Saturated hydraulic conductivity: $\mu > \mu_1$

$$K_1 = K_{SAT} = \frac{B^4\left(K_s\left(v + 2\tau\tan\left(\frac{\gamma}{2}\right)\right) + K_d\, 2\tau^2\,\delta\tan\left(\frac{\gamma}{2}\right)\right)}{A_T} \tag{104}$$

Separated interfaces – capillary menisci anchored at pit edges: $\mu_1 \geq \mu > \mu_2$

$$K_2(\mu) = \frac{KF(\mu)2vBh(\mu) + KC(\mu)\,\delta\left[2\tau B\tan\left(\frac{\gamma}{2}\right)\left(\tau B + \sqrt{r(\mu)^2 - \tau^2 B^2\tan\left(\frac{\gamma}{2}\right)^2}\right) - 2r(\mu)^2\, a\sin\left(\frac{\tau B\tan\left(\frac{\gamma}{2}\right)}{r(\mu)}\right)\right]}{A_T} \tag{105}$$

Separated interfaces – capillary menisci tangent pit surfaces: $\mu \leq \mu_2$

$$K_3(\mu) = \frac{2KF(\mu)h(\mu)\left(Bv + \frac{2B\tau}{\cos\left(\frac{\gamma}{2}\right)} - \frac{2r(\mu)}{\tan\left(\frac{\gamma}{2}\right)}\right) + 2KC(\mu)\,\delta\, r(\mu)^2 F_\gamma}{A_T} \tag{106}$$

where K_s, K_d, $KF(\mu)$, and $KC(\mu)$ are the average hydraulic conductivities given in Eqs.98 to102, and δ is a groove connectivity factor with values ranging from zero to one [*Or and Tuller, 2000*] that accounts for partial connectivity among neighboring pits or grooves in the direction of flow. The parameter δ ensures that isolated pits are not considered as part of the K_d and $KC(\mu)$ contributions in Eqs.104 to 106. For fracture geometry that satisfies the inequality in Eq. (90) we use Eq.104 for $\mu > \mu_1$, and Eq.106 for all matric potentials $\mu \leq \mu_1$.
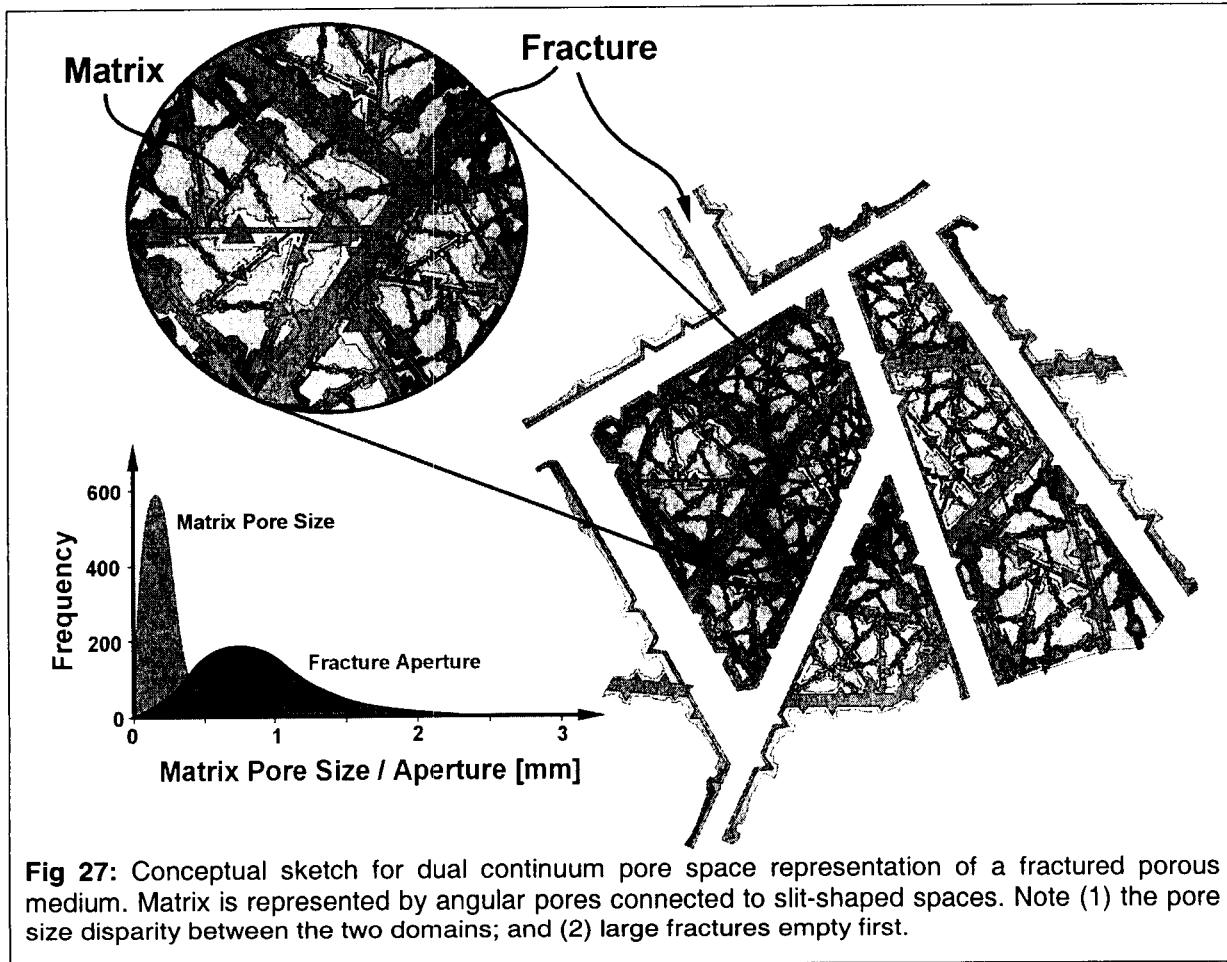
Remark:
- Note that employing $KC(\mu)$ (Eq.102) in Eq.105 leads to a slight underestimation of $K_1(\mu)$ within the narrow matric potential range from μ_1 to μ_2 that may be neglected for all practical purposes.

A framework similar to the one described here was instrumental in deriving pore scale expressions for liquid retention and hydraulic conductivity for matrix pore space comprising of angular central pores connected to slit-shaped spaces [*Tuller et al.*, 1999; *Or and Tuller*, 1999; and *Tuller and Or*, 2001]. See also previous notebook.

04/28/01 – Upscaling Considerations

For representation of FPM hydraulic properties at the sample scale we employ a statistical upscaling scheme, assuming a bimodal distribution for pore sizes and fracture apertures accounting for the two disparate pore scales and porosity of matrix and fractures as depicted in Fig.27.

Fig 27: Conceptual sketch for dual continuum pore space representation of a fractured porous medium. Matrix is represented by angular pores connected to slit-shaped spaces. Note (1) the pore size disparity between the two domains; and (2) large fractures empty first.

The individual contributions of matrix pores and fractures to liquid saturation and unsaturated hydraulic conductivity are calculated separately using the appropriate pore sizes and aperture distributions. The resultant saturation curves are weighted by the porosities of the respective domains and summed up to obtain the composite medium response. A similar approach was taken by *Wang and Narasimhan* [1993] in their Eqs.7.3.3 and 7.3.4 to represent the composite liquid retention and hydraulic conductivity functions for the fracture and matrix domains.

Pore-scale expressions for liquid saturation and unsaturated conductivity and upscaling considerations for the matrix domain are discussed in the previous notebook. Further information may be obtained from *Tuller et al.* [1999], *Or and Tuller* [1999], and *Tuller and Or* [2001]. To avoid duplication we briefly explain the upscaling scheme for the fracture domain, which is similar to the scheme applied for the matrix domain, and refer to previous publications whenever appropriate. To facilitate mathematical tractability and derivation of analytical solutions, and to match observable positive skewness of matrix pore length and fracture aperture distributions, we employ a gamma distribution for their representation [see also *Wang and Narasimhan*,1993]. The gamma density function is dependent on two parameters ξ and ω [*Rice*, 1995]:

$$f(B) = \frac{B^{\xi}}{\xi! \omega^{\xi+1}} \exp\left(-\frac{B}{\omega}\right) \qquad B \geq 0 \qquad (107)$$

where B is the fracture aperture, and the parameter ξ is limited to integer values. Calculations involving expectations of f(B) are greatly simplified by the choice of $\xi=2$, which provides a balance between flexibility and tractability ($\xi=2$ was used in this study).

Sample-scale expressions for liquid saturation and unsaturated hydraulic conductivity are obtained by taking expectations or integrating pore scale expressions (Eqs.92 to 94 for liquid saturation, and Eqs.104 to 106 for unsaturated hydraulic conductivity) with the gamma distribution (Eq.107) over portions of the fracture population associated with the different filling stages discussed under "Equilibrium Liquid Configurations Within a Unit Fracture Element". The integration limits separating the fracture population are obtained by rearranging Eqs.89 and 91 and solving for the fracture apertures $B_1(\mu)$ and B_2 that separate the fracture filling stages at a certain potential as depicted in Fig.28. Individual contributions of all population groups are finally summed up for the entire matric potential range under consideration to receive the sample-scale saturation and hydraulic conductivity curves.
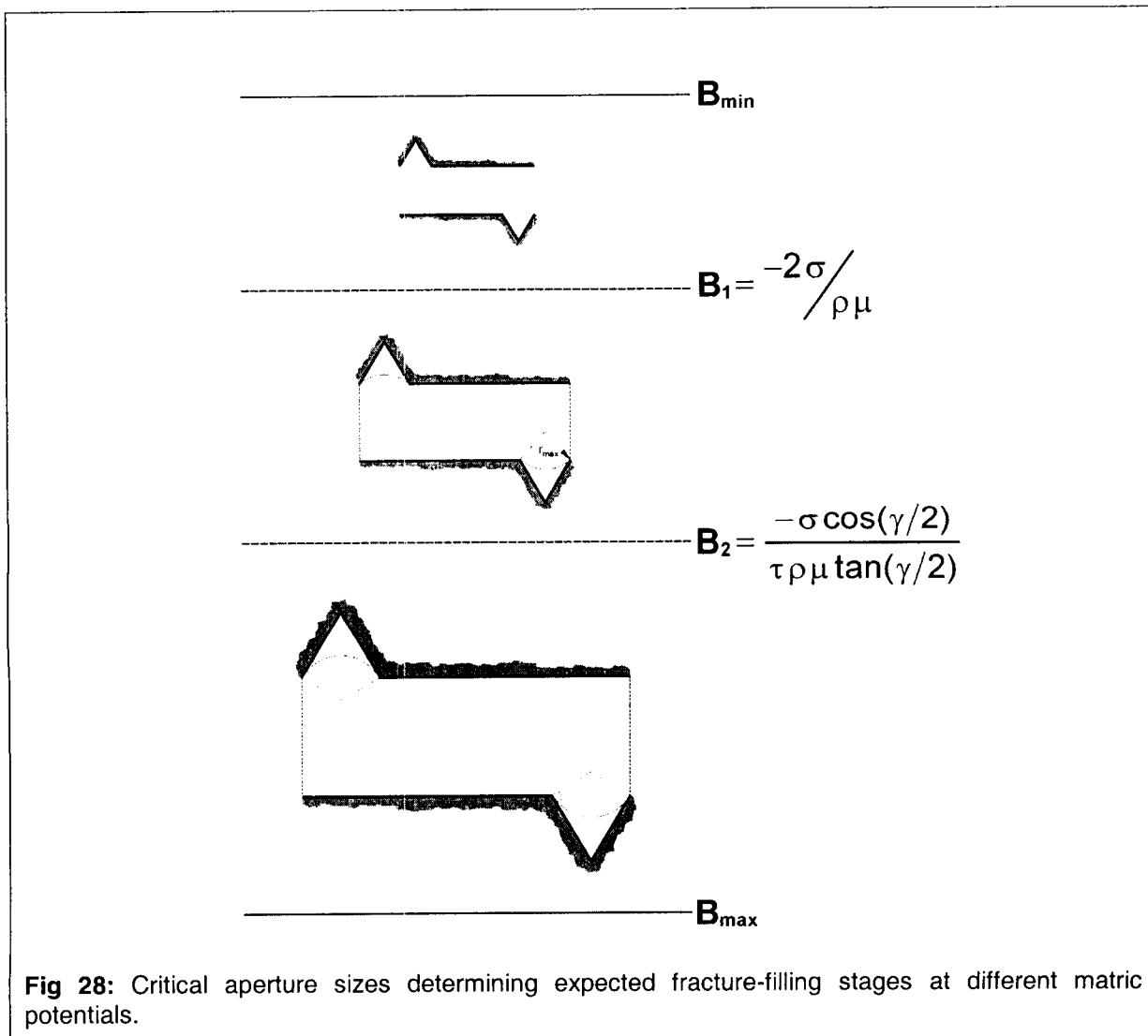

Fig 28: Critical aperture sizes determining expected fracture-filling stages at different matric potentials.

For illustration purpose we derive the upscaled hydraulic conductivity for the completely saturated fraction of the fracture population that ranges from the smallest aperture B_{min} to $B_1(\mu)$ (see Fig.28):

$$K_{1u-F}(\mu) = \int_{B_{min}}^{B_1(\mu)} \overbrace{\left[\frac{B^4\left(K_s\left(v+2\tau\tan(\gamma/2)\right)+2K_d\tau^2\tan(\gamma/2)\right)}{A_T}\right]}^{K_1 \text{ for a single fracture element (Eq.104)}} \overbrace{\left[\frac{B^2}{2\omega^3}\exp\left(-\frac{B}{\omega}\right)\right]}^{\text{Gamma distribution with }\xi=2} dB \qquad (108)$$

with subscript u standing for "upscaled" and F for "fracture". Note that the saturated hydraulic conductivity (all fractures completely saturated) is readily calculated employing Eq.108 by changing the upper integration limit to the maximum aperture B_{max}. The same procedure is applied to Eqs.105 and 106 with integration limits $B_1(\mu)$ - B_2, and B_2 - B_{max}, respectively. The upscaled expressions are then added to yield the composite response of the whole fracture population at a certain matric potential.

$$K_{u-F}(\mu) = \overbrace{K_{1u-F}(\mu)}^{Eq.108} + \overbrace{K_{2u-F}(\mu)}^{upscaled\ Eq.105} + \overbrace{K_{3u-F}(\mu)}^{upscaled\ Eq.106} \qquad (109)$$

For geometrical configurations with pit scaling parameters $\tau \geq \cos(\gamma/2)/(\tan(\gamma/2))$ (Eq.90), the upscaled expressions can be solved analytically as shown in Appendix A. Note that these analytical solutions cover a wide variety of different geometrical configurations. Only cases with $\tau < \cos(\gamma/2)/(\tan(\gamma/2))$ require numerical evaluation of the upscaled expressions (Fig.29).
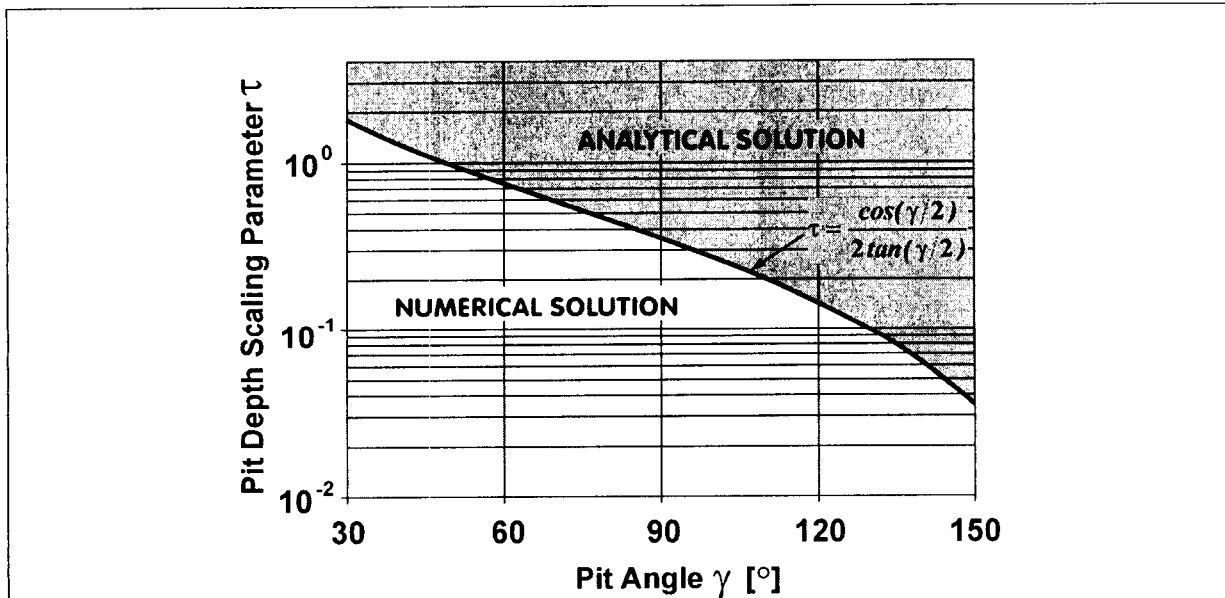

Fig 29: Relationship between pit angle and pit depth scaling parameter separating analytical and numerical solutions for the proposed sample scale expressions for liquid saturation and hydraulic conductivity.

The same scheme applies for liquid saturation (Eqs.92 to 94) with the composite response of the entire population calculated as:

$$S_{u-F}(\mu) = \overbrace{S_{1u-F}(\mu)}^{upscaled\ Eq.92} + \overbrace{S_{2u-F}(\mu)}^{upscaled\ Eq.93} + \overbrace{S_{3u-F}(\mu)}^{upscaled\ Eq.94} \qquad (110)$$

Remark:
- Note that the contribution of completely saturated fractures $S_{1u-F}(\mu)$ is obtained by simply integrating the gamma distribution (Eq.107) between B_{min} and $B_1(\mu)$, since the relative saturation of a saturated fracture element is 1.

A similar upscaling scheme was applied for the matrix domain yielding $S_{u-M}(\mu)$ and $K_{u-M}(\mu)$ [*Or and Tuller*, 1999; *Tuller and Or*, 2001]. See also previous notebooks. The individual contributions of the matrix and fracture domains to liquid saturation are added and weighed by the porosities of the individual domains to obtain the composite saturation curve for the FPM:

$$S_{FPM}(\mu) = \frac{S_{u-M}(\mu)\phi_M + S_{u-F}(\mu)\phi_F}{\phi_M + \phi_F} \tag{111}$$

where ϕ_M and ϕ_F are the matrix and fracture porosities. The composite hydraulic conductivity curve is obtained by simple addition of individual contributions:

$$K_{FPM}(\mu) = K_{u-M}(\mu) + K_{u-F}(\mu) \tag{112}$$

Note that the matrix and fracture conductivity functions are already weighted by their respective porosities (i.e., the expressions are divided by total cross-sectional areas including associated solid shells).

05/07/01 – Model Application

Dani Or

Estimation of model parameters

The analytical sample-scale expressions for the matrix and fracture domains contain a number of free model parameters that can be either obtained from direct measurements or via fitting to measured properties (e.g., saturated hydraulic conductivity).

If the aperture distribution is known from measurements, we are left with four free model parameters for the fracture domain saturation and hydraulic conductivity functions. These parameters, related to fracture geometry, are the dimensionless fracture lengths and pit depth scaling parameters v and τ, the pit connectivity factor δ, and the pit angle γ. For cases where information about fracture geometry is available, the free parameters can be further reduced (e.g., average pit angle γ, pit depth τB, and pit spacing vB could be obtained from image analyses of fracture cross-sections).

The proposed sample-scale model for matrix liquid saturation and hydraulic conductivity [*Tuller and Or*, 2001] contains four free parameters; the dimensionless slit length parameter β, the gamma distribution parameter ω, the matric potential μ_d at the onset of drainage (air entry value) to determine the largest pore length L_{max}, and the distribution overlap parameter λ that relates the dimensionless slit spacing parameter α to the largest L_{max} and the mean pore length [*Or and Tuller*, 1999]. These model parameters are estimated by fitting the sample scale expression for liquid saturation to measured liquid retention data (drainage or imbibition branch), while imposing constraints on medium specific surface area and porosity [*Or and Tuller*, 1999; *Tuller and Or*, 2001]. The resulting model parameters are used to calculate the sample-scale saturation curve, to predict sample-scale liquid-vapor interfacial area [*Or and Tuller*, 1999], and to predict sample-scale unsaturated and saturated hydraulic conductivities [*Tuller and Or*, 2001]. A conceptual flow chart of the proposed parameter estimation scheme is depicted in Fig.30.
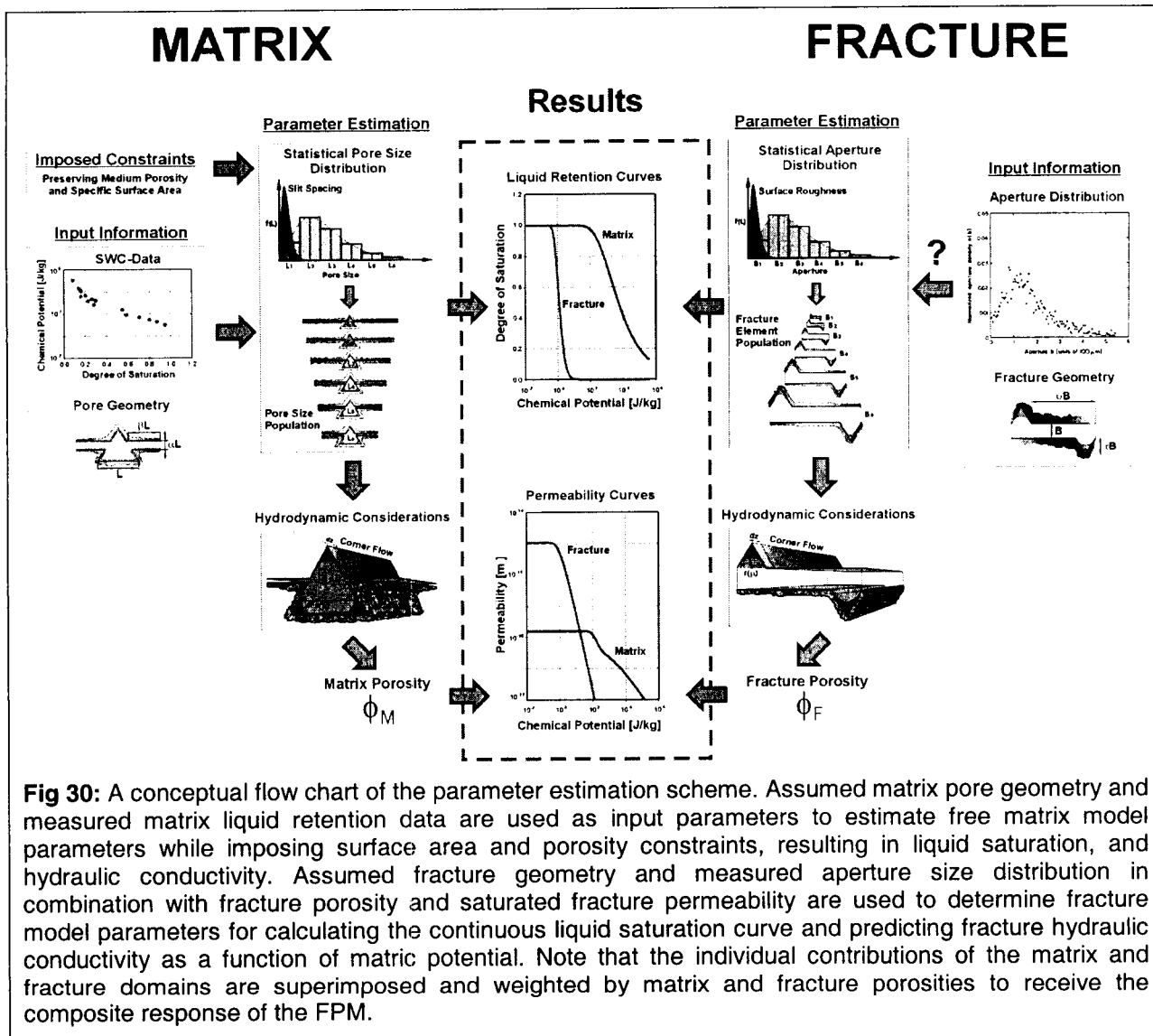

Fig 30: A conceptual flow chart of the parameter estimation scheme. Assumed matrix pore geometry and measured matrix liquid retention data are used as input parameters to estimate free matrix model parameters while imposing surface area and porosity constraints, resulting in liquid saturation, and hydraulic conductivity. Assumed fracture geometry and measured aperture size distribution in combination with fracture porosity and saturated fracture permeability are used to determine fracture model parameters for calculating the continuous liquid saturation curve and predicting fracture hydraulic conductivity as a function of matric potential. Note that the individual contributions of the matrix and fracture domains are superimposed and weighted by matrix and fracture porosities to receive the composite response of the FPM.

Datasets

Datasets containing information on matrix and fracture liquid retention and unsaturated permeability, as well as other physical properties of the two domains, are virtually non-existent. A comprehensive search of relevant literature spanning the last few decades yielded only a few incomplete datasets suitable to test the proposed model. In the following, we use data for Tiva Canyon welded tuff reported by *Wang and Narasimhan* [1993] to illustrate the primary features of the proposed model, and a dataset for crystalline rock reported by researchers at the Swiss Federal Institute of Technology (SFIT) [*Fischer et al.*, 1998; *Gimmi et al.*, 1997] for model applications.

The Tiva Canyon welded tuff (TCwt) dataset [*Wang and Narasimhan*, 1993] contains information about matrix porosity, saturated matrix and fracture permeabilities, *van Genuchten* [1980] parameters α_{VG} and n_{VG} for the matrix liquid saturation – matric potential relationship (water characteristic curve), and fracture spacing and effective aperture for vertical fractures. Fracture porosity for a unit volume is calculated by dividing the effective aperture through aperture spacing. The shape of the aperture distribution is approximated with the gamma distribution (Eq.107) with $\xi=2$ and B_{min} and B_{max} set to values of 1×10^{-9}m and 5×10^{-4}m, respectively. The second gamma distribution shape parameter ω is calculated, based on the

assumption that the critical aperture size (discussed below) is equal to the mean of the distribution m(B) = $\omega(\xi+1)$. Reported and derived model input parameters for TCwt are listed in Table 3.

The SFIT dataset [Fischer et al., 1998; Gimmi et al., 1997] is for a sample from a fracture zone at Grimsel Test Site (Switzerland) [Fischer et al., 1998] with granodiorite rock matrix. This dataset contains measured water characteristic and gas permeability data, measured saturated matrix and fracture permeabilities, matrix and fracture porosities, and aperture size distribution. Gas permeability measurements obtained at various water saturations were converted to equivalent water permeability to be useful for model evaluation. The first step was to fit gas permeability data to the following parametric van Genuchten – Mualem relationship [Dury et al., 1999]

$$K_{nw}(S_w) = (1 - S_w)^{0.5} (1 - S_w^{1/m})^{2m} \tag{113}$$

where K_{nw} is the relative non-wetting phase (gas) permeability, S_w is the relative wetting phase (water) saturation, and m is the empirical van Genuchten shape parameter. The shape parameter m obtained from fitting Eq.113 to measured K_{nw} data was subsequently used to calculate the relative wetting phase (water) permeability K_w as:

$$K_w(S_w) = S_w^{0.5} \left[1 - \left(1 - S_w^{1/m}\right)^m\right]^2 \tag{114}$$

The conversion from nonwetting phase to wetting phase permeability for the SFIT data is depicted in Fig.31. Reported SFIT data are listed in Table 3. Physical constants used in the illustrative calculations are listed in Table 4.

Table 3: Reported and derived model input parameters for the TCwt and SFIT datasets

Property	TCwt [a]	SFIT [b]
Matrix Porosity	1.14×10^{-1}	3.75×10^{-2}
Matrix α_{VG} [(J/kg)$^{-1}$]	8.40×10^{-4}	NA
Matrix n_{VG}	1.558	NA
Matrix Saturated Permeability [m^2]	2.55×10^{-18}	3.00×10^{-18}
Effective Aperture [m]	1.09×10^{-3}	NA
Aperture Spacing [m]	0.180	NA
Fracture Porosity	6.10×10^{-4}	8.50×10^{-3}
Fracture Saturated Permeability [m^2]	1.18×10^{-12}	3.00×10^{-13}
Aperture Distribution Parameter ω (ξ=2) [m]	3.30×10^{-5}	2.10×10^{-4}
Minimum Aperture B_{min} [m]	1.00×10^{-9}	6.00×10^{-8}
Maximum Aperture B_{max} [m]	5.00×10^{-4}	4.00×10^{-3}

   NA is not applicable
[a] Source is Wang and Narasimhan [1993]
[b] Source is Fischer et al. [1998] and Gimmi et al. [1997]

Table 4: Physical constants and dimensions used in the illustrative example calculations

Property	Symbol		Unit
Acceleration of gravity	g	9.81	m s^{-2}
Density of Water (20°C)	ρ	998.21	kg m^{-3}
Hamaker Constant (solid-vapor through liquid)	A_{svl}	-6.0×10^{-20}	J
Surface Tension of Water (20°C)	σ	0.0728	N m^{-1}
Viscosity of Water (20°C)	η_0	0.001002	kg m^{-1} s^{-1}

Results: Tiva Canyon Data Set [Wang and Narasimhan, 1993]

The lack of complete and definitive data sets for model testing introduces undesired degrees of freedom into the evaluation. We thus view the use of the Tiva Canyon welded tuff data [*Wang and Narasimhan*, 1993] as an illustrative example rather than a test of the model in the strict sense. Input parameters used in the scheme illustrated in Fig.30 are given in Table 3. Figure 32a depicts the resulting water characteristic curves for matrix and the fracture domains (Note the fracture domain is seen on the bottom left corner of Fig.32a). As expected, the matrix domain dominates the saturation-matric potential relationships. In contrast, the permeability function (Fig.32b) is dominated by the fracture domain at low matric potentials (close to complete saturation).
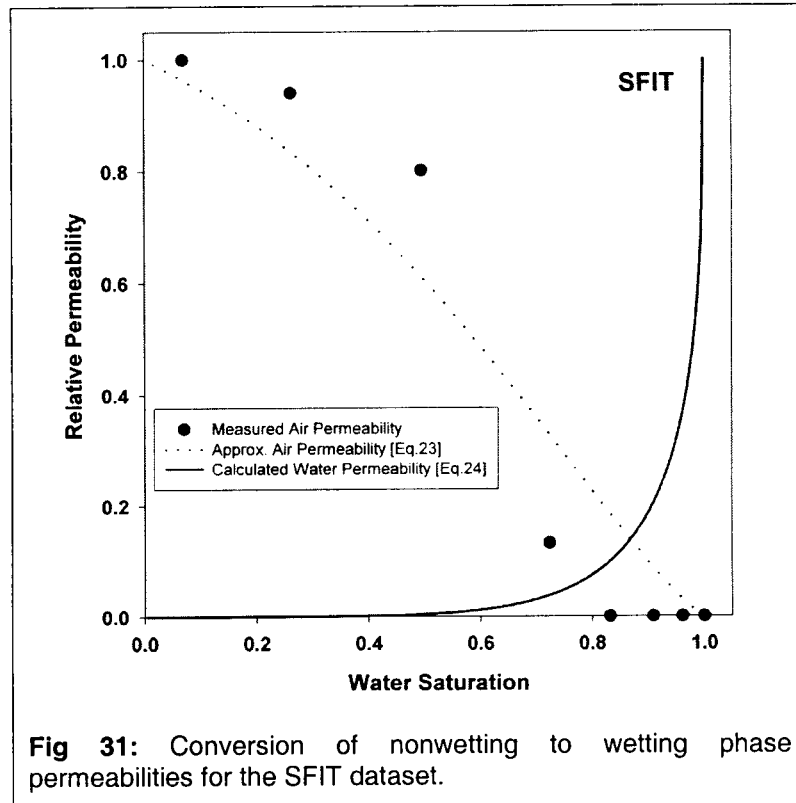

Fig 31: Conversion of nonwetting to wetting phase permeabilities for the SFIT dataset.
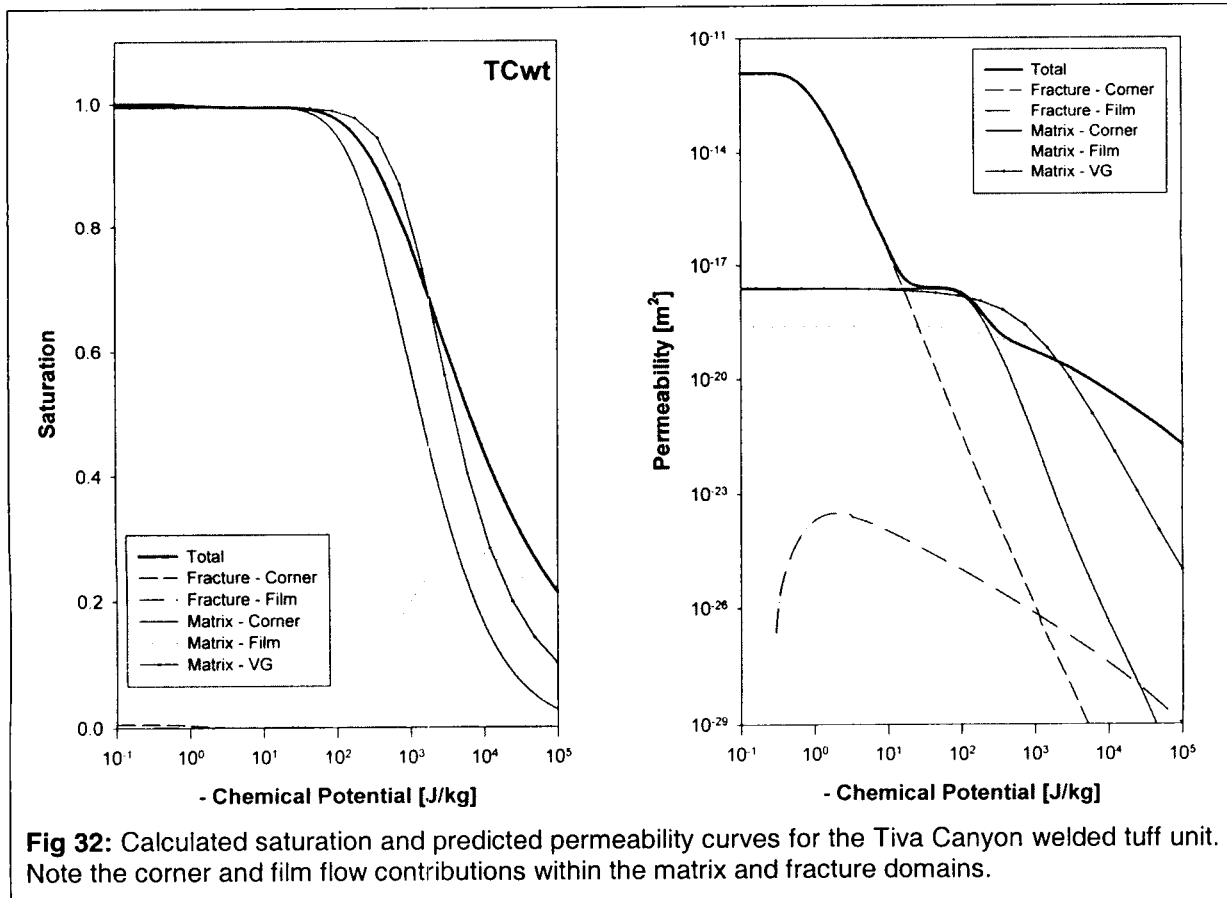

Fig 32: Calculated saturation and predicted permeability curves for the Tiva Canyon welded tuff unit. Note the corner and film flow contributions within the matrix and fracture domains.

The transition between fracture to matrix permeability occurs at a potential of about 50 J/kg, and a second transition occurs at potentials of 2000 J/Kg where matrix film flow provides the dominant contribution to the medium permeability. The resulting unsaturated permeability curve contains three "humps" – one for each of the processes. It is interesting to note that fracture film flow on separated surfaces provides only a marginal contribution to transport processes, probably because of the presence of only a few and mostly small aperture-size fractures. Finally, all model-fitting parameters are summarized in Table 4.

> **Remark:**
>
> ● The Excel spreadsheets for calculation of matrix and fracture saturation and unsaturated hydraulic conductivity and for total system response are stored in Notebook/Calculations. The filenames are *Matrix-Tiva-Canyon-Tuff*, *Fracture-Tiva-Canyon-Tuff*, and *Combined-Tiva-Canyon-Tuff*.

Results: SFIT Data Set [Fischer et al., 1998; Gimmi et al., 1997]

The SFIT data set was even less complete than the previous data set. Following a similar path, we present the model fit to water characteristic data (Fig.33a) for matrix and fracture domains. The resulting fracture size distribution is then used to predict the unsaturated hydraulic conductivity function. The resulting function manifests the influences of the various domains and mechanisms, namely the dominance of the fracture domain near saturation, a transition to matrix corner and capillary flow, and finally matrix film flow ($\mu \approx$ 2000-3000 J/Kg) [*Tuller and Or*, 2001]. Model parameters for SFIT are given in Table 4. Attempts to use the fracture aperture distribution reported by *Fischer et al.*, [1998] failed to reproduce either saturation or permeability values. One possibility for this discrepancy is the fact that the fractures were filled with porous material [*Fischer et al.*, 1998], hence, in terms of our model, a fracture size distribution with a smaller mean was needed to reproduce measured hydraulic functions.
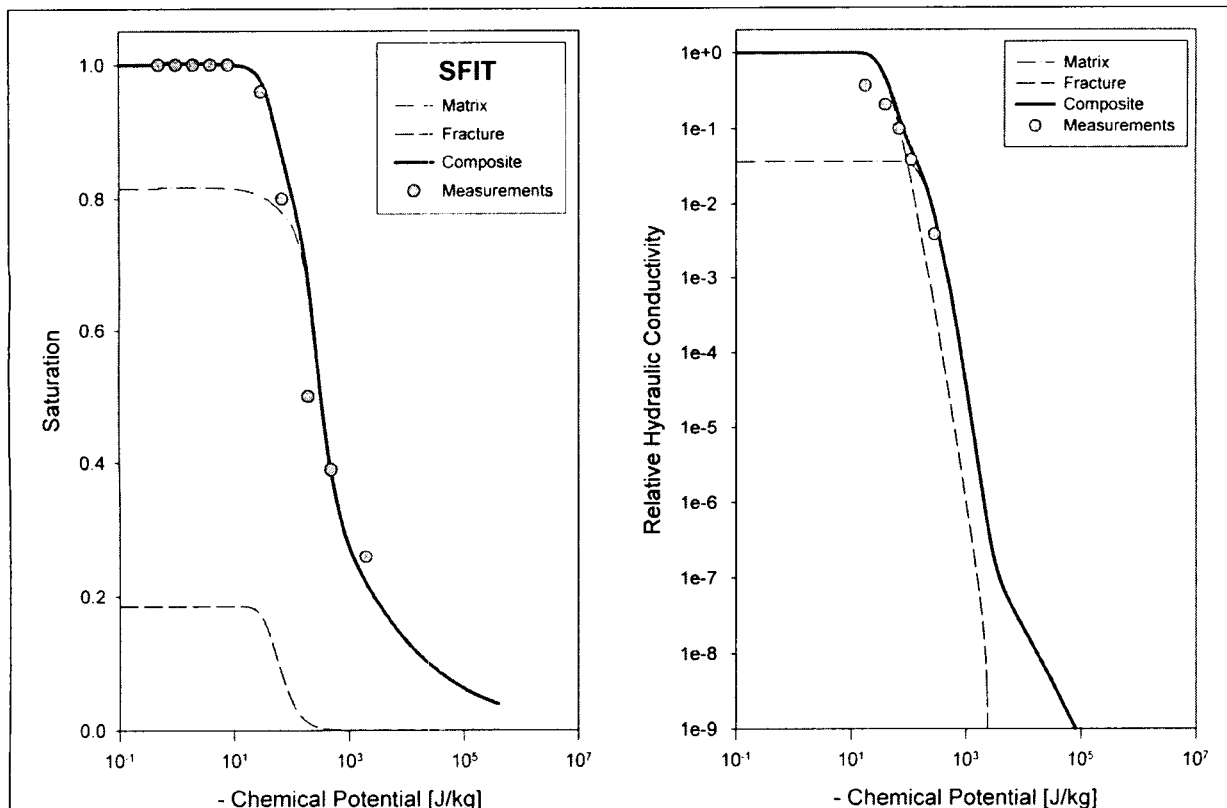

Fig 33: Calculated saturation and predicted permeability curves for the Tiva Canyon welded tuff unit. Note the corner and film flow contributions within the matrix and fracture domains.

Remark:

● The Excel spreadsheets for calculation of matrix and fracture saturation and unsaturated hydraulic conductivity and for total system response are stored in Notebook/Calculations. The filenames are *Matrix-Swiss-06, Fracture-Swiss-06,* and *Combined-Swiss-06.*

Table 4: Fitted model parameters for the TCwt and SFIT datasets

Datasets	TCwt	SFIT
Matrix Model Parameters [a]		
Slit Length Scaling Parameter β	80000	10
Pore Size Distribution Parameter ω [m]	6.1×10^{-7}	2.8×10^{-7}
Matric Potential μ_d at the Onset of Drainage [m]	-3.5	-5.0
Distribution overlap parameter λ	57	15
Fracture Model Parameters		
Fracture Length Scaling Parameter υ	5	10
Pit Depth Scaling Parameter τ [b]	8.0×10^{-1}	3.5×10^{-2}
Pit Connectivity Factor δ	0.3	1.0
Pit Angle γ [°]	60	150

[a] See Or and Tuller [1999].
[b] The pit depth scaling parameter was set to $\tau \geq \cos(\gamma/2)/(\tan(\gamma/2))$ to facilitate analytical solutions.

Dani Or

05/14/01 – Hydraulic Conductivity Function for Non-Equilibrium Conditions

Thus far, the analyses and resulting hydraulic conductivity functions were based on the assumption of hydraulic equilibrium between matrix and fracture domains. Obviously, there is great interest in hydraulic functions for situations where matrix and fractures are not in equilibrium, such as arrival of a rapid wetting front from a rainfall event via preferential pathways or ventilation of the fracture domain. It should be emphasized that details regarding rates and amounts of liquid exchange between the domains are beyond the scope of medium characterization. These questions are in the realm of solution of a particular flow problem rather than medium characterization under standard steady state conditions. Nevertheless, when exchange between the domains is ignored (e.g., due to relatively long time scales relative to uncoupled downward flow), we assemble the unsaturated permeability function for different values of potential differential $(\Delta\mu)$. For the example depicted in Fig.34 we assume that the matrix domain is wetter than the fracture domain $(\Delta\mu=\mu_{matrix}-\mu_{fracture}>0)$. Under these conditions, for each value of matrix permeability at a given potential μ, we calculate fracture domain permeability at $\mu+\Delta\mu$ and combine the contributions according to Eq.112. The resulting family of permeability curves (Fig.34) reflects the dependency on the "distance" from equilibrium to the point where no flow through the fracture domain occurs (e.g., for $\Delta\mu>20$ J/kg). The situation where the fracture domain is wetter than the matrix is trivial, due to the large disparity in permeability near saturation; the composite permeability function will not be significantly different than the original equilibrium case.

Remark:

● The Excel spreadsheets for calculation of matrix and fracture saturation and unsaturated hydraulic conductivity and for total system response are stored in Notebook/Calculations. The filenames are *Matrix-Tiva-Canyon-Tuff-Curve-Bundle, Fracture-Tiva-Canyon-Tuff-Curve-Bundle,* and *Tiva-Canyon- Curve-Bundle.*
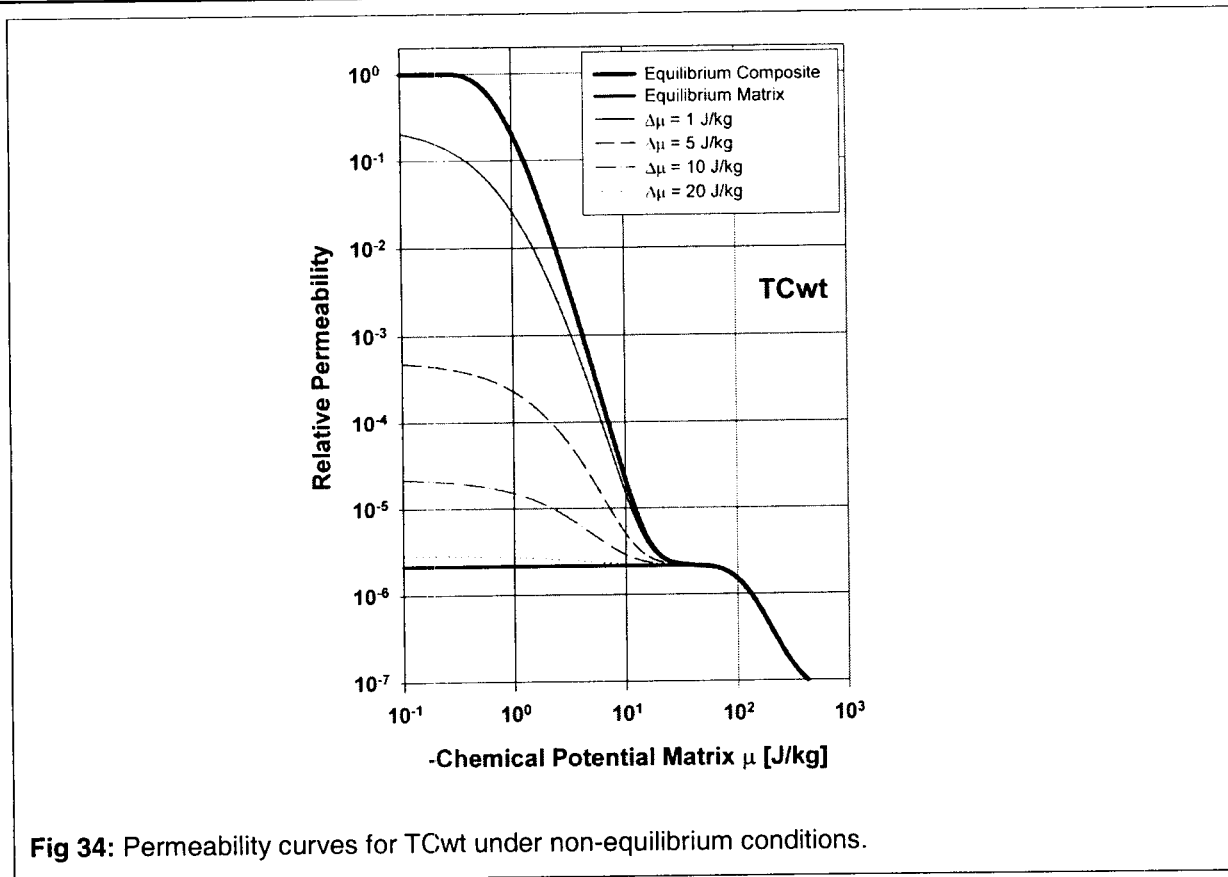

Fig 34: Permeability curves for TCwt under non-equilibrium conditions.

05/16/01 – Approximations for Three-Dimensional Network Effects

An obvious limitation of the foregoing analysis is the description of hydraulic properties for a two-dimensional (2-D) cross-section neglecting potentially important three-dimensional (3-D) network effects. Two relatively simple approach-es are proposed for incorporation of 3-D influences into the 2-D model. The first is to measure the saturated hydraulic conductivity or permeability of the fractured porous medium and use it as input parameter for the model. Such a measurement, which presumably incorporates the 3-D nature of the fracture network, will provide a constraint for estimation of geometrical distribution of aperture sizes. We envision that the resulting fracture aperture distribution will be a 2-D equivalent that faithfully preserves the 3-D hydrodynamics (for fully saturated conditions). In the absence of detailed information regarding fracture size distribution, we have tested this approach for the Tiva Canyon data set (TCwt).

Alternatively, a theoretical approach based on concepts of Critical Path Analysis (CPA) from percolation theory [*Ambegaokar et al.*, 1971; *Friedman and Seaton*, 1998; *Banavar and Johnson*, 1987] is proposed. The implementation of CPA in this context is based on a the following argument; given a broad aperture distribution forming a 3-D fracture network, we begin by removing all the fractures, and then replace the fracture segments in order of decreasing size back to their original location. The aperture size that completes a conductive pathway across the network is labeled as the "critical" aperture size. According to CPA, all aperture sizes larger than the "critical" are essentially in series (all flow must pass through the "critical" size), and all aperture sizes smaller than the "critical" size could be in parallel but are much less conductive, thus providing a limited contribution to the overall hydraulic conductivity. Consequently, the hydraulic conductivity of the fracture network can be represented by the hydraulic conductivity of the "critical" unit fracture element. The critical fracture size is determined by finding the cumulative fraction of fracture sizes larger than the critical size (B_{cr}) that equals the percolation threshold of the network (p_c):

$$p_c = \int\limits_{B_{cr}}^{\infty} f(B)dB \qquad (115)$$

The percolation threshold is the minimal fraction of aperture sizes that span a conductive pathway, and its value depends mainly on the dimensionality of the network (d=1, 2, or 3) and on the coordination number, Z. For simple cubic lattices p_c=0.2488, other values may be estimated as [*Sahimi*, 1995]:

$$Z\,p_c \cong \frac{d}{d-1} \qquad (116)$$

The value of the coordination number Z is difficult to determine a-priori, however, evidence suggests that for diluted fracture networks (and soil macropore networks), Z values close to 3 are common [Doyen, 1988; Sahimi, 1995; Perret et al., 1999]. Hence, for Z=3 in a 3-D fracture network the value of p_c=0.5, and the critical aperture size is equal to the mean value of the aperture size distribution. The value of B_{cr} can be used to estimate the saturated hydraulic conductivity of a unit fracture element (using Eq.104) to represent the entire fracture domain and the FPM. Performing this calculation (3-D network, Z=3, p_c=0.5) for the SFIT dataset yields a K_{SAT} of 4.6×10^{-15} m^2 compared to 6.1×10^{-15} m^2 calculated with Eq.108. In summary, we propose to constrain our estimates of fracture size distribution such that the calculated planar (2-D) saturated hydraulic conductivity will match the 3-D estimated from the critical aperture identified by CPA. This could be an iterative process constrained by other input parameters, such as measured saturated hydraulic conductivity.

05/19/01 – Status

Dani Or

A paper on constitutive relationships for matrix-fracture hydraulic conductivity is in preparation for journal submission (Water Resource Research) and started on the CNWRA technical and programmatic process. Hence, it is a good idea to re-assess at this point the status of the work and where it may be heading.

Open issues (pertaining to the TEF/USFIC- KTI) for future model improvement

- Issues of 3-D network effects will require evaluation using measurements and other models. We are interested primarily in the independent evaluation of the Critical Path Analysis approximation.

- The scarcity of data of flow in unsaturated fractures present a challenge to progress and ability to provide reliable predictions relevant to performance assessment of the YM proposed repository. We believe that an initiative to gather definitive data on flow properties of unsaturated fractures is imperative.

- The dynamics matrix-fracture interactions were not treated in this work – some of the rates of such interactions would be useful to capture the essence of potential bypass flow through these fracture surfaces (e.g., as liquid flux encounter low porosity/permeability layer such as the PTN).

References

Ambegaokar, V., N.I. Halperin, and J.S. Langer. Hopping conductivity in disordered systems. *Phys. Rev. B,* 4, 2612-2620, 1971.

Banavar, J.R., and D.L. Johnson, Characteristic pores sizes and transport in porous media, *Phys. Rev. B, 35, 7283-7286, 1987.*

Dury O., U. Fischer, and R. Schulin, A comparison of relative nonwetting-phase permeability models, *Water Resour. Res., 35*(5), 1481-1493, 1999.

Fischer, U., B. Kulli, and H. Flühler, Constitutive relationships and pore structure of undisturbed fracture zone samples with cohesionless fault gauge layers, *Water Resour. Res., 34*(7), 1695-1701, 1998.

Friedman, S.P., and N.A. Seaton, Critical path analysis of the relationship between permeability and electrical conductivity of three dimensional pore networks, *Water Resour. Res., 34*(7), 1703-1710, 1998.

Gimmi, T., M. Schneebeli, H. Flühler, H. Wydler, and T. Baer, Field-scale transport in unsaturated crystalline rock, *Water Resour. Res., 33*(4), 589-598, 1997.

Or, D. and M. Tuller, Liquid retention and interfacial area in variably saturated porous media: Upscaling from pore to sample scale model, *Water Resour. Res., 35*(12), 3591-3605, 1999.

Or, D. and M. Tuller, Flow in unsaturated fractured porous media: Hydraulic conductivity of rough surfaces, *Water Resour. Res., 36(5)*, 1165-1177, 2000.

Ransohoff, T.C., and C.J. Radke, Laminar flow of a wetting liquid along the corners of a predominantly gas-occupied noncircular pore, *J. Colloid and Interface Sci., 121,* 392-401, 1988.

Rice, J.A., Mathematical Statistics and Data Analysis, 2nd ed., Duxbury Press, Belmont, California, 1995.

Sahimi, M., Flow and transport in porous media and fractured rock: From classical   methods to modern approaches, ISBN: 3527292608, John Wiley & Sons, New York, 1995.

Tuller, M., D. Or, and L.M. Dudley, Adsorption and capillary condensation in porous media: Liquid retention and interfacial configurations in angular pores, *Water Resour. Res., 35*(7), 1949-1964, 1999.

Tuller, M., and D. Or, Hydraulic conductivity of variably saturated porous media - Laminar film and corner flow in angular pore space, *Water Resour. Res., 37*(5), 1257-1276, 2001.

van Genuchten, M.T., A closed-form equation for predicting the hydraulic conductivity of unsaturated soils, *Soil Sci. Soc. Am. J., 44,* 892-898, 1980.

Wang, J.S.Y., and T.N. Narasimhan, Unsaturated flow in fractured porous media, In: Bear, J., Ch.-F. Tsang, and G. de Marsily, Flow and contaminant transport in fractured rock, pp. 325- 394, Academic Press Inc., San Diego, 1993.

APPENDIX - A

Analytical Solution for Sample Scale Liquid Saturation and Hydraulic Conductivity for the Fracture Domain

For all geometrical configurations with $\tau \geq \cos(\gamma/2)/(\tan(\gamma/2))$ (Eq.90), we are able to obtain closed-form expressions for the sample-scale response of the fracture domain by multiplying the single element expressions for liquid saturation (Eqs.92 and 94) and hydraulic conductivity (Eqs.104 and 106) with the gamma distribution for aperture sizes, and integrating the resulting expressions over part of the fracture population associated with the different filling stages. The resulting integral equations may be expressed by the following general integral:

$$H = \int_{B_l}^{B_L} \left(c_1 B^4 + c_2 B^2 + c_3 B + c_4\right) Exp\left[-\frac{B}{\omega}\right] dB \tag{A1}$$

where H represents the sample-scale hydraulic function, B_L and B_U are the lower and upper integration limits, and c_1, c_2, c_3, and c_4 are constants or variables listed in Table 5. The analytical solution of the integral in Eq.A1 is given as:

$$H = F(B_L) - F(B_U) \tag{A2}$$

with

$$F(B) = \omega \left\{ e^{-B/\omega} \left[B \left(B^3 c_1 + B c_2 + c_3 \right) \right. \right.$$
$$+ c_4 + \omega \left(4 B^3 c_1 + 2 B c_2 + c_3\right)$$
$$\left. \left. + 2\omega^2 \left(6 B^2 c_1 + c_2\right) + 24 \omega^3 B c_1 + 24 \omega^4 c_1 \right] \right\} \tag{A3}$$

Tab.4: Integration limits, constants, and variables used to calculate sample scale liquid saturation, and saturated and unsaturated hydraulic conductivities employing the general Eq.A1.

	Lower Integration Limit B_L	Upper Integration Limit B_U	c_1	c_2	c_3	c_4
			Degree of Saturation			
$S_{1u-F}(\mu)$ Complete Saturation	B_{min}	$B_1(\mu)$	0	$\frac{1}{2\omega^3}$	0	0
$S_{3u-F}(\mu)$ Partially Saturated	$B_1(\mu)$	B_{max}	0	0	$\dfrac{h(\mu)\left[2\tau + v\cos\left(\frac{\gamma}{2}\right)\right]}{\omega^3\left[v\cos\left(\frac{\gamma}{2}\right) + 2\tau(1+\tau)\sin\left(\frac{\gamma}{2}\right)\right]}$	$\dfrac{F_\gamma\, r(\mu)^2 - 2h(\mu)r(\mu)\cot\left(\frac{\gamma}{2}\right)}{\omega^3\left[v + 2\tau(1+\tau)\tan\left(\frac{\gamma}{2}\right)\right]}$
			Hydraulic Conductivity			
$K_{1u-F}(\mu)$ Saturated Conductivity	B_{min}	$B_1(\mu)$	$\dfrac{\phi_F\left[K_a\left(v + 2\tau\tan\left(\frac{\gamma}{2}\right)\right) + 2K_d\tau^2\delta\tan\left(\frac{\gamma}{2}\right)\right]}{2\omega^3\left[v + 2\tau(1+\tau)\tan\left(\frac{\gamma}{2}\right)\right]}$	0	0	0
$K_{3u-F}(\mu)$ Unsaturated Conductivity	$B_1(\mu)$	B_{max}	0	0	$\dfrac{\phi_F\, KF(\mu)h(\mu)\left[2\tau + v\cos\left(\frac{\gamma}{2}\right)\right]}{\omega^3\left[v\cos\left(\frac{\gamma}{2}\right) + 2\tau(1+\tau)\tan\left(\frac{\gamma}{2}\right)\right]}$	$\dfrac{\phi_F\left[KC(\mu)r(\mu)^2 F_\gamma\,\delta - 2KF(\mu)h(\mu)r(\mu)\cot\left(\frac{\gamma}{2}\right)\right]}{\omega^3\left[v + 2\tau(1+\tau)\tan\left(\frac{\gamma}{2}\right)\right]}$

ADDITIONAL INFORMATION FOR SCIENTIFIC NOTEBOOK #: 354E

Document Date:	06/30/1999
Availability:	Southwest Research Institute® Center for Nuclear Waste Regulatory Analyses 6220 Culebra Road San Antonio, Texas 78228
Contact:	Southwest Research Institute® Center for Nuclear Waste Regulatory Analyses 6220 Culebra Road San Antonio, TX 78228-5166 Attn.: Director of Administration 210.522.5054
Data Sensitivity:	■"Non-Sensitive" □ Sensitive □"Non-Sensitive - Copyright" □ Sensitive - Copyright
Date Generated:	06/29/1999
Operating System: (including version number)	Windows
Application Used: (including version number)	Microsoft Word 8.0; Microsoft Excel
Media Type: (CDs, 3 1/2, 5 1/4 disks, etc.)	1 zip drive
File Types: (.exe, .bat, .zip, etc.)	Various
Remarks: (computer runs, etc.)	Media contains: contents of electric scientific notebook as of 06/29/1999

Vol. 2

Dani Or
Utah State University
Scientific Notebook #354

Vol. 2

Dani Or
Utah State University
Scientific Notebook #354

Volume 2—Dripping into Cavities from Unsaturated
Fractures Under Evaporative Conditions

Volume 2: Dripping into Cavities from Unsaturated Fractures under Evaporative Conditions

Thermal Effects - Key Technical Issue - Dani Or - 06/30/99

Account Number: 20-1402-661
Collaborators: Teamrat A. Ghezzehei (USU), Randall Fedors, Ron Green (CNWRA)
Directories: C:/dripping_notebook

Objective: the objectives of this study are to develop analytical tools for predicting the conditions and rates of liquid drop formation at intersection of vertical unsaturated fractures with larger subterranean cavities. Drop size, dripping rates, and solute concentration are sought under evaporative conditions.

Initial Entry – 2/17/99:

Dripping Flux Supplied by Unsaturated Flow on Rough Fracture Surfaces

A new model for flow on rough surfaces of unsaturated rock fractures, proposed by Or and Tuller [1999] is used to calculate the flux required to generate dripping. The details of the model are provided in the above mentioned paper and accompanying Volume 1 of this scientific notebook (#354). We have selected only the derivations, related to the calculation of liquid flux contributing to drop formation.

The model considers a unit cross-sectional segment of a fracture with wide aperture, and consists of flow regimes in thin films (film flow) and in partially filled grooves (corner flow). For the purposes of this study, we will use a surface roughness element with cross sectional view as depicted in Fig (1) comprising a vertical groove and adjacent plane surface. Flow of water occurs in thin films over the plane surface element of width (β L) and in the groove defined by the depth (L) and angle (γ).

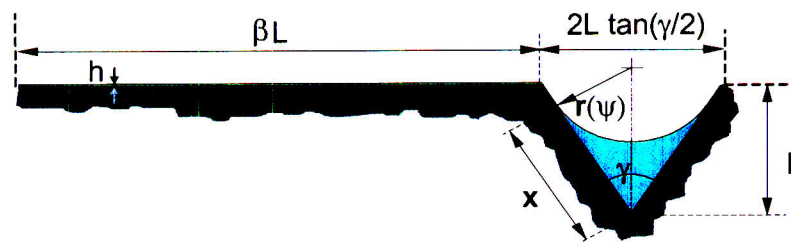**Figure 1.** Definition sketch of a unit fracture element in a horizontal cross-section. The groove is defined by its depth (L) and angle (γ). The plane over which film flow occurs is defined by its relation to the groove depth (β).

A curved liquid-vapor interface in equilibrium with the matric potential at ambient atmosphere (ψ) is maintained in the groove. The interface curvature follows the Young-Laplace relationships until a geometry-dependent critical matric potential (ψ_c) is reached, above which the groove is completely, liquid filled. The critical matric potential (ψ_c) is given by,

$$\psi_c = \frac{\sigma}{L} \frac{\cos(\gamma/2)}{\tan(\gamma/2)} \tag{1}$$

where

γ .... Groove angle

L .... Groove depth [m]

σ .... Surface tension at the liquid-vapor interface [0.0729 N m-1]

ψ_c .... Critical matric potential separating partially filled and full pits [J m^{-3} = Pa]

The radius of curvature of the liquid-vapor interface (r_{LV}) in the groove, prior to complete filling by liquid, is given by the Young-Laplace equation,

$$r_{LV} = \frac{\sigma}{\psi} \tag{2}$$

where

r_{LV} .... Radius of liquid-vapor interface curvature [m]

ψ .... Matric potential [J m-3]

When the matric potential is greater than the critical matric potential ($\psi > \psi_c$) the groove is filled-up completely with water.

The film thickness (h) over the plane area is related to the matric potential by [Iwamatsu and Horii, 1996],

$$h = \sqrt[3]{\frac{A_{SVL}}{6\pi\psi}} \tag{3}$$

where

A_{svl} .... Hamaker constant (a thermodynamic adsorption parameter for solid-vapor interactions through the intervening adsorbed liquid) [- 6.0×10^{-19} J]

h .... Film thickness [m]

The volumetric flux of liquid flow [m^3 sec^{-1}] across the cross-sectional area of the

element (Fig 1) under a unit gravitational gradient was calculated by Or and Tuller [1999]. The individual contributions of film- and groove flow to the total flux prior and after groove fill-up are given below.

(a) Partially saturated pits/grooves ($\psi < \psi_c$)

Expressions for film flow are derived from standard Navier-Stokes equations with appropriate boundary conditions, and from consideration of changes in the contributing area to film flow with changes in the matric potential:

Film:
$$Q_F = \frac{h^3 \rho g}{3\eta}\left(\beta L + 2\left(\frac{L}{\cos(\gamma/2)} - \frac{r_{LV}}{\tan(\gamma/2)}\right)\right) \tag{4}$$

Expressions for average liquid velocity in corners/grooves bounded by a liquid-vapor interface were derived by Ransohoff and Radke [1988] expressed as:

Groove/Corner:
$$Qc = \frac{r_{LV}{}^4 F \rho g}{\varepsilon \eta} \tag{5}$$

Where

ε .... Flow resistance parameter [dimensionless], [Ransohoff and Radke, 1988; Or and Tuller, 1999].

F is a dimensionless angularity factor, defined by groove geometry as,

$$F = \frac{1}{\tan(\gamma/2)} - \pi\frac{180 - \gamma}{360} \tag{6}$$

(b) Completely filled pits/grooves ($\psi > \psi_c$ – close to saturation)

Film:
$$Q_F = \frac{h^3 \rho g}{3\eta}\left(\beta L + 2L\tan(\gamma/2)\right) \tag{7}$$

Groove/Corner:
$$Q_C = L^2 \tan(\gamma/2)\frac{r_{LV}{}^2 \rho g}{\varepsilon \eta} \tag{8}$$

The total flux due to film flow and corner flow is assumed to converge at the bottom tip of the corner and result in drop formation. This flux is given by,

$$Q = Q_F + Q_C \tag{9}$$

where

F .... Angularity factor [dimensionless]

g .... Acceleration due to gravity [m sec^{-2}]

Q .... Total volumetric liquid flux due to film and corner flow [m^3 sec^{-1}]

Q_F .... Volumetric liquid flux due to film flow [m^3 sec^{-1}]

Q_C .... Volumetric liquid flux due to corner flow [m^3 sec^{-1}]

β .... Parameter relating plane area to groove depth [dimensionless]

ε .... Flow resistance parameter [dimensionless]

η .... Liquid viscosity [Pa s]

ρ .... Density of the liquid [kg m^{-3}]

Note: Both h and r_{LV} are given as functions of the matric potential ψ in Eq (2) and (3). Hence, the fluxes Eq (4)-(9) are also functions of matric potential (ψ).

2/24/99: One-Dimensional Axisymetric Dripping Model

Adaptation of Wilson's solution [1987] to dripping from fractures

We consider liquid emerging from the bottom of a vertical groove at a very slow flow velocity that does not induce jetting, as shown in Fig (2). The liquid forms a drop that grows slowly and stretches under its own weight until it raptures and detaches. During drop growth, a force balance between viscosity, gravity, and surface tension determines its evolution. The effect of inertia on drop formation and detachment is neglected. For simplicity, we start by presenting the evolution of the first drop from the emergence of the first liquid element at the groove tip to its detachment. Later, the periodicity and evolution of all subsequent drops are considered.

At the base of a fracture, liquid leaves the groove at a volumetric flux Q given by Eq (9). If the grooves are partially filled, the liquid cross-sectional area at the bottom tip feeding the drop (Ao) is given by,

$$Ao = Fr_{LV}{}^2 \qquad (10)$$

where

Ao .... Liquid cross-sectional area at groove bottom tip [m^2]

If the grooves are completely filled with water, the liquid cross-sectional at the bottom-tip is given by,

$$Ao = L^2 \tan(\gamma/2) \qquad (11)$$

The liquid leaving the groove bottom-tip forms itself into an axisymmetrical drop. We employ a Lagrangian coordinate system, as shown in Fig (2b), to track the growth and detachment of the drop.
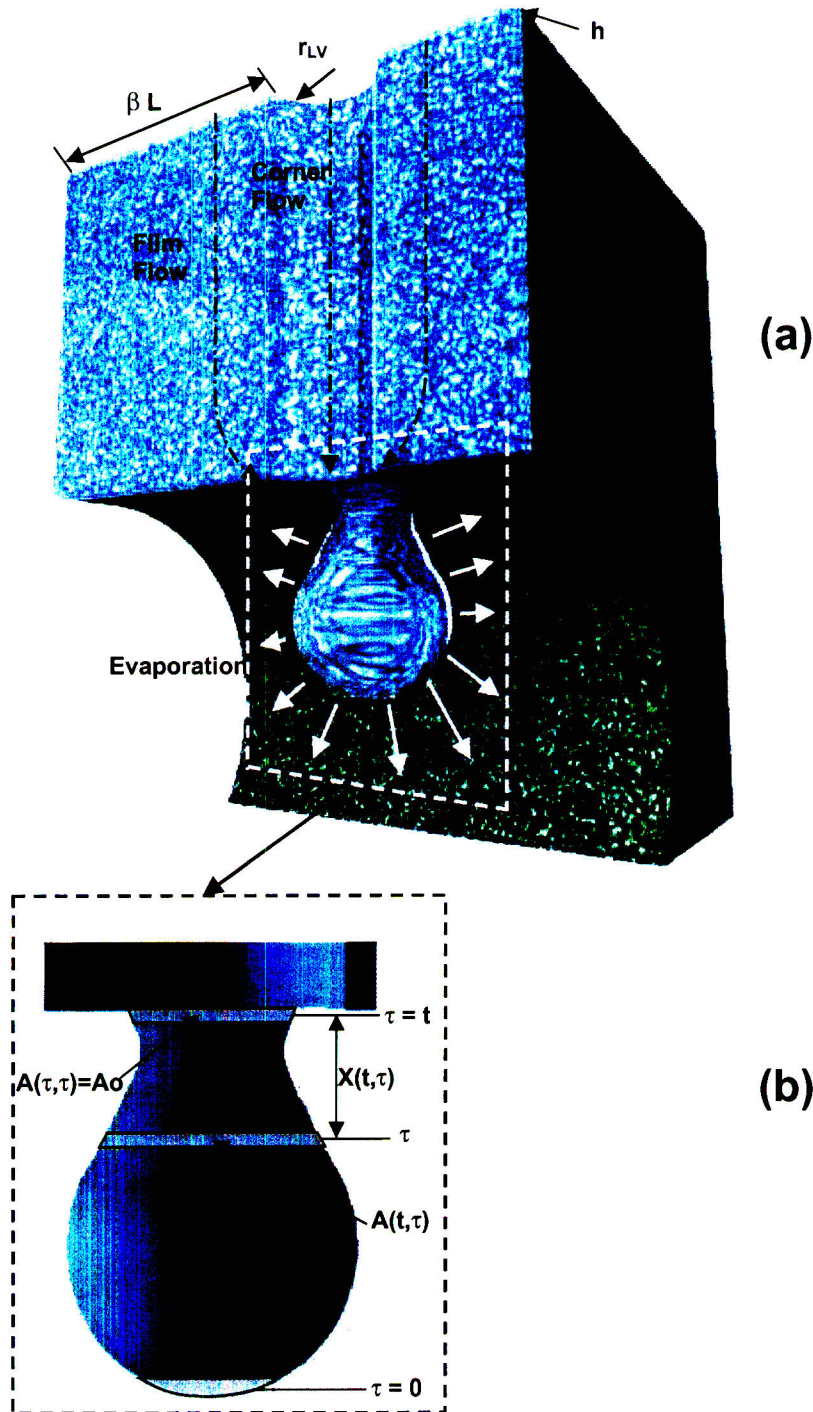

Figure 2. Definition diagram showing (a0 a drop forming into a cavity from face of a vertical fracture, and (b) elements of drop in horizontal plane are marked by a moving (in time) Lagrangian coordinate system.

The fluid elements are labeled by their time of emergence (τ) from the groove, and the actual time is denoted by (t). The first element to leave the grove is labeled by $\tau = 0$, and the element just leaving at present time t is labeled by $\tau = t$, and $0 \leq \tau \leq t$ on all other points. Let $X_{t,\tau}$ be the distance bellow the groove bottom of a typical element labeled by t, at time t, and let $A_{t,\tau}$ be the cross-sectional area of the drop corresponding to that element. Considering two neighboring elements τ and $\tau + d\tau$, the conservation of volume (assuming the liquid is incompressible) leads to,

$$Q \, d\tau = -A_{t,\tau} \, dX_{t,\tau} \tag{12}$$

First, we consider a drop forming in the absence of the effect of surface tension. We consider force balance between the two neighboring elements τ and $\tau + d\tau$, where the longitudinal stress on the horizontal section is denoted by $S_{t,\tau}$. Then,

$$(S \, A)_\tau - (S \, A)_{\tau + \Delta\tau} = \rho \, g \, A_{t,\tau} \, dX_{t,\tau} = \rho \, g \, Q \, d\tau \tag{13}$$

Thus,

$$\frac{\partial}{\partial\tau}(S \, A) = \rho \, g \, A \, \frac{\partial X}{\partial\tau} = \rho \, g \, Q \tag{14}$$

Then, Eq (14) can be integrated to give,

$$S \, A = \rho \, g \, Q\tau \tag{15}$$

The interpretation of Eq (15) is simply; the longitudinal force at any element t equals the weight of the fluid underneath it. In terms of liquid volume suspended below any element $V_{t,\tau}$ Eq (15) can be written as,

$$(S \, A)_{t,\tau} = \rho \, g \, V_{t,\tau} \tag{16}$$

where V is defined by,

$$V_{t,\tau} = Q \, \tau \tag{17}$$

The effect of liquid surface tension acting against the gravity can be introduced into Eq (15). The surface tension of the liquid acts along the perimeter $P_{t,\tau}$ of the drop.

$$S_{t,\tau} = \left(\frac{\rho \, g \, Q \, \tau - P \, \sigma}{A}\right)_{t,\tau} \tag{18}$$

where

$S_{t,\tau}$............... Vertical stress acting in a horizontal cross-section of drop at element i
          [Pa]

$P_{t,\tau}$.................. Perimeter of drop cross-section at element i [m]

$A_{t,\tau}$.................. Liquid cross-section of drop at element i [m]

The rate of extension of the drop is related to the stress by constitutive equation of elongational flow assuming a Newtonian flow,

$$S = -3\eta\frac{1}{A}\frac{\partial A}{\partial t} - \frac{1}{2}\frac{P}{A}\sigma \tag{19}$$

where η is the viscosity of water. The second term on the RHS of Eq (19) is a correction accounting for resistance to extension of cross-sectional area due to surface tension.

Note: The first term on the RHS originates from equation of state for Newtonian liquid under extension $\sigma_s = \lambda\,\dot{\varepsilon}_z$, where $\sigma_s = S$ is stress of extension, $\dot{\varepsilon}_z = \dfrac{\partial A/\partial t}{A}$ is extensional strain rate, and λ is Newtonian viscosity in extension. The latter is related to viscosity in shearing (η) by $\lambda = 2\eta(1+\upsilon)$. For incompressible liquid $\upsilon=0.5$, hence, $\lambda=3\eta$. The second term on the RHS denotes the effect of surface tension on the cross-sectional plane. Surface tension acting on the perimeter of the drop in the axial direction is given by $F = P\sigma$. The lateral stress of surface tension resisting the extension of drop area is related to the axial stress by the Poisson ratio ($\upsilon=0.5$): $0.5\,P\sigma/A$.

Equations (18) and (19) are combined to give the following, first-order differential equation,

$$\frac{\partial A(t)}{\partial t} = \frac{-\rho g Q\tau + \pi\sigma R(t)}{3\eta} \tag{20}$$

Equation (20) was integrated (using *MATHEMATICA* 3.0 – see appendix A) to give,

$$A(t) = \frac{(UQ\tau)^2}{W}\left\{1 + \mathrm{Pr\,oductLog}\left(\frac{-\exp\left[-1+\dfrac{W(t-C)}{6\eta UQ\tau}\right]}{UQ\tau}\right)\right\}^2 \tag{21}$$

Where

$U = \rho\,g,$

$W = \pi\,\sigma^2,$

ProductLog (z) = ω is the solution to $z = \omega\,e^{\omega}$, and

C is constant of integration.

When $\tau = t$, the element is just emerging from the groove and we know that A = Ao (Fig 2). This reduce Eq (21) to,

$$Ao = \frac{(UQ\tau)^2}{W}\left\{1 + \mathrm{ProductLog}\left(\frac{-\exp\left[-1 + \frac{W(\tau - C)}{6\eta UQ\tau}\right]}{UQ\tau}\right)\right\}^2 \tag{22}$$

By applying the definition of ProductLog to Eq (22), it can be rewritten as,

$$\left(\frac{\sqrt{Ao\,W}}{UQ\tau} - 1\right)\exp\left[\frac{\sqrt{Ao\,W}}{UQ\tau} - 1\right] = \frac{-\exp\left[-1 + \frac{W(\tau - C)}{6\eta UQ\tau}\right]}{UQ\tau} \tag{23}$$

Now, Eq (23) can be solved for C (constant of integration), by inverse method,

$$C = \frac{\tau}{W}\left(W - 6\eta UQ - 6\eta UQ \ln\left[-\exp\left[-1 + \frac{\sqrt{Ao\,W}}{UQ\tau}\right]\right]\sqrt{Ao\,W} - UQ\,\tau\right) \tag{24}$$

The drop is pinched and detaches in a finite time (t) when the cross sectional area A(t) goes to zero. The time at which this occurs is obtained by substituting Eq (24) into Eq (21) and solving it using similar method as in Eq (23) with A(t) set to zero,

$$t = \tau - 6\eta\sqrt{\frac{Ao}{W}}\left(1 + \frac{\tau}{\Omega}\ln\left[1 - \frac{\Omega}{\tau}\right]\right) \tag{25}$$

Where

$$\Omega = \frac{\sqrt{Ao\,W}}{UQ}$$

The drop element (plane) that vanishes first also satisfies an additional condition: $dt/d\tau = 0$. Differentiating Eq (25) and setting it to zero leads to an implicit solution for the critical time of breakage or detachment ($\tau = \tau_c$),

$$0 = 1 - 6\eta\sqrt{\frac{Ao}{W}}\left(\frac{1}{\tau_c - \Omega} + \frac{1}{\Omega}\ln\left[1 - \frac{\Omega}{\tau_c}\right]\right) \tag{26}$$

where

τ_c .... Time to detachment [sec]

Values of τ_c for different matric potentials and geometries are obtained by an iterative (numerical) solution of Eq (26). The time at which the first drop detaches is obtained by substituting τ_c into Eq (25). The drop volume (V_d) is obtained simply by integrating the volumetric flux over the duration of drop formation τ_c.

$$V_d = \tau_c \, Q \qquad\qquad (27)$$

where

V_d .... Drop volume [m^3]

At the time of detachment of the first drop (t^1_c), a portion of the extruded liquid at the tip of the groove remains behind, whose volume (known in literature as the *recoil volume*) is associated with the time difference ($\tau_0 = t^1_c - \tau_c$). Because all subsequent drops are built on existing recoil volume, the period of detachment after the first drop pinches is reduced by the time equivalent to the recoil volume (τ_0),

$$t_c = t^1_c - \tau_0 = \tau_c \qquad\qquad (28)$$

where

t^1_c .... Time to detachment of first drop [sec]

t_c .... Time to detachment of all drops subsequent to the first [sec]

τ_c .... Lagrangian time for the detaching element [sec]

τ_0 .... Lagrangian time for the recoil volume [sec]

Note: In other words, Eq (28) states that the volume of liquid extruded from the outlet during an interval between two successive drops is equal to the drop volume.

3/6/99: Evaporation from Drop Surface

For the relatively slow rates of unsaturated surface flows in fractured porous media, evaporation from drop surface can greatly increase the time required for drop detachment, especially under drier conditions. Low matric potentials induce reduction in influx (Q) and extension of detachment period (t_c), thereby increasing the opportunity time for evaporation. At the same time, evaporative demand by the surrounding atmosphere increases with reduced vapor pressure.

A diffusion type equation of radial evaporation from a suspended drop was derived by Ho [1997]. In this study, Ho's solution is incorporated to the situation of growing drop. It

is used to combine the competing effects of evaporation on drop growth and detachment period.

For this analysis, we assume that a drop has a hemispherical shape during most of the drop formation period. This is evidenced from the time sequence photographs in Fig. (3) for a water drop forming and detaching [Zhang and Basaran, 1995]. In Fig. (3a), it is shown that the drop shape is approximately hemispherical for greater than $^4/_5$ of the entire period (denoted as *drop formation period*). Deviation from hemispherical shape takes place for only short period before detachment (*detachment period*). The rapid detachment period is less sensitive to variation in flux than the formation period. Figure (3b) shows that detachment period from a fixed inlet area remains approximately constant as flux decreases, while the drop formation period increases by a few orders of magnitude. This further justifies the hemispherical assumption, because evaporation starts to affect drop formation and detachment significantly only when the flux is very low.

The instantaneous rate of evaporation from a droplet of radius (r_b) can be assumed as isothermal diffusion represented by Fick's law [Ho, 1997],

$$\frac{dr_b}{dt} = -\frac{D}{\rho}\frac{dC}{dr}\bigg|_{r=r_b} \tag{29}$$

where

     dr_b/dt............ rate of change in the drop radius [m s^{-1}]

     D................... binary diffusion coefficient of water vapor [m^2 s^{-1}]

     dC/dr .... the water vapor concentration gradient [kg m^{-3} m^{-1}].

The binary diffusion coefficient of water vapor at ambient temperature (T) is related to binary diffusion coefficient at standard temperature and pressure (D^o) by [Campbell, 1986],

$$D = D^o\frac{10^5}{P}\left(\frac{T}{273.15}\right)^{1.8} \tag{30}$$

where

     P................... the total, gas-pressure [1.0x10^5 Pa at sea level]
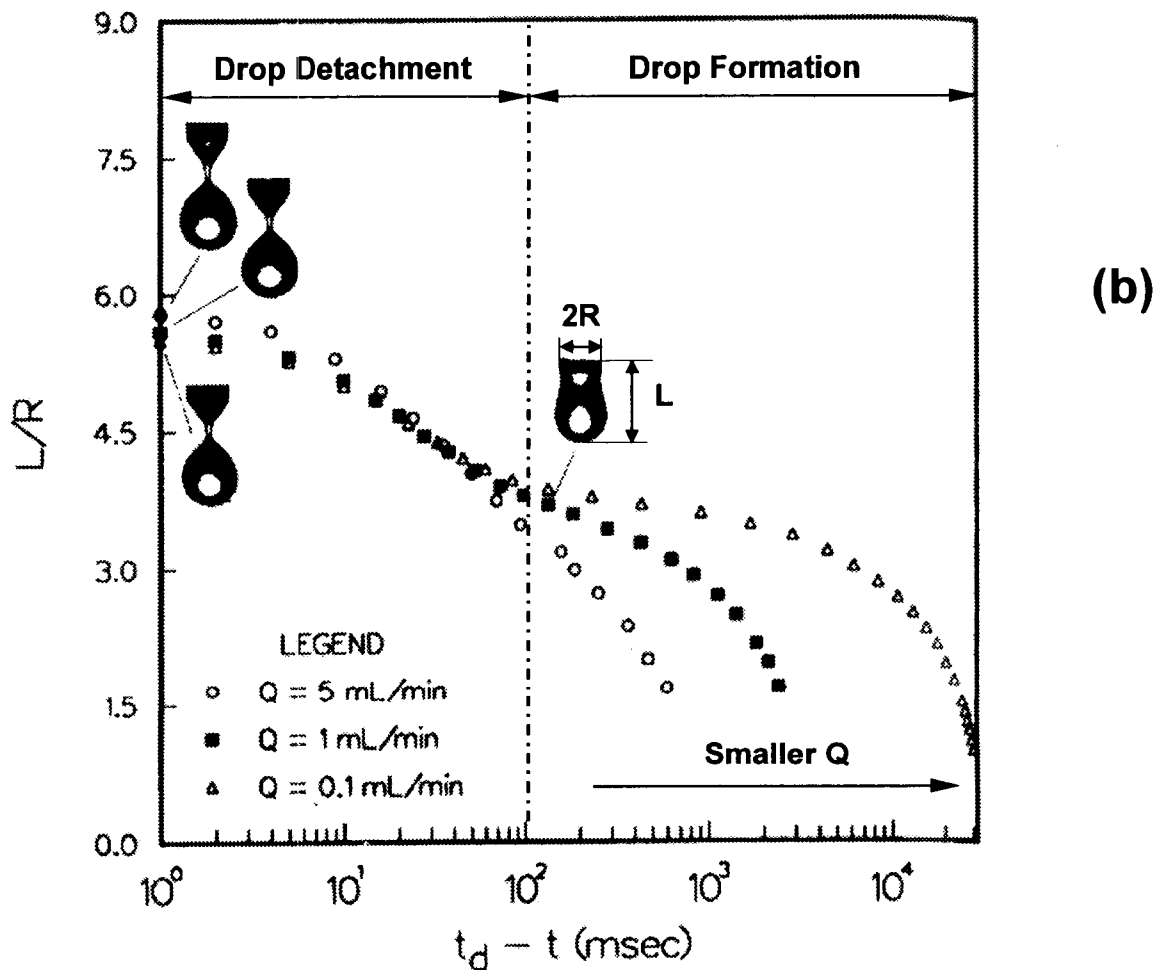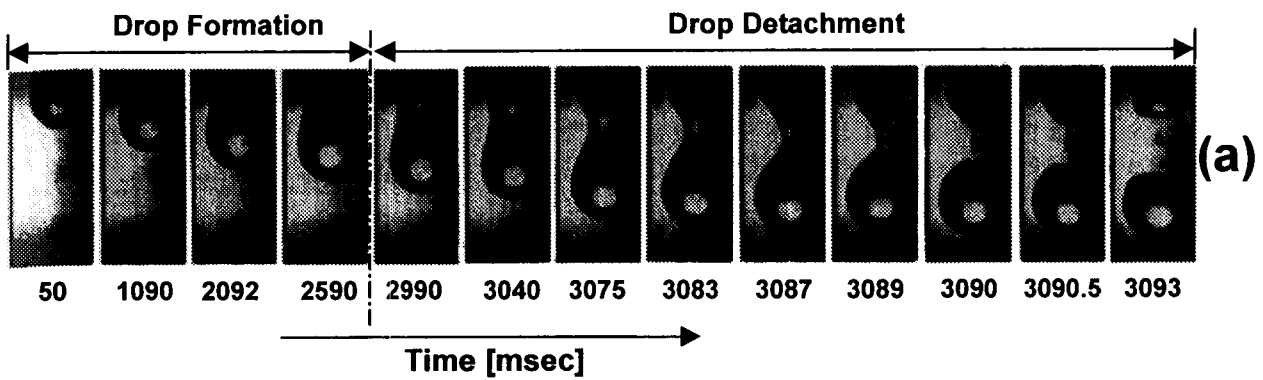
Figure 3.   Time sequence photographs of water drop formation and detachment, (a) water drops forming out of a tube of outer radius of 0.16 cm at liquid flow rate of 1 mL min^{-1}. The drop has approximately hemispherical shape for the first 4/5 time of the total formation period (drop formation period), in the remaining ¼ of the period the drop forms a neck and detaches (drop detachment period), (b) Evolution of dimensionless drop length (L/R) vs. (td-t) countdown time to detachment. As Q gets smaller the total dripping time becomes smaller, however, time of necking and detachment remains almost unchanged. [Adapted from Zhang and Basaran, 1995]

The concentration gradient of water vapor at the drop surface is obtained by solving for radial diffusion from the drop surface [Ho, 1997],

$$\left.\frac{dC}{dr}\right|_{r=r_b} = \frac{\Delta P_v}{r_b R^* T} \tag{32}$$

where

R^* .... water vapor gas constant [R^*=462 J kg^{-1}K^{-1}]

ΔP_v .... difference in vapor pressure between the drop surface and the surrounding environment.

The pressure difference (ΔP_v) is related to the matric potential (ψ) and the saturated vapor pressure at ambient temperature (P_{sat}) by:

$$\Delta P_v = P_{sat}\left[1 - \exp\left(\frac{\psi \rho}{R^* T}\right)\right] \tag{33}$$

The initial radius (r_{bo}) for a hemispherical drop in the absence of evaporation is related to the flux by,

$$r_{bo}(\tau) = \sqrt[3]{\frac{3Q}{2\pi}\tau} \tag{34}$$

Integration of Eq (29) with the initial condition given by Eq (34) leads to an expression for the instantaneous drop radius,

$$r_b(\tau)^2 = \frac{2D\Delta P_v}{\rho R^* T}\tau + r_{bo}(\tau)^2 \tag{35}$$

The corresponding drop volume after evaporation would be,

$$V(\tau) = \frac{2\pi}{3}r_b(\tau)^3 = \frac{2\pi}{3}\left[\frac{2D\Delta P_v}{\rho R^* T}\tau + \left(\frac{3Q}{2\pi}\tau\right)^{\frac{2}{3}}\right]^{\frac{3}{2}} \tag{36}$$

The net flux would be derived from Eq (36) at any given τ as,

$$Q_{net} = \frac{V(\tau)}{\tau} = \frac{2\pi}{3\tau}\left(M\tau + N\tau^{\frac{2}{3}}\right)^{\frac{3}{2}} \tag{37}$$

where:

$$M = -\frac{2D\,\Delta P_v}{\rho R^* T}$$

$$N = \left(\frac{3Q}{2\pi}\right)^{\frac{2}{3}}$$

In the presence of evaporation, the flux (Q) in Eq (21) is replaced by Q_{net} in Eq (37). Following the same algebraic manipulations we arrive at a similar expression for time-to-detachment,

$$t = \tau - 6\eta\sqrt{\frac{Ao}{W}}\left(1 + \frac{\left(N\tau^{\frac{2}{3}} + M\tau\right)^{\frac{3}{2}}}{\Omega'}\ln\left[1 - \frac{\Omega'}{\left(N\tau^{\frac{2}{3}} + M\tau\right)^{\frac{3}{2}}}\right]\right) \tag{38}$$

Where

$$\Omega' = \frac{3\sqrt{AoW}}{2\pi U}$$

Similarly, the first drop element to reach this pinching state satisfies the additional condition $dt/d\tau = 0$

$$0 = 1 - 3\eta\sqrt{\frac{Ao}{W}}\left(2N\tau_c^{-1/3} + 3M\right)\left(\frac{\sqrt{Y}}{Y^{3/2} - \Omega'} + \frac{\sqrt{Y}}{\Omega'}\ln\left[1 - \frac{\Omega'}{Y^{\frac{3}{2}}}\right]\right) \tag{39}$$

where

$$Y = N\tau_c^{\frac{2}{3}} + M\tau_c$$

Equation (39) is evaluated iteratively using a Newton-Raphson scheme. The argument of the logarithm on the RHS of Eq (39) evolves from a large negative number to small positive numbers in very short time period. The function has large negative results at points immediately next to the singularity and levels off to value of one within short distance in (τ). The numerical scheme used approaches the solution only from the real side, with a step size that is a very small fraction of the standard Newton-Raphson scheme. Details of a FORTRAN 90 code that implement this scheme is given in the Appendix B of this scientific notebook.

3/10/99: Maximum Detachment Time

$\boxed{\text{Dani Or}}$

For liquid drops to be formed and eventually detach, the net liquid flux feeding them needs to be positive at all stages. If, at any stage of drop formation, the net flux becomes negative, the drop would decrease in size (due to evaporation rate greater than influx) and never attain sufficient weight to break off. Any situation that results in non-positive net flux (Q_{net}) leads to non-dripping situation. For any given matric potential (vapor pressure), the time (τ) which equates the term on RHS of Eq (37) to zero, represents the maximum opportunity time (τ_{max}) within which the drops should be formed and detach (if they form at all),

$$\tau_{max} = \left(\frac{R^* T \rho}{2 D \Delta P_v}\right)^3 \left(\frac{3 Q}{2 \pi}\right)^2 \tag{40}$$

Drop detachment time (τ_c) is obtained as a solution to Eq (39), and is always less than the maximum opportunity time (τ_{max}). Equation (39) is mathematically undefined for times greater than τ_{max}.

The volume of the drops is obtained by integrating the net flux Eq (37) over the duration of drop formation to its maximum volume using MATHEMATICA 3.0 (Appendix A).

$$V_d = 4\pi \frac{\left(-8N^4\sqrt{N\tau_c^{\frac{2}{3}}} + \left(N + M\tau_c^{\frac{1}{3}}\right)^2 \left(8N^2 - 20MN\tau_c^{\frac{1}{3}} + 35M^2\tau_c^{\frac{2}{3}}\right)\sqrt{N\tau_c^{\frac{2}{3}} + M\tau_c}\right)}{315M^3 \tau_c^{\frac{1}{3}}} \tag{41}$$

This analytical expression of drop volume Eq (41) becomes mathematically unstable at high values of matric potential (i.e., very wet conditions). However, numerical integration of Eq (37) reveals that the numerical and analytical integrals coincide for all values roughly less than the critical potential of groove filling (ψ_c). In the range where Eq (41) is unstable there is little evaporation effect (dripping rate is very fast with detachment times <<1 sec), hence drop volume is almost equal to the total influx to the cavity. The total volume of water that leaves the groove is given by integrating the constant influx over the duration of drop formation

$$V_t = Q \tau_c \tag{42}$$

The difference between the total flux (V_t) and the drop volume (V_d) being the volume of water that evaporates during drop formation.

3/18/99: Solute Concentration of Liquid Drops

During evaporation, water is preferentially evaporated leaving behind non-volatile solutes (salts) thereby changing solute concentration of a growing drop. The ratio of the total liquid volume to drop volume can be interpreted as the relative increase in solute concentration of a drop at the time of detachment.

$$C_{rel} = \frac{C_{drop}}{C_o} = \frac{V_t}{V_d} \tag{43}$$

where

C_{drop} .... solute concentrations of the drop water [ppm]

C_o .... solute concentrations of the bulk water feeding the drop [ppm]

C_{rel} .... relative solute concentration of drops [dimensionless]

Dryer conditions induce slow flow rates and longer detachment times, as well as higher evaporative demand. When these processes are coupled they result in high solute concentrations in drops formed under low matric potentials (dry conditions). The effect of increasing solute potential on evaporation rates, potential gradients, and solute diffusion are not considered in this analysis, and require further investigation.

3/21/99: Alternate Solution for Experimental Purposes

Tests of the fracture-dripping model presented in the previous sections of this scientific notebook require an experimental setup in which accurately controlled flux and vapor pressure induce dripping. Such an experiment could be designed around accurate control of vapor pressure in the experimental fracture and cavity. However, the fact that liquid flux and evaporation are inseparable presents a formidable challenge to practical experimental systems. To alleviate the above shortcomings we present a decoupled solution in which the liquid influx and evaporation are controlled independently. This approach can also be used in investigating real life problems where drop formation under equilibrium state vapor pressure is not possible (e.g. actively vented cavities).

We consider a setup consisting of a sample of fractured media similar to Fig 2, in which the plane width parameter is set as $\beta=0$ (considering flow in grooves only). A controlled steady state volumetric flux is applied at the groove top (Q_V). This influx of liquid substitutes the chemical-potential-dependent flux (Q) of previous calculations.

The applied flux is not permitted to overflow out of the grooves (by keeping the flux sufficiently small or using deep grooves). Thus, the flow mechanism is that of corner flow in partially filled grooves given in Eq (5). Drop inlet area is approximated by the

liquid-vapor interface curvature equivalent to the specified volumetric flux Eq. and the corresponding inlet area formula Eq (10), leading to cross-sectional area dependent on flux,

$$ Ao = \left(\frac{Q_V \, \epsilon \eta F}{\rho g} \right)^{\frac{1}{2}} \tag{44} $$

The maximum flux (Q_{vmax}) that can be applied is that which fills the grooves completely. This can be calculated from Eq (1) and (5)

$$ Q_{V\,max} = \left(\frac{L \tan(\gamma/2)}{\cos(\gamma/2)} \right)^4 \frac{F \rho g}{\epsilon \eta} \tag{45} $$

The rate of evaporation is determined by the vapor pressure (matric potential) as previously.
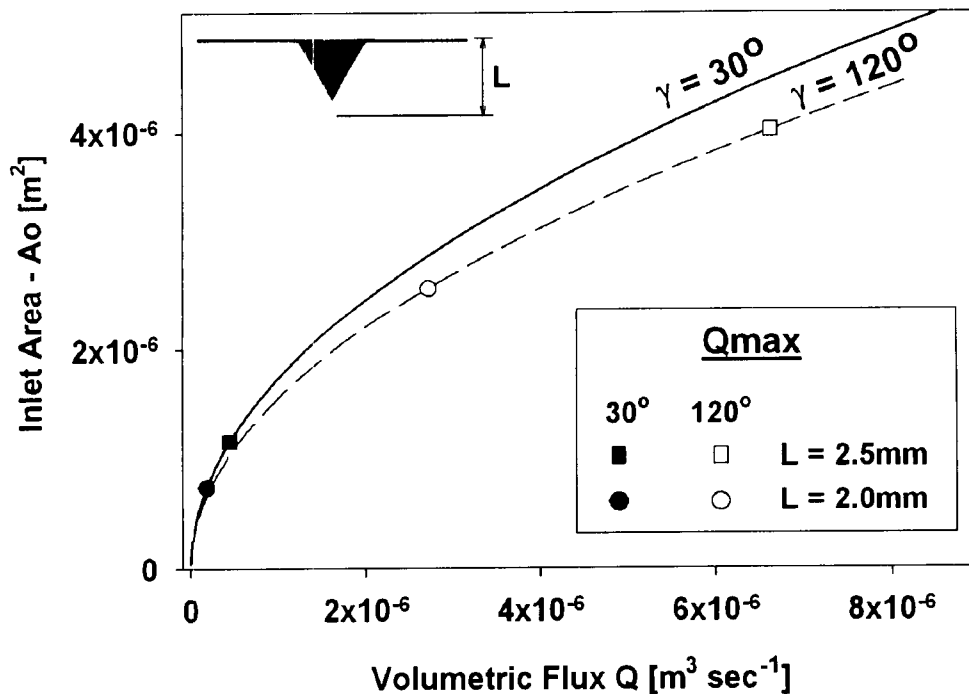
Figure 4: Liquid Cross sectional area at the base of fracture (Ao) dependent on the liquid influx (Q_V), shown for two groove angles (γ). The maximum flux for stable flow in the grooves is indicated by symbols for two groove-depths (L).

In Fig (4), the inlet area (Ao liquid cross-sectional area – Eq. (44) is depicted as a function of volumetric flux (Q_V) for two groove angles. The curves define the increase in cross sectional area with increase in volumetric flux for all groove depths. Maximum values of stable flux (Q_{Vmax}) as defined by Eq (45) for two groove-depths (L) are indicated by symbols. The dependence of cross-sectional area (Ao) on the groove angle (γ) is overshadowed by the high sensitivity of the cross-sectional area to the influx (Q_V). However, the groove angle is the major factor in determining the maximum flux, and hence maximum cross-sectional area.

The net flux (Q_{net}) given in Eq (37) is modified by substituting Q with Q_V. The drop detachment time is obtained by solving Eq (39) using the modified net flux Eq (45). The numerical solution methods are identical to those discussed in previous sections. The evaporation from drop surfaces is determined by the matric potential (ψ) in the cavity.

4/5/99

Illustrative Examples of Coupled Dripping and Evaporation

The following illustrative example considers dripping in a phenomenon where the flux inducing vapor pressure and evaporation inducing vapor pressure are in equilibrium and numerically identical (ψ). It makes use of the set of equations given in the section of dripping under evaporative conditions. The following parameters were considered to define the fracture geometry:

L.................... 2 mm deep (equivalent to typical surface roughness observed by Tokunaga and Wan [1997]).

β...................... 1

γ.................... 30, 60 and 120 degrees

ψ.................... 10 - 3000 Pa. In the following examples matric potential is measured in units of energy per unit volume [$J\ m^{-3}$] ($1\ J\ m^{-3} = 1\ Pa = 10^{-3}\ J\ kg^{-1} = 0.1\ mm\ H_2O$).

Illustrative calculations of drop detachment period, drop volume and relative concentration at detachment as functions of matric potential (ψ) are presented in Figs. (5) to (7). The water flow considered is induced by a unit gravitational gradient, however, the solutions presented can be used for any gradient other than unity. It is assumed that the matric potentials in the fracture and the cavity are at equilibrium.

Note: The implicit functions of detachment period for non-evaporative and evaporative conditions, Eq(26) and (39) respectively, are ill posed. For τ_c very close to the actual solution, the functions have very steep slope, and standard Newton-Raphson iterations fail to converge unless the initial guess is very close to the actual solution. We used a FORTRAN 90 code that implements Newton-

Raphson iterations with damping factor, and uses solution of preceding matric potential as an initial guess for the current solution. As the matric potential decreases (gets drier) the slope of the function increases, and we used smaller steps in matric potential to overcome the difficulty in obtaining solution. The FORTRAN solutions (Appendix B) were cross-checked with solutions obtained using MATHEMATICA 3.0 for selected matric potential values and geometry, as shown in Appendix C.

Detachment Time (Fig 5)

Out of the three geometric parameters (L, β and γ) that define the fractured media, the corner angle (γ) results in much higher variations of drop size and detachment. The effect of groove depth (L) is limited to determining the matric potential of complete filling of the grooves. Hence, its effect is visible only near saturation matric potentials (near zero). The parameter β does not have significant effect on dripping rate and drop size, since corner flow dominates film flow by several orders of magnitude in the range of matric potential where drop formation is possible. Detachment period (τ_c) for non-evaporating Eq (26) and evaporating Eq (39) conditions and the maximum opportunity time (τ_{max}) Eq for two groove angles are depicted in Fig (5).
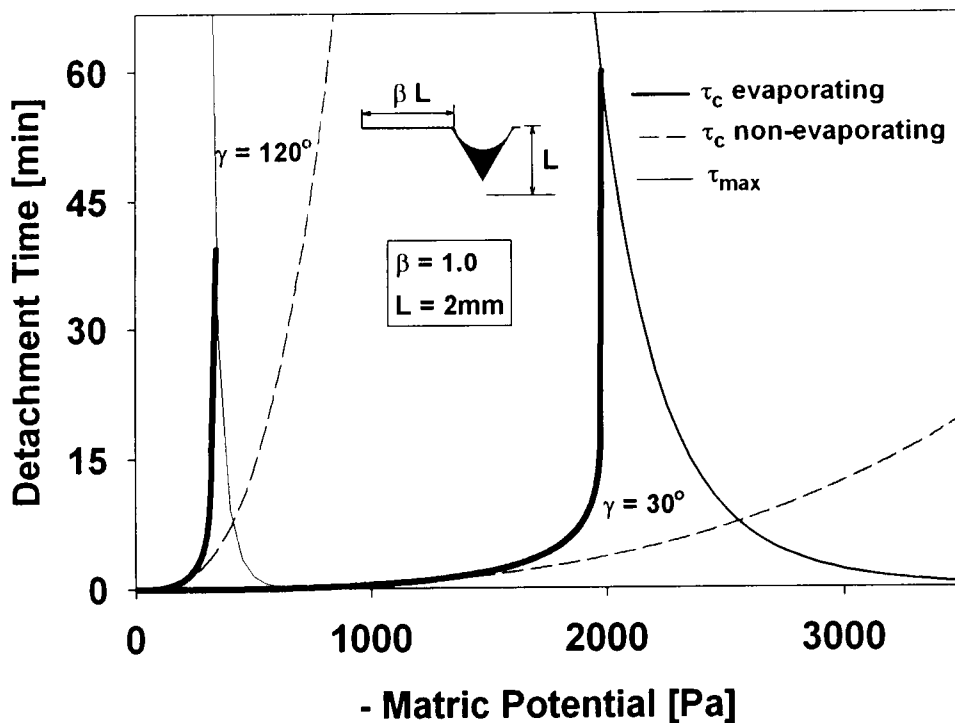

Figure 5: Drop detachment time (τ_c) under evaporative and non-evaporative conditions dependent on the equilibrium state matric potential (ψ) of cavities and fractures, and maximum opportunity time (τ_{max}) for detachment.

As the matric potential decreases (becomes more negative), the total influx to the drop decreases while evaporation increases. Dripping continues at progressively lower rates until the influx equals the evaporation rate. The crossover of drop detachment time (τ_c) with maximum opportunity time (τ_{max} - Eq (40)) denotes the minimum potential (driest conditions) at which drop formation is possible for a given geometry. When critical drop-forming potential is approached, the detachment time (duration of drop formation τ_c) becomes very sensitive to slight variations in ambient conditions to the extent that even small variations in barometric pressure or temperature could induce vastly different dripping rates and drop chemistry. In contrast, under non-evaporating conditions (Eq. (26), drop formation continues indefinitely with no bounds on minimum matric potential.

Drop Volume (Fig 6)

The volume of individual drops in evaporative conditions as a function of the matric potential Eq (41) is shown in Fig (6a). The drop volume is determined by the inlet area (liquid cross sectional area at the corner or lip), and time to detachment. The abrupt change in inlet area (liquid cross-sectional area) at the critical matric potential of complete groove filling (ψ_c) results in a large decrease in drop volume. In the remaining range of matric potential changes (before and after complete groove filling) a further decrease in matric potential (hence, inlet area) is accompanied by gradual decrease in drop volume.
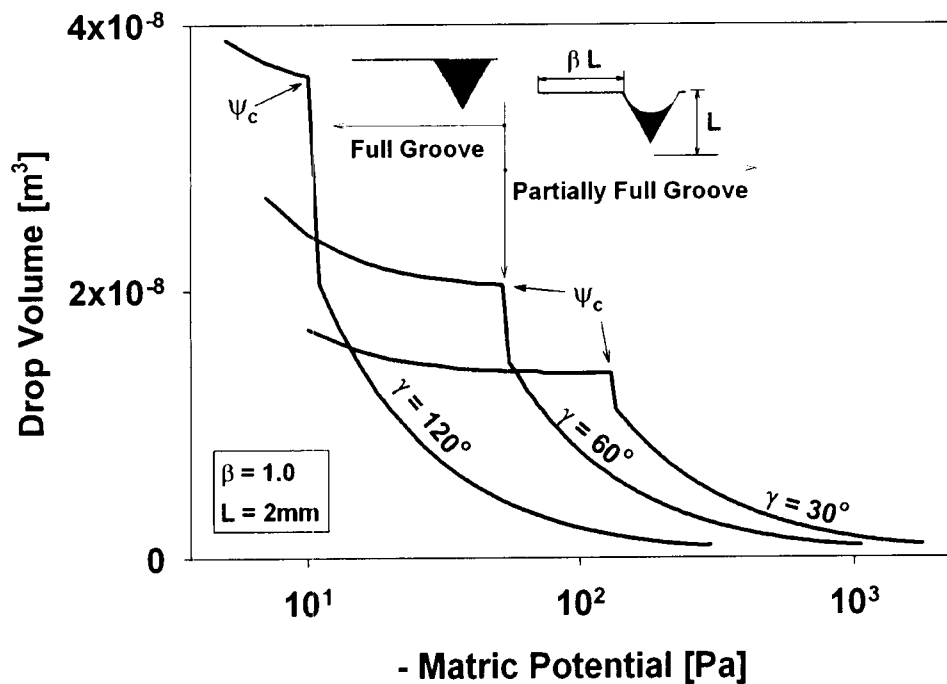

Figure 6: Drop volume at detachment for different groove angles (γ) under evaporative condition.

The dependence of drop volume on the duration of drop formation is through the rate of viscous extension. A faster extension process Eq (19) tends to add-up to drop weight resulting in smaller drop volume than a drop emanating from the same cross sectional area but at a slower flux. However, this dependency is overshadowed by the effect of matric potential which induces several orders of magnitude variations in liquid flux and liquid cross sectional area. Therefore, significant differences in drop size between evaporating Eq (41) and non-evaporating Eq (27) conditions are observable only when the matric potential is close to its critical minimum before cessation of dripping (under evaporating conditions) as shown in Fig 6b. Differences are observable near this critical potential due to the rapid increase in drop formation time where the slow extension rate reduces the stress.

Solute Concentration of Drops (Fig 7)

Under evaporative conditions, both, the matric potential (or equilibrium vapor pressure), and groove-geometry, determine the solute concentration of drops. Sample calculations (using Eq (43)) of drop concentrations at time of detachment are shown in Fig (7) for the three groove-angles (γ) as functions of the matric potential (ψ).

The effect of lower matric potential on drop solute concentration is through the decrease in dripping rate that allows more evaporation to take place. At potentials close to minimum drop forming potential, the time required for drop formation increases rapidly thereby allowing for extended evaporation opportunity times. Near this region (see Fig.
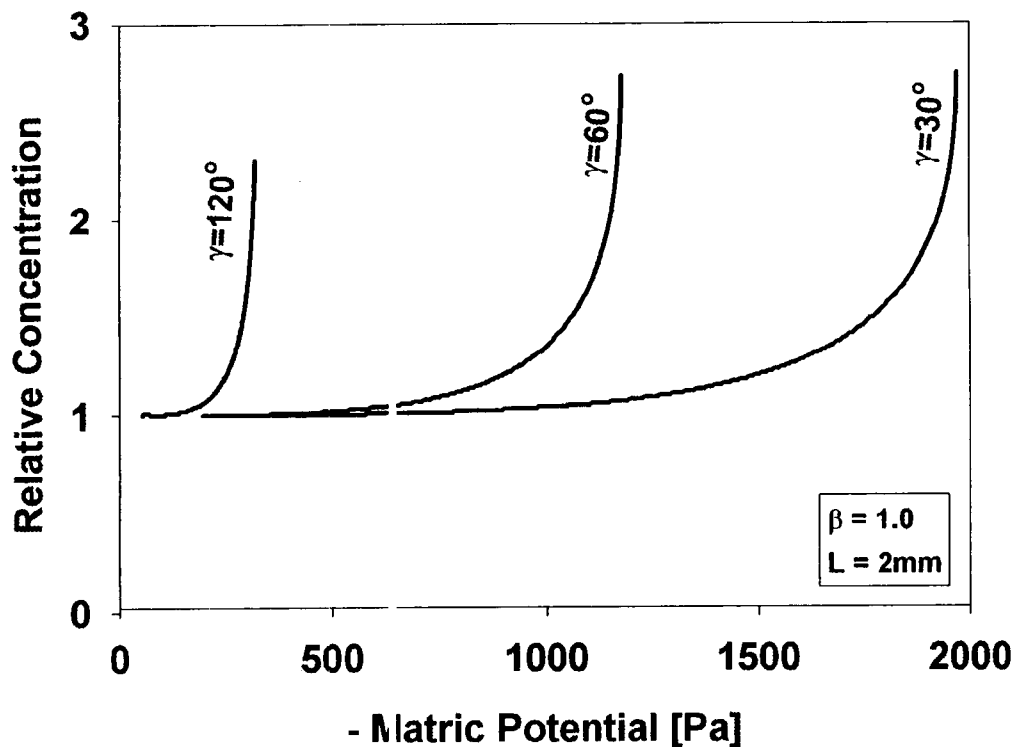

Figure 7. Relative solute concentration of drops (in relation to the bulk influx) at detachment for different groove angles (γ) under evaporative condition.

5 for the fast rise in formation time), the concentration more than doubles by only a slight decrease in potential (or vapor pressure). It is important to note that the minimum drop forming potential (below which dripping stops) is completely determined by the groove geometry. This sensitivity to groove geometry and matric potential variations guarantees that even under similar ventilation conditions, variations in individual dripping rates among grooves (on the same fracture lip) would produce drops with different solute concentrations. In general, slow pathways would result in higher relative solute concentration of drops by allowing longer evaporation duration. Even slight variations in matric potential (e.g., at a range that could be induced even by barometric pressure or temperature variations) near the minimum drop forming matric potential (depends on the groove geometry) could substantially alter solute concentration of drops.

Comparison of Drop Volume with Alternative Solution of Scheele-Meister (Fig 8)

We compared our drop volume calculations with a widely used semi-empirical equation of Scheele and Meister [1968]. The original equation was developed based on two-stage process of formation of a liquid drop (growing and necking) into a different liquid. For liquid drop forming in air the Scheele-Meister equation can be reduced to [Zhang and Basaran, 1995]:

$$V_{SM} = F_{HB}\left[\frac{2\pi\sigma Ro}{g\rho} - \frac{4Q^2}{3\pi Ro^2 g} + 7.14\left(\frac{Q^2 Ro^2 \sigma}{g^2 \rho}\right)^{\frac{1}{3}}\right] \qquad (46)$$

where

Ro .... Radius of circular inlet area [m],

F_{HB} .... Harkins-Brown correction factor to account for the proportion of an ideal (static) drop that detaches [dimensionless].

We compared our drop volume calculations of Eq (27) under non-evaporative condition, with that of Scheele-Meister Eq (46). Using the Harkins-Brown factor as fitting parameter (F=0.48) resulted in good agreement as shown in Fig (6), for most of the matric potential range used in this study. For the wet end of matric potential, however, the Scheele-Meister equation fails by resulting in decreasing drop volumes with increasing flux. In extreme cases (very close to saturation), negative drop volumes are predicted by Scheele-Meister equation.
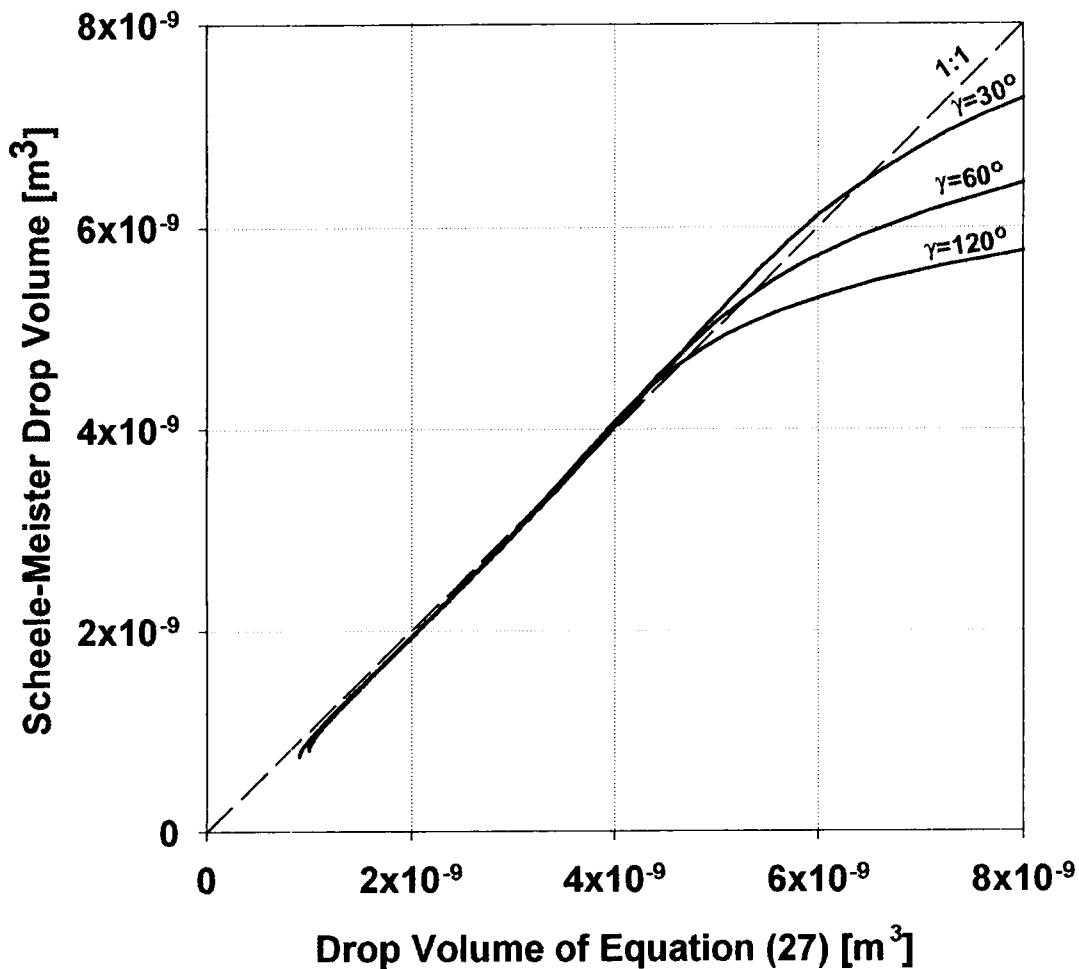
Figure 8. Comparison of Scheele-Meister drop volume [Zhang and Basaran,1995] and Equation (28) for different groove angles (γ) under evaporative condition.

Detachment Time using the Alternate Solution for Experimental Purposes (Fig 9)

Sample calculations of drop detachment times (τ_c) for a series of fluxes (Q_V) and different matric potentials (ψ) are shown in Fig (9).

The net flux decreases with decrease in the matric potential (or relative humidity) of the cavity, leading to increase in detachment time. A singularity is encountered in Eq (39) when Qnet $\leq$ 0, indicating that the conditions are too dry or flux is too small. The minimum volumetric fluxes (Q_{min}) associated with limiting ambient vapor pressures in the experimental fracture cavity where singularity is likely to arise are depicted in Fig (9) by arrows. When the vapor pressure of the cavity is close to saturation (e.g. ψ = 1kPa), the effect of evaporation is negligible and drops can be formed even at infinitely small volumetric fluxes.
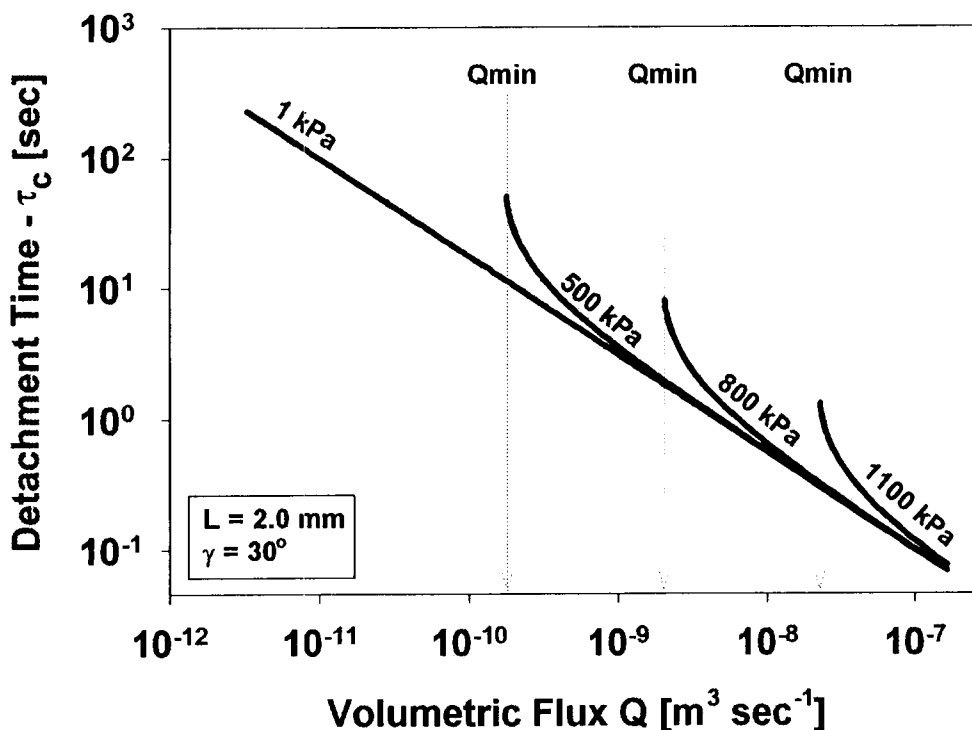
Figure 9. Detachment time of drops formed under different evaporative conditions (chemical potentials) dependent on volumetric flux supplying the grooves. The minimum fluxes that can lead to drop formation under the given evaporative conditions are indicated by arrows. In terms of relative humidity: 1kPa = RH 0.9999, 500kPa = RH 0.9963, 800kPa = 0.9942, 1100kPa = 0.9920.

The drop volume is obtained by integrating the modified net flux equation Eq (37) over the drop formation period (τ_c). The calculated volume of liquid drops is shown in Fig (10) as a function of the volumetric flux applied to two groove angles (γ). The drop volume is mainly dependent on the inlet area (liquid cross-sectional area, Ao). The drop volume is less sensitive to the groove angle (γ) because the inlet area is also less sensitive to γ as discussed above (Fig 8).

4/15/99: Status Report

<u>4/15/99</u>: Status Report

Limitations and future model improvements

● Several questions remain open regarding the convergence of film flows adjacent to a groove. In other words, does the formation of a liquid drop (where liquid is at lower potential energy per unit volume) attracts liquid to the "supply zone"?

● It is unclear whether the assumed cross-sectional area feeding the drop (A_o) is indeed defined by the equilibrium liquid configuration in the groove.

● There is growing interest to expand this work to deal with drop formation on inclined surfaces (cavity ceiling) and the potential migration downslope. The interest is motivated by the likelihood of drops landing on canisters, but this is also important for flow-routing at fracture intersections (to tie with Stu Stothoff work on discrete fractures).

● We believe that asperities and other geometrical "irregularities" cause liquid accumulation at these "low energy traps" with subsequent discharge of critical liquid mass or volume (similar to drop detachment process). There is a distinct possibility of using derivations from this study to identify volumes and rates of liquid discharge in such systems which cause the high degree of intermittent flows observed in many experiments.

● Experimental work in artificial fracture surfaces will focus first on evaluating flow in grooves to assess model predictions of dripping rates and volumes in the absence of evaporation. Subsequent work (with actual YM rock samples?) will attempt to highlight effects of evaporation for very low fluxes (using chambers with controlled temperature and relative humidity).

● Note two appendices are attached: (1) Appendix A includes detailed mathematical derivations using Mathematica 3.0 (the worksheet is also attached); and (2) the computer

References

Campbell, G. S., *An introduction to Environmental Biophysics*, Springer-Verlag, New York, 1986.

Eggers, J., Non linear dynamics and breakup of free-surface flows, *Rev. Mod. Phys.*, 69(3), 865-929, 1997.

Eggers, J., and T. F. Dupont, Drop formation in a one-dimensional approximation of the Navier-Stokes equation, *J. Fluid Mech.*, 262: 205-221,1994.

Iwamatsu, M., and K. Horii, Capillary condensation and adhesion of two wetter surfaces, J. Colloid Interface Sci., 182, 400-406, 1996.

Ho, C. K., Evaporation of pendant water droplets in fractures, *Water Resor. Res.* 33(12), 2665-2671,1997.

Or, D., and M. Tuller, Flow in unsaturated fractured porous media – Hydraulic conductivity of rough fracture surfaces, (in review)

Ransohoff, T.C. and C.J. Radke, Laminar flow of a wetting liquid along the corners of a predominantly gas-occupied noncircular pore, J. Colloid and Interfac. Sci., 121:392-401, 1988.

Scheele, G. F., and B. J. Meister, Drop formation at low velocities in liquid-liquid systems, *AiChE J*, 14(1), 9-15, 1968.

Tokunaga, T. K. and J. Wan, Water film flow along fracture surfaces of porous rock, *Water Resour. Res.* 33(6), 1287-1295, 1997.

Wilson, S. D. R., The slow dripping of viscous fluid, *J. Fluid. Mech.*, 190, 561-570, 1988.

Zhang, X. and O. A. Basaran, An experimental study of dynamics of drop formation, *Phys. Fluids* 7(6), 1184-1203, 1995.

Appendix A: 4/15/99

Drop Formation and Detachment under Non-Evaporative and Evaporative Conditions

Note: Corresponding MATHEMATICA 3.0 file is attached as APPENDIXA.NB

Force balance and Cross-sectional Area of Axisymetric Drop

■ Force Balance

At a given time t, the weight of material below an element represented by τ and the surface tension over the perimeter are balanced by an axial stress over the cross-section:

$$SA == -2\pi R\gamma + \rho g Q \tau;$$

$$S == \frac{-2\pi R\gamma + \rho g Q \tau}{A};$$

■ Stress Equation

Constitutive relations of elongational deformation of viscous body with a correction term for effect of surface tension at a fixed τ

$$S == -3\eta \frac{1}{A[t]} \partial_t A[t] - \frac{\gamma}{R[t]};$$

■ Evolution of Cross-Sectional Area

Force balnce and stress equations are solved simultaneously to yiled an ordinary differential equation. Combining both equations yields,

$$\frac{-2\pi R \, t \, \gamma + \rho g Q \tau}{A \, t} == -3\eta \frac{1}{A \, t} \partial_t A \, t - \frac{\gamma}{R \, t};$$

$$3\eta \frac{1}{A[t]} \partial_t A[t] == -\frac{\gamma}{R[t]} - \frac{2\pi R[t] \gamma}{A[t]} - \frac{\rho g Q \tau}{A[t]};$$

using the relation $\dfrac{1}{R[t]} = \sqrt{\dfrac{\pi}{A[t]}}$, we obtain the following ordinary differential equation,

$$EQ1 = \partial_t A[t] == \frac{\gamma \sqrt{\pi}}{3\eta} \sqrt{A[t]} - \frac{\rho g Q \tau}{3\eta};$$

EQ1 is the basic differential equation for dripping. Wilson (1988) solved EQ1 by introducing non-dimensionalizing transformations. In order to be able to intriduce effect of evaporation at latter stage (and added adavantage of

MATHEMATICA to handle the orginal problem), we contnue solving the equation without introducing the non-dimentional forms used by Wilson.

```
EQ2 = DSolve[EQ1, A[t], t];
```

```
InverseFunction::ifun : Warning: Inverse functions are being used. Values
    may be lost for multivalued inverses.
```

```
Solve::ifun :
    Inverse functions are being used by Solve, so some solutions may not be found.
```

EQ2 is the solution to the differential equation. The simplified form of the solution is given by,

A[t] == Simplify[EQ2[[1, 1, 2]]]

$$A[t] == \frac{g^2 \, Q^2 \, \rho^2 \, \tau^2 \left(1 + \text{ProductLog}\left[-\frac{E^{-1 + \frac{\pi \gamma^2 \, (t - c[1])}{6 \, g \, Q \, \eta \, \rho \, \tau}}}{g \, Q \, \rho \, \tau} \right] \right)^2}{\pi \, \gamma^2}$$

By re-arranging the terms to separate the **ProductLog** function:

$$EQ3 = \frac{\sqrt{\pi} \, \gamma \, \sqrt{A[t]}}{g \, Q \, \rho \, \tau} - 1 == \text{ProductLog}\left[-\frac{E^{-1 + \frac{\pi \gamma^2 \, (t - C1)}{6 \, g \, Q \, \eta \, \rho \, \tau}}}{g \, Q \, \rho \, \tau} \right];$$

To solve for the constant of integration C1 we use the initial condition **A=Ao** at **t=τ**,

```
EQ4 = EQ3 /. {A[t] → Ao, t → τ}
```

$$-1 + \frac{\sqrt{Ao} \, \sqrt{\pi} \, \gamma}{g \, Q \, \rho \, \tau} == \text{ProductLog}\left[-\frac{E^{-1 + \frac{\pi \gamma^2 \, (-C1 + \tau)}{6 \, g \, Q \, \eta \, \rho \, \tau}}}{g \, Q \, \rho \, \tau} \right]$$

with $\omega = -1 + \dfrac{\sqrt{Ao} \, \sqrt{\pi} \, \gamma}{gQ\rho\tau}$ and $z = -\dfrac{E^{-1 + \frac{\pi\gamma^2(-C1 + \tau)}{6gQ\eta\rho\tau}}}{gQ\rho\tau}$ we obtain $\omega == \textbf{ProductLog[z]}$.

By definition we have $z = \omega \, E^{\omega}$,

```
EQ5 = z == ω E^ω ;
```

Substituting ω and z into EQ5(definition of ProductLog),

$$EQ6 = EQ5 /. \left\{ z \rightarrow -\frac{E^{-1 + \frac{\pi \gamma^2 \, (-C1 + \tau)}{6 \, g \, Q \, \eta \, \rho \, \tau}}}{g \, Q \, \rho \, \tau}, \ \omega \rightarrow -1 + \frac{\sqrt{Ao} \, \sqrt{\pi} \, \gamma}{g \, Q \, \rho \, \tau} \right\};$$

The constant of integration C1 is obtained by solving EQ6 for C1,

```
EQ7 = Solve[EQ6, C1];
```

```
Solve::ifun :
  Inverse functions are being used by Solve, so some solutions may not be found.
```

CONST = EQ7[[1, 1, 2]]

$$-\frac{-\pi\gamma^2\tau + 6gQ\eta\rho\tau + 6gQ\eta\rho\tau\,\mathrm{Log}\left[gQ\rho\left(E^{-1+\frac{\sqrt{Ao}\sqrt{\pi}\gamma}{gQ\rho\tau}} - \frac{\sqrt{Ao}\,E^{-1+\frac{\sqrt{Ao}\sqrt{\pi}\gamma}{gQ\rho\tau}}\sqrt{\pi}\gamma}{gQ\rho\tau}\right)\tau\right]}{\pi\gamma^2}$$

We substitute C1 in EQ3. we repeat the above procedures to solve for A[t]

EQ8 = Simplify[

$$\mathrm{EQ3}\,/.\,\mathrm{C1}\rightarrow \frac{\tau\left(\pi\gamma^2 - 6gQ\eta\rho - 6gQ\eta\rho\,\mathrm{Log}\left[-E^{-1+\frac{\sqrt{Ao}\sqrt{\pi}\gamma}{gQ\rho\tau}}\left(\sqrt{Ao}\sqrt{\pi}\gamma - gQ\rho\tau\right)\right]\right)}{\pi\gamma^2}\;]$$

$$-1+\frac{\sqrt{\pi}\gamma\sqrt{A[t]}}{gQ\rho\tau} == \mathrm{ProductLog}\left[\frac{E^{\frac{\pi t\gamma^2 + 6\sqrt{Ao}\sqrt{\pi}\gamma\eta - (\pi\gamma^2 + 6gQ\eta\rho)\tau}{6gQ\eta\rho\tau}}\left(\sqrt{Ao}\sqrt{\pi}\gamma - gQ\rho\tau\right)}{gQ\rho\tau}\right]$$

we use the definition of ProductLog again to solve for A[t]

From EQ8 we have $\quad \omega = -1 + \dfrac{\sqrt{\pi}\,\gamma\sqrt{A[t]}}{gQ\rho\tau}\quad$ and $\quad z = \dfrac{E^{\frac{\pi t\gamma^2 + 6\sqrt{Ao}\sqrt{\pi}\gamma\eta - (\pi\gamma^2 + 6gQ\eta\rho)\tau}{6gQ\eta\rho\tau}}\left(\sqrt{Ao}\sqrt{\pi}\,\gamma - gQ\rho\tau\right)}{gQ\rho\tau}$

Substituting ω and z to the definition of ProductLog leads to,

EQ6 =

$$\mathrm{EQ5}\,/.\,\left\{z\rightarrow\frac{E^{\frac{\pi t\gamma^2 + 6\sqrt{Ao}\sqrt{\pi}\gamma\eta - (\pi\gamma^2 + 6gQ\eta\rho)\tau}{6gQ\eta\rho\tau}}\left(\sqrt{Ao}\sqrt{\pi}\gamma - gQ\rho\tau\right)}{gQ\rho\tau}\,,\,\omega\rightarrow -1+\frac{\sqrt{\pi}\gamma\sqrt{A[t]}}{gQ\rho\tau}\right\};$$

Now, EQ6 can be solved for A[t]

SOLN = Solve[EQ6, A[t]];

```
InverseFunction::ifun : Warning: Inverse functions are being used. Values
    may be lost for multivalued inverses.

Solve::ifun :
  Inverse functions are being used by Solve, so some solutions may not be found.
```

A simplified form of the above solution is separated from SOLN,

EQ10 = A[t] == Simplify[SOLN[[1, 1, 2]]]

$$A[t] == \frac{g^2\, Q^2\, \rho^2\, \tau^2 \left(1 + \mathrm{ProductLog}\left[E^{\frac{\pi t \gamma^2 + 6\sqrt{Ao}\,\sqrt{\pi}\,\gamma\,\eta - (\pi\gamma^2 + 6gQ\eta\rho)\,\tau}{6gQ\eta\rho\tau}} \left(-1 + \frac{\sqrt{Ao}\,\sqrt{\pi}\,\gamma}{gQ\rho\,\tau}\right)\right]\right)^2}{\pi\,\gamma^2}$$

Using substitution for the constant terms $U = \rho\, g$; $W = \pi\,\gamma^2$;

$$\mathrm{EQ11} = A[t] == \frac{Q^2\, U^2\, \tau^2 \left(1 + \mathrm{ProductLog}\left[E^{\frac{t W + 6\sqrt{Ao}\,\sqrt{W}\,\eta - (W + 6UQ\eta)\,\tau}{6UQ\eta\,\tau}} \left(-1 + \frac{\sqrt{Ao}\,\sqrt{W}}{UQ\,\tau}\right)\right]\right)^2}{W}$$

$$A[t] == \frac{Q^2\, U^2\, \tau^2 \left(1 + \mathrm{ProductLog}\left[E^{\frac{t W + 6\sqrt{Ao}\,\sqrt{W}\,\eta - (6Q\eta U + W)\,\tau}{6Q\eta U\,\tau}} \left(-1 + \frac{\sqrt{Ao}\,\sqrt{W}}{QU\,\tau}\right)\right]\right)^2}{W}$$

Drop Formation Under Non-evaporative Condition

Drop detachment is induced by reduction of cross-sectional area and eventual pinching. At the drop element where pinching occurs the cross-sectional area A[t]goes to zero in finite time. This reduces EQ11 to,

$$\mathrm{EQ12} = 0 == 1 + \mathrm{ProductLog}\left[E^{\frac{t W + 6\sqrt{Ao}\,\sqrt{W}\,\eta - (W + 6UQ\eta)\,\tau}{6UQ\eta\,\tau}} \left(-1 + \frac{\sqrt{Ao}\,\sqrt{W}}{UQ\,\tau}\right)\right]$$

$$0 == 1 + \mathrm{ProductLog}\left[E^{\frac{t W + 6\sqrt{Ao}\,\sqrt{W}\,\eta - (6Q\eta U + W)\,\tau}{6Q\eta U\,\tau}} \left(-1 + \frac{\sqrt{Ao}\,\sqrt{W}}{QU\,\tau}\right)\right]$$

From EQ12 we have $\omega = -1$, and $z = E^{\frac{t W + 6\sqrt{Ao}\,\sqrt{W}\,\eta - (W + 6UQ\eta)\tau}{6UQ\eta\tau}} \left(-1 + \frac{\sqrt{Ao}\,\sqrt{W}}{UQ\tau}\right)$.

By the definition of ProductLog (EQ5) we have,

$$\mathrm{EQ13} = \mathrm{EQ5}\ /.\ \left\{\omega \to -1,\ z \to E^{\frac{t W + 6\sqrt{Ao}\,\sqrt{W}\,\eta - (W + 6UQ\eta)\,\tau}{6UQ\eta\,\tau}} \left(-1 + \frac{\sqrt{Ao}\,\sqrt{W}}{UQ\,\tau}\right)\right\}$$

$$E^{\frac{t W + 6\sqrt{Ao}\,\sqrt{W}\,\eta - (6Q\eta U + W)\,\tau}{6Q\eta U\,\tau}} \left(-1 + \frac{\sqrt{Ao}\,\sqrt{W}}{QU\,\tau}\right) == -\frac{1}{E}$$

The time of pinching is obtained by solving EQ13 for t,

```
EQ14 = Solve[EQ13, t] ;
```

```
Solve::ifun :
    Inverse functions are being used by Solve, so some solutions may not be found.
```

The simplified form of t is separated from EQ14

```
EQ15 = t == Simplify[EQ14[[1, 1, 2]]]
```

$$t == -\frac{6\sqrt{Ao}\,\eta}{\sqrt{W}} + \tau - \frac{6\,Q\eta\,U\,\tau\,\text{Log}\left[1 - \frac{\sqrt{Ao}\,\sqrt{W}}{QU\tau}\right]}{W}$$

Which can be simplified by dividing the first and third terms by $\dfrac{6\sqrt{Ao}\,\eta}{\sqrt{W}}$,

$$EQ16 = t == \tau - \frac{6\sqrt{Ao}\,\eta}{\sqrt{W}}\left(1 + \frac{Q\,U\,\tau\,\text{Log}\left[1 - \frac{\sqrt{Ao}\,\sqrt{W}}{QU\tau}\right]}{\sqrt{Ao}\,\sqrt{W}}\right)$$

$$t == \tau - \frac{6\sqrt{Ao}\,\eta\left(1 + \frac{QU\tau\,\text{Log}\left[1 - \frac{\sqrt{Ao}\,\sqrt{W}}{QU\tau}\right]}{\sqrt{Ao}\,\sqrt{W}}\right)}{\sqrt{W}}$$

The time of detachment also satisfy another additional condition $\partial_\tau\, t = 0$ which leads to,

$$EQ16 = \text{Simplify}[D[EQ16, \tau]]$$

$$0 == 1 + \frac{6\sqrt{Ao}\,Q\,U\,\eta}{\sqrt{W}\left(\sqrt{Ao}\,\sqrt{W} - Q\,U\,\tau\right)} - \frac{6\,Q\,U\,\eta\,\text{Log}\left[1 - \frac{\sqrt{Ao}\,\sqrt{W}}{QU\tau}\right]}{W}$$

Which again can be simplified with $\Omega = \dfrac{\sqrt{Ao\,W}}{Q\,U}$

$$0 == 1 + \frac{6\sqrt{Ao}\,\eta}{\sqrt{W}}\left(\frac{1}{\tau c - \Omega} + \frac{1}{\Omega}\,\text{Log}\left[1 - \frac{\sqrt{Ao}\,\sqrt{W}}{QU\tau}\right]\right)$$

The simplified form of EQ16 is an implicit solution for the time to detachment.

NOTE: In MATHEMATICA Log[ ] stands for Natural Logarithm.

■ Drop Formation under Evaporative Condition

Evaporation from a Hemispherical Drop

When a drop is fed by a constant flux Q, at any given time τ (in the Lagrangian coordinate) the volume of liquid suspended below the τ element in the absense of evaporation evolves as,

$$V == Q\tau$$

Assuming, the drop has a hemispherical shape (see the Scientifi Notebook for justification), the drop radius volves as,

$$Ro = \sqrt[3]{\frac{3\,Q\,\tau}{2\,\pi}}$$

The instantaneous rate of evaporation from a droplet of radius rb can be given Fick's law (assuming isothermal diffusion),

$$EQ17 = \partial_t \; rb \; == \; -\frac{D}{\rho} \; \partial_r \; C \; \Big|_{r=rb} = -\frac{D}{\rho} \; \frac{\Delta P_v}{rb \, R \, T}$$

Integrating EQ17,

$$rb^2 = \frac{D}{\rho} \; \frac{\Delta P_v}{rb \, R \, T} \; \tau + C$$

the constant of integration C is obtained from the initial condition (initial radius in the absence of evaporation),

$$rb^2 = \frac{D}{\rho} \; \frac{\Delta P_v}{rb \, R \, T} \; \tau + \left(\frac{3 Q \tau}{2 \pi}\right)^{\frac{2}{3}}$$

The radius of a hemisphere evolves as it evaporates in accordance to:

$$R = \sqrt{\frac{D}{\rho} \; \frac{\Delta P_v}{rb \, R \, T} \; \tau + \left(\frac{3 Q \tau}{2 \pi}\right)^{\frac{2}{3}}}$$

And the volume of the hemisphere evolves as,

$$V == \frac{2}{3} \pi \left(\frac{2 \, D \, \Delta P \, \tau}{R T \rho} + \left(\frac{3}{2\pi}\right)^{2/3} (Q \tau)^{2/3}\right)^{3/2}$$

■ Dripping under Evaporative Conditions

The net flux can be back calculated from the volume evolution equation as

$$Q_e = \frac{V}{\tau}$$

$$Q_e == \frac{2 \pi \left(\frac{2 D \Delta P \tau}{R T \rho} + \left(\frac{3}{2\pi}\right)^{2/3} (Q \tau)^{2/3}\right)^{3/2}}{3 \tau}$$

Using the following variable transformations a, and a the net flux can be written as

$$Q_e == \frac{2 \pi \left(M \tau + N \, (\tau)^{2/3}\right)^{3/2}}{3 \tau}$$

This corrected flux is what forms the weight of the drop, substituting in EQ11 we obtain

$$EQ18 = EQ11 \; / . \; Q \to \frac{2 \pi \left(M \tau + N \, (\tau)^{2/3}\right)^{3/2}}{3 \tau}$$

$$A[t] == \frac{1}{9 \, W} \Bigg(4 \pi^2 \, U^2 \; (N \, \tau^{2/3} + M \, \tau)^3$$

$$\left(1 + \text{ProductLog}\left[E^{\frac{t \, H + 6 \sqrt{A_o} \; \sqrt{W} \; \eta - (6 \, Q \, \eta \, U + W) \, \tau}{6 \, Q \, \eta \, \tau}}\left(-1 + \frac{3 \sqrt{A_o} \; \sqrt{W}}{2 \pi \, U \; (N \, \tau^{2/3} + M \, \tau)^{3/2}}\right)\right]\right)^2\Bigg)$$

At the time of pinching the cross-sectional area goes to zero, A[t]=0, leading to

$$1 + \text{ProductLog}\left[E^{\frac{tW + 6\sqrt{Ao}\,\sqrt{W}\,\eta - (6Q\eta U + W)\tau}{6Q\eta U\tau}}\left(-1 + \frac{3\sqrt{Ao}\,\sqrt{W}}{2\pi U\,(N\tau^{2/3} + M\tau)^{3/2}}\right)\right] == 0$$

with $\omega = -1$ and $z = E^{\frac{tW + 6\sqrt{Ao}\,\sqrt{W}\,\eta - (6Q\eta U + W)\tau}{6Q\eta U\tau}}\left(-1 + \frac{3\sqrt{Ao}\,\sqrt{W}}{2\pi U\,(N\tau^{2/3} + M\tau)^{3/2}}\right)$,

EQ19 = EQ5 . $z \to E^{\frac{tW + 6\sqrt{Ao}\,\sqrt{W}\,\eta - 6Q\eta U + W\tau}{6Q\eta U\tau}} \quad -1 + \frac{3\sqrt{Ao}\,\sqrt{W}}{2\pi U\,N\tau^{2\,3} + M\tau}^{3\,2}$, $\omega \to -1$

$$E^{\frac{tW + 6\sqrt{Ao}\,\sqrt{W}\,\eta - (6Q\eta U + W)\tau}{6Q\eta U\tau}}\left(-1 + \frac{3\sqrt{Ao}\,\sqrt{W}}{2\pi U\,(N\tau^{2/3} + M\tau)^{3/2}}\right) == -\frac{1}{E}$$

EQ19 can be solved for the time of pinching t,

EQ20 = Solve[EQ19, t] ;

```
Solve::ifun :
   Inverse functions are being used by Solve, so some solutions may not be found.
```

EQ21 = EQ20[[1, 1, 2]]

$$\frac{6\sqrt{Ao}\,\sqrt{W}\,\eta + 6Q\eta U\tau - W\tau + 6Q\eta U\tau\,\text{Log}\left[\frac{1}{E} - \frac{3\sqrt{Ao}\,\sqrt{W}}{2E\pi U\,(N\tau^{2/3} + M\tau)^{3/2}}\right]}{W}$$

Differentiating with respect to τ

D[EQ21, τ]

$$-\frac{1}{W}\left(-W + 6QU\eta + \frac{27\sqrt{Ao}\,Q\sqrt{W}\,\eta\,(M + \frac{2N}{3\tau^{1/3}})\,\tau}{2E\pi\,(N\tau^{2/3} + M\tau)^{5/2}\left(\frac{1}{E} - \frac{3\sqrt{Ao}\,\sqrt{W}}{2E\pi U\,(N\tau^{2/3} + M\tau)^{3/2}}\right)} + \right.$$

$$\left. 6QU\eta\,\text{Log}\left[\frac{1}{E} - \frac{3\sqrt{Ao}\,\sqrt{W}}{2E\pi U\,(N\tau^{2/3} + M\tau)^{3/2}}\right]\right)$$

EQ 21 is a general solution for drop formation. The solution of non-evaporative condition can obtained as a special cse solution where M is zero,

EQ22 = EQ21 /. M -> 0

$$-\frac{1}{W}\left(-W + 6QU\eta - \frac{18\sqrt{Ao}\,QU\sqrt{W}\,\eta}{3\sqrt{Ao}\,\sqrt{W} - 2N\pi U\sqrt{N\tau^{2/3}}\,\tau^{2/3}} - \right.$$

$$\left. 6QU\eta\left(1 + \text{Log}[2] - \text{Log}\left[2 - \frac{3\sqrt{Ao}\,\sqrt{W}}{\pi U\,(N\tau^{2/3})^{3/2}}\right]\right)\right)$$

$$1 + \frac{18\sqrt{Ao}\,QU\eta}{\sqrt{W}\,(3\sqrt{Ao}\,\sqrt{W} - 2\pi U\,(N\tau^{2/3})^{3/2})} + \frac{6QU\eta\,\text{Log}[2]}{W} - \frac{6QU\eta\,\text{Log}\left[2 - \frac{3\sqrt{Ao}\,\sqrt{W}}{\pi U\,(N\tau^{2/3})^{3/2}}\right]}{W}$$

■ Drop Volume under Evaporative Conditions

The drop volume under evaporative conditions is obtained by integrating the net flux equation,

$$\int_0^{\tau C} \frac{2\,\pi}{3}\; \frac{1}{\tau}\; (M\,\tau + N\,\tau^{2/3})^{\,3/2}\; d\tau$$

General::spell1 :
  Possible spelling error: new symbol name "τC" is similar to existing symbol "τ".

Integrate::gener : Unable to check convergence

$$-\frac{32\,N^3\,\pi\,(N\,\tau C^{2/3})^{\,3/2}}{315\,M^3\,\tau C} + \frac{4\,\pi\,(N + M\,\tau C^{1/3})^{\,2}\,(8\,N^2 - 20\,M\,N\,\tau C^{1/3} + 35\,M^2\,\tau C^{2/3})\,\sqrt{N\,\tau C^{2/3} + M\,\tau C}}{315\,M^3\,\tau C^{1/3}}$$

Appendix B: 4/15/99 $\boxed{\text{Dani Or}}$

This short fortran90 code was compiled using the Microsoft FORTRAN PowerStation 4.0 compiler, and run on a 200 MHz Pentium Pro personal computer running Windows NT (4.00). This code is for this single use only, it will not be used by other researchers or for other tasks. The code was validated in using MATHEMATICA 3.0 as described in Appendix C. Input instructions are as follows: The parameters γ, L, and β are specified in the input file, whereas the vapor pressure, "P" in the code (used to calculate the diffusion coefficient for the evaporation component) is hard-coded; the program must be re-compiled when it is modified. Units for the inputs and constants are specified in the main text.

NOTE: Corresponding FORTRAN 90 source code file and executable file are attached as <u>DRIPPING.F90</u> and <u>DRIPPING.EXE</u> respectively. Example input and output files are attached as <u>INPUT.TXT</u> and <u>OUTPUT.TXT</u> respectively

```
! A GENERAL PROGRAM TO CALCULATE THE CRITICAL TAU FOR DROP DETACHMENT FROM
!     GROOVE DEFINED BY CORNER ANGLE (GAMA), GROOVE DEPTH (L) AND RATIO OF
!                    PLANEWIDTH: GROOVE DEPTH (BETA)
USE MSFLIB
USE PORTLIB
IMPLICIT NONE

!*******************************************************
!*                                                    *
!*              VARIABLE DECLARATION                  *
!*                                                    *
!*******************************************************
REAL(8),EXTERNAL::FNC,DERIV
CHARACTER(30)        ::FILE1,FILE2,VERSION
REAL(8)              ::REALTIME,RHO,G,SIGMA,ETA,DNOT,R,T,BETA,GAMA
REAL(8)              ::BETAS,D,F,MUC,MO,U,W,PSAT,SING,SING1,SLOPE
REAL(8)              ::DMU,MU,MU1,DP,AO,Q,M,N,HAMAK,L,PAI,E,P
REAL(8)              ::RAD,DEP,AOC,AOCC,AF1,AF2,KC,KF,QC,QF

WRITE(*,'(1X,//,1A,)')  '   CRTICAL TIME FOR DROP DROP DETACHMENT'
WRITE(*,'(1X,1A,/)')    '       UNDER EVAPORATIVE CONDITIONS'
WRITE(*,'(1X,1A,/)')    '-------------------------------------------'

REALTIME=TIMEF()
PRINT*, 'ENTER OUTPUT FILE NAME'
READ(*,*) FILE1
PRINT*, 'ENTER INPUT FILE NAME'
READ(*,*) FILE2
OPEN(UNIT=10,FILE=FILE1,STATUS='UNKNOWN')
OPEN(UNIT=20,FILE=FILE2,STATUS='UNKNOWN')

!************************************************************
!*                                                        *
!*                     CONSTANTS                          *
!*                                                        *
!************************************************************
```

```
PAI    = 3.14159265359          ! PAI
E      = 2.71828182846          ! BASE OF NATURAL LOGARITHM
RHO    = 998                    ! DENSITY OF WATER
G      = 9.8                    ! GRAVITATIONAL ACCELERATION
SIGMA = 7.29/10.**2             ! SURFACE TENSION
ETA    = 1./10.0**3             ! VISCOSITY
DNOT  = 2.13/10.0**5            ! BINARY DIFFUSION COEFFICIENT
R      = 462.                   ! GAS CONSTANT
T      = 293.                   ! TEMPERATURE
HAMAK = 1.9/10.0**19            ! HAMMAKER CONSTANT SOLID,LIQUID VAPOR
PSAT  = 2337                    ! SATURATED VAPOR PRESSURE
P      = 9.0*10**4              ! PRESSURE
!***********************************************************
!*                                                       *
!*                GEOMETRIC VARIABLES                     *
!*                                                       *
!***********************************************************

READ(20,*) GAMA                 ! CORNER ANGLE
READ(20,*) L                    ! GRROVE DEPTH
READ(20,*) BETA                 ! WIDTH TO DEPTH RATIO

!***********************************************************
!*                                                       *
!*                DERIVED CONSTANTS                       *
!*                                                       *
!***********************************************************
BETAS = 0.966*EXP(0.051*GAMA*180./PAI)+7.89
F      = 1./TAN(GAMA/2.) - (PAI-GAMA)/2.
MUC    =   SIGMA*COS(GAMA/2.) /(L*TAN(GAMA/2.))
D      = -DNOT*((10.0**5)/P)*(T/273.15)**1.8
U      = RHO*G
W      = PAI*SIGMA**2
MO     = RHO*R*T

!***********************************************************
!*                                                       *
!*                OUTPUT HEADERS                          *
!*                                                       *
!***********************************************************

WRITE(10,'(1X,4A20)') 'MU','TAU','FUNCTION','SLOPE','ITERATIONS'
WRITE(*,'(1X,/,1A,/)') '   THE FOLLOWING INPUT PARAMETERS ARE BEING USED'
WRITE(*,'(1X,1A20,1F20.5,/)') 'ANGLE= ',   GAMA*180./PAI
WRITE(*,'(1X,1A20,1F20.5,/)') 'LENGTH= ', L
WRITE(*,'(1X,1A20,1F20.5,//)') 'BETA= ', BETA
PAUSE 'PRESS ENTER TO CONTINUE, Ctrl+C TO STOP'

!***********************************************************
!*                                                       *
!*                INTITIALIZATION                         *
!*                                                       *
!***********************************************************
MU      = 0.                    ! INITIAL CHEMICAL POTENTIAL
DMU     = 5                     ! STEP SIZE
SING    = 1./10.**2             ! PAST TAU
SING1   = 5./10.**3             ! PAST PAST TAU
```

```
!***********************************************************
!*                                                        *
!*                    MAIN LOOP                           *
!*                                                        *
!***********************************************************

DO
      MU1      = MU                                 ! PAST TAU
      MU       = MU+DMU                             ! PAST PAST TAU
      DP       = PSAT*(1.-EXP(-MU*RHO/(R*T)))       ! PRESSURE GRADIENT


      !*****************
      !*     CORNER    *
      !*****************
      RAD      = SIGMA/MU                           ! LV INTERFACE CURVATURE
      AOC      = (L**2.)*TAN(GAMA/2.)               ! AREA AFTER FILLING
      AOCC  = RAD**2.*F                             ! AREA BEFORE FILLING
      KC       = (RAD**2.)*RHO*G/(BETAS*ETA)        ! CONDUCTIVITY


      !*****************
      !*     FILM      *
      !*****************
      DEP      = (HAMAK/(6.*PAI*MU))**(1./3.)                        ! FILM THICKNESS
      AF1      = DEP*(L*BETA+2.*(L/COS(GAMA/2.)-RAD/TAN(GAMA/2.)))   ! AFTER FILLING
      AF2      = DEP*(L*BETA+2.*L*TAN(GAMA/2.))                      ! BEFORE FILLING
      KF       = DEP**2.*RHO*G/(3.*ETA)                             ! CONDUCTIVITY


      !*****************
      !* BEFORE FILLING *
      !*****************
      IF (MU.GT.MUC) THEN
            QC       = AOCC*KC
            QF       = AF1*KF
            AO       = AOCC


      !*****************
      !*  AFTER FILLING *
      !*****************
      ELSE
            QC       = AOC*KC
            QF       = AF2*KF
            AO       = AOC
      END IF

      Q        = QC+QF
      M        = 2.*D*DP/MO
      N        = (3.*Q/(2.*PAI))**(2./3.)
      CALL SOLV(AO,Q)
            !*****************
      !*STEP ADAPTATION *
      !*****************
      IF (SLOPE.GE.0002.) DMU=0.500
      IF (SLOPE.GE.0010.) DMU=0.200
      IF (SLOPE.GE.0100.) DMU=0.010
      IF (SLOPE.GE.0400.) DMU=0.005
      IF (SLOPE.GE.0600.) DMU=0.0001
      IF (SLOPE.GE.2000.) DMU=0.00001
      IF (SLOPE.GE.2000.) EXIT
```

```
END DO

REALTIME=TIMEF()
WRITE(*,'(///,1X,A,F5.2)') 'Real Time Elapsed :=',REALTIME
WRITE(10,'(///,1X,1A20,1F20.5)') 'ANGLE= ', GAMA*180./PAI
WRITE(10,'(1X,1A20,1F20.5)') 'LENGTH= ', L
WRITE(10,'(1X,1A20,1F20.5)') 'BETA= ', BETA
WRITE(10,'(///,1X,A, I3,A,F5.2)') 'Real Time Elapsed
:=',INT(REALTIME/60),':',REALTIME-(INT(REALTIME)/60)*60.


!*******************************************************
!*                                                    *
!*              INTERNAL FUNCTIONS                     *
!*                                                    *
!*******************************************************

CONTAINS

FUNCTION FCN(TAU,AO,Q)
REAL(8):: TAU,AO,Q,FCN
FCN= -((-W + 6.*Q*U*ETA -(9.*DSQRT(Ao)*Q*U*DSQRT(W)*ETA*(2.*N +   &
     3*M*TAU**(1./3.)))/ ((N + M*TAU**(1./3.))*  (3*DSQRT(Ao)*   &
     DSQRT(W)-2.*PAI*U*(N + M*TAU**(1./3.))* TAU**(2./3.)*       &
     DSQRT(N*TAU**(2./3.) + M*TAU))) -6.*Q*U*ETA* (1. + LOG(2.)-&
     DLOG(2. - (3.*DSQRT(Ao)*DSQRT(W))/(PAI*U*(N*TAU**(2./3.) + &
     M*TAU)**1.5))))/W)
END FUNCTION FCN

SUBROUTINE SOLV(AO,Q)
      INTEGER      ::FLAG
      REAL(8)  ::TAU,TAU1,TR1,AO,Q,DS,TR,DELTA,BRAKE,STEP
      !
      ! INITIAL TAU: SHOOT BY FIVE TIMES THE LAST DIFFERENCE IN TAU
      ! USE LARGER ESTIMATES TO ACCOUNT FOR THE INCREASING SLOPE
      !
      TAU=SING+DABS(SING-SING1)*(5.)           !
      DS= DABS(SING-SING1)/(MU*10.)    !5./((10.**4))

      IF (GAMA.GE.PAI/1.8) THEN
           TAU=SING+DABS(SING-SING1)*(10.)         !
           DS= DABS(SING-SING1)/(MU*30.)    !5./((10.**4))
      END IF
      FLAG=0
      TR=FCN(TAU,AO,Q)
      TR1=0.
      BRAKE =1./10.
      STEP=1.
      DO
           TR=FCN(TAU,AO,Q)
           SLOPE=(TAU-SING)/(MU-MU1)
           IF((TR.LE.BRAKE).OR.(ABS(TAU-TAU1).LT.1./10.**6)) THEN
           WRITE(10,'(1X,1F20.4,3E20.10,1I20)') MU, TAU,TR,SLOPE,FLAG
           WRITE(* ,'(1X,1F10.1,E22.16,3E12.5,1I8)') MU,TAU,TR,TR1,SLOPE,FLAG
           EXIT
           END IF
           IF (TR.LT.(MU-1.)/MU) THEN
           DELTA= -(.1/MU)*TR*((TAU-TAU1)/(TR-TR1)) !(TR-TRR)
           ELSE
```

```
            DELTA=-DS*STEP
            END IF
            TAU1=TAU
            TAU=TAU + DELTA
            FLAG=FLAG+1
            TR1=TR
      END DO
      SING1=SING
      SING=TAU
END SUBROUTINE SOLV

END
```

Appendix C (part 1) 4/15/99

Cross check of FORTRAN calculations with MATHEMATICA

For a groove geometry given below, time to drop detachment were calculated using MATHEMATICA. The results agree with the FORTRAN calculations.

Groove Geometry:

g	60°
L	0.002 [m]
b	1

μ [Pa]	FORTRAN 90	MATHEMATICA 3.0	FOR/MATH
60	2.611827348E-02	2.597557246E-02	1.005493662
100	1.202271999E-01	1.200753637E-01	1.001264507
300	3.252505750E+00	3.252342701E+00	1.000050133
500	1.538334198E+01	1.538316504E+01	1.000011502
1000	1.826626636E+02	1.826622120E+02	1.000002472
1175.1000	8.846857637E+02	8.846660957E+02	1.000022232
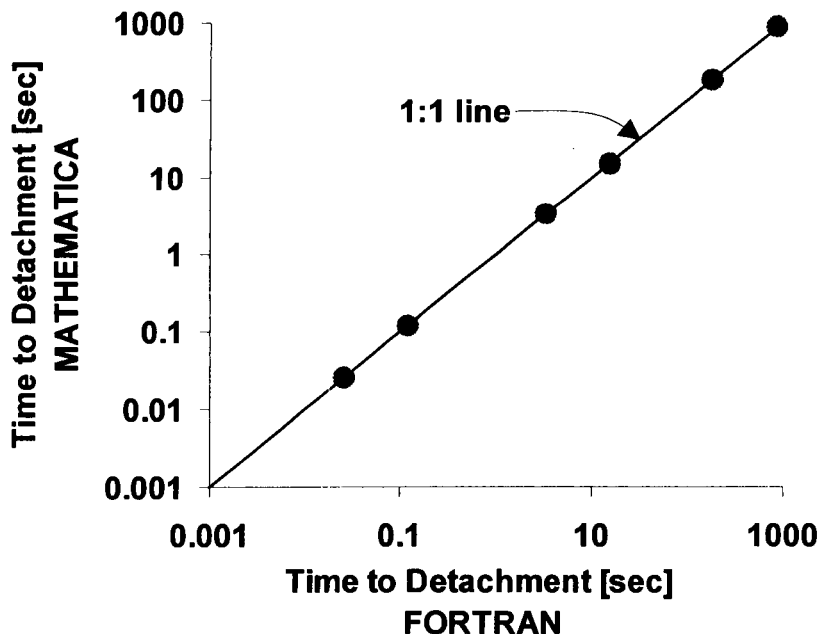
FIG C1. Cross Check of FORTRAN results with MATHEMATICA

Selected Output points from FORTRAN Program

MU	TAU	FUNCTION	SLOPE	ITERATIONS
5	1.828455693E-04	5.17E-01	-1.96E-03	358
10	5.759481878E-04	5.50E-01	7.86E-05	533
20	2.050545486E-03	6.09E-01	1.71E-04	625
30	4.463629278E-03	6.49E-01	2.65E-04	964
40	7.823564020E-03	6.79E-01	3.60E-04	1285
50	1.213384190E-02	7.03E-01	4.55E-04	1595
60	2.611827346E-02	7.62E-01	1.19E-03	2553[1]
70	4.136056378E-02	7.89E-01	1.64E-03	2620
80	6.164599685E-02	8.12E-01	2.16E-03	3047
90	8.769526061E-02	8.31E-01	2.76E-03	3468
100	1.202271999E-01	8.46E-01	3.42E-03	3886
200	9.611642659E-01	9.19E-01	1.41E-02	7971
300	3.252505750E+00	9.45E-01	3.21E-02	11999
400	7.764511097E+00	9.58E-01	5.83E-02	16010
500	1.538334198E+01	9.66E-01	9.42E-02	20014
600	2.725886364E+01	9.72E-01	1.44E-01	24011
700	4.509712338E+01	9.75E-01	2.14E-01	28001
800	7.179550179E+01	9.77E-01	3.23E-01	31979
900	1.130580617E+02	9.79E-01	5.13E-01	35935
1000	1.826620636E+02	9.79E-01	9.19E-01	39835
1090.0	3.076519604E+02	9.78E-01	2.04E+00	43161
1090.5	3.087073206E+02	9.78E-01	2.11E+00	53613
1091.0	3.097691563E+02	9.78E-01	2.12E+00	43739
1091.5	3.108375365E+02	9.78E-01	2.14E+00	43760
1100.5	3.312752922E+02	9.78E-01	2.40E+00	44121
1149.5	5.171751972E+02	9.76E-01	6.29E+00	46038
1150.0	5.203698966E+02	9.76E-01	6.39E+00	46056
1150.5	5.236164035E+02	9.76E-01	6.49E+00	46074
1169.9	7.276163976E+02	9.72E-01	1.88E+01	46822
1170.1	7.314568938E+02	9.72E-01	1.92E+01	46824
1170.3	7.353849240E+02	9.72E-01	1.96E+01	46826
1175.1	8.846857637E+02	9.70E-01	5.53E+01	46151
1175.3	8.970800926E+02	9.70E-01	6.20E+01	45934
1175.5	9.113253983E+02	9.70E-01	7.12E+01	45599
1175.7	9.284185029E+02	9.69E-01	8.55E+01	45017
1175.9	9.507926544E+02	9.69E-01	1.12E+02	43748
1175.91	9.521517863E+02	9.69E-01	1.36E+02	58428
1175.92	9.535445983E+02	9.69E-01	1.39E+02	46985
1175.93	9.549735378E+02	9.69E-01	1.43E+02	46975
1175.94	9.564413667E+02	9.69E-01	1.47E+02	46963
1175.95	9.579512138E+02	9.69E-01	1.51E+02	46950
1176.1283	1.010196697E+03	9.68E-01	2.03E+03	46059

ANGLE=	60
LENGTH=	0.002
BETA=	1
Computation Time:=	11:23.0

---

[1] Shaded points are used for cross-checking with MATHEMATICA

Appendix C (Part 2) 4/15/99

Illustrative Example: Dripping Under Evaporative Conditions

Note Corresponding MATHEMATICA 3.0 file is attached as APPENDIXC.NB

■ Constants

■ Physical Constants [MKS system]

$$\rho = 998;$$
$$g = 9.8;$$
$$\sigma = 7.29 \ 10^{-2};$$
$$\eta = 10^{-3};$$
$$DO = 2.13 \ 10^{-5};$$
$$R = 462;$$
$$T = 293;$$
$$Psat = 2337;$$
$$P = 9 \ 10^{4};$$
$$Aslv = 1.9 \ 10^{-19};$$

■ Fracture Geometry

$$\gamma = \frac{\pi}{3};$$
$$L = 2 \ 10^{-3};$$
$$\beta = 1;$$

■ Derived Constants

$$\beta s = 0.966 \ e^{0.051 \ \gamma \ 180/\pi} + 7.89;$$
$$U = \rho \ g;$$
$$W = \pi \ \sigma^{2};$$
$$DD = DO \ \frac{10^{5}}{P} \left(\frac{T}{273.15}\right)^{1.8};$$

$$F = \frac{1}{Tan[\gamma / 2]} - \frac{\pi - \gamma}{2};$$
$$AOCo = L^{2} \ Tan[\gamma / 2];$$
$$\mu c = \frac{\sigma}{L} \ \frac{Cos[\gamma / 2]}{Tan[\gamma / 2]};$$
$$MO = \rho \ R \ T;$$

■ Flow Regimes at Matric Potential of μ [Pa]

■ Flow in Corner

$$r = \frac{\sigma}{\mu} \, ;$$

$$AOCf = F \, r^2 \, ;$$

$$Kc = \frac{\rho \, g}{\beta s \, \eta} \, r^2 \, ;$$

$$AO = AOCf \, ;$$

■ Flow in Film

$$h = \sqrt[3]{\frac{Aslv}{6 \, \pi \, \mu}} \, ;$$

$$Afl = h \left(L \beta + 2 \left(\frac{L}{Cos[\gamma / 2]} - \frac{r}{Tan[\gamma / 2]} \right) \right) \, ;$$

$$Af2 = h \, (L \beta + 2 \, L \, Tan[\gamma / 2]) \, ;$$

$$Kf = \frac{\rho \, g}{3 \, \eta} \, h^2 \, ;$$

■ Combined Flow

Note: Calculations of AO above as well as Qc and Qf below are done for all matric potentials less than (drier than) the critical matric potential (μc)

$$Qc = AO \, Kc \, ;$$

$$Qf = Afl \, Kf \, ;$$

$$Q = Qc + Qf \, ;$$

■ Adjustments for Flow under Evaporative Conditions

$$\Delta P = Psat \left(1 - Exp\left[-\frac{\mu \, \rho}{R \, T} \right] \right) \, ;$$

$$M = -\frac{2 \, DD \, \Delta P}{MO} \, ;$$

$$NN = \left(\frac{3 \, Q}{2 \, \pi} \right)^{\frac{2}{3}} \, ;$$

$$EQUATION = -\frac{1}{W} \left| -W + 6 \, Q \, U \, \eta + \frac{27 \sqrt{AO} \, Q \sqrt{W} \, \eta \, (M + \frac{2 \, NN}{3 \, \tau^{1/3}}) \, \tau}{2 \, E \, \pi \, (NN \, \tau^{2/3} + M \, \tau)^{5/2} \left(\frac{1}{E} - \frac{3 \sqrt{AO} \, \sqrt{W}}{2 \, E \, \pi \, U \, (NN \, \tau^{2/3} + M \, \tau)^{3/2}} \right)} + \right.$$

$$\left. 6 \, Q \, U \, \eta \, Log\left[\frac{1}{E} - \frac{3 \sqrt{AO} \, \sqrt{W}}{2 \, E \, \pi \, U \, (NN \, \tau^{2/3} + M \, \tau)^{3/2}} \right] \right| \, ;$$

■ Test 1: μ=60 Pa

```
EQ1 = EQUATION == 0 /. {μ → 60};
```

```
t1 = FindRoot[EQ1, {t, 0.026}, MaxIterations → 100000, DampingFactor → 0.001]
```

$\{\tau \rightarrow 0.0259756\}$

```
FUNCTION = N[EQUATION /. {μ → 60, t → t1[[1, 2]]}]
```

9.99663×10^{-7}

```
N[t1[[1, 2]], 16]
```

0.02597557246466978

■ Test 2: μ=100 Pa

```
EQ2 = EQUATION == 0 /. {μ → 100};
```

```
t2 = FindRoot[EQ2, {t, 0.12023}, MaxIterations → 200000, DampingFactor → 0.01]
```

$\{\tau \rightarrow 0.120075\}$

```
FUNCTION = EQUATION /. {μ → 100, t → t2[[1, 2]]}
```

9.93299×10^{-7}

```
N[t2[[1, 2]], 16]
```

0.1200753637039623

■ Test 3: μ=300 Pa

```
EQ3 = EQUATION == 0 /. {μ → 300};
```

```
t3 = FindRoot[EQ3, {t, 3.2525}, MaxIterations → 200000, DampingFactor → 0.0001]
```

```
FindRoot::frmp :
 Machine precision is insufficient to achieve the accuracy 1.00000000000000066`*^-6.
```

$\{\tau \rightarrow 3.25234\}$

```
FUNCTION = EQUATION /. {μ → 300, t → t3[[1, 2]]}
```

0.00314703

```
N[t3[[1, 2]], 16]
```

3.25234270089859

■ **Test 4:** μ=500 Pa

EQ4 = EQUATION == 0 /. {μ → 500};

τ4 = FindRoot[EQ4, {τ, 15.38334}, MaxIterations → 20000, DampingFactor → 0.001]

FindRoot::fmp :
 Machine precision is insufficient to achieve the accuracy 1.00000000000000066`*^-6.

{τ → 15.3832}

FUNCTION = EQUATION /. {μ → 500, τ → τ4[[1, 2]]}

0.00242057

N[τ4[[1, 2]], 16]

15.38316503951751

■ **Test 5:** μ=1000 Pa

EQ5 = EQUATION == 0 /. {μ → 1000};

τ5 = FindRoot[EQ5, {τ, 182.6626}, MaxIterations → 40000, DampingFactor → 0.001]

FindRoot::fmp :
 Machine precision is insufficient to achieve the accuracy 1.00000000000000066`*^-6.

{τ → 182.662}

FUNCTION = EQUATION /. {μ → 1000, τ → τ5[[1, 2]]}

0.0361488

N[τ5[[1, 2]], 16]

182.6622120196749

■ Test 6: $\mu=1175.1$ Pa

```
EQ6 = EQUATION == 0 /. {μ → 1175.1};
```

```
τ6 = FindRoot[EQ6, {τ, 884.6857}, MaxIterations → 40000, DampingFactor → 0.001]
```

FindRoot::fmp :
 Machine precision is insufficient to achieve the accuracy 1.00000000000000066`*^-6.

{τ → 884.666}

```
FUNCTION = EQUATION /. {μ → 1000, τ → τ5[[1, 2]]}
```

0.0361488

```
N[τ6[[1, 2]], 16]
```

884.6660957447211

I have reviewed this scientific notebook and find it in compliance with QAP-001 There is sufficient information regarding procedures used for conducting tests, acquiring and analyzing data so that another qualified individual could repeat the activity

7/15/99

Volume 2: Dripping into Cavities from Unsaturated Fracture under Evaporative Conditions
II. Experiments, Liquid Bridges and Liquid Fingers

Thermal Effects - Key Technical Issue - Dani Or - 11/23/1999

Account Number: 20-1402-661

Collaborators: Teamrat A. Ghezzehei (USU), Randall Fedors, Ron Green (CNWRA)

Directories: C:/dripping_notebook

Objective: the objective of this study is to design an experimental setup to test the analytical model of dripping into cavities from unsaturated fractures, presented in the first part of the current volume of scientific notebook (Or and Ghezzehei, 1999).

Initial Entry – 5/17/99:

In the first part of this scientific notebook (#354) volume 2, an analytical model of dripping from unsaturated fractures to wide subterranean cavities was presented. In the present section, testing of the model with laboratory experiment is presented.

Dripping from Fracture Model: Experimental
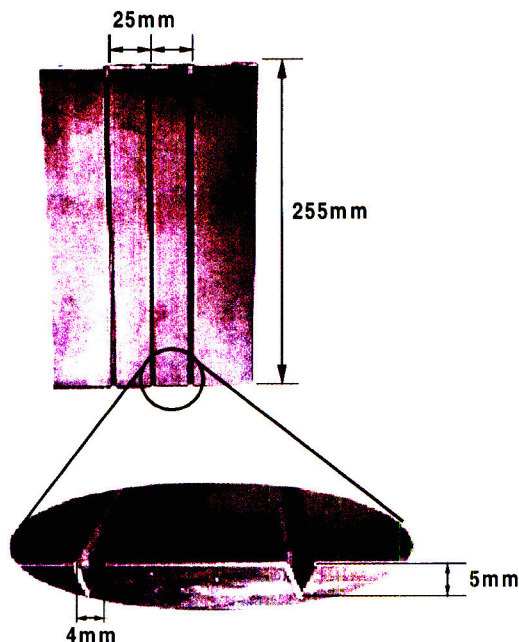
Figure 10. Model for fractured rock wall made of grooved aluminum slab.

An experimental setup was designed to test the analytical model of dripping from fractured porous media developed previously.

A fracture model, similar to the one used to develop the model, was constructed from aluminum slab 6.9mm in thickness. Three parallel grooves of 45° angle, and 5-mm depth were made on one surface of the aluminum block, as shown in Fig (10). The surface of the aluminum was washed with 80% H_2O_2, to oxidize greasing that has been introduced during machining. Wettability of the grooved surface was checked visually. Upon exposure to air, the aluminum surface is oxidized rapidly resulting in a wettable surface that can mimic rock surface.

A schematic diagram of the experimental setup is depicted in Fig (11). The aluminum slab was mounted inside a closed chamber with the grooves vertically upright. The top ends of the grooves were covered with fine,
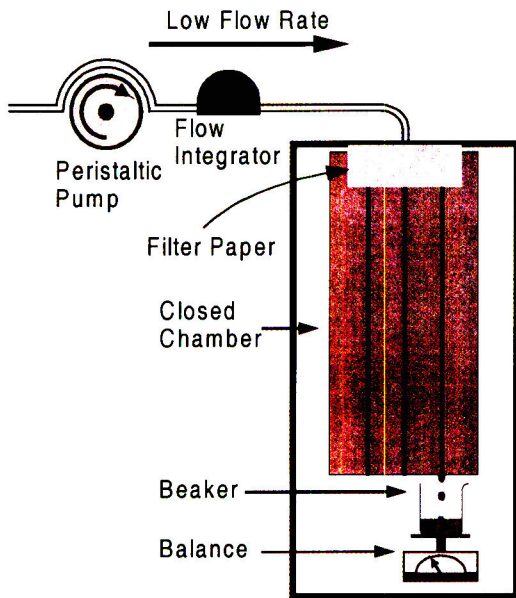
Figure 11. Schematic diagram of dripping experiment

ceramic filter papers to distribute the water influx evenly to all the grooves. Water was supplied to the top of the fracture model using a peristaltic pump operated at several low flow rates. When steady state dripping rate is attained, tarred glass beaker was placed under a selected groove, and the number of drops collected in the beaker within 10 minutes were counted.

The volumetric flux in each run was calculated from the mass of water accumulated in the beaker as,

$$Q = \frac{M}{\rho\, t} \qquad (47)$$

where Q is volumetric flux (in $m^3\ sec^{-1}$), M is accumulated mass of water (gm), ρ is density of water (1000 $kg\text{-}m^{-3}$), and t is duration of test (sec). The time-averaged dripping period of individual drops is calculated from the number of drops as,

$$P = \frac{t}{N} \qquad (48)$$

where P is drop-period (sec) and N is number of drops collected in the specified time duration of test (t). The raw data collected from the experiment is given in Appendix (A).

Model predictions were calculated using Eq (39) and (44) of Vol. (2). For the relatively rapid dripping rates tested, evaporation was assumed negligible (matric potential of cavity very close to saturation). Comparison of the experimental data with the model predictions has shown one order of magnitude difference in dripping period as depicted in Fig (12). These observations led to closer examination of the dripping process, especially liquid behavior near dripping plane.
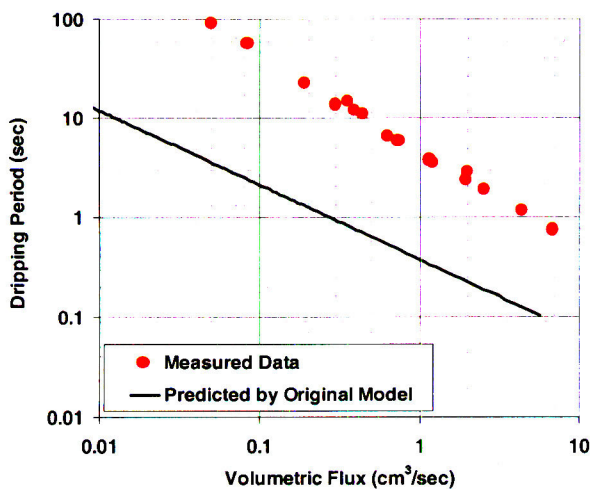
Figure 12. Comparison of measured dripping period with prediction by original model

5/20/99: Semi-Empirical Adjustment of Drop Anchoring Area

To provide better understanding of the dripping mechanism low-magnification video-microscopic images of drop formation and detachment were examined closely (Fig 13). At all stages of dripping, accumulation of water close to the dripping plane was observed. The liquid profile near the dripping plane appears to be independent of the flux and drop formation stage. Consequently, unlike the proposed model the drop anchoring area is independent of flux. Generally, the observed area (Ao) is larger than what is predicted by the model. The underestimation of the drop anchoring area (Ao) by the model resulted in low dripping period and drop volume as depicted in Fig (12).
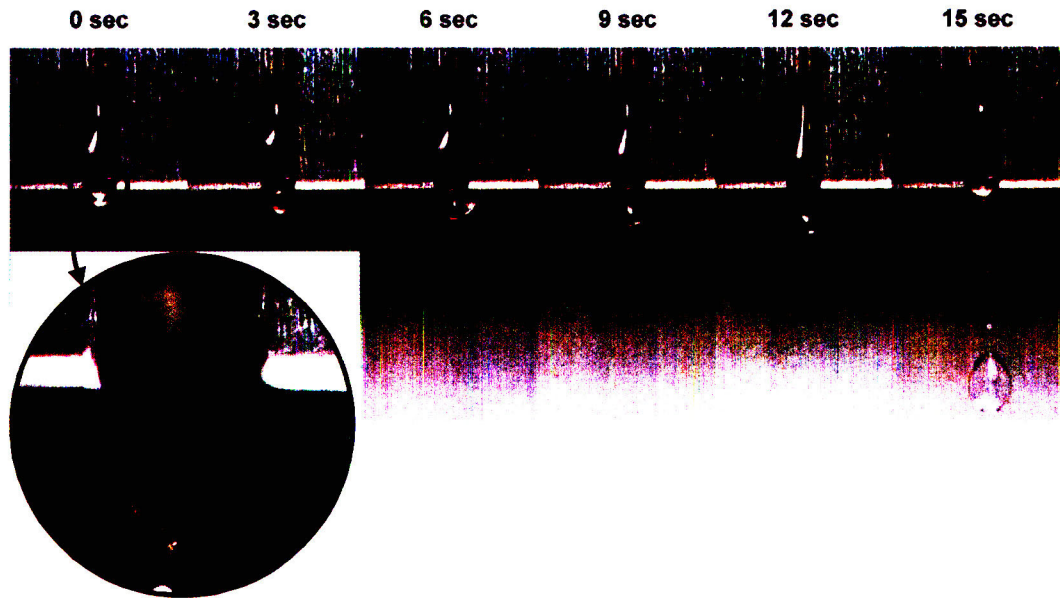
Figure 13. Sequence of drop formation stages from a fracture model. Insert: close-up of liquid configuration at groove-tip. Arrows indicate relatively stable liquid configuration near dripping plane. Ao_t and Ao_c refer to triangular and circular approximations of the observed drop anchoring area Ao.

As a first step to test the model, it was proposed to introduce semi-empirical adjustments to the model, which correct the drop anchoring area. The adjustments involve replacing the flux-dependent drop anchoring area (Ao) Eq. (44), by geometry dependent-formula that resembles the observed shapes (Fig 13). The first approximation considers the drop base area to be equal to the triangular cross-sectional area of the groove,

$$Ao_t = L^2 \tan\left(\frac{\gamma}{2}\right) \tag{49}$$

The second approximation that resembles more closely to the observed cross-sectional area considers the area of a circle circumscribing the triangular cross-section of the groove,

$$Ao_C = \pi \left(\frac{L}{\cos(\gamma)+1} \right)^2 \tag{50}$$

Note The area approximations presented in Eq (49) and (50) assume that the bottom part of the groove is completely filled with liquid. This assumption is not necessarily applicable to other groove geometries other than the one tested.
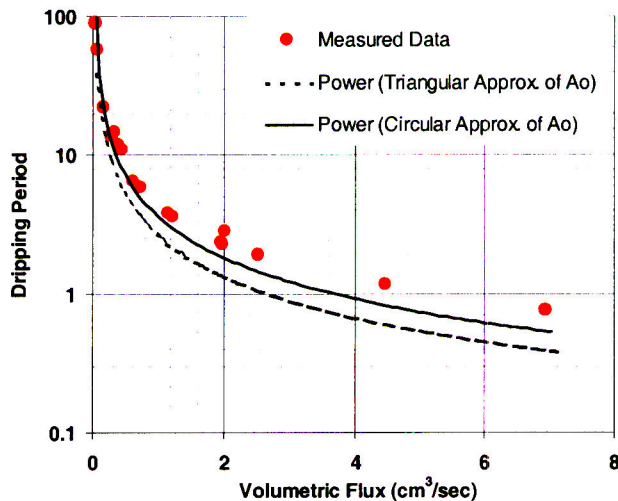
Figure 14. Sequence of drop formation stages from a fracture model. Insert: close-up of liquid configuration at groove-tip.

The geometry-dependent approximations of Ao (Eq (49) and (50)) are independent of the flux. The model with the proposed adjustments was evaluated by substituting Eq (49) and (50) in place of Eq (44).

The adjustments resulted in improved prediction over the original model, as shown in Fig (14). The circular approximation was more close to the observed drop anchoring area Ao (insert in Fig 13), hence, Eq (50) had better fit than the triangular approximation Eq (49). However, these adjustments are not applicable for other geometries. Physically based prediction methods are required to eliminate this empirical component if the model.

7/25/99: Energy Transition and Liquid Profile near Dripping Plane

The flow domain in vertical grooves dripping into a wide cavity can be classified into three distinct zones, as demarcated in Fig (15). The outlines in Fig (15) correspond to drop- and transitional- profiles calculated using methods discussed in this entry.

In the uniform groove-flow zone, liquid profile and flux are entirely controlled by the matric potential (vapor pressure) of the ambient rock-fracture environment, with little boundary-effects emanating from dripping plane. The profile of pendant drop zone is a result of interaction between capillary forces, surface tension and gravity. The transitional region provides the necessary pressure adjustment between the pendant drop (superatmospheric) and the capillary liquid of the grooves (subatmospheric) with gravitational pressure gradient. The primary focus of this section is to present a simplified approach for calculating the liquid profiles in (1) the pendant-drop zone and (2) transitional zone that allows for the determination of drop anchoring area (Ao). Detailed derivations and comparisons that consider wide range of conditions will be reported in future work.

Equilibrium Shape of Liquid Drop Pendant from Fractured Ceiling

Equilibrium-state weight (volume) and shape of pendant and sessile drops have been studied extensively for over a century primarily because of their convenience and fair accuracy for determination of surface tension of several liquids [Boucher, 1975]. The drop weight method for surface tension determination is an old technique that uses a simple expression for the drop weight given by,

$$m\,g = 2\,\pi\,r\,\sigma \tag{51}$$

where

    m .... Drop mass [kg]

    r .... Radius of drop forming tube [m]

The above expression Eq (51) (commonly referred to as Tate's law) assumes that the entire liquid emerging below the tube detaches. A correction factor that accounts for the portion of the pendant drop that remains behind as the drop detaches was introduced by Harkins and Brown [1919]. The drop-weight method does not consider the drop shape; and may not be directly useful for obtaining drop-base area required for our analysis.

Figure 15. Classification of the dripping flow regime into capillary-, transitional- and drop- zones. Solid outlines are theoretical profiles of transitional- and drop- profiles calculated according to simplified methods discussed in appendix (A) (fixed variables: L=3.5 mm, γ=60°, θ=0°, λ=1.3; solved variables: ϕ=0.02, α=0.75, a=4.5mm, R=5.7mm).

The drop shape is a result of balance of forces due to surface tension, pressure and gravity. The pressure difference across the liquid-vapor interface of a pendant drop hanging from a solid ceiling (Fig 16) at any vertical distance (z) below the supporting ceiling is given by the Young-Laplace equation,

$$\Delta p(z) = \sigma\left(\frac{1}{R1(z)} + \frac{1}{R2(z)}\right) \tag{52}$$

where

    z .... Vertical distance from the supporting ceiling [m]

    $\Delta p(z)$ .... Pressure difference across the drop surface at z,[Pa], will be denoted by p(z) hereafter.

    R1(z), R2(z). Principal radii of curvature at z [m]

The pressure gradient along the vertical axis of symmetry is given by,

$$\frac{dp(z)}{dz} = -\rho\,g \qquad (53)$$

An implicit expression for the drop profile is obtained by integrating Eq (53) and equating it to Eq (52),

$$\sigma\left(\frac{1}{R1(z)} + \frac{1}{R2(z)}\right) = -\rho\,g\,z + \tilde{p} \qquad (54)$$

where

$\tilde{p} = \dfrac{2\sigma}{ro}$ .... Positive pressure at the bottom tip of the drop [Pa]

ro .... Radius of curvature at the bottom tip of the drop [m]

Analytical solution to Eq (54) is not available. Standard methods of numerical integration are not applicable because of singularity at the bottom boundary. However, liquid drop profiles have been calculated by introducing simplifying expressions and choosing some arbitrary parameters [Freud and Harkins, 1929; Nemchinsky, 1994].
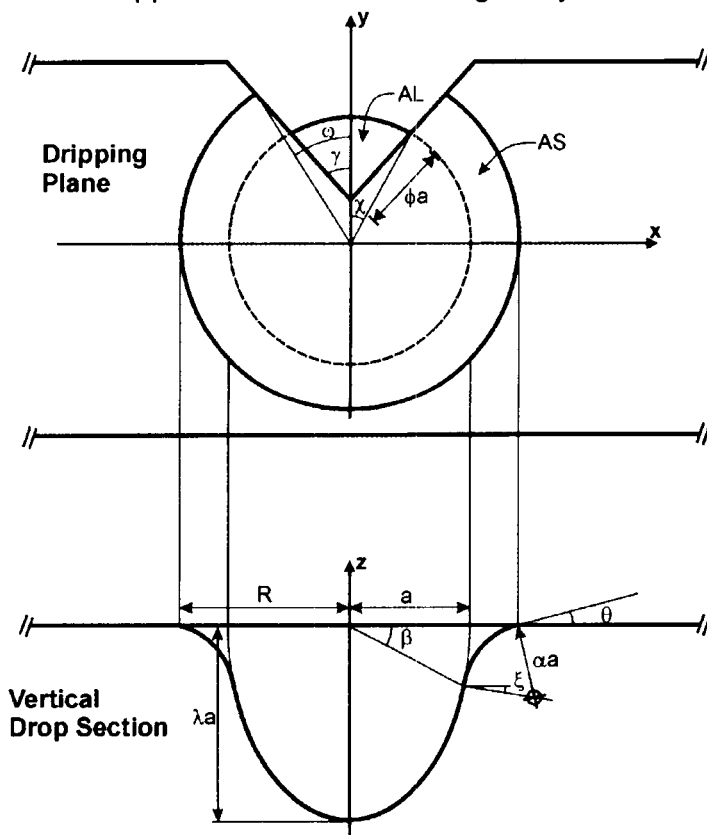
By employing minimum energy configuration, Pitts [1973; 1974] calculated profiles of stable, pendant liquid drops. This method seeks the equilibrium drop shape of a fixed drop volume, using variational calculus to minimize the total energy of the liquid drop.

Both of the above approaches for determination of liquid drop profile provide satisfactory tools based on first principles. However, due to the tremendous amount of computations involved and complexity to introduce the effect of grooved inlet, we opted for a simpler geometrical shape that captures most of the physical principles involved.

Figure 16. Schematic diagram of the simplified drop model used to calculate drop anchoring area and drop profile.

We define the profile of pendant drop by a semi-ellipsoid [Erbil and Meric, 1997] with the radius in the dripping plane

given by a, and λ is the aspect ratio, as shown in Fig (16). The negative liquid-pressure beneath the dripping plane required to anchor the drop is created by an arc, with negative curvature of αa, tangential to the ellipsoid and approaching the supporting ceiling at an angle θ (solid-liquid-vapor contact angle). The actual radius of the drop anchoring area is denoted by R. Other geometrical dimensions of the proposed drop shape required to calculate various areas and pressures are defined in Fig (16).

We consider vertical force balance equations at the cavity ceiling or dripping plane. At z=0 the liquid pressure and surface tension are in balance with the weight of the drop suspended beneath

$$\overline{P}\,(AS + AS) + 2\,(\pi - \omega)\,R\,\sin(\theta) = V\,\rho\,g \tag{55}$$

Where,

AS .... portion of the drop anchoring area in contact with solid(cavity ceiling)

AL .... portion of the drop anchoring area in contact with groove liquid

θ .... Solid-liquid-vapor contact angle [radian]

Note: The contact angle (θ) is not necessarily the actual contact angle of the liquid. It may have different values if the ceiling is initially wet or dry.

Note: the ceiling is considered as a reference plane with zero gravitational potential energy.

The first term on the LHS of Eq (55) is force due to mean liquid pressure ($\overline{P}$) acting over the liquid anchoring area (AS+AL). The second term on the LHS of Eq (55) corresponds to the upward component of the surface tension acting along the solid-liquid-vapor contact line (perimeter of drop cross-section). The RHS of Eq (55) denotes the weight of the pendent drop. The area-averaged mean liquid pressure is given by,

$$\overline{P} = \left[\sigma\left(\frac{1}{R} - \frac{1}{\alpha\,a}\right)AS + \frac{2\sigma}{a}\,AL\right]\bigg/(AS + AL) \tag{56}$$

An additional constraint requires that the vertical pressure gradient given in Eq (53) be satisfied. This may be stated as: the difference in capillary pressure between the top and the bottom of the drop is due to the difference in gravitational potential energy,

$$\overline{P} - \frac{2\,\sigma}{ro} = -\rho\,g\,(\lambda\,a) \tag{57}$$

where

ro .... is the positive and uniform radius at the drop tip (ro = λa)

The horizontal position of the pendant drop in relation to the groove is defined by the relative wetted length of the groove face (ϕ) in Fig (16). Lateral force balance in the direction of the axis of symmetry of the groove (passing through the apex) provides the necessary conditions to determine the horizontal location of the drop. The forces acting

in the horizontal direction are due to capillary pressure, and surface tension along the solid-liquid-vapor contact line. The positive pressure in the liquid-liquid contact area and negative pressure in the solid-liquid contact area tend to pull the drop towards the groove (outwards). While surface tension, acting along the solid-liquid-vapor contact line pulls the drop away from the groove (inwards).

$$\frac{2\sigma}{a}\sin(\chi) - \sigma\left(\frac{1}{R} - \frac{1}{\alpha a}\right)\sin(\varpi) = 2\,\varpi\,R\,\sigma \qquad (58)$$

The drop shape that satisfies the above three balance equations and constraints for fixed contact angle (θ) and aspect ratio (λ) is obtained by solving Eq (55), (57) and, (58) simultaneously for (a), (α) and (ϕ). The superposition of calculated drop profile over drop image, shown in Fig (16), indicates good agreement (values of the variables used/solved is given in the caption).

Table 1. Calculated Drop Anchoring Radius (R) for two groove angles (γ) and two contact angles (θ).

λ	R [mm] γ = 30° θ = 0°	R [mm] γ = 30° θ = 30°	R [mm] γ = 120° θ = 0°	R [mm] γ = 120° θ = 30°
1	5.73	4.99	5.73	4.89
1.1	5.74	5.02	5.75	4.95
1.2	5.76	5.03	5.76	4.97
1.3	5.77	5.05	5.77	5.01
1.4	5.79	5.07	5.71	4.95
1.5	5.80	5.27	5.70	5.19

The primary result of these calculations is the drop anchoring area ($A_o \cong \pi R^2$) that provides the boundary condition necessary for solving the one-dimensional axi-symmetric dripping model. The drop base area obtained in this fashion has been found to be weakly dependent on the groove angle (γ) but significantly dependent on the contact angle (θ) as shown in Table (1). It has also been shown that the drop radius varies slightly with the drop aspect ratio (λ), or indirectly with drop volume. The results indicate that the value of drop anchoring radius (R) has a narrow range (4.9mm to 5.9mm) and radius of the ellipsoid (a) is approximately 85 percent of R. Experimental observations of pendant drops suspended from grooved aluminum slab further assert the stability of drop anchoring radius (Fig 13). This is also supported by observations of Curl [1972] on the existence of a minimum radius of stalactites (2.6 mm), which also implies the existence of minimum drop anchoring area. Consequently, we used drop base area (Ao) that corresponds to the mean drop volume (λ=1.5) to approximate a constant boundary condition for the drop detachment model. Constant drop-anchoring areas (Ao) that can be used in calculating dripping are listed in Table (1).

Liquid Profile in the Groove's Transitional Zone

The pressure profile in the transition region is determined by integrating Eq (53) with initial condition given by the pressure in the liquid-liquid cross section of the drop (AL),

$$P(z) = \frac{2\sigma}{a} - \rho\,g\,z \qquad (59)$$

where $P(z) \geq \psi$. Upper in the groove (in the capillary zone) where $P(z)$ is less than the ambient matric potential ($P(z)<\psi$), the liquid configuration in the grooves is in equilibrium with the ambient matric potential. The liquid profile is obtained by substituting the pressure profile of Eq (59) in Young-Laplace equation as,

$$r_{Lv}(z) = -\frac{\sigma}{P(z)} \qquad (60)$$

Comparison of the calculated liquid profile with observed liquid profile in the transitional region (Fig 15) showed good agreement.

Model predictions of dripping period and drop volume using the revised physical analysis of drop shape show excellent match with measured data as shown in Fig (17). The current solution is fully based on physical principles and is expected to work for any groove-geometry and flux combinations provided the flow regime satisfies the non-jetting and low inertia conditions.
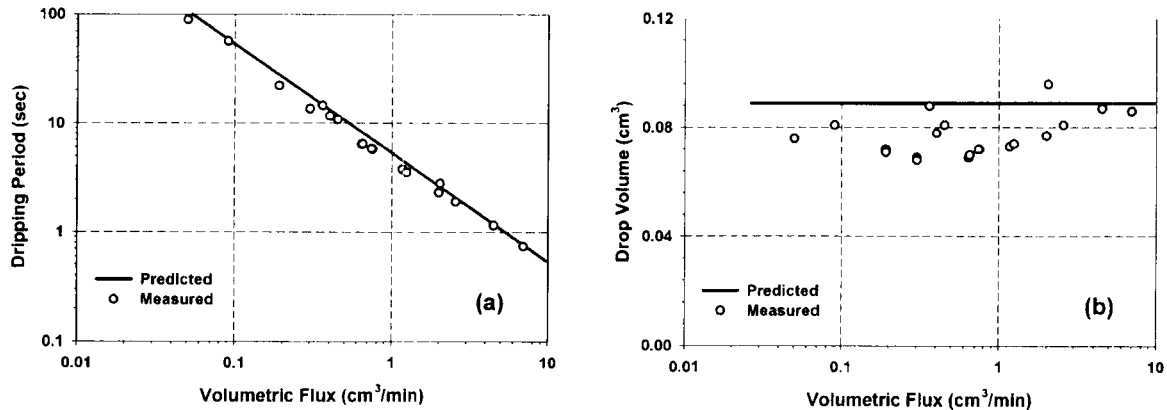
Figure 17. Results of laboratory experiment in non-evaporative conditions for the grooved aluminum slab; (a) dripping rate and (b) drop volume at different volumetric fluxes.

The effect of groove geometry on dripping period is mainly due to dependence of flux on groove angle (γ) and depth (L). In these experiments, however, flux was controlled independently. Hence, the dripping period was insensitive to groove angle. Drop volume predictions were close to experimental measurements (Figure 17b). The drop volume largely depends on the drop anchoring area (Ao), which is a result of local force balance at the groove-drop interface. The effect of flux on drop volume becomes significant only at low fluxes and high evaporation (more discussion in subsequent entry of 9/25/99 on dripping in natural caves). The slight fluctuations of experimental drop volumes may be due to measurement errors.

Further experimental work to validate the model is underway. Thick slabs of aluminum and quartz, and several groove angles are used under a wide range of fluxes and ventilation conditions. Preliminary experiments with natural rock specimens under similar conditions have shown promising results; tests that are more elaborate are currently going on.

9/25/99 Model Testing on Dripping from Natural Caves $\boxed{\text{Dani Or}}$

The dripping model predicts rate of dripping from grooves into cavities as a function of matric potential (vapor pressure) of the fracture and the dripping cavity. The vapor pressure of the fracture determines the flux in the grooves, while the cavity vapor pressure determines rate of evaporation from drops. In addition, the flux in the grooves at any given vapor pressure varies with the groove angle. The original model considers equilibrium between the cavity- and fracture- matric potentials. This situation can be realized in long term in the absence of ventilation of the cavity.

Dripping from stalactites and grooves are similar. Once the liquid leaves the feeding solid (base of groove or stalactite), the physical principles that determine the mechanics of drop formation and growth are identical. The model considers a constant wetted area that supports drops. Method of approximating the drop anchoring area was presented in previous entry; however, measured stalactite cross-sectional area can be used instead, if available.

The separate influences of the vapor pressure on flux and evaporation varies depending on (1) the ratio of fracture- to cavity- matric potential (vapor pressure), and (2) the groove angle.

Model prediction for ventilated (evaporative) conditions covering a wide range of fluxes was tested by comparison with data of dripping from stalactites (Fig 18), as reported by Genty and Deflandre (1998). The drip rate and seepage rate from one stalactite (soda straw) in the Père Noël cave (Belgium) has been studied since 1991. The cave is located 70 m below surface, and the overlying ground surface consists of vegetation growing in shallow soil (5 to 30 cm thick). The reported data included dripping rate (number of drops per unit time) and drop volume measured by an automatic station during five hydrological cycles (1991/92 - 1995/96). A constant drop anchoring area of 6 mm, and groove angle of 45° were assumed to be feeding the drops. Finally, the matric potential in the cavity was assumed to be three times the matric potential of the rock to represent a mildly ventilated cavity (-100 to -250 Pa in rock and -300 to −750 Pa in cavity).

Figure 18. Comparison of measured drop volumes at different dripping rates (Genty and Deflander, 1998) with model predictions (Or and Ghezzehei,

The variation in drop volume with flux is associated to the viscous extension of the drops. At low matric potentials (dry), the competitive effect of high evaporation rate and low flux lead to slow net increase in drop volume especially just before it detaches. This

leads to low energy dissipation due to viscous flow and provide more force to carry additional drop weight.

10/12/99 Numerical Evaluation of Analytical Solution $\boxed{\text{Dani Or}}$

The analytical solutions and FORTRAN programs designed to solve them, presented in Vol. (2), involve tremendous computation. Further simplification of the solution that unifies both evaporative and non-evaporative solutions was sought. The equations describing the drop detachment period under non-evaporative and evaporative conditions, given by Eq (26) and (39) respectively, can be rewritten in general form as,

$$1 - 6\eta \sqrt{\frac{Ao}{W}} \left(\frac{1}{Q\,\tau_c - \Omega} + \frac{1}{\Omega}\ \ln\left[1 - \frac{\Omega}{Q\,\tau_c}\right] \right) \frac{\partial}{\partial \tau}(Q\ \tau) = 0 \qquad (61)$$

Where

         Ao .... Drop anchoring area given in Table (1)

$$\Omega = \frac{\sqrt{Ao\,W}}{U}$$

$$U = \rho g U = \rho \ulcorner g$$

$$W = \pi \sigma 2$$

$$Q = \begin{cases} Q(\psi) & Eq(9) \\ Q_{net}(\psi,\tau) & Eq(37) \end{cases}$$

The difference between the non-evaporative and evaporative conditions lies in the dependence of the flux (Q) on the drop growth-stage (τ). For non-evaporative conditions, the entire influx reaching the groove tip contributes to drop formation and is independent of the stage of drop growth, hence, $\partial(Q\tau)/\partial\tau = Q$. For evaporative conditions, on the other hand, the net flux (Q_{net}) is dependent on the drop growth stage (due to dependence of evaporation rate on drop radius) and $\partial(Q\tau)/\partial\tau$ has more complicated form.

$$\frac{\partial}{\partial \tau}(Q_{net}(\tau_c)\,\tau_c) = \frac{\pi}{3}\left(N\tau_c^{\,2/3} + M\tau_c\right)^{1/2}\left(2N\tau_c^{\,-1/3} + 3M\right) \qquad (62)$$

The LHS of Eq (61) has real values only for $Q\tau > \Omega$, (for positive argument of the logarithm). The function has a very steep slope in a narrow range near the solution ($\tau = \tau_c$), and a very flat slope when $\tau > \tau_c$. Both these features make standard methods of solving implicit equations (e.g. Newton-Raphson iteration) inapplicable. The revised numerical scheme used in this notebook seeks the solution only in the region of real values by method of bisection, starting at the point of singularity ($\tau = \Omega/Q$). This method

of solution is more efficient than the one presented in Vol. (2), and can be implemented easily in symbolic mathematical software. A MATHEMATICA program that implements this solution is provided in Appendix C.

The illustrative examples of dripping characteristics (dripping, period, drop volume, solute concentration) presented in the previous model were revised according to the modifications presented in this volume. In Fig (19, 20 and 21) sample calculations of dripping period, drop volume and solute concentration at 30- and 120-degree groove angles are shown. Similarly, comparison of drop volume calculated using current model with that of Scheele and Meister (1986) and decoupled solution of dripping under varying degrees of ventilation were revised. The revised results are given in Fig (10)-(13).

Dripping Period

The drop shape and anchoring-area are not significantly affected by the groove geometry. However, groove geometry significantly affects the dripping by varying the flux (Q) associated with any given matric potential (ψ). Of the three geometric parameters (L, β and γ) that define the fracture surface roughness, the groove angle (γ) results in the largest variations in dripping rates. Narrow groove angle can support larger cross-sectional area of capillary water; hence, higher liquid flux at any given matric potential. The effect of groove depth (L) is limited to determining the matric potential of complete filling of the grooves. The parameter β does not have significant effect on dripping rate and drop size, since corner flow dominates film flow by several orders of magnitude in the range of matric potential where drop formation is possible (near saturation).

Detachment period (τ_c) for evaporating and non-evaporating conditions for two groove angles are depicted in Fig (19). As the matric potential decreases (becomes more negative), the total influx (Q) decreases resulting in longer dripping period of individual liquid drops. When we consider evaporative condition, as matric potential decreases, the competition between the decreasing influx and increasing evaporation rate results in significant rise in dripping period until a limiting minimum matric potential is reached. At ambient condition drier than the limiting minimum matric potential, there would not be enough flux to exceed the evaporative demand, and dripping ceases. In contrast, under non-evaporating conditions, drop formation continues indefinitely with no bounds on minimum matric potential. At any given matric potential, because narrow

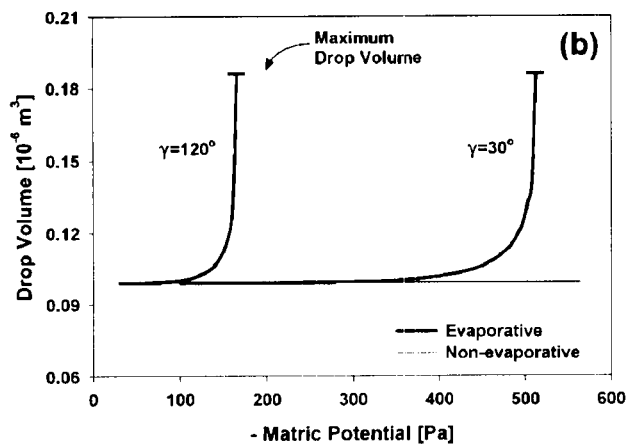**Figure 19. Theoretical Drop detachment time (τ_c) under evaporative and non-evaporative conditions dependent on coupled matric potentials (ψ) of cavities and fractures.**

groove angles (γ) result in higher flux (while evaporative demand is independent of the groove geometry) they have lower, limiting-minimum matric potential.

Drop Volume

The volume of individual drops as a function of the matric potential is shown in Fig (20). The drop volume is primarily determined by the drop-anchoring area (Ao), and time to detachment (τ_c). The drop-anchoring area does not change with groove geometry and matric potential; hence, there is no significant change in drop size (volume) associated with the drop anchoring area (Ao).

The dependence of drop volume on the duration of drop formation is through the rate of viscous extension Eq (19) Vol. (2). Under evaporative conditions, the net flux - Eq (37) decreases during the growth period of individual drop, reaching a minimum just before detachment ($\tau=\tau_c$). As the ambient matric potential approaches the limiting-minimum matric potential (indicated by the vertical marker in Fig 4a), the minimum net flux (Q_{net}) approaches to zero due to increased evaporative demand. Hence, the downward stress component due to viscous extension decreases as the drop grows. The additional upward stress component allows more drop weight to be suspended as indicated by the rapid rise in drop detachment period in Fig (19) as the limiting-minimum matric potential is approached. The maximum drop volume corresponds to the maximum equilibrium drop weight that can be suspended in the absence of viscous energy dissipation, hence, is independent of flux as shown in Fig (11).

Figure 20. Theoretical Drop volume at detachment under evaporative and non-evaporative conditions dependent on coupled matric potentials (ψ) of cavities and fractures.

Solute Concentration

Solute concentration of individual drops is directly related to the volume of the evaporated water (difference between the total influx and the net flux). Solute concentration of drops at time of detachment ($\tau=\tau_c$) are shown in Fig (21) for two groove-angles (γ) as functions of the matric potential (ψ).

The effect of lower matric potential on drop solute concentration is through the decrease in dripping rate that allows more evaporation to take place. At potentials close to limiting minimum matric potential, the time required for drop formation increases rapidly thereby allowing for extended evaporation opportunity times. Near this region (see Fig. 19 for the fast rise in formation time), the concentration more than doubles by only a slight decrease in potential (or vapor pressure). It is important to note that the limiting
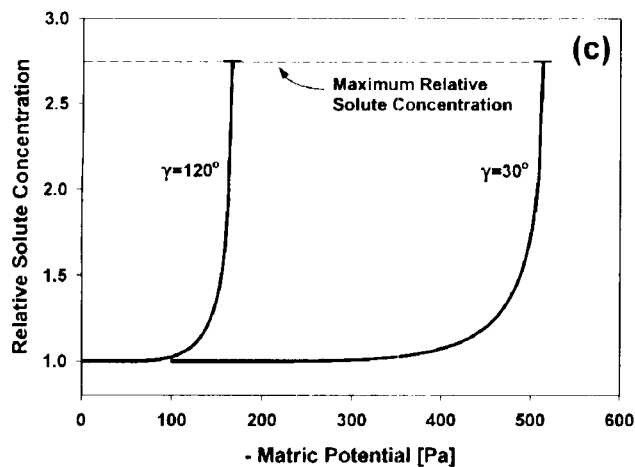
Figure 21. Theoretical Relative solute concentration of drops at detachment time dependent on coupled matric potentials (ψ) of cavities and fractures.

minimum potential (below which dripping stops) is completely determined by the groove angle (γ). This sensitivity to groove angle and matric potential variations guarantees that even under similar ventilation conditions, variations in individual dripping rates among grooves of different groove angles would produce drops with different solute concentrations. In general, slow pathways would result in higher relative solute concentration of drops by allowing longer evaporation duration. Similarly, even slight variations in matric potential (e.g., at a range that could be induced even by barometric pressure or temperature variations) near the minimum drop forming matric potential could substantially alter solute concentration of drops.

There are nominal changes that do not take into consideration the effect of deposition such as observed in Karst system where P_{CO_2} is lower in the cavity [White 1988].

Dripping Period under Decoupled Flux and Evaporation

We consider a setup consisting of a sample of fractured media similar to Fig 2, in which the plane width parameter is set as $\beta=0$ (considering flow in grooves only). A controlled steady state volumetric flux is applied at the groove top (Q_V). This influx of liquid substitutes the chemical-potential-dependent flux (Q) of previous calculations.

The applied flux is not permitted to overflow out of the grooves (by keeping the flux sufficiently small or using deep grooves). Thus, the flow mechanism is similar to that of corner flow in partially filled grooves given in Eq (5) of Vol. (2).

The net flux (Q_{net}) given in Eq (37is modified by substituting Q with Q_V. The drop detachment time is obtained by solving Eq (61) using the modified net flux and methods discussed in previous entry. The evaporation from drop surfaces is determined by the matric potential in the cavity (ψ_{cav}). Sample calculations of drop detachment times (τ_c) for a series of fluxes (Q_V) and different cavity matric potentials (ψ_{cav}) are shown in Fig (22a). For a given condition of cavity matric potential (ψ_{cav}), the net flux decreases with decrease in flux, leading to increase in detachment time. When the flux approaches a critical minimum, the competition between influx and evaporation is intensified leading to rapid rise in dripping period, and finally termination of dripping. The minimum volumetric fluxes (Q_{min}) and maximum dripping periods associated with a wide range of ambient vapor pressures of fracture cavity are depicted in Fig (22b). When the vapor pressure of the cavity is close to saturation (e.g. $\psi = -1Pa$), the effect of evaporation is negligible and drops can be formed from very small volumetric fluxes in very long dripping period. More ventilated cavities (lower cavity matric potential - ψ_{cav}), on the
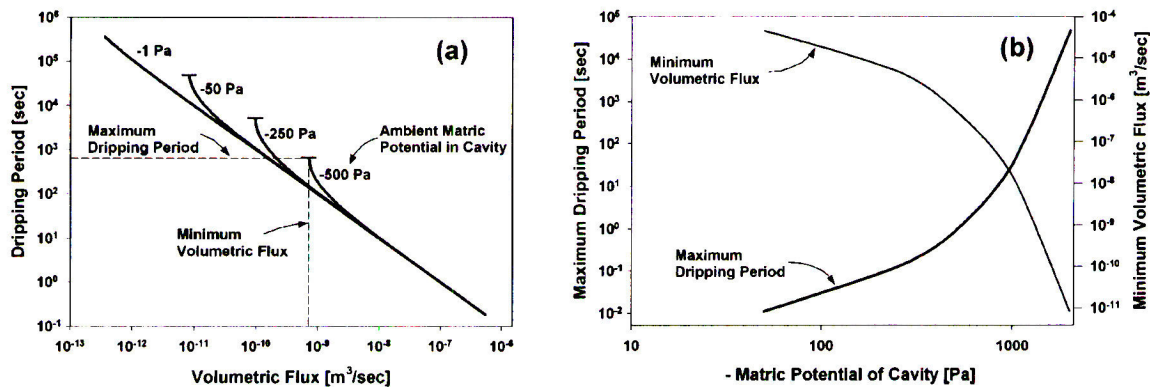
Figure 22. Theoretical dripping characteristics determined by decoupled (independent) liquid flux and evaporative conditions (matric potential of cavity) for a groove angle $\gamma=30°$. (a) dripping period under different cavity ventilation conditions (matric potentials) dependent on volumetric flux. (b) minimum volumetric flux required to generate dripping under different ventilation conditions (matric potential of cavity) and the associated maximum dripping period.

other hand, require higher minimum-volumetric-flux to generate dripping and consequently, have lower maximum dripping period.

10/25/99 Intermittent Flow in Fractures - Introduction

Intermittent flow of liquid in fractured porous media can occur in the form of moving liquid bridges. This phenomenon is particularly important at near-saturation state. The objective of this study is to develop a physical model for formation of liquid bridges in fractures and subsequent intermittent rivulet and finger flow.

Information potentially subject to copyright protection was redacted from this location. The redacted material (Fig. 23) is from the following reference:

Nicholl, M.J., M.J. Glass, and S.W. Wheatcraft. "Gravity Driven Infiltration Instability in initially Dry Nonhorizontal Fractures. Water Resources Research. Vol. 30, No. 9. pp. 2,533-2,546. 1994.

The modeling framework is divided into two stages of increasing complexity. The first stage is to model equilibrium configuration of fixed-volume liquid-bridge between inclined parallel planes. This simplified equilibrium-state model can be used to analyze growth and stability of liquid-bridges for discrete range of liquid volumes (which presumably change due to interception of surface- or matrix- fluxes, or due to vapor condensation). The maximum liquid volume for which equilibrium shape exists determines the onset of motion. Two forms of motion

can be identified: (1) motion of the entire bridge (Fig 24), or (2) breakup of the bridge into smaller stable pieces.

In the first condition, the liquid-bridge moves at constant velocity that generates enough viscous (frictional) drag to carry the excess drop liquid weight. This type of motion is likely to occur on smooth fracture walls that cannot provide enough viscous drag. In the second condition, the smaller pieces form either stable liquid-bridges or liquid drops if the geometry permits.

Information potentially subject to copyright protection was redacted from this location. The redacted material (Fig. 24) is from the following reference:

Nicholl, M.J., M.J. Glass, and S.W. Wheatcraft. "Gravity Driven Infiltration Instability in initially Dry Nonhorizontal Fractures. Water Resources Research. Vol. 30, No. 9. pp. 2,533-2,546. 1994.

The second stage of the modeling framework considers continuous growth or (decrease) of bridge volume. This approach includes the rate-dependent viscous effect on growth of stationary liquid-bridge. This is in direct analogy with growth and detachment of free liquid drops.

The following phenomena will be investigated (or modeled) in-depth.

- Attainment of steady liquid-bridge velocity moving on smooth and rough surfaces by matching viscous drag and body forces either by reducing the mass (as it streaks over the fracture surface) or increasing the velocity.

- Formation and motion of liquid-fingers by flow of liquid bridges on rough and dry surfaces. Develop characteristic finger length and elongation velocity depending on the fracture surface-roughness and wetness condition.

- Formation of rivulets from (1) drops near inclined walls, (2) moving liquid bridge in the presence of abrupt increase in aperture size.

- Inertial mechanism of dripping from liquid bridges due to abrupt change in fracture surface-roughness.

Equilibrium State Liquid Bridge Configuration

Geometric Considerations

Consider parallel plates of narrow spacing (2b) placed in Cartesian coordinate system as shown in Figure (25). The plates are wide enough so that the size of liquid-bridges formed in between them is not affected by the boundaries. The plates can be inclined at angle (β) about the y-axis. The spacing is small enough that the effect of gravity on the

shape of the liquid menisci is negligible. However, for $\beta<90$, there exists distortion in the shape of the liquid bridge due to gravitational potential difference between the higher and lower ends. The fracture geometry is determined by the inclination angle (β), and the spacing (2b). The surface roughness of fracture walls (R) defines the ratio of the actual surface area to that of a perfectly smooth surface. Other geometric variables are as defined in Fig (14).

The total surface area and perimeter of the liquid-solid interface on the z'y planes are given by,

$$A = 4 \cdot C \cdot D + \pi \cdot C^2 \qquad (63)$$

$$P = 4 \cdot D + \pi \cdot C \qquad (64)$$

The volume of the liquid-bridge can be approximated by,
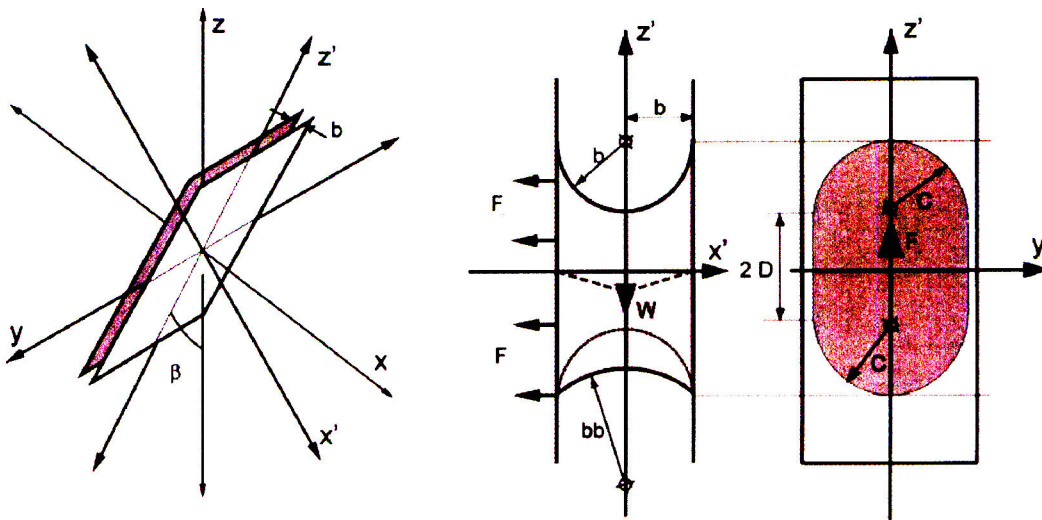
Figure 25. Schematic diagram of liquid bridge formation between parallel plates

$$V = A \cdot b \qquad (65)$$

The liquid pressures at the top and bottom ends of the liquid bridge are given by Young-Laplace equation as,

$$Pt = \left(\frac{1}{C} - \frac{1}{b} \right) \qquad (66)$$

$$Pb = \left(\frac{1}{C} - \frac{1}{bb} \right) \qquad (67)$$

The pressure difference between the top and bottom ends of the liquid bridge is attributed to difference gravitational potential energy,

$$Pt = Pb + 2 \cdot (C + D) \cdot \rho \cdot g \qquad (68)$$

If we assume the contact angle of the liquid vapor interface at top end is zero, the curvature and contact angle at the bottom are obtained from Eq (66), (67) and (68) as,

$$bb = \frac{b\,\sigma}{\left(b - 2\,(C+D)\,g\,\rho\,\cos(\beta)\right)} \tag{69}$$

$$\theta = a\cos\left(\frac{b}{bb}\right) \tag{70}$$

Forces Acting on Liquid Bridge

Two forms of static forces pulling the liquid-bridge upwards can be considered:

(1) Force due to surface tension acting on the top curved portion of the solid-liquid-vapor contact line

$$F_\sigma = 2C\sigma\left(1 - \frac{b}{bb}\right) \tag{71}$$

(2) Vertical component of the negative liquid pressure acting on the wetted area

$$F_P = A\frac{Pt + Pb}{2}\left(\frac{b - bb + bb\sin(\theta)}{b}\right) \tag{72}$$

If the condition permits, the liquid bridge is assumed to be in motion at constant velocity (v). The force resulting from viscous drag can be given by,

$$F_V = \frac{32}{2}RC\eta v \tag{73}$$

For a given fixed volume of liquid bridge, the configuration is obtained by equating the resultant upward force to the weight of the liquid drop,

$$(F_\sigma + F_P + F_V)\cos(\beta) = V\rho g \tag{74}$$

The solution to Eq (74) can be obtained by standard numerical methods.

Illustrative example of solving Eq (74) using MathCAD program is provided in Appendix D. In Fig (14), the aspect ratio of the solid-liquid contact area (wetted region) is shown as a function of volume of liquid bridge for two inclinations. The spacing of the parallel plates in these examples was 1.5mm, and surface roughness R=1000 was used. In all conditions, the velocity of the liquid bridges was calculated to be zero (v=0).

Addition of more constraints and
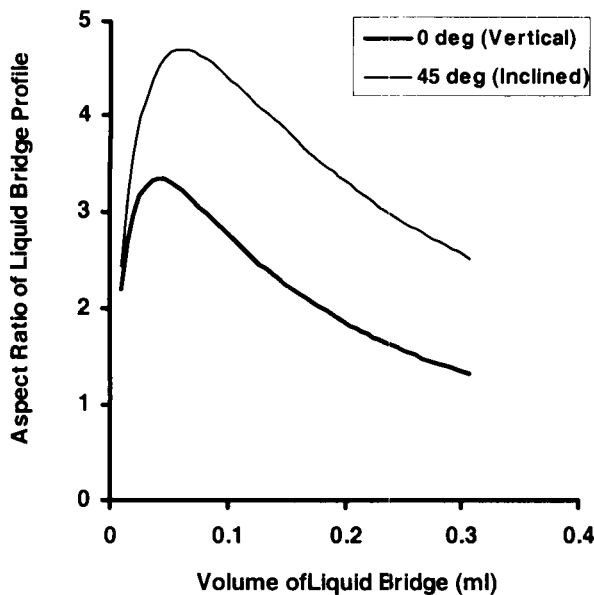
Figure 26. Aspect ratio of liquid bridge, formed between parallel plates of 1.5mm spacing R=1000 surface roughness, as function of bridge volume for 0° and 45° inclinations from the vertical axis.

refinement of the solution methods are currently being pursued.

Elongation and Detachment of Liquid Fingers

Slow feeding of liquid bridges formed between rough fracture surfaces results in lingering extension of the bridge, forming slender liquid fingers. The liquid finger extends under its own weight until it raptures and detaches forming smaller liquid bridges. The forces that determine its evolution are surface tension, gravity and viscous resistance to extension.

Consider a liquid finger being fed by a continuous stream from above as shown in Fig. (27). Initially, before the onset of elongation the bridge has circular outline. The Cartesian coordinate system is centered at the origin of the circular outline of the liquid bridge. The time scale is set to zero at the onset of elongation. Further extension is tracked in Lagrangian coordinate system as in the case of free liquid drops. For simplicity, we assume that the semi-circular bottom end of the liquid finger remains unaltered. Extension of the liquid finger occurs in the region between the semi-circular bottom and the origin.

The following force components operate in the vertical direction,

- Weight of liquid suspended below the element τ, including the bottom semi-

Cartesian coordinate system
t=0   t>0

Lagrangian coordinate system

Force Components
① SL- Interfacial Stress
② LV- Interfacial Stress
③ Viscous drag (no-slip)
④ Resistance to shrinkage
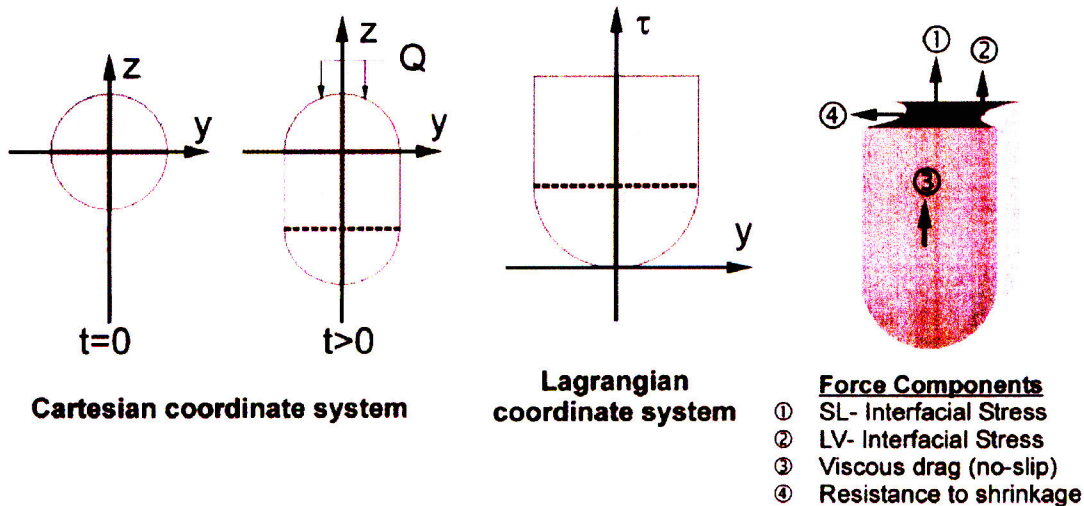
Figure 27. Schematic diagram of elongation of liquid bridge to liquid finger. Evolution is tracked in Lagrangian coordinate system, and involves balance between several force components.

circular portion

- Interfacial stresses along the liquid-vapor (LV) and liquid-solid (LS) contact lines supporting the weight (1 and 2 in Fig 27).

- Viscous drag along the liquid-solid contact area below the element τ (3 in Fig 27)

$$S_{t,\tau} = \rho g\left(2 \cdot b \cdot \pi \cdot ro^2 + Q\tau\right) - \left[+2\pi b\sigma_{LV} + 4y\sigma_{LS} + \frac{\eta}{\tau}\frac{d\tau}{dt}\right] \tag{75}$$

Additional forces resist the lateral extension (or reduction) of the finger cross-section. The vertical component of these stresses is related to the lateral stress by the Poisson ratio ($\upsilon=0$ for incompressible fluid). These stresses include (4 in Fig 27),

- Pressure difference across the liquid-vapor interface resisting shrinkage of the liquid cross section

- Interfacial stresses along the liquid-vapor and liquid-solid contact lines of the liquid cross-section, resisting shrinkage of the liquid cross section

- Viscous resistance to reduction of the liquid cross section

$$S_{t,\tau} = \upsilon\left[\left(\frac{1}{b}+\frac{1}{y}\right)\sigma_{LV} + 2\pi b\sigma_{LV} + 4y\sigma_{LS} + \frac{3\eta}{y}\frac{dy}{dt}\right] \tag{76}$$

The above stresses combined together describe the evolution of the liquid-finger.

$$\frac{dy}{dt} = \frac{y}{3\eta}\left\{2\rho g\left(2\cdot b\cdot \pi\cdot ro^2 + Q\tau\right) - 3[2\pi b\sigma_{LV} + 4y\sigma_{LS}] - \frac{2\eta}{\tau}\frac{d\tau}{dt} - \left(\frac{1}{b}+\frac{1}{y}\right)\sigma_{LV}\right\} \tag{77}$$

By solving the differential equation (77), it is possible to obtain an expression for the width of the liquid finger ($y(t,\tau)$). The element that goes to zero at the earliest time represents the element that pinches. This analysis is currently under study.

11/01/99: Status Report

- Wettability of the aluminum slab is not necessarily similar to that of rock walls. In some instances there were visual indications non-uniform wetting and the contact angle between the liquid-vapor interface and the solid (aluminum slab) surface was not known. Furthermore, the experimental data reported reflect only rapid dripping rate. More experimental work is underway using aluminum and quartz slabs of various geometries (groove angle and slab thickness) under wider flux range and conditions that can induce evaporation (using chambers with controlled temperature and relative humidity)

- Further experimental work will focus on dripping from rock samples (actual YM rock samples?) with natural and/or artificial roughness.

- Fundamental principles that govern formation and stability/motion of liquid bridges in fractures are laid in the current volume. Further refinement of the current model and inclusion of transient effects of flux are required. The models will be tested using laboratory experiments. The experiments will provide quantitative and qualitative (possibly using image analysis) data of liquid bridge formation and motion.

- Note that four appendices are attached. Appendix A includes raw experimental data and calculations. The first part of appendix B contains MATHEMATICA program that implements the modified numerical solution technique presented in entry of 8/15/99. In the second part of appendix B, a MathCAD worksheet that calculates drop volume using the detachment time obtained from the MATHEMATICA program is presented. Appendix C contains MathCAD program that solves equilibrium state drop shape and liquid profile near the dripping plane. Appendix D contains an illustrative example of solving equilibrium state configurations of liquid-bridges formed between inclined fracture spaces.

References

Boucher, E. A., and M. J. B. Evans, Pendant drop profiles and related capillary phenomena, *Proc. R. Soc. Lond. A.*, 346, 349-374, 1975.

Boucher, E. A., and M. J. B. Evans, XII Properties of fluid bridges between solids in a gravitational field, *J. Coll. Int. Sci.*, 75(2), 407-418, 1980.

Curl, R. L., Minimum diameter stalactites, *Bull. Nat. Spel. Soc.*, 34(4), 129-136, 1972

Erbil, Y. H., and R. A. Meric, Evaporation of sessile drops on polymer surfaces: Ellipsoidal cap geometry, *J. Phys. Chem. B*, 101: 6867-6873, 1997.

Freud B. B. and W. D. Harkins, The shapes of drops, and determination of surface tension, J. Phys. Chem, 33: 1217-1234, 1929.

Genty, D., and G. Deflandre, Drip flow variations under stalactite of the Père Noël cave (Belgium). Evidence of seasonal variations and air pressure constraints, *J. Hydrology*, 211:208-232, 1998.

Ho, C. K., Evaporation of pendant water droplets in fractures, *Water Resour. Res.*, 33(12), 2665-2671, 1997.

Nemchinsky, V. A. Size and shape of the liquid droplet at the molten tip of an arc electrode, j. Phys. D, 27:1422-1442, 1994

Nicholl, M. J., M. J. Glass, and S. W. Wheatcraft, Gravity driven infiltration instability in initially dry nonhorizontal fractures, Water Resour. Res. 30(9) 2533-2546, 1994.

Or, D., and M. Tuller, Flow in unsaturated fractured porous media – Hydraulic conductivity of rough fracture surfaces", *Water Resour. Res.*, in review.

Or, D., and T.A. Ghezzehei, Dripping into subterranean cavities from unsaturated fractures under evaporative conditions, *Water Resour. Res.*, in press.

Scheele, G. F., and B. J. Meister, Drop formation at low velocities in liquid-liquid systems, *AIChE J*, 14(1), 9-15, 1968.

White, W. B., *Geomorphology and Hydrology of Karst Terrains*, Oxford University Press, New York, 1988.

Wilson, S. D. R., The slow dripping of viscous fluid, *J. Fluid. Mech.*, 190, 561-657, 1988.

Appendix D: Dripping Experimental Data (5/17/1999)

Nominal Flux cc/min	Groove	Beaker wt gm	Duration min	Beaker+Drop Wt gm	# of Drops	Tot. Drop Wt gm	Flux gm/min (cc/min)	Period sec	Drop Wt (vol) gm (cc)
3	1	48.43	10	54.87	93	6.44	0.64	6.452	0.069
3	1	48.43	10	54.90	93	6.47	0.65	6.452	0.070
3	3	48.43	10	60.11	159	11.68	1.17	3.774	0.073
3	3	48.43	10	60.87	169	12.44	1.24	3.550	0.074
3	2	48.43	10	68.36	259	19.93	1.99	2.317	0.077
3	2	48.43	10	68.47	260	20.04	2.00	2.308	0.077
1	1	48.43	10	51.45	44	3.02	0.30	13.636	0.069
1	1	48.43	10	51.44	44	3.01	0.30	13.636	0.068
1	2	48.43	10	50.37	27	1.94	0.19	22.222	0.072
1	2	48.43	10	50.36	27	1.93	0.19	22.222	0.071
1	3	48.43	10	55.89	104	7.46	0.75	5.769	0.072
1	3	48.43	10	55.86	103	7.43	0.74	5.825	0.072
5	1	48.43	10	52.43	51	4	0.40	11.765	0.078
5	1	48.43	10	52.9	55	4.47	0.45	10.909	0.081
5	2	48.43	10	68.81	213	20.38	2.04	2.817	0.096
5	3	48.43	10	74.05	316	25.62	2.56	1.899	0.081
8	3	48.43	5	70.95	260	22.52	4.50	1.154	0.087
10	3	48.43	5	83.23	405	34.8	6.96	0.741	0.086
0.75	2	48.43	10	52.03	41	3.6	0.36	14.634	0.088
0.5	1	48.43	9.5	49.24	10	0.81	0.09	57.000	0.081

Appendix E: Drop Shape and Liquid Profile Near Dripping Plane

Constants and Initial Guesses

Numerical tolerance

$$TOL := 10^{-2}$$

Physical constants

$$\rho := 998 \qquad g := 9.81 \qquad \sigma := 0.0792 \qquad \theta := 0 \cdot \frac{\pi}{180} \qquad \gamma := \frac{\pi}{6}$$

Variable parameters (unknowns)

$$a := 4.544 \cdot 10^{-3} \qquad \alpha := 0.4 \qquad \beta := \frac{\pi}{10} \qquad \phi := 1.8$$

Fixed parameter

$$\lambda := 1.05$$

Dimensions on vertical section

$$b(a, \lambda) := a \cdot \lambda \qquad\qquad \text{Drop length}$$

$$r(a, \theta, \lambda) := \sqrt{\frac{a^2 \cdot b(a, \lambda)^2}{a^2 \cdot \sin(\theta)^2 + b(a, \lambda)^2 \cdot \cos(\theta)^2}} \qquad\qquad \text{Radius of elliptic cross-section in polar coordinates}$$

$$\xi(\beta, \lambda) := \frac{\pi}{2} - \operatorname{atan}\left(\frac{\lambda^2}{\tan(\beta)}\right)$$

$$R(a, \beta, \lambda) := r(a, \beta, \lambda) \cdot \cos(\beta) + \alpha \cdot a \cdot \cos(\xi(\beta, \lambda)) \qquad\qquad \text{Wetted radius at drop top}$$

$$R2(a, \lambda) := a \cdot \left(2 \cdot \lambda - \sqrt{\lambda^2 - 1}\right) \qquad\qquad \text{Radius of curvature at drop bottom}$$

Dimensions on horizontal section

$$\chi(\phi) := \operatorname{asin}(\sin(\gamma) \cdot \phi)$$

$$\alpha(a, \alpha, \beta, \lambda, \phi) := \operatorname{asin}\left[\sin(\gamma) \cdot \frac{\phi \cdot a + (R(a, \beta, \lambda) - a)}{R(a, \beta, \lambda)}\right]$$

$$c(a, \phi) := \frac{\phi \cdot a \cdot \sin(\gamma - \chi(\phi))}{\sin(\chi(\phi))}$$

$$A(a, \phi) := 2 \cdot \int_0^{a \cdot \phi \cdot \sin(\gamma)} \left(\sqrt{a^2 - x^2} - c(a, \phi)\right) dx \qquad\qquad \text{Liquid filled groove area}$$

Pressure at Top and bottom of drop profile

$$PT(a,\alpha,\beta) := \sigma \cdot \left(\frac{1}{R(a,\beta,\lambda)} - \frac{1}{a \cdot \alpha} \right) \qquad \qquad \textit{Top}$$

$$PB(a,\lambda) := \frac{2 \cdot \sigma}{\left(\frac{a}{\lambda} \right)} \qquad \qquad \textit{Bottom}$$

Lateral Force Balance

$$Fout(a,\beta,\lambda,\phi) := 2 \frac{\sigma}{a} \cdot (2 \cdot \sin(\chi(\phi)) \cdot a) \cdot (r(a,\beta,\lambda) \cdot \sin(\beta))$$

$$Fin(a,\alpha,\beta,\lambda,\phi) := \sigma \cdot R(a,\beta,\lambda) \cdot \sin(\omega(a,\alpha,\beta,\lambda,\phi)) - -\sigma \cdot \left[\frac{1}{(R(a,\beta,\lambda)) \cdot 0 + (r(a,\beta,\lambda) \cdot \cos(\beta))} - \frac{1}{a \cdot \alpha} \right] \cdot (2 \cdot \sin(\omega(a,\alpha,\beta,\lambda,\phi)) \cdot R(a,\beta,\lambda)) \cdot (r(a,\beta,\lambda) \cdot \sin(\beta))$$

Vertical Force Balance

$$xmin(a,\beta,\lambda) := r(a,\beta,\lambda) \cdot \cos(\beta)$$

$$xmax(a,\beta,\lambda) := R(a,\beta,\lambda) \qquad\qquad \textit{Limits of volume integration}$$

$$V3(a,\beta,\lambda) := 2 \cdot \pi \cdot \int_{xmin(a,\beta,\lambda)}^{a} x \cdot \sqrt{(a^2 - x^2) \cdot \lambda^2} \, dx$$

$$V2(a,\beta,\lambda) := (2 \cdot \pi) \left[\int_{xmin(a,\beta,\lambda)}^{xmax(a,\beta,\lambda)} x \cdot \left[\sqrt{(\alpha \cdot a)^2 - (x - xmin(a,\beta,\lambda) - \alpha \cdot a \cdot \cos(\xi(\beta,\lambda)))^2} - \alpha \cdot a \cdot \cos(\theta) \right] dx \right]$$

$$V1(a,\lambda) := \frac{2}{3} \cdot \pi \cdot a^3 \cdot \lambda$$

$$V(a,\beta,\lambda) := V1(a,\lambda) + (V2(a,\beta,\lambda) - V3(a,\beta,\lambda))$$

$$W(a,\beta,\lambda) := V(a,\beta,\lambda) \cdot \rho \cdot g$$

$$F(a,\alpha,\beta,\lambda,\phi) := (PT(a,\alpha,\beta)) \cdot \left(\pi \cdot R(a,\beta,\lambda)^2 - A(a,\phi) \right) + \frac{2 \cdot \sigma}{a} \cdot A(a,\phi) - (\sigma \cdot 2) \cdot (\pi - \omega(a,\alpha,\beta,\lambda,\phi)) \cdot (R(a,\beta,\lambda)) \cdot \sin(\theta)$$

Linear Solver Block

Given

Geometric equation

$$\frac{\alpha \cdot a \cdot \cos(\theta) - r(a,\beta,\lambda) \cdot \sin(\beta)}{\alpha \cdot a} = \sin(\xi(\beta,\lambda))$$

Vertical force balance

$$W(a,\beta,\lambda) + F(a,\alpha,\beta,\lambda,\phi) = 0$$

Vertical pressure balance

$$(PB(a,\lambda) - \rho \cdot g \cdot a \cdot \lambda) = PT(a,\alpha,\beta)$$

Lateral force balance

$$Fin(a,\alpha,\beta,\lambda,\phi) = Fout(a,\beta,\lambda,\phi)$$

Maximum groove wetting

$$\phi < 2 \cdot \cos(\gamma)$$

$$\begin{bmatrix} a \\ \alpha \\ \beta \\ \phi \end{bmatrix} := Find(a,\alpha,\beta,\phi)$$

Graphic Drop Profile

$$\psi := 0, 0.01 .. 2 \cdot \pi$$

$$xst := r(a,\beta,\lambda) \cdot \cos(\beta)$$

$$yst := -r(a,\beta,\lambda) \cdot \sin(\beta)$$

$$x := 0, 0.1 .. 10 \qquad y(x) := \tan\left(\frac{\pi}{2} - \gamma\right) \cdot x + \left(\frac{\sin(\gamma - \chi(\phi))}{\sin(\gamma)}\right) \cdot a \cdot 10^3$$

$$xe(\psi) := \begin{vmatrix} r(a,\psi,\lambda) \cdot \cos(\psi + \pi) & \text{if } \psi \le \pi - \beta \\ xst & \text{otherwise} \end{vmatrix}$$

$$ye(\psi) := \begin{vmatrix} r(a,\psi,\lambda) \cdot \sin(\psi + \pi) & \text{if } \psi \le \pi - \beta \\ yst & \text{otherwise} \end{vmatrix}$$

$$xin(\psi) := a \cdot \cos(\psi) \qquad xout(\psi) := R(a,\beta,\lambda) \cdot \cos(\psi)$$

$$yin(\psi) := a \cdot \sin(\psi) \qquad yout(\psi) := R(a,\beta,\lambda) \cdot \sin(\psi)$$

$$ys(\psi) := \begin{vmatrix} \left(\alpha \cdot a \cdot \sin\left(\psi + \frac{\pi}{2}\right)\right) - \alpha \cdot a \cdot \cos(\theta) & \text{if } \left(\psi \le \frac{\pi}{2} - \xi(\beta,\lambda)\right) \\ yst & \text{otherwise} \end{vmatrix}$$

$$xs(\psi) := \begin{vmatrix} \alpha \cdot a \cdot \cos\left(\psi + \frac{\pi}{2}\right) + r(a,\beta,\lambda) \cdot \cos(\beta) + \alpha \cdot a \cdot \cos(\xi(\beta,\lambda)) & \text{if } \left(\psi \le \frac{\pi}{2} - \xi(\beta,\lambda)\right) \\ xst & \text{otherwise} \end{vmatrix}$$

OUTPUT ARRAY

$i := 0 .. 100$ $\Psi_i := i \cdot \dfrac{2 \cdot \pi}{100}$

$Xe_i := xe(\Psi_i)$ $Xs_i := xs(\Psi_i)$

$Ye_i := ye(\Psi_i)$ $Ys_i := ys(\Psi_i)$

Liquid Profile Near Dripping Plane

Length range $z := 0.0001, 0.0002 .. 0.1$

Bottom Pressure $Q := PT(a, \alpha, \beta)$ *Groove width* $W := \dfrac{4 \cdot 10^{-3}}{2}$

Radius of LV interfcae curvature $r(z) := \dfrac{\sigma}{\rho \cdot g \cdot z - Q}$

$l(z) := \begin{vmatrix} W & \text{if } \left[r(z) \cdot \sin\left[\dfrac{\pi}{2} - (\theta + \gamma) \right] \right] \le 0 \\[2mm] r(z) \cdot \sin\left[\dfrac{\pi}{2} - (\theta + \gamma) \right] & \text{otherwise} \end{vmatrix}$

Liquid Profile in horizontal axis

$L(z) := \begin{vmatrix} l(z) & \text{if } l(z) \le W \\ W & \text{otherwise} \end{vmatrix}$

OUTPUT ARRAY $i := 0 .. 50$ $Z_i := i \cdot \dfrac{0.008}{50}$ $LL_i := L(Z_i)$

Remarks: Output arrays are plotted in Sigma Plot 4.0

Appendix F
(i) Drop Detachment Period for Dripping from Unsaturated Grooves under Evaporative Conditions

■ Constants

... Physical Constants [MKS system]

The constants listed below denote; water density, acceleration of gravity, surface tension of water, viscosity of water, binary diffusion coefficient of water vapor, gas constant, absolute temperature (20 oC), Hammaker constant, saturated vapor pressure, atmospheric pressure, solid-liquid-vapor contact angle

$\rho := 998;$

$g = 9.8;$

$\sigma = 7.29\,10^{-2};$

$\eta = 10^{-3};$

$DO = 2.13\,10^{-5};$

$R = 462;$

$T = 293;$

$Aslv = 1.9\,10^{-19};$

$Psat = 2337;$

$P = 9\,10^{4};$

$\theta = \dfrac{\pi}{6};$

$\psi cav = 250;$

... Fracture Geometry

Groove angle, groove depth, groove depth:plane width, fracture angularity factor

$$\Upsilon = \frac{\pi}{6};$$
$$L = 5\ 10^{-3};$$
$$\beta = 1;$$
$$Fg[\Upsilon\_] := \frac{1}{Tan[\Upsilon / 2]} - \frac{\pi - \Upsilon}{2};$$

... Drop Base Area

$$AO = 5.6382\ 10^{-5};$$

... Derived Constants [MKS system]

$$U = \rho\ g;$$
$$W = \pi\ \sigma^2;$$
$$DD = -DO\ \frac{10^5}{P}\left(\frac{T}{273.15}\right)^{1.8};$$
$$\Omega = \frac{3}{2}\ \frac{\sqrt{AO\ W}}{\pi\ U};$$

■ Functions

...Flow Resistance Parameter (Ransohoff and Radke, 1988; Or and Tuller, 1999]

$$\epsilon[\Upsilon\_] := 0.966\ Exp\left[0.051\ \frac{\Upsilon\ 180}{\pi}\right] + 7.89$$

...Radius of Curvature of Capillary Meniscus

$$rLV[\psi\_] := \frac{\sigma}{\psi}$$

Appendix F

(ii) Drop Volume and Solute Concentration

Constants

$$\text{TOL} := 10^{-10}$$

$$\rho := 998$$

$$g := 9.8$$

$$\sigma := 7.29 \cdot 10^{-2}$$

$$\eta := 10^{-3}$$

$$\text{DO} := 2.13 \cdot 10^{-5}$$

$$R := 462$$

$$T := 293$$

$$\text{Psat} := 2337$$

$$P := 9 \cdot 10^{4}$$

$$D := -\text{DO} \cdot \frac{10^{5}}{P} \cdot \left(\frac{T}{273.15}\right)^{1.8}$$

Functions

$$M(\psi) := -\frac{2 \cdot D \cdot \text{Psat} \cdot \left(1 - \exp\left(\frac{\psi \cdot \rho}{R \cdot T}\right)\right)}{\rho \cdot R \cdot T}$$

$$N(Q) := \left(\frac{3 \cdot Q}{2 \cdot \pi}\right)^{\frac{2}{3}}$$

$$\text{Qnet}(\psi, Q, \tau) := \frac{2 \cdot \pi}{3 \cdot \tau} \cdot \left(M(\psi) \cdot \tau + N(Q) \cdot \tau^{\frac{2}{3}}\right)^{\frac{3}{2}}$$

File Reading

$$i := 0 .. 66 \quad \psi := \text{READPRN}(\text{"Y-30.prn"}) \qquad Q := \text{READPRN}(\text{"Q-30.prn"}) \qquad \tau c := \text{READPRN}(\text{"T-30.prn"})$$

Volumes and Concentration

Volume of drop
$$Vd_i := \int_0^{\tau c_i} \text{Qnet}\left(\psi_i, Q_i, \tau\right) d\tau$$

Total volume
$$Vt_i := Q_i \cdot \tau c_i$$

Solute Concentration
$$C_i := \frac{Vt_i}{Vd_i}$$

Compiled Output for Graphing

$$\text{Data30}_{i,0} := \psi_i \quad \text{Data30}_{i,1} := \tau c_i \quad \text{Data30}_{i,2} := Vd_i \quad \text{Data30}_{i,3} := C_i$$

100	0.183	$9.941 \cdot 10^{-8}$	1
107	0.24	$9.924 \cdot 10^{-8}$	1
114	0.31	$9.936 \cdot 10^{-8}$	1
121	0.393	$9.937 \cdot 10^{-8}$	1
128	0.492	$9.933 \cdot 10^{-8}$	1
135	0.608	$9.917 \cdot 10^{-8}$	1
142	0.745	$9.904 \cdot 10^{-8}$	1
149	0.903	$9.929 \cdot 10^{-8}$	1
156	1.085	$9.924 \cdot 10^{-8}$	1
163	1.293	$9.928 \cdot 10^{-8}$	1
170	1.53	$9.926 \cdot 10^{-8}$	1
177	1.798	$9.921 \cdot 10^{-8}$	1
184	2.1	$9.928 \cdot 10^{-8}$	1
191	2.439	$9.919 \cdot 10^{-8}$	1.001
198	2.817	$9.936 \cdot 10^{-8}$	1.001
205	3.237	$9.929 \cdot 10^{-8}$	1.001

Data30

$$V(Q,\psi,\tau) := 4 \cdot \pi \cdot \frac{\left[-8 \cdot N(Q)^4 \cdot \sqrt{N(Q) \cdot \tau^{\frac{2}{3}}} + \left(N(Q) + M(\psi) \cdot \tau^{\frac{1}{3}}\right)^2 \cdot \left(8 \cdot N(Q)^2 - 20 \cdot M(\psi) \cdot N(Q) \cdot \tau^{\frac{1}{3}} + 35 \cdot M(\psi)^2 \cdot \tau^{\frac{2}{3}}\right) \cdot \sqrt{N(Q) \cdot \tau^{\frac{2}{3}} + M(\psi) \cdot \tau}\right]}{315 \cdot M(\psi)^3 \cdot \tau^{\frac{1}{3}}}$$

$$\text{Vanalytic}_i := V\left(Q_i, \psi_i, \tau c_i\right)$$
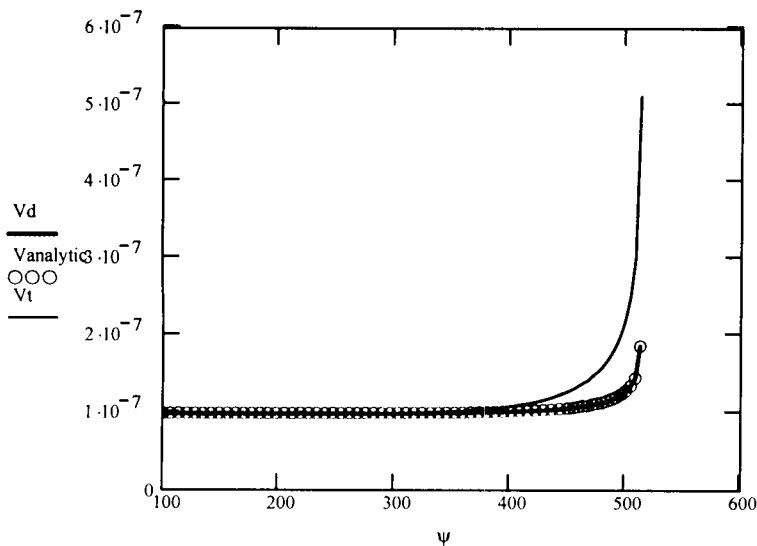
Appendix G

DYNAMIC LIQUID BRIDGE BETWEEN INCLINED PARALLEL PLATES

Physical Constants

$$\rho := 998 \qquad TOL := 10^{-4}$$

$$g := 9.8 \qquad \sigma := 7.29 \cdot 10^{-2} \qquad \eta := 0.1307 \cdot 10^{-2}$$

Geometric Considerations

Fracture Geometry: Spacing (b), Inclination (β) and Roughness (R)

$$b := 0.75 \cdot 10^{-3}$$

$$\beta := \frac{\pi \cdot 0}{2.4} \qquad\qquad R := 10^{3} \qquad\qquad \beta \cdot \frac{180}{\pi} = 0$$

Solid-Liquid Contact Area A, and Solid-Liquid-Vapor Contact Length

$$A(C,D) := 4 \cdot C \cdot D + \pi \cdot C^{2} \qquad P(C,D) := 2 \cdot \pi \cdot C + 4 \cdot D$$

Liquid Volume and Weight

$$V(C,D) := A(C,D) \cdot 2 \cdot b$$

$$W(C,D,v) := V(C,D) \cdot \rho \cdot g$$

Liquid-vapor interface: top half defined by radii = **C** and **b** and zero contact angle; bottom half defined by radii = **C** and **bb** and contact angle = θ

$$bb(C,D) := \frac{-\sigma \cdot b}{-\sigma + 2 \cdot (C + D) \cdot b \cdot \rho \cdot g \cdot \cos(\beta)}$$

$$\theta(C,D) := acos\left(\frac{b}{bb(C,D)}\right)$$

Forces

Force due to pressure

$$FP_{lat}(C,D) := \frac{-\sigma}{2} \cdot \left[\left(\frac{1}{C} - \frac{1}{b}\right) + \left(\frac{1}{C} - \frac{1}{bb(C,D)}\right) \right] \cdot A(C,D)$$

$$FP_{up}(C,D) := \left(FP_{lat}(C,D)\right) \cdot \frac{b - bb(C,D) \cdot (1 - \sin(\theta(C,D)))}{b}$$

Force due to surface tension

$$FS(C,D) := 2 \cdot C \cdot \sigma \cdot (1 - \cos(\theta(C,D)))$$

Force due to viscous drag

$$FV(C,D,v) := \frac{32}{3} \cdot R \cdot C \cdot \eta \cdot v$$

Total Upward force along the inclined plane

$$FUP(C,D,v) := FP_{up}(C,D) + FS(C,D) + \frac{FV(C,D,v)}{2}$$

Total Downward force along the inclined plane

$$FDN(C,D,v) := W(C,D,v) \cdot \cos(\beta)$$

Illustrative Example

Guesses $C := \dfrac{b}{2}$ $D := 0$ $v := 10^{-3}$ $TOL := 10^{-9}$ $q := 30 \cdot 10^{-4}$

Solution I: Static

Given

$$FDN(C,D,v) = 2 \cdot FUP(C,D,v) \qquad D \geq 0$$

$$WT = W(C,D,v) \qquad v = 0$$

$$S(WT) := Find(C,D,v)$$

Solution II: Dynamic

Given

$$FDN(C,D,v) = 2 \cdot FUP(C,D,v) \qquad D \geq 0$$

$$WT = W(C,D,v) \qquad v \geq 0$$

$$S1(WT) := Find(C,D,v)$$

Solution III: Dynamic, minimum Velocity

Given

$$FDN(C,D,v) = 2 \cdot FUP(C,D,v) \qquad D \geq 0$$

$$q = W(C,D,v) \qquad v \geq 0$$

$$S2 := Minimize(FV,C,D,v)$$

$$S(q) \cdot 10^3 = \begin{bmatrix} 6.836 \\ 2.11 \\ 0 \end{bmatrix} \qquad S1(q) \cdot 10^3 = \begin{bmatrix} 6.831 \\ 2.119 \\ 0.325 \end{bmatrix} \qquad S2 \cdot 10^3 = \begin{bmatrix} 6.836 \\ 2.11 \\ 0 \end{bmatrix} \qquad AS(WT) := \dfrac{S(WT)_0 + S(WT)_1}{S(WT)_0}$$

$$WT := 1 \cdot 10^{-4}, 1.5 \cdot 10^{-4} .. 30 \cdot 10^{-4}$$

Aspect Ratio

(y-axis: Aspect Ratio of S-L Contact Area; x-axis: Drop Weight (1e4 N))
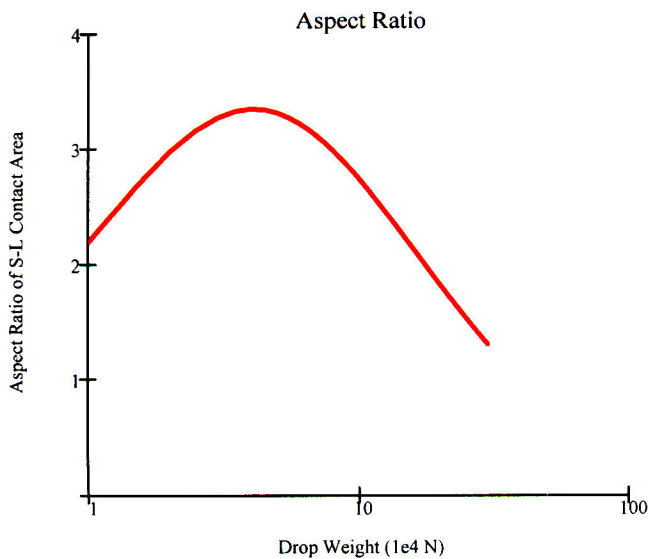
Fracture Geometry
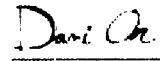
Inclination	$\beta \cdot \dfrac{180}{\pi} = 0$	
Spacing	$2 \cdot b \cdot 10^3 = 1.5$	
Roughness	$R = 1 \cdot 10^3$	

Volume 2: Dripping into Cavities from Unsaturated Fracture under Evaporative Conditions

III. Liquid Bridges and Liquid Fingers, Dripping Experiments under Evaporative Conditions

Unsaturated and Saturated Flow under Isothermal Conditions –
Key Technical Issue - Dani Or - 9/22/2000
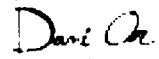
Account Number: 20-01402-861

Collaborators: Teamrat A. Ghezzehei (USU), Randall Fedors

Directories: C:/dripping_notebook
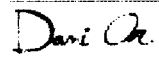
Objective: this study is a sequel to the second part of the current volume. The objectives of the study are to present more detailed description of liquid-bridge formation, fingering and intermittent flow in unsaturated fractures; and design an experimental setup to test the analytical model of dripping into cavities from unsaturated fractures, presented in the first part of the current volume of scientific notebook (Or and Ghezzehei, 1999), with special emphasis on effects of evaporation.

Initial Entry – 02/10/2000:

In the second part of this scientific notebook (#354) introduction to intermittent flow in unsaturated fractures was presented. Further developments to the model and illustrative examples, and preliminary experimental results are presented in the current section. Experimental testing of the analytical dripping model presented in first and second section of the current volume (#354) with special emphasis to effect of evaporation is also discussed.

02/15/2000 Suspended Stationary Liquid Bridge

Model Development

Modeling of liquid configuration between two confining parallel surfaces has been a topic of numerous theoretical studies. However, most analyses either ignored effects of gravity [Carter, 1988] or considered liquid bridges in horizontal gaps only [Meseguer,1983; Padday et al., 1997]. Modeling the behavior of a liquid bridge between non-horizontal parallel plates in the presence of gravitational forces presents a challenge as will be shown shortly. The starting point for the analysis is the configuration and growth of a small (initially circular) liquid bridge. There are several possible mechanisms by which a "seed" bridge can be formed, including: abrupt narrowing of fracture aperture, the presence of asperity contact, and a residual (trapped) liquid element too small to flow. Because the liquid in the "seed" bridge is likely to be at a lower energy state than the liquid in films and matrix (due to lower interfacial area per unit liquid volume), it attracts liquid flow causing a gradual increase

in bridge volume with subsequent changes in its configuration. Assuming (as a first approximation) that the flux feeding the bridge is constant, two primary questions of interest are: (1) the maximum bridge size that could exist in the fracture; and (2) the optimal configuration of the bridge. Answers to these two questions should provide estimates for subsequent finger size and length (as will be shown next). Furthermore, description of liquid-vapor configurations for a growing bridge facilitates investigation of dynamic aspects of bridge breakup (and motion) under its own weight.

A definition diagram for the geometry of the problem is given in Fig.28. A liquid bridge is suspended between parallel solid surfaces spaced at 2·b. The upper and lower portions of the liquid bridge are represented by circular arcs of radius C_t and C_b, respectively. The
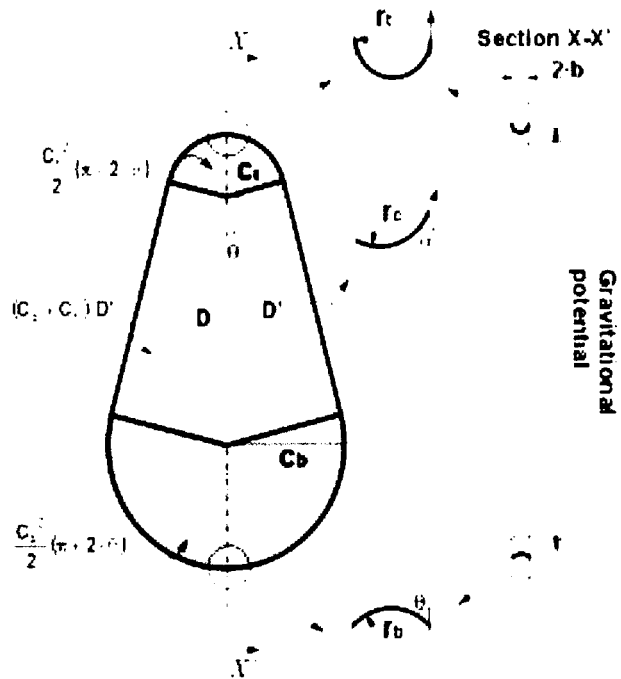
Figure 28: A definition sketch for a liquid bridge suspended in a gap between parallel solid surfaces representing a fracture with aperture size of 2b.

tangential lines connecting the arcs are off the vertical by an angle of θ. The centers of the arcs are separated by D. The wetted area of one plane can be approximated by,

$$A = V/(2 \cdot b) \tag{78}$$

The radius of the bottom arc (C_b) and the distance between the centers of the arcs (D) can be expressed in terms of Ct, A, b and θ as,

$$f = \frac{C_b}{C_t} = \sqrt{\frac{\dfrac{A}{C_t^2} - \dfrac{\pi}{2} + \theta + \dfrac{1}{\tan(\theta)}}{\dfrac{\pi}{2} + \theta + \dfrac{1}{\tan(\theta)}}} \tag{79}$$

$$D = \frac{C_b - C_t}{\sin(\theta)} \tag{80}$$

Assuming a perfectly wettable plate surface, the radius of equilibrium curvature at the top of the liquid bridge is equal to the aperture size (2·b). The difference in capillary pressure between the top and the bottom of the liquid-bridge is due to the difference in

gravitational potential energy,

$$\sigma \cdot \left(\frac{1}{C_t} - \frac{1}{b} \right) - \sigma \cdot \left(\frac{1}{C_b} - \frac{1}{r_b} \right) = -\rho\, g\,(C_t + C_b + D) \tag{81}$$

Then, the bottom radius of curvature (r_b) can be obtained by rearranging Eq (81),

$$r_b = \cfrac{1}{\cfrac{1}{b} + \cfrac{1}{C_t}\left(\cfrac{1}{f} - 1 \right) - \cfrac{\rho \cdot g \cdot C_t}{\sigma}\left(1 + f + \cfrac{f-1}{\sin(\theta)} \right)} \tag{82}$$

Similarly, the radius of curvature at the midpoint of the side-walls (r_c), is given by,

$$r_c = \cfrac{1}{\cfrac{1}{b} - \cfrac{1}{C_t} - \cfrac{\rho \cdot g \cdot C_t}{\sigma}\left(1 + \cfrac{f-1}{\sin(\theta)} \right)} \tag{83}$$

The liquid wetting contact angle at the bottom (α) and the midpoint of the sidewalls (β) are given by,

$$\alpha = a\cos\left(\frac{b}{r_b} \right) \tag{84}$$

$$\beta = a\cos\left(\frac{b}{r_c} \right) \tag{85}$$

The liquid bridge is held in place by a balance between liquid-vapor surface tension and gravitational forces. For vertical parallel plates the surface tension forces are those that act on all the solid-liquid-vapor contact line. The vertical components acting on the top arcs, sidewalls and bottom arc are given by, respectively,

$$F_{top} = 2 \cdot \sigma \cdot C_t \cdot (\cos(2 \cdot \theta) + 1) \tag{86}$$

$$F_{side} = 4 \cdot \sigma \cdot D \cdot \cos(\theta) \cdot \sin(\theta) \cdot \cdot \sin(\beta) \tag{87}$$

$$F_{bottom} = -2 \cdot \sigma \cdot C_t \cdot (\cos(2 \cdot \theta) + 1) \cdot \cos(\alpha) \tag{88}$$

The capillary force exerted by the liquid-vapor-solid interface is balanced by the liquid weight (W).

$$W = V \cdot \rho \cdot g \tag{89}$$

The configuration of a liquid bridge must satisfy the following force balance equation:

$$F_{top} + F_{side} + F_{bottom} = W \tag{90}$$

When the liquid volume is increased beyond the critical maximum, two processes can follow. The first mechanism is marked by the onset of motion of the entire liquid bridge as a unit. Viscous drag along the liquid-solid interface of the path provides the force required to carry the excess weight, where the liquid bridge attains a constant velocity proportional to the excess weight. More details on the calculation of velocity of the liquid bridge traveling in this manner and reconfiguration of the liquid-bridge shape are underway. The second potential mechanism is the elongation of the liquid bridge under the excess weight, and eventual breakage of the bottom part of the bridge. The occurrence of this mechanism is more likely when the bridge is initially formed around an asperity, or when the bridge is anchored to a solid surface that prohibits motion of the liquid bridge as a unit. Determination of the largest liquid bridge size that can develop under an asperity is shown in the next subsection, followed by analysis of the elongation and breakage phase of the growth (see Appendix H for details).

Results

For illustration purposes, herein are provided sample calculations for the configuration of stationary liquid bridges of different volumes that form between parallel fracture surfaces with various apertures. For any aperture size (2·b), and liquid volume (V), several combinations of θ and C_t can satisfy the force balance Eq. (90) as shown in Fig 29a. The configuration selected is that results in minimum surface area (also representing minimum free energy per unit volume of the liquid). Since the spacing restricts the liquid thickness, the length of the liquid-solid-vapor contact line can represent surface area. The selected θ value results in minimum perimeter as shown in Fig 29b.

There exists a maximum limit of liquid volume that can be supported
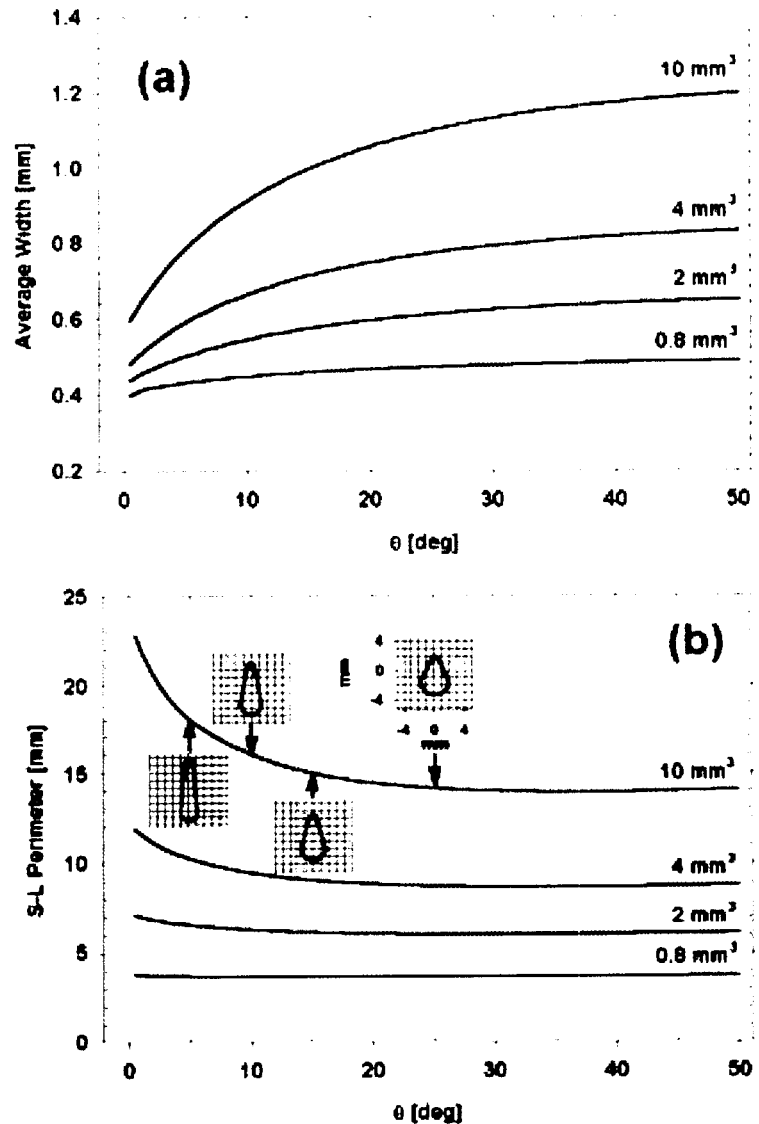
Figure 29: Sample calculations for stationary bridges formed in a 0.8 mm fracture aperture with: (a) average bridge width (C_{top}) for different volumes as a function of bridge spanning angle (θ) and (b) solid-liquid perimeter length (a measure of interfacial energy per unit volume) as a function of θ.

by surface tension alone. This maximum liquid volume associated with particular plate spacing could be described by a maximum permissible liquid-contact angle (α) at the bottom of the liquid bridge. The maximum angle that can exist as a contact angle is α=90°. However, smaller angles can also be selected, e.g., if only negative radius of curvature is allowed then the maximum limit is α=90°.

Experimental results of Su et al. [1999] depicting slowly moving water bridges in a rough-glass fracture model are shown in Fig. 30 (for aperture size of 0.66 mm) along with calculated liquid

Figure 30: Measured and predicted liquid bridges in artificial fracture made of rough glass surfacs with aperture size of 0.66 mm [Su et al., 1999]. The measured bridges/fingers are in motion at a rate of about 0.5 cm/s. The calculated shape of the stationary bridges will likely be less elongated under the influence of a drag force.

bridge configurations. The same liquid volume of 200 mm3 was used for the calculations with different bridge angle θ (other conditions such as fracture inclination angle, etc., were kept similar to the experimental values reported by Su et al., [1999] for their experiment C. The calculated bridge size is within the range of measured bridge sizes, however, because the measured bridges were in motion (at a rate of about 0.5 cm/s) their shape is expected to be less elongated than the calculated stationary bridges due to the influence of a drag force. Additional experimental examples of liquid bridges provided by Glass et al. [1994] (not shown) are in reasonable agreement (considering these were also slowly moving bridges/fingers). Work is underway to introduce drag force to the force equations and calculate equilibrium liquid bridge configuration under steady velocity (including consideration of surface roughness effects on advance and mass-loss rates and the resulting "fingers"). Additional experiments are required to verify the usefulness of the calculated liquid bridge configurations.

02/20/2000: Liquid Bridge Suspended from Fracture

Discontinuity or Contact Asperity

A special type of asperity is considered in this we section. The lateral extent of a solid-solid contact asperity (a solid spacer) forming between parallel fracture surfaces is considerably wider than the largest stationary liquid bridge feasible, as shown in Fig 31. A liquid bridge 2·r wide is suspended below the spacer. The liquid body consists of rectangular shape (α·r x 2·r) and semi-circular bottom of radius r. The radius of

---

curvature just below the solid support is equal to the half-spacing (b).

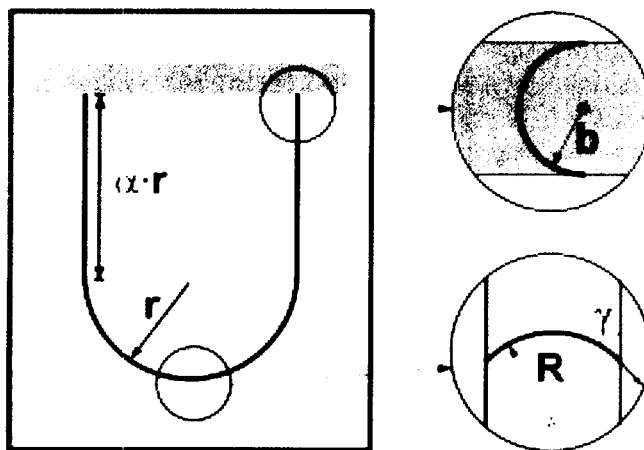The liquid-solid contact area under this support is given by,

Figure 31: Geometry and liquid-vapor interfacial curvatures for a liquid bridge suspended below an asperity or fracture discontinuity.

$$A = 4 \cdot b \cdot r \tag{91}$$

The radius of curvature and liquid contact angle at the bottom of the bridge are determined using similar approaches as described in subsection (2.1),

$$\frac{1}{R} = \frac{1}{b} - \frac{\rho \cdot g \cdot r}{\sigma}(1+\alpha) + \frac{1}{r} \tag{92}$$

$$\gamma = a\cos\left(\frac{r}{R}\right) \tag{93}$$

where α is aspect ratio of the rectangular liquid body. The major force supporting the liquid bridge is capillary force acting on the solid spacer of area A (91).

$$Fc = \frac{\sigma}{b}\left(4 \cdot b \cdot r - \pi \cdot b^2\right) \tag{94}$$

In addition, surface tension acts along the solid-liquid-vapor contact lines at the spacer and the bottom arc,

$$Fs = 2 \cdot \sigma \cdot \pi(b - r \cdot \cos(\gamma)) \tag{95}$$

The shape of the liquid bridge satisfies balance between the capillary/surface tension forces and weight of the liquid bridge,

$$Fc + Fs = 2 \cdot b \cdot \rho \cdot g \cdot r^2 \cdot \left(2 \cdot \alpha + \frac{\pi}{2}\right) \tag{96}$$

For a given aperture size (2·b) several sets of α and r satisfy the force balance equation (96). The relationship between the liquid bridge width (and volume) and aspect ratio parameter (α) for selected apertures (2·b) is shown in Fig. 32. For a particular aperture the liquid volume attains a maximum value at a unique combination of α and r (denoted by symbols in Fig 32). It is assumed that the liquid bridge grows until it reaches the maximum volume and proceeds to elongation and breakage phase. Then follows a similar line of reasoning as Or and Ghezzehei [2000] for suspended pendant drop in designating bridge width (2·r) at the maximum volume (that also satisfies the force balance equation) as an initial condition in subsequent analysis of elongation and breakage of liquid bridges. The relationship between the liquid bridge width (2·r) and aperture size (2·b) can be derived from Fig 32, as depicted in Fig 33. The increase in curvature (hence, capillary pressure) with decreasing aperture size (2·b) results in wider liquid-bridges. It is also interesting to note that the bridge anchoring area is practically constant for aperture sizes up to 1.5 mm (see Appendix I for details).
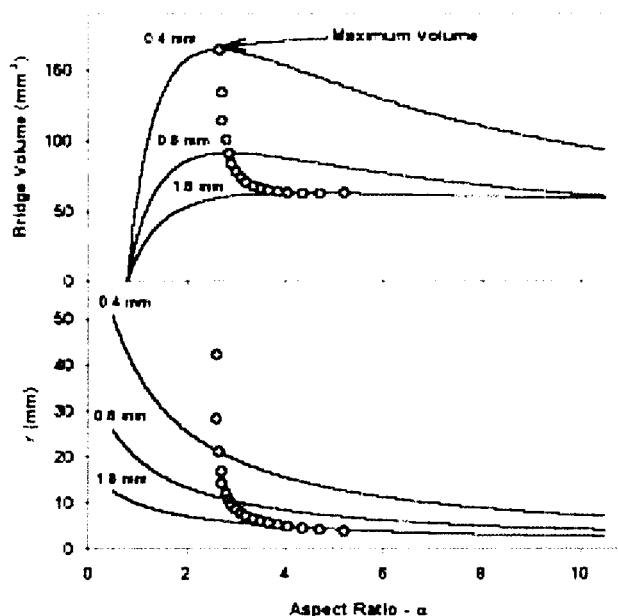
Figure 32: Suspended bridge volume (top) and bridge radius (bottom) as a function of aspect ratio (α) and three aperture sizes. (Symbols signify values of maximum bridge volume)
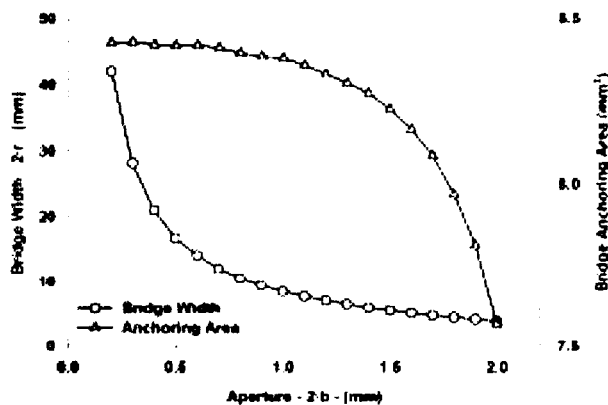
Figure 33: The width of the largest bridge volume and the associated liquid bridge anchoring area as a function of fracture aperture size.

04/10/2000: Elongation and Breakage of Liquid bridges

The analysis of bridge rupture (or internal dripping such as described by Kneafsy and Pruess, 1998) follows a similar path as the analysis of liquid dripping from fractures into subterranean cavities [Or and Ghezzehei, 2000]. As the liquid bridge elongates, the interplay between capillary, gravity and viscous forces determines the conditions and location of a potential rupture plane. The primary difference between "dripping" in

fractures and in free air is the presence of restraining forces for an elongating bridge due to solid-liquid interactions absent in dripping in free air [Or and Ghezzehei, 2000]. Additionally, liquid-vapor interfacial configurations and contribution to the viscous elongation and rupture process are slightly different. Consequently, "dripping" rates within fractures for a given flux are expected to be slower than dripping in free air.

The growth and detachment of liquid bridges between rough parallel-plates is tracked in a Lagrangian coordinate system (see Fig. 34). The process of elongation occurs in the rectangular region of the liquid bridge. At the beginning of the process (t=0) only the semi-circular portion of the liquid bridge is considered. A constant flux (Q) contributes to buildup of liquid mass below the anchoring plane

Lagrangian coordinate system

Force Components
① SL- Interfacial Stress
② LV- Interfacial Stress
③ Viscous drag (no-slip)
④ Resistance to shrinkage

Figure 34: Force components, their origin and direction in an elongating suspended liquid bridge (stresses due to viscous extension rates are not marked). Liquid elements are labeled by τ (a one-dimensional time-like element tracking Lagrangian coordinate).

(and above the semi-circular region). Subsequently, viscous extension due to increased liquid weight occurs in this portion of the liquid bridge. All fluid elements above the semi-circle are labeled by Lagrangian time variable (τ), representing the elapsed time since an element joined the elongating bridge. Longitudinal and lateral forces acting at any fluid element (τ) are considered.

Longitudinal forces

The longitudinal forces represent a balance between gravitational (weight of the liquid bridge) and surface tension. The weight of liquid supported by any fluid element (τ) consists of a constant weight of the semi-circular leading portion (note this also represents a recoil volume), and a variable extending portion. The constant weight of the semi-circular leading portion is function of the aperture only (see section 2.2). The weight of the extending liquid portion is function of time and flux.

$$W = \rho \cdot g \cdot \left(\pi \cdot r^2 \cdot b + Q \cdot \tau\right) \tag{97}$$

Surface tension of the liquid-vapor interface on both sides of a cross-section resists axial extension of the interface according to,

$$F_{LV} = 2 \cdot \pi \cdot b \cdot \sigma \tag{98}$$

The solid-liquid contact line along the wetted portion of the plates resists extension in a manner similar to the liquid-vapor interface. The actual solid-liquid contact line is longer than the apparent length due to surface roughness. A roughness factor (ratio of actual length to apparent length) is introduced to account for the increases length (and force).

$$F_{LS} = 4 \cdot R \cdot y \cdot \sigma_{LS} \tag{99}$$

where σ_{LS} is liquid-solid surface tension, R is roughness coefficient ($R \geq 1$), and y is wetted (solid) length.

Extension of the liquid bridge between parallel plates involves viscous shearing of liquid molecules adjacent to the fracture walls. The resistance due to shearing is analogous to settlement of zero-thickness discs in viscous fluid (bridge wetting area can be represented as an equivalent disc in anticipation of reconfiguration of the detached element). The force due to shearing can be written as,

$$F_V = \frac{24}{Re} \cdot \frac{A_w \cdot \rho}{2} \cdot v^2 \tag{100}$$

where Re is Reynolds' number, A_w is the wetted area below τ, and v is longitudinal velocity of extension.

The net longitudinal stress acting across element τ, is obtained by summing up Eqs (97)-(100),

$$S = \frac{W - (F_{LV} + F_{LS} + F_V)}{A} \tag{101}$$

where $A = 4 \cdot y \cdot b$ is liquid cross-sectional area at element τ.

Lateral forces

The liquid-vapor and liquid-solid interfaces at element t, resist lateral shrinkage of the liquid bridge according to,

$$F_H = 2 \cdot \pi \cdot b \cdot \sigma + 4 \cdot R \cdot y \cdot \sigma_{LS} \tag{102}$$

The first term in (102) is due to liquid-vapor interface resistance, and the second term is due to liquid-solid resistance.

Viscous dissipation of energy due to shrinkage of the liquid cross-section results in resistive force proportional to the rate of extension. This term provides the rate dependence of the liquid elongation and detachment process.

$$F_\eta = A \cdot \lambda \frac{1}{y} \cdot \frac{dy}{dt} \tag{103}$$

where $A = 4 \cdot y \cdot b$ is liquid cross-sectional area at element t, and $\lambda = 3 \cdot \eta$ is liquid viscosity in compression (η is shearing viscosity) assuming liquid incompressibility (i.e., Poisson's ratio of 0.5).

The resultant lateral stress at element τ, has a longitudinal component given by,

$$S = \frac{F_H + F_\eta}{A} \cdot \upsilon \tag{104}$$

where $\upsilon = 0.5$, is Poisson's ratio for incompressible liquid.

Bridge detachment

With the cross-sectional stress at any element τ is given by (101) and (104), we equate these two expressions to derive a general expression for liquid bridge breakage,

$$W - \left(F_{LV} + F_{LS} + F_V\right) = \left(F_H + F_\eta\right) \cdot \upsilon \qquad (105)$$

The problem can be simplified if we consider pre-wetted walls where pits and grooves on the rough surfaces are "primed", i.e., completely liquid-filled. We can then ignore solid-liquid interactions and write (105) in its expanded form as,

$$\frac{dy}{dt} = -\frac{\pi \cdot \rho \cdot g \cdot b \cdot r^2 - \pi \cdot b \cdot \sigma + \rho \cdot g \cdot Q \cdot \tau}{6 \cdot \eta \cdot b} \qquad (106)$$

Upon integration (106) gives,

$$y(t) = -\frac{\pi \cdot \rho \cdot g \cdot b \cdot r^2 - \pi \cdot b \cdot \sigma + \rho \cdot g \cdot Q \cdot \tau}{6 \cdot \eta \cdot b} \cdot t + C \qquad (107)$$

where C is a constant of integration, that can be obtained from the boundary condition at the top of the liquid bridge, $y(\tau) = r$ (see also Fig 34).

$$C = -\frac{-6 \cdot \eta \cdot b \cdot r - \pi \cdot \rho \cdot g \cdot b \cdot r^2 \cdot \tau - \pi \cdot b \cdot \sigma \cdot \tau - \rho \cdot g \cdot Q \cdot \tau^2}{6 \cdot \eta \cdot b} \qquad (108)$$

Detachment of the liquid bridge occurs when the cross-section of the liquid bridge goes to zero. The time of detachment can be obtained by setting Eq. (107) to zero,

$$t = -\frac{-6 \cdot \eta \cdot b \cdot r - \pi \cdot \rho \cdot g \cdot b \cdot r^2 \cdot \tau - \pi \cdot b \cdot \sigma \cdot \tau - \rho \cdot g \cdot Q \cdot \tau^2}{\pi \cdot \rho \cdot g \cdot b \cdot r^2 - \pi \cdot b \cdot \sigma + \rho \cdot g \cdot Q \cdot \tau} \qquad (109)$$

The fluid element that detaches first satisfies additional constraint, $dt/d\tau = 0$. This leads to an explicit solution for the first element that ruptures,

$$\tau = \frac{6 \cdot \eta \cdot b \cdot r \cdot \rho \cdot g \cdot Q + \pi \cdot b \cdot \left(-\rho \cdot g \cdot r^2 + \sigma\right)}{\rho \cdot g \cdot Q} \qquad (110)$$

The time at which the first element detaches is obtained by substituting τ_c into Eq (109). The volume of the detached liquid bridge (V_d) is obtained simply by integrating the volumetric flux over the duration of bridge elongation cycle (from $\tau = 0$ to $\tau = \tau_c$).

$$V_d = \tau_c \, Q \qquad (111)$$

At the time of detachment of the first bridge ($t^1{}_c$), a portion of the liquid suspended at the tip of the spacer remains behind. The volume of the remaining liquid (analogous to the

recoil volume in free dripping) is associated with the time difference ($\tau_o = t^1{}_c\text{-}\tau_c$). Because all subsequent bridges start their cycle with an existing recoil volume, the period of detachment after the first bridge pinches is reduced by the time equivalent to the recoil volume (τ_o),

$$t_c = t^1{}_c - \tau_o = \tau_c \qquad\qquad (112)$$

In other words, Eq (112) states that the volume of liquid extruded from the outlet during an interval between two successive bridge breakup events is equal to the volume of the detached bridge element (details of the above derivation are shown in Appendix J(a)).

Results

The first set of calculations of liquid bridge detachment focused on the role of aperture size and flux on detachment interval (period). Results shown in Fig. 35a reveal that the period between adjacent detachment events increases for narrower apertures (and with smaller fluxes). The primary reason for the longer period in fractures with smaller apertures is the restraining effects of solid-liquid interactions that become more dominant (per unit liquid volume) in smaller fractures.

The force that supports the liquid weight is mainly contributed by the wetted solid area. The specific force (per unit volume) increases as the aperture size decreases; hence, narrow fracture apertures generally support larger liquid bridges. The effect of volumetric flux on bridge volume is through rate of viscous extension. However, the effect of changes in volumetric flux is very minimal compared to the effect of change in aperture size, as
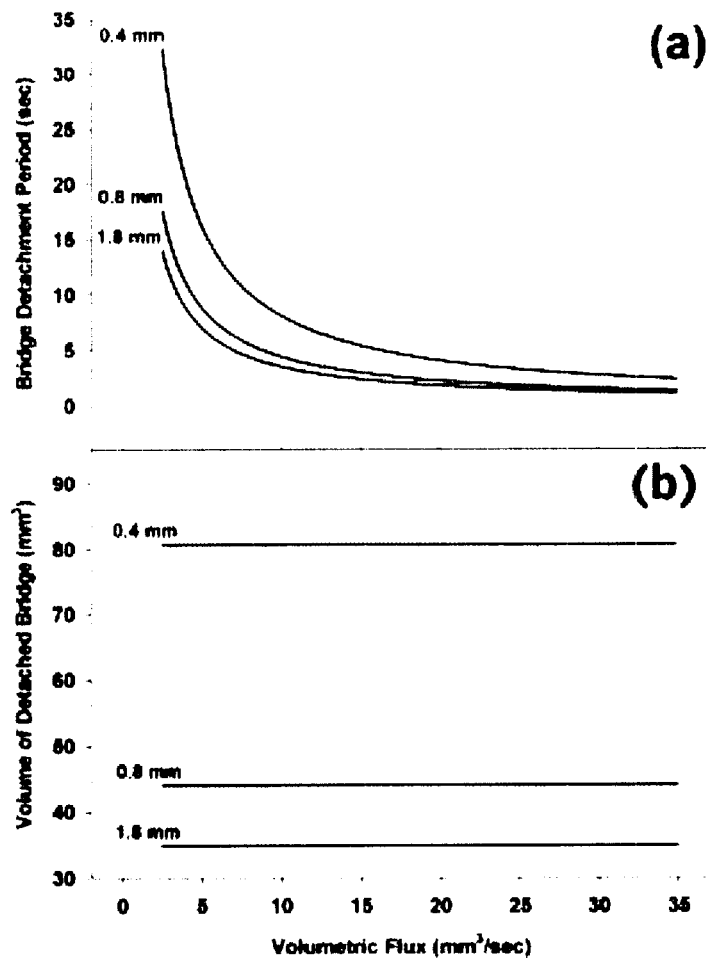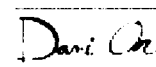

Figure 35: Calculated detachment intervals (a) and volume of detached liquid bridge (b) as functions of volumetric flux in three different fracture apertures.
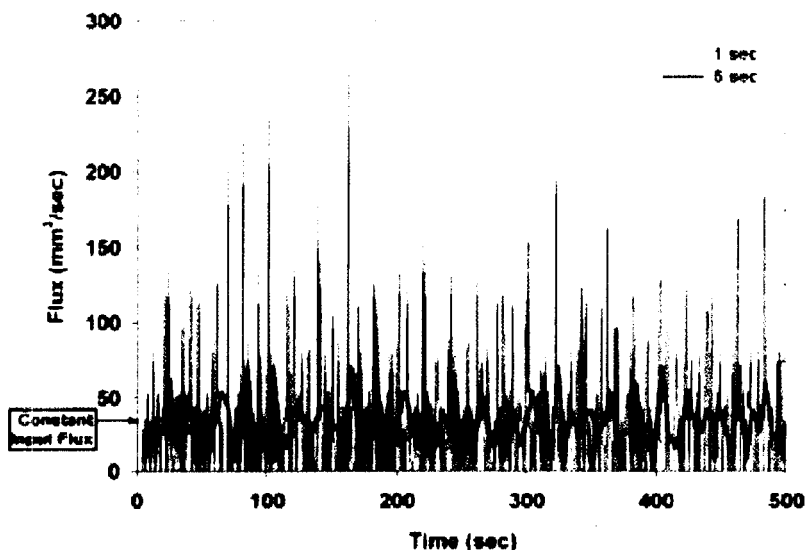
shown in Fig. 35b.

04/30/2000: Role of Bridge Detachment in Intermittent Flow

The primary motivation for modeling liquid bridge detachment is the potential effect of such periodical events on the onset of intermittent flow in unsaturated FPM. Two aspects of this cyclic process are of interest: (1) the detachment volume and the period associated with a particular fracture aperture/asperity and a certain liquid flux; and (2) the size and spatial distribution of geometrical attributes giving rise to bridge detachment within a fracture section. For illustration purposes, we consider only non-interacting bridges that contribute to flow from a fracture section (length). In real FPM, one should consider interactions among detaching liquid elements such as modeled by Cheng et al., [1989]. Such interactions are likely to involve avalanche-like processes depending on the spatial distribution of bridges, detaching liquid mass, path length, and surface characteristics (roughness, wetness, etc.). It will be shown that even with a simple superposition such as employed in this study, the resulting flux behavior at the bottom of a hypothetical fracture becomes very intermittent with chaotic-like patterns.

Sample calculations show that even small variations in aperture geometry and roughness induce a relatively rich temporal behavior of the resultant flux. For illustration purposes, consider temporal variations in liquid flux collected from a fracture with five local aperture variations that is fed by a steady flux (30 mm^3/sec) from the top. The result depicted in Fig. 36 reveals a flux pattern that appears erratic (at the 1 sec sampling interval). The average input flux could be recovered with larger sampling window (>5 sec). The remarkable result from only five local perturbations are quite similar to experimental data of Prazak et al. [1992] shown in Fig. 37. Time averaging calculations are given in Appendix J(b).

Aperture - b (mm)	Period - t (sec)	Volume - V (mm^3)
0.2	20.127	140.91
0.4	11.530	80.71
0.6	7.711	53.97
0.8	6.280	43.96
1.8	4.985	34.91

Figure 36: Volumetric flux fluctuations from a fracture with five different asperity/local aperture sizes (see table above) fed by a steady flux of 30 mm^3/sec. Two averaging periods (sampling periods)

The processes giving rise to such a complex flux pattern could be considered as characteristic of chaotic behavior [Pruess et al., 1999; Faybashinko et al., 1998]. Several points are of interest here: first, the resulting pattern is repeatable over considerably long periods of the order of the product of individual "dripping" periods in the fracture. Second, there is a distinct possibility of extracting aspects of fracture internal geometry from the seemingly "chaotic" pattern, given the average flux (long time average should equal input flux) and fracture nominal aperture size. Although the details of the proposed inversion procedure are beyond the scope of this review, it is a simple matter to visualize application of Fourier analysis for extraction of characteristic frequencies (periods) that could then be associated with local aperture/roughness combinations. In short, the complex behavior produced by a few aperture perturbations is not chaotic in the classical sense, but rather represents a convoluted temporal response due to interplay between geometry, viscous, gravity and surface tension forces.
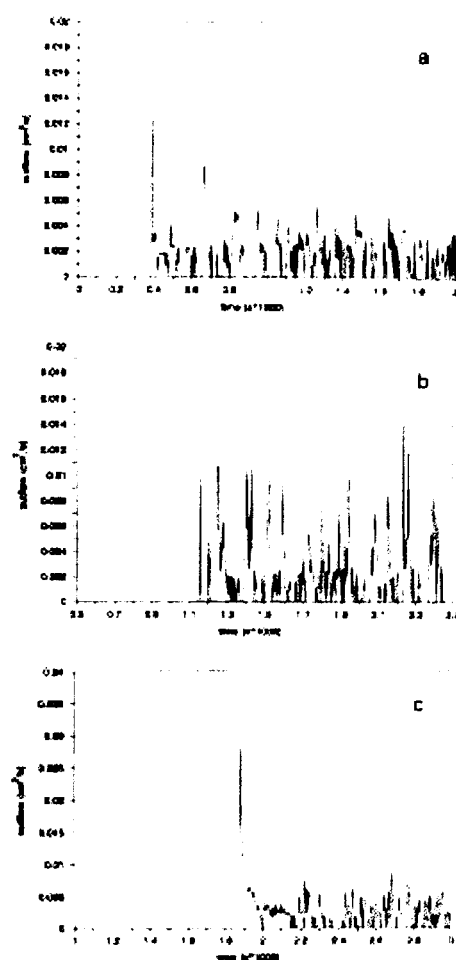

Figure 37: Outflow from gravity-driven flow in coarse porous medium (a) dry medium point inflow; (b) wet medium point inflow; and (c) wet medium - inflow distributed over surface (Prazak et al., 1992]

Fingering and liquid channeling

Following passage of a liquid bridge the finger-shaped wetted surface presents considerably different conditions for flow than the surrounding dry surfaces. Surface depressions become liquid-filled, hence contact angle and drag forces for subsequent liquid bridges are likely to be considerably lower. These modifications also result in an increase in the travel velocity of liquid bridges sliding down the fracture. Moreover, these wet fingers represent preferential pathways with less resistance to flow than other regions on the fracture surface (this does not mean that the resulting pathways were not preferential in some sense from the outset of flow). Application of relatively high flux could induce formation of continuous liquid threads [Su et al., 1999] with considerable temporal variations but remarkably stable areal coverage [Pruess et al., 1999]. The onset and location of a finger is probably associated with local geometrical perturbations

such as abrupt changes in surface roughness or aperture size, and the presence of an asperity contact. Additionally, liquid accumulation and behavior at regions above the plane of interest could also affect the position of a finger, for example by introduction of localized inertial perturbations (directly below a bridge forming at a higher position).

Invasion percolation studies [Glass et al., 1998] attribute the formation of continuous liquid clusters (channels) to networks of narrow apertures (and asperity contacts) forming between two rough-walls of a fracture. These types of studies are primarily based on capillary behavior and are probably more applicable for (1) near-horizontal fractures where gravitational forces are negligible; or (2) for fractures with very small nominal aperture size. These models also provide a means for describing phase entrapment and dissolution behavior, including derivation of constitutive hydraulic properties for

Figure 38: Simulated fingering developing during liquid flow in a fracture plane with (top) low fracture effective permeability; and (bottom) higher permeability [Pruess, 1999].

such systems [Pruess and Tsang, 1990; Glass and Nicholl, 1995]. They, however, do not provide insights into intermittent flow behavior.

In a recent study by Pruess [1999], synthetic permeability fields within rough-walled (vertical) fractures were used to illustrate formation of fingering and channeling patterns within the 2-D simulation space (Fig. 38). The fracture plane with the high permeability $(10^{-7}~m^2)$ shows more pronounced fingering than low in the top plane with higher permeability $(10^{-9}~m^2)$. This effect that resulted from application of a continuum approach (Richards equation) could also be explained simply by the more dominant role of gravity in the fracture with higher permeability. Although, the phenomenon of fingering and liquid channeling was not investigated in this study, it is a natural outcome of introduction of motion to stationary bridges (when a certain mass threshold is exceeded). Expanding on the ideas of Glass et al. [1994] by treatment of formation and dynamics of clusters or discrete liquid elements as basic units would lead to a better understand fingering in fractures.
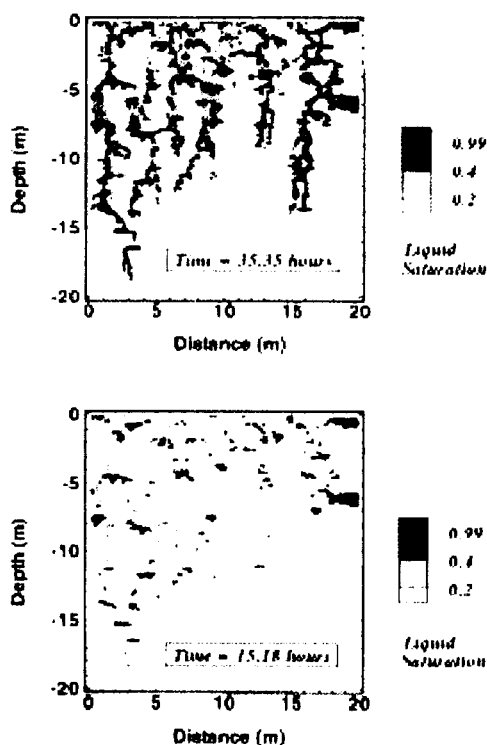
05/10/2000: Preliminary experimental results –

Bridge detachment dynamics

A limited number of experiments were conducted in a fracture model made of two parallel rough-walled glass plates. Several aspects of the proposed theory were tested, focusing here on results pertaining to bridge detachment behavior. The experimental system (Fig. 39) consisted of a calibrated peristaltic pump with a regulator (to reduce flow oscillations) supplying a steady flux to the top of a glass fracture model. Glass
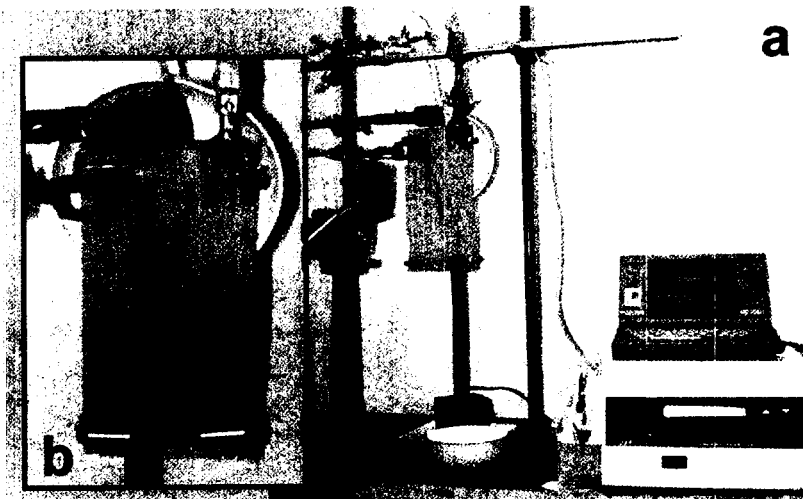

Figure 39: (a) Experimental setup used for testing bridge detachment dynamics; and (b) A close-up of a finger (wet path) and a bridge forming at the top of the fracture glass model.

spacers were used to determined fracture aperture (typical thickness of 0.4, 0.6, 0.8, and 1.6 mm). A filter paper was placed at the top inlet to spread the liquid (tap water) flux and to provide anchoring surface for formation of bridges. A sequence of images depicting liquid bridge formation and subsequent elongation and detachment is shown in Fig. 40.
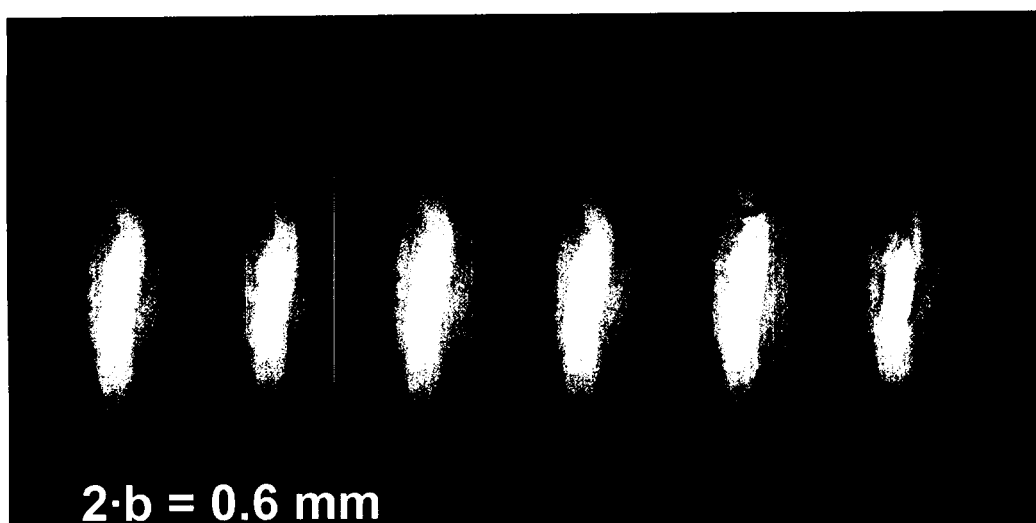

Figure 40: A sequence of water bridge formation, elongation, and detachment in a 0.6 mm fracture model (the time interval between images is not constant). Note the formation of a liquid thread feeding the "detaching" bridge volume similar to observations by Su et al. [1999].

An experiment was conducted to determine bridge detachment intervals for two different fracture aperture sizes (0.8 and 1.6 mm) and five different fluxes (fluxes were determined from the digital readout of the calibrated pump and were confirmed by collecting and measuring outflow volumes). Model predictions were based on an assumed anchoring radius of 2.5 mm (as observed on imagery from the experiment). Model
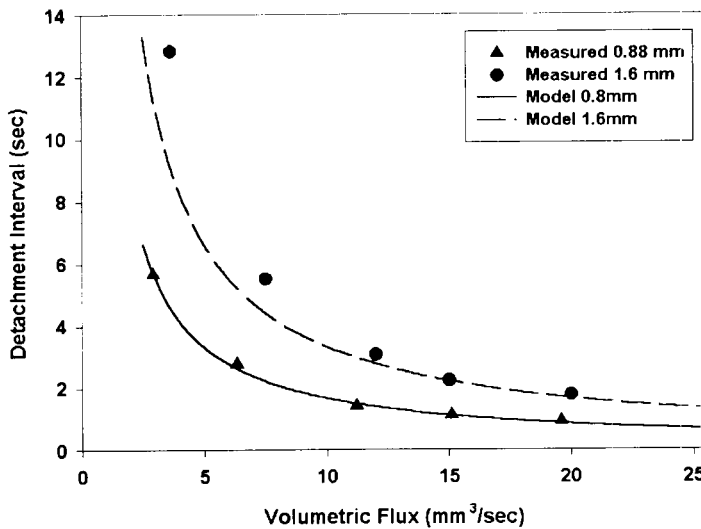

Figure 41: Measurements (symbols) and model predictions (lines) of bridge detachment intervals as a function of input flux within two aperture sizes.

predictions (Fig. 41) were in excellent agreement with measured values. The details of the model predictions are shown in Appendix J(c). The agreement with theoretical anchoring radius was very close for the 0.8-mm fracture, but was underestimated for the 1.6-mm fracture. These results are of preliminary nature and offer only a limited support for the proposed model. Additional experiments are needed to provide definitive tests for the various aspects of the discrete liquid bridge model.

05/23/2000: Experiments on Dripping under

Controlled Vapor Pressure

Dani Or.

Experiments reported in section two of the current volume (#354) have shown good agreement with the proposed analytical model for dripping from unsaturated fractures under relatively rapid flux and minimal effect of evaporation. The objective of the current experiments is to verify the analytical model in the presence of evaporative effects.

The general design of the experiments is similar to those described in the second section of the current volume (#354). Water was supplied to the dripping plane using peristaltic pump at low flux. Dripping from grooved fracture surfaces (used in previous experiments) during prolonged dripping period induces evaporation from the drop surface as well as the fracture surface. Evaporation also occurs from receiving pan after the drop detaches. The primary design of the current experiments was to minimize all the unwanted sources of evaporation except from drop surface (see schematic diagram in Fig. 42). To this end, the experiments were conducted using tube (o.d=7mm; i.d.=0.1mm) for channeling influx and as a drop anchoring area; and the drops were received by long stem funnel and collected in a flask with long and narrow neck. Water

was pumped with precision peristaltic pump. The experiments were conducted in two different fluxes. The vapor pressure of the sealed chamber in which drops were formed was controlled by dew point generator. Humid condition was induced by setting the dew point temperature to slightly higher than the room temperature, and dry condition was induced by setting very low dew point temperature. Five or more drops were collected and weighed for each humidity condition. To reduce evaporation from the flasks, the dry condition was replaced by experiment in open chamber (room relative humidity ~35%), and drops were weighed individually, immediately after detachment. Summary of the experimental conditions and results is shown in Table 1.
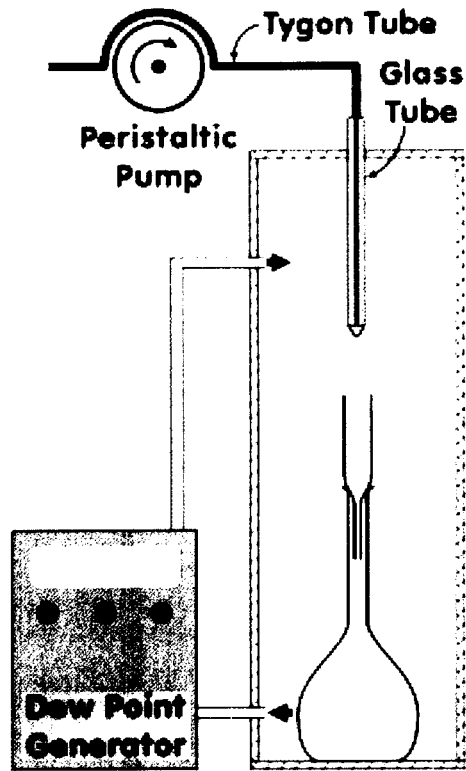

Figure. 42: Experimental setup for dripping under controlled humidity conditions.

Table 1. Summary of experimental parameters and main results

Flux (cm³/sec)	Humid				Dry			
	RH (%)	Temp (°C)	Period (min)	Mass (gm)	RH (%)	Temp (°C)	Period (min)	Mass (gm)
10	100	26.5	7.2	0.101	25	27.25	7.6	0.100
5	100	25.5	16.6	0.108	10	25.5	21.4	0.079
					Room (~35%)	25.5	19.1	0.093

The results in the Table 1 clearly show the increase (by up to 29%) in dripping period at dry conditions, in agreement with the analytical model. However, the mean drop mass in dry condition was either equal or slightly less than the humid condition, in contrast to the model prediction of larger drop mass when evaporation and liquid influx approach equality. Two major deficiencies of the experimental could contribute to the unexpected results:

(1) Evaporation/condensation from the collecting flask in the controlled dry/humid

conditions, respectively. The significant difference in drop mass between the controlled dry and room conditions validates the above argument.

(2) The relatively short dripping period may not be adequate for manifestation of evaporative effects.

06/06/2000: Experiments on Dripping Under Variable Fluxes

Two major modifications were introduced to the previous experimental design.

(1) The relative humidity was fixed and flux was varied from rapid to very slow, instead of comparing different relative humidity values under constant flux. Graphical comparison of the two approaches using model predictions is shown in Figure 43 (see Figure 22a and discussions in pages 39-40 of section II). The advantages of the modified design are: (a) it provides several intermediate points (instead of "dry" and "humid" only), and (b) it does not require precise control of relative humidity, and allows individual weighing of drops immediately after detachment.

(2) The dripping period was further extended by providing larger drop anchoring area (aluminum rod O.D.=12.7mm with I.D.=2.0mm borehole see Figure 44), hence, large final drop mass.

The calibration of the peristaltic pump was conducted by continuously monitoring the mass of the source cup. To minimize calibration errors due to evaporation, the source cup was sealed and long and narrow tubing was provided for ventilation. For extra caution, the cup was sealed within the chamber of precision analytical balance. The resulting pump curve is shown in Figure 45. For simplicity, subsequent results are
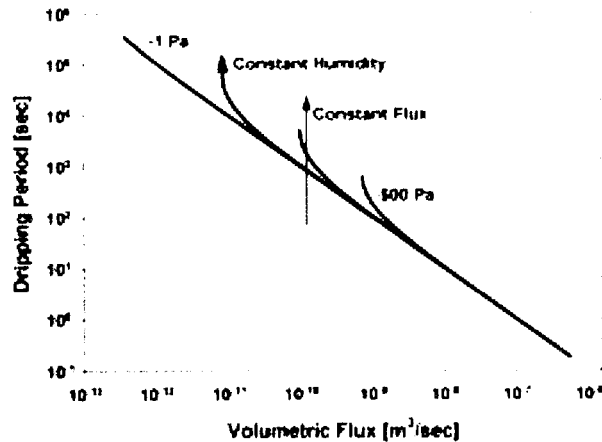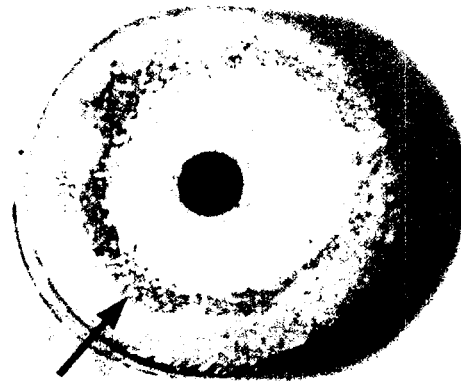
Figure. 43: Comparison of constant flux and constant humidity experimental designs (for explanations of above figure see Fig 22a and discussion in page39-40 of section II).

Figure. 44: Aluminum drop anchoring tip (O.D. = 12.7mm with I.D.=2.0mm borehole).

reported as functions of pump rotor speed (in RPM).

The volume and mass of drops from the above experiments are shown in Figure 46, each point representing an individual drop. The four fluxes used in the experiments are designated by different symbols.

Marked variability in mass of drops at the same flux was observed for all the fluxes. There is no significant difference in drop mass among all the fluxes except 15RPM.

There was noticeable difference in the width of the anchoring area. In Figure 44, the watermark on the drop anchoring area indicates the size for low flux (1RPM), while high flux experiments had drop-anchoring area that covers nearly all the available area.

The foregoing suggests that the observed differences in drop mass within and between different fluxes could be attributed to liquid configuration around the anchoring area.
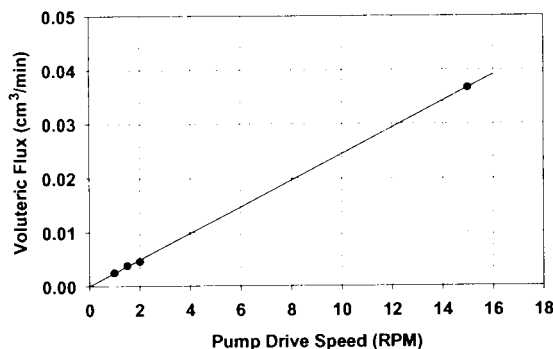

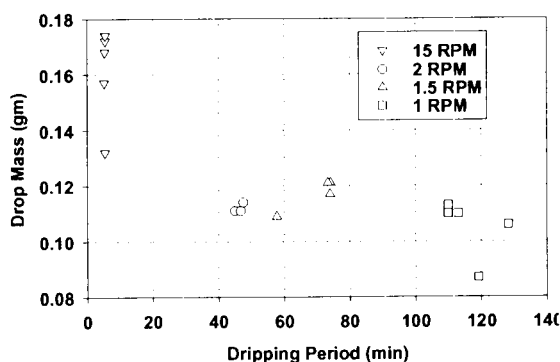**Figure. 45:** Pump curve for TY-10 tubing.

Figure. 46: Dripping results under variable fluxes.

06/11/2000: Experiments on Dripping from

Controlled Drop Anchoring Area

To minimize the variability of the anchoring-area shown in the previous tests, the aluminum anchoring area was replaced by a glass tube of 10.0mm O.D. with beveled tip (see Figure 47). The underlying assumption of the improved tip design is that the drop anchoring area will be fixed, and resulting difference in mass would be attributed to only dripping dynamics.

Experiments were conducted in flux range of 2-15 RPM as shown in Figure 48. In Figure 48a, each set of tests for a given flux was started without any liquid extruded from the glass tip. This allows configuration of the drop anchoring area to be affected by liquid dynamics under the given flux. These experiments
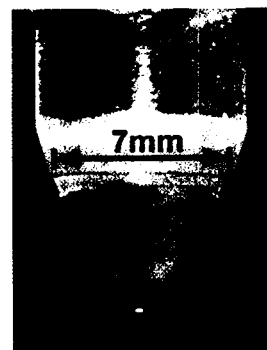

Figure. 47: Beveled glass tip (O.D. = 10mm, I.D. = 7mm).

showed that the drop mass generally decreases with decreasing flux. A closer look at the replicates in 5- and 10-RPM shows that the drop mass was increasing progressively from the first to the last replicate. This indicates that the configuration around the drop anchoring area did not attain optimal state during the first few drippings. To further check these phenomena, a different set of tests was conducted in which the flux was reduced (begiuning at 10RPm and ending 2RPM) without interruption at a step of 1RPM (replicates of 4 to 7 drops were collected before adavancing to next step). In figure 48b the results of the even fluxes (10-8-6-4-2RPM) are shown. In a separate set the flux was reduced from 10RPM to 2RPM without interruption (solid symbol in Figure 48b). When the flux is reduced without interruption the reduction in mass with decreasing flux is less steep compared to interrupted (independent) tests (Figure 48a). Moreover, the drop at 2RPM (initiated under configuration of 10RPM) was larger in mass than the independent 2RPM drops. If all the three drop masses (2- from 0- RPM, 2- from 3-RPM, and 2- from 10- RPM) are compared the higher the preceding fluxes the larger the drop mass. In conclusion, there appears to be initial condition (most likely configuration of drop anchoring area) that dictates the drop mass more than the flux itself.

To further examine the effects of initial-condition sharper and even glass-tip was used. It was also tested if the drop mass increases at higher fluxes (as high as 40RPM). These results are shown in Figure 49a. Each flux was started from zero flux to avoid with at least 30 minutes gap to avoid any influence from the preceding flux (exception is marked). These results show (1) the drop mass does not increase significantly for fluxes above 20RPM, and (2) previous configuration at higher flux increases mass as shown with 10 RPM drops.
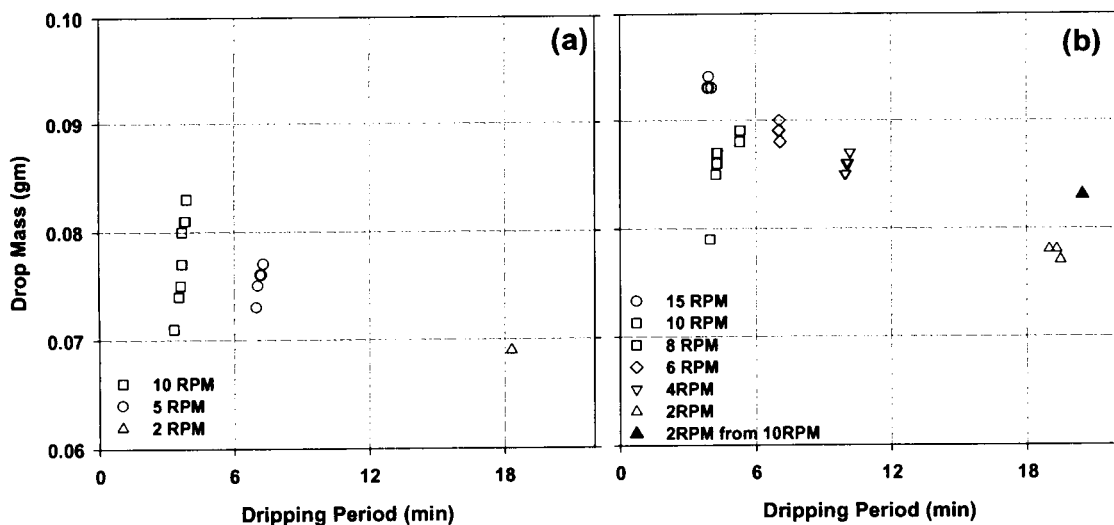

Figure 48: Dripping data from beveled glass tip: (a) restarted from zero at each flux with minimum 30 minutes interval between two successive flux sets, and (b) flux was reduced at step of 1RPM from 10RPM to 2RPM.
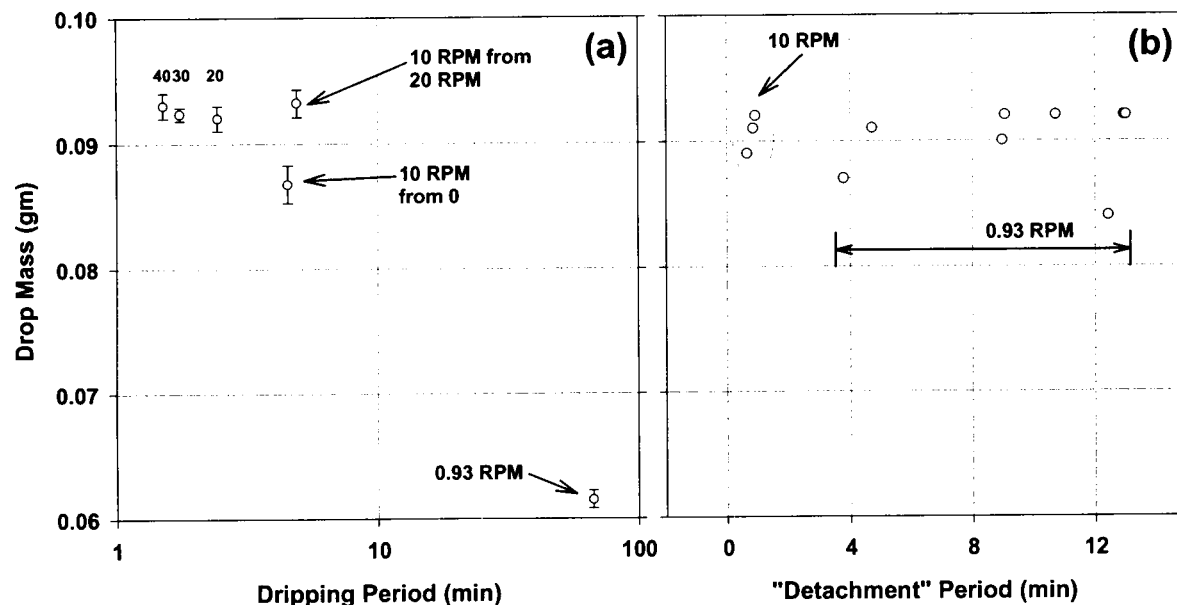
Figure 49: Dripping data from sharper glass tip: (a) restarted from zero at each flux with minimum 30 minutes interval between two successive flux sets except indicated, and (b) flux was reduced to 10- or 0.93 after the drop was formed for 20.25 minutes at 20RPM. The time shown indicates the remaining detachment phase period.

According to the model being tested drop mass increases at low flux due to competing effects of evaporation and low influx. The competition becomes more critical at the final moments before detachment as evaporation increases due to high surface area and reduced curvature. All other aspects of the dynamics are similar for high and low flux drops. Therefore, it is logical to expect manifestation of evaporative effects even if it is invoked only for the final moments of the drop. The advantage of this type of test (if the underlying assumptions are true) is that it reduces the effect of initial configuration.

In Figure 49b, the drops shown were formed under 20RPM flux for 2.25 minutes (dripping period of 20RPM is 2.5 minutes) and then the flux was reduced to the desired flux (10 and 0.93 RPM in this case). The time shown in the figure is the time after the flux was reduced near/during the "detachment" phase. The drop mass for 10RPM and 0.93 RPM was not significantly different from 20RPM. These results suggest that the drop mass differences shown in these experiments could be entirely due to initial conditions.

References

Carter, W.C., The forces and behavior of fluids constrained by solids. *Acta. Metall. 36*, 2283-2292,1988.

Cheng, Z., S. Render, P. Meakin, and F. Family. Avalanche dynamics in a deposition model with "sliding". *Phys. Rev. A 40*, 5922-5935, 1989.

Dexter, A.R., Heterogeneity of unsaturated, gravitational flow of water through beds of

large particles. *Water Resour. Res., 29*, 1859-1862, 1993.

Firoozabadi, A, and J. Hague. Capillary pressure in fractured porous media. *J. Pet. Technol., June 1990*, 784-791, 1990.

Friedman, S. P., Dynamic contact angle explanation of flow rate-dependent saturation-pressure relationships during transient liquid flow in unsaturated porous media. *J. Adhesion Sci. Technol., 13*, 1495-1518, 1999.

Glass, R.J., and D.L. Norton. Wetted-region structure in horizontal unsaturated fractures. in *High Level Radioactive Waste Management, Proceedings of the Third Annual International Conference*, pp. 717-726, Am. Nucl. Soc., LaGrange Park, Ill., 1992.

Glass, R.J., and M.J. Nicholl. Quantitative visualization of entrapped phase dissolution within a horizontal flowing fracture, *Geophys. Res. Lett. 22(11)*, 1413-1416. 1995.

Glass, R.J., M.J. Nicholl, and L. Yarrington. A modified invasion percolation model for low-capillary number immiscible displacements in horizontal rough-walled fracture: Influence of local in plane curvature. *Water Resour. Res. 34*, 3215-3234, 1998.

Kneafsey, T.J., and K. Pruess. Laboratory experiments of heat-driven two phase flows in natural and artificial rock fractures. *Water Resour. Res. 34*, 3349-3367, 1998.

Liu, H.H., C. Doughty, and G.S. Bodvarsson. An active fracture model for unsaturated flow and transport in fractured rocks. *Water Resour. Res. 34*, 2633-2646, 1998.

Meseguer, J., The breaking of axisymmetric slender liquid bridges. *J. Fluid Mech., 130*, 123-151, 1983.

Moreno, L., Y. W. Tsang, C. F. Tsang, F. V. Hale and I. Neretnieks. Flow and tracer transport in a single fracture: A stochastic model and its relation to some field observations, *Water Resour. Res., 24*(12), 2033-2048, 1988.

Nicholl, M.J., and R.J. Glass. Wetting phase permeability in partially saturated horizontal fracture. in *High Level Radioactive Waste Management, Proceedings of the Fifth Annual International Conference*, pp. 2007-2019, Am. Nucl. Soc., LaGrange Park, Ill., 1994.

Nicholl, M.J., R.J., Glass, and S.W. Wheatcraft. Gravity-driven infiltration instability in initially dry nonhorizontal fractures. *Water Resour. Res. 30*, 2533-2546, 1994.

Or, D., and T. A. Ghezzehei. Dripping into subterranean cavities from unsaturated fractures under evaporative conditions. *Water Resour. Res., 36*, 381-393, 2000.

Or, D., and M. Tuller. Flow in unsaturated fractured porous media: Hydraulic conductivity of rough surfaces. *Water Resour. Res.* 2000 (in press).

Padday, J.F., G. Petre, C.G. Rusu, J. Gamero, and G. Wozniak. The shape, stability and breakage of pendant liquid bridges. *J. Fluid Mech., 352*, 177-204, 1997.

Prazak, J., M. Sir, F. Kubik, J. Tyoniak, and C. Zarcone. Oscillation phenomena in gravity-driven drainage in coarse porous media. *Water Resour. Res., 28*, 1849-

1855, 1992.

Pruess, K., A mechanistic model for water seepage through thick unsaturated zones in fractured rocks of low matrix permeability. *Water Resour. Res., 35*, 1039-1051, 1999.

Pruess, K., and Y.W. Tsang. On two-phase relative permeability and capillary pressure of rough-walled rock fractures. *Water Resour. Res., 26*, 1915-1926, 1990.

Pruess, K., B. Faybishenko, and G.S. Bodvarsson. Alternative concepts and approaches for modeling flow and transport in thick unsaturated zones of fractured rocks. *J. Contam. Hydrol. 38*, 281-322, 1999.

Su, G.W., J.T. Geller, K. Pruess, and F. Wen. Experimental studies of water seepage and intermittent flow in unsaturated, rough-walled fractures. *Water Resour. Res., 35*, 1019-1037, 1999.

Tokunaga, T. K., and J. Wan, Water film flow along fracture surfaces of porous rock, *Water Resour. Res., 33*(6), 1287-1295, 1997.

Tsang, Y. W., and C. F. Tsang, Channel model of flow through fractured media, *Water Resour. Res., 23*(3), 467-479, 1987.

Wang, J.S.Y., and T.N. Narasimhan, Hydrologic mechanisms governing fluid flow in partially saturated, fractured, porous medium, *Water Resour. Res., 21*, 1861-1874, 1985.

Zimmerman, R.W., and G.S., Bodvarsson, Hydraulic conductivity of rock fractures, *Transp. Porous Media, 23*, 1-30, 1996.

Appendix H

Determination of Equilibrium Bridge Shape: I Stationary Bridge

Physical Constants

$$\sigma := 0.0729 \qquad \rho := 998 \qquad g := 9.8 \cdot \cos\left[(90-70)\cdot\frac{\pi}{180}\right] \qquad \eta := 0.1307 \cdot 10^{-2} \qquad \text{TOL} := 10^{-7}$$

Geometric Functions

Area

$$A(V,b) := \frac{V}{2 \cdot b}$$

Radius ratio

$$f(V,b,Ct,\theta) := \sqrt{\dfrac{\dfrac{A(V,b)}{Ct^2} - \dfrac{\pi}{2} + \theta + \dfrac{1}{1 \cdot \tan(\theta)}}{\dfrac{\pi}{2} + \theta + \dfrac{1}{1 \cdot \tan(\theta)}}}$$

Bottom Radius

$$Cb(V,b,Ct,\theta) := Ct \cdot f(V,b,Ct,\theta)$$

Center to Center Length

$$D(V,b,Ct,\theta) := \frac{Cb(V,b,Ct,\theta) - Ct}{\sin(\theta)}$$

Bottom Radius of Curvature

$$rb(V,b,Ct,\theta) := \frac{1}{\dfrac{1}{b} + \dfrac{1}{Cb(V,b,Ct,\theta)} - \dfrac{1}{Ct} - \dfrac{\rho \cdot g}{\sigma} \cdot (Ct + Cb(V,b,Ct,\theta) + D(V,b,Ct,\theta))}$$

Bottom Contact Angle

$$\alpha(V,b,Ct,\theta) := \text{acos} \frac{b}{rb(V,b,Ct,\theta)}$$

Side Radius of Curvature

$$rc(V,b,Ct,\theta) := \frac{1}{\dfrac{1}{b} - \dfrac{1}{Ct} - \dfrac{\rho \cdot g}{\sigma} \cdot Ct + \dfrac{D(V,b,Ct,\theta)}{2}}$$

Side Contact Angle

$$\beta(V,b,Ct,\theta) := \text{acos} \frac{b}{rc(V,b,Ct,\theta)}$$

Force Components due to Surface Tension

Top arc $\text{TOPARC}(V,b,Ct,\theta) := 2 \cdot (\sigma \cdot Ct \cdot (\cos(2 \cdot \theta) + 1))$

Side walls $\text{SIDEWALL}(V,b,Ct,\theta) := 4 \cdot D(V,b,Ct,\theta) \cdot \cos(\theta) \cdot \sin(\theta) \cdot \cos(\beta(V,b,Ct,\theta))$

Bottom Arc $\text{BOTTOMARC}(V,b,Ct,\theta) := -2 \cdot ((\cos(2 \cdot \theta) + 1) \cdot \cos(\alpha(V,b,Ct,\theta)) \cdot Cb(V,b,Ct,\theta) \cdot \sigma)$

Total Forces

Resultant Force $\text{FUP}(V,b,Ct,\theta) := \text{TOPARC}(V,b,Ct,\theta) + \text{SIDEWALL}(V,b,Ct,\theta) + \text{BOTTOMARC}(V,b,Ct,\theta)$

Weight $W(V) := V \cdot \rho \cdot g$

Solution Block

Initial Guess $Ct := 0.0001$

Solver Block   Given $\text{FUP}(V,b,Ct,\theta) = W(V)$ $\text{Ctop}(V,b,\theta) := \text{Find}(Ct)$

Selection of θ

Several combinations of the inclination angle of the side wall (θ) and radius of top arc (Ct) result in equilibrium cinfiguration of the liquid bridge. A unique solution is selected by considering θ that results in minimum specific surface energy. The length of the solid-liquid-vapor contact line is used here as a measure of surface energy.

Perimeter $P(V,b,\theta) := \text{Ctop}(V,b,\theta) \cdot (\pi - 2 \cdot \theta) + (Cb(V,b,\text{Ctop}(V,b,\theta),\theta)) \cdot (\pi + 2 \cdot \theta) + 2 \cdot D(V,b,\text{Ctop}(V,b,\theta),\theta)$

Aspect ratio $R(V,b,\theta) := \dfrac{\text{Ctop}(V,b,\theta) \cdot (\pi - 2 \cdot \theta) + (Cb(V,b,\text{Ctop}(V,b,\theta),\theta)) \cdot (\pi + 2 \cdot \theta) + D(V,b,\text{Ctop}(V,b,\theta),\theta)}{\text{Ctop}(V,b,\theta) \cdot (\pi - 2 \cdot \theta) + (Cb(V,b,\text{Ctop}(V,b,\theta),\theta)) \cdot (\pi + 2 \cdot \theta)}$

θ-Array $N1 := 75$ $j := 1 .. N1$ $\theta_j := \dfrac{\pi}{180} + (j - 1) \cdot \dfrac{\pi}{180}$
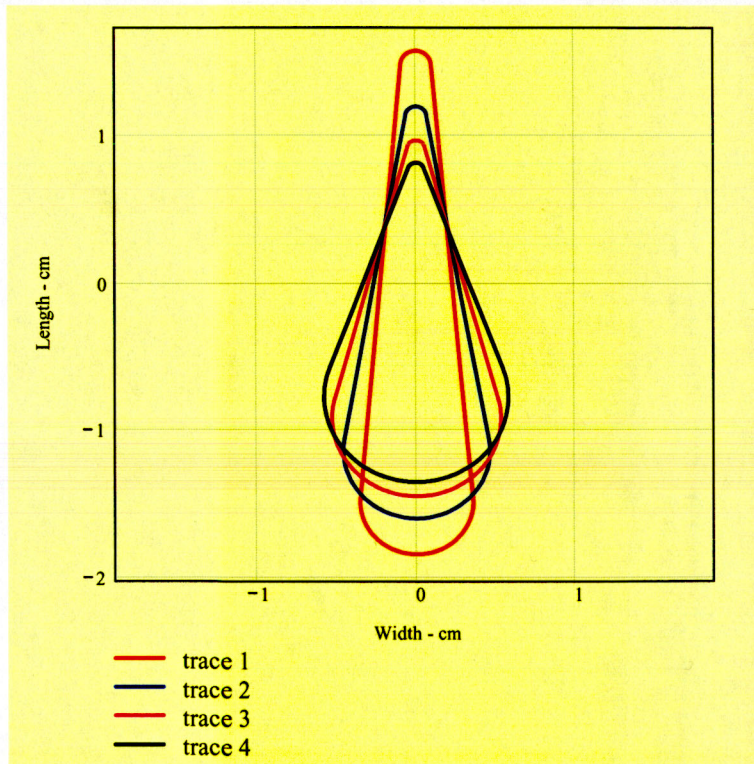
Geometrical Arrays

$V1 := 102 \cdot 10^{-9}$ $b1 := 0.33 \cdot 10^{-3}$ $N2 := 100$ $i := 0 .. N2$ $l := 0 .. 2 \cdot N2 + 1$

$k := 1 .. 4$ $\beta_1 := 5 \cdot \dfrac{\pi}{180}$ $\beta_2 := 10 \cdot \dfrac{\pi}{180}$ $\beta_3 := 15 \cdot \dfrac{\pi}{180}$ $\beta_4 := 20 \cdot \dfrac{\pi}{180}$ $Ctq_k := \text{Ctop}(V1,b1,\beta_k)$ $Cbq_k := Cb(V1,b1,\text{Ctop}(V1,b1,\beta_k),\beta_k)$ $D_k := \dfrac{Cbq_k - Ctq_k}{\sin \beta_k}$

$$\alpha t_{i,k} := \beta_k + i \cdot \frac{\pi - 2 \cdot \beta_k}{N2} \qquad xt_{i,k} := Ctq_k \cdot \cos(\alpha t_{i,k}) \qquad yt_{i,k} := Ctq_k \cdot \sin(\alpha t_{i,k}) + \frac{D_k}{2} \qquad \alpha b_{i,k} := \pi - \beta_k + i \cdot \frac{\pi + 2 \cdot \beta_k}{N2} \qquad xb_{i,k} := Cbq_k \cdot \cos(\alpha b_{i,k}) \qquad yb_{i,k} := Cbq_k \cdot \sin(\alpha b_{i,k}) - \frac{D_k}{2}$$
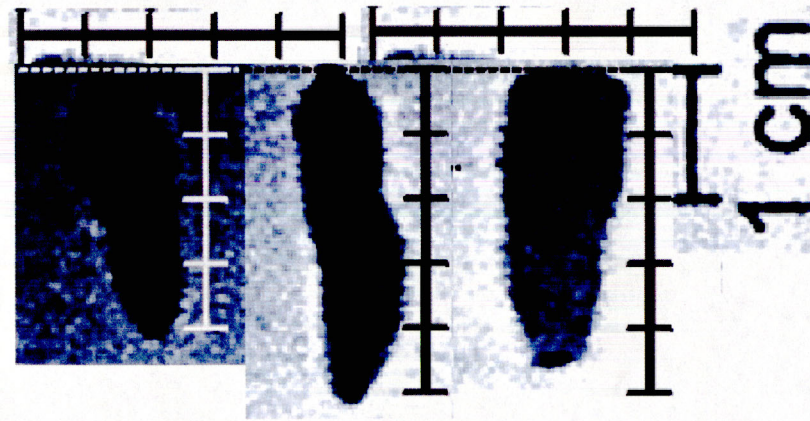
$$X_{i,k} := xt_{i,k} \qquad X_{N2+i,k} := xb_{i,k} \qquad X_{N2\cdot2+1,k} := xt_{0,k} \qquad Y_{i,k} := yt_{i,k} \qquad Y_{N2+i,k} := yb_{i,k} \qquad Y_{N2\cdot2+1,k} := yt_{0,k}$$

$$a := \frac{Ctq_1 + Cbq_1 + D_1}{2} \cdot 10^2 \cdot 1.1 \qquad t := \left(Ctq_1 + \frac{D_1}{2}\right) \cdot 1 \cdot 10^2 \cdot 1.1 \qquad b := \left(Cbq_1 + \frac{D_1}{2}\right) \cdot 1 \cdot 10^2 \cdot 1.1 \quad A := 1 \quad B := 2 \quad C := 3 \qquad d := 4$$

| trace 1 |
| trace 2 |
| trace 3 |
| trace 4 |

Liquid Dimensions (degrees and cm)

$\beta_k \cdot \dfrac{180}{\pi} =$	$\left(\dfrac{Cbq_k + Ctq_k}{2}\right) \cdot 10^2 \cdot 2 =$	$(Ctq_k + Cbq_k + D_k) \cdot 10^2 =$	$Ctq_k \cdot 10^2 \cdot 2 =$	$Cbq_k \cdot 10^2 \cdot 2 =$
5	0.449	3.412	0.19	0.707
10	0.525	2.791	0.131	0.918
15	0.584	2.411	0.111	1.057
20	0.626	2.164	0.101	1.152

Remarks: Pictures from Su are bridges in motion at an average velocity of 0.5 cm/sec

0.07   0.08   0.1

Appendix I

Determination of Equilibrium Bridge Shape: II Stationary bridge attached to solid surface

Physical Constants

$$\sigma := 0.0729 \qquad \rho := 998 \qquad g := 9.8 \qquad \eta := 0.1307 \cdot 10^{-2} \qquad TOL := 10^{-8}$$

Geometrical Functions

Top Area

$$A = 4 \cdot b \cdot r - \pi \cdot b^2$$

Top Pressure

$$P_t = \sigma \cdot \left[-\frac{1}{b} - \frac{1}{s \cdot b} \right]$$

Top Pressure

$$P_b = -\sigma \cdot \left[\frac{1}{r} - \frac{1}{R} \right]$$

Pressure Difference

$$\Delta P = P_b - P_t = \rho \cdot g \cdot r \cdot (1 + \alpha)$$

Bottom Radius

$$\frac{1}{R} = \frac{1}{b} + \frac{1}{(s \cdot b)} - \rho \cdot \frac{g}{\sigma} \cdot r \cdot (1 + \alpha) + \frac{1}{r}$$

Bottom Contact angle

$$\theta = acos\left[\frac{r}{R}\right] = acos\left[\left[\frac{1}{b} + \frac{1}{(s \cdot b)} - \rho \cdot \frac{g}{\sigma} \cdot r \cdot (1 + \alpha) + \frac{1}{r}\right] \cdot r\right]$$

Force Components

Capillary force

$$F_C = -P_t \cdot A = -\sigma \cdot \left[-\frac{1}{b} - \frac{1}{s \cdot b} \right] \cdot \left[4 \cdot b \cdot r - \pi \cdot b^2 \right]$$

Surface tension up

$$FU_{lv} = 2 \cdot \sigma \cdot \pi \cdot b$$

Surface tension down

$$FD_{lv} = 2 \cdot \sigma \cdot \pi \cdot r \cdot cos(\theta)$$

Bridge weight

$$W = \rho \cdot g \cdot 2 \cdot b \cdot r^2 \cdot \left[2 \cdot \alpha + \frac{\pi}{2} \right]$$

Total Forces

$$f(r) = F_C + FU_{lv} - FD_{lv} + W = 0$$

$$f(r) = A(\alpha, b, s) \cdot r^3 + B(\alpha, b, s) \cdot r^2 + C(\alpha, b, s) \cdot r + D(\alpha, b, s)$$

where

$$A(\alpha, b, s) := 2 \cdot \pi \cdot \rho \cdot g \cdot (1 + \alpha)$$

$$B(\alpha, b, s) := \left[-2 \cdot \sigma \cdot \pi \cdot \left[\frac{1}{b} + \frac{1}{(s \cdot b)} \right] \right] - 2 \cdot \rho \cdot g \cdot b \cdot \left[2 \cdot \alpha + \frac{1}{2} \cdot \pi \right]$$

$$C(\alpha, b, s) := \left[-4 \cdot \sigma \cdot \left[\frac{-1}{b} - \frac{1}{(s \cdot b)} \right] \cdot b - 2 \cdot \sigma \cdot \pi \right]$$

$$D(\alpha, b, s) := \left[\sigma \cdot \left[\frac{-1}{b} - \frac{1}{(s \cdot b)} \right] \cdot \pi \cdot b^2 + 2 \cdot \sigma \cdot \pi \cdot b \right]$$

then, $\qquad f(\alpha, b, s, r) := A(\alpha, b, s) \cdot r^3 + B(\alpha, b, s) \cdot r^2 + C(\alpha, b, s) \cdot r + D(\alpha, b, s)$

The real root of the above third order polynomial is given by the function r_{soln}

$$S(\alpha,b,s) := -2 \cdot B(\alpha,b,s)^3 + 9 \cdot A(\alpha,b,s) \cdot B(\alpha,b,s) \cdot C(\alpha,b,s) - 27 \cdot A(\alpha,b,s)^2 \cdot D(\alpha,b,s)$$

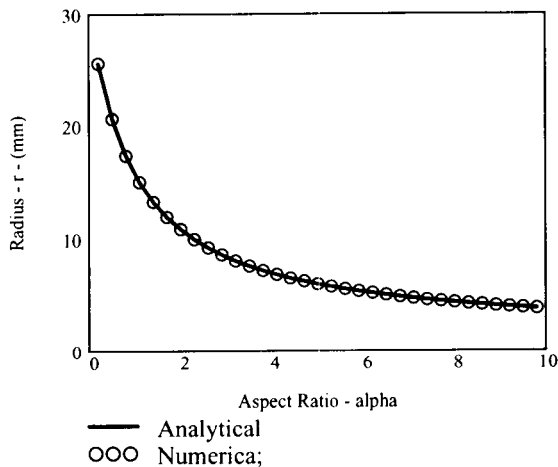$$P(\alpha,b,s) := \left[S(\alpha,b,s) + \sqrt{4 \cdot \left(-B(\alpha,b,s)^2 + 3 \cdot A(\alpha,b,s) \cdot C(\alpha,b,s)\right)^3 + (S(\alpha,b,s))^2} \right]^{\frac{1}{3}}$$

$$r_{soln}(\alpha,b,s) := -\frac{B(\alpha,b,s)}{3 \cdot A(\alpha,b,s)} - \frac{2^{\frac{1}{3}} \cdot \left(-B(\alpha,b,s)^2 + 3 \cdot A(\alpha,b,s) \cdot C(\alpha,b,s)\right)}{3 \cdot A(\alpha,b,s) \cdot P(\alpha,b,s)} + \frac{P(\alpha,b,s)}{3 \cdot 2^{\frac{1}{3}} \cdot A(\alpha,b,s)}$$

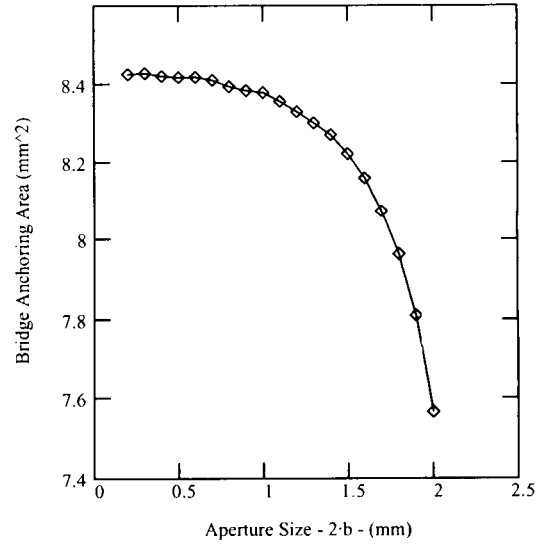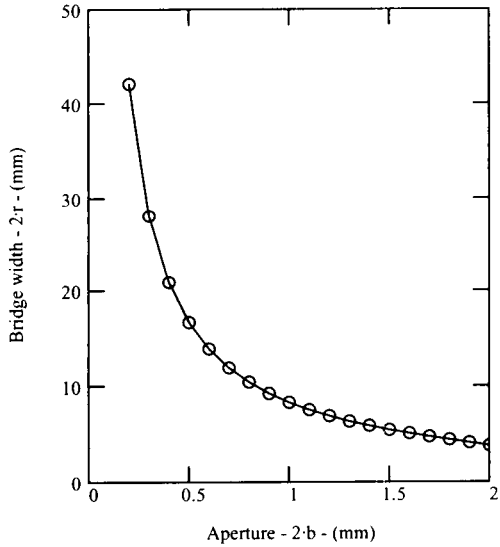The above solution is compared with numerical root in the following graph

Solver Block

$$r := 0.1 \qquad soln(\alpha,b,s) := root(f(\alpha,b,s,r),r)$$

$$\alpha := 0.2, 0.5 .. 10 \qquad b1 := 0.2 \cdot 10^{-3} \qquad b2 := 0.4 \cdot 10^{-3} \quad b3 := 1 \cdot 10^{-3} \quad s := 1$$

Aspect Ratio - alpha

——— Analytical
OOO Numerica;

Identification of Maximum Volume

$$s := 100 \quad Nj := 18 \quad j := 0 .. Nj \qquad Ni := 1500 \quad i := 0 .. Ni$$

$$b_j := 1 \cdot 10^{-4} + j \cdot \frac{9 \cdot 10^{-4}}{Nj} \qquad\qquad \alpha_i := 0.5 + i \cdot \frac{9.5}{Ni}$$

$$rad_{i,j} := Re\left(r_{soln}\left(\alpha_i, b_j, s\right)\right) \qquad V_{i,j} := 2 \cdot b_j \cdot rad_{i,j}^2 \cdot \left(2 \cdot \alpha_i - \frac{\pi}{2}\right)$$

$$k_j := \begin{vmatrix} cmax \leftarrow 1 \\ \text{for } i \in 1 .. Ni \\ \quad cmax \leftarrow \begin{vmatrix} i & \text{if } V_{i,j} > V_{cmax,j} \\ cmax & \text{otherwise} \end{vmatrix} \end{vmatrix}$$

Remarks: The following figures are shown as Figure 32-33 in the main document

Aspect Ratio - alpha
- - - - 0.4 mm
——— 0.8 mm
— - 1.8 mm
OOO Max Volume

Aspect ratio - alpha
- - - - 0.4 mm
——— 0.8 mm
— - 1.8 mm
OOO Max. Volume

Aperture - 2·b - (mm)

Aperture Size - 2·b - (mm)
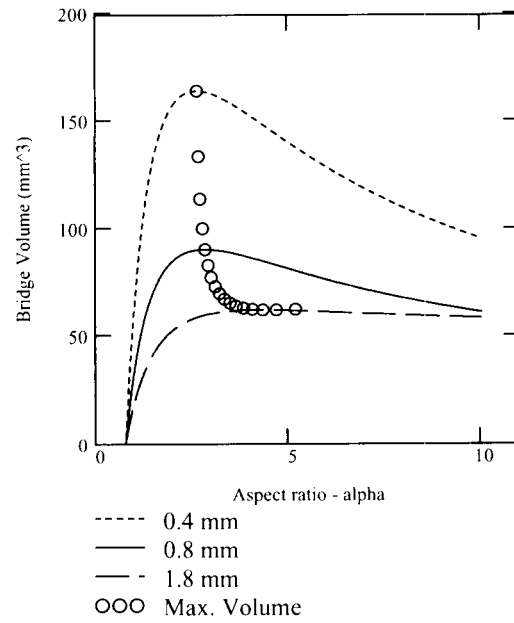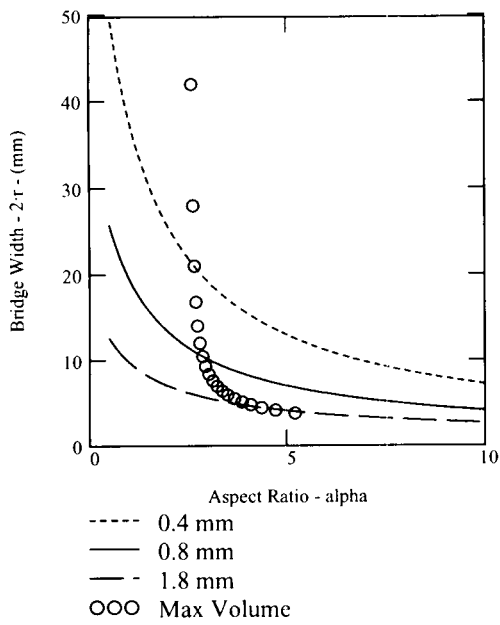
Appendix J (a)
Growth and Detachment of Liquid Bridges

The growth and detachment of liquid bridges forming between rough parallel-plates is tracked in a Lagrangian coordinate system (similar to free drops).

■ Longitudinal Forces

The following forces acting in the axial direction are considered:

■ Liquid Weight

The weight of the liquid at any reference τ, consists of the weight of constant semi-circular leading portion (which may porbably reprsent recoil volume), and an extending portion (a function of the flux).

$$W = \rho\, g\, (\pi\, ro^2\, b + Q\, \tau)$$

■ Liquid-vapor surface tension

Surface tension of the liquid-vapor interface on both sides of a cross-section resists extension of the interface according to:

$$FLV = 2\,\pi\, b\, \sigma LV$$

■ Liquid-solid interfacial tension

The solid-liquid contact line along the wetted portion of the plates resists extension in a manner similar to the liquid-vapor interface. The actual Solid-liquid contact line is likely to be longer than the apparent length. This is pronounced especially when rough surfaces are considered. A roughness factor (ratio of actual length to apparent length) is introduced to account for the increased resistance. Note that this portion of resistance to extension could vanish when the extension occurs on pre-wetted path (more on this is provided later).

$$FLS = R\, 4\, y\, \sigma LS$$

■ Viscous Drag

Extension of liquid bridge between parallel plates involves viscous shearing of liquid molecules adjacent to the plate walls. The resistance due to shearing of water can be given by a simple analogy with settlement of zero-thickness discs in viscous fluid (see Or, xxxx):

$$FD = \frac{24}{Re}\, \frac{A\,\rho}{2}\, v^2$$

where Re is Reynolds number, A is wetted area, and v is average flow velocity of the bridge. Consider the following expressions for the Reynolds number, and disc-equivalent diameter of the bridge, respectively:

$$Re = \frac{v\,D\,\rho}{\eta}\,,$$

$$D = \sqrt{\frac{A}{\pi}}$$

the average flow velocity of the bridge is difficult to quantify, for simplicity we can relate it to the rate of lateral extension (dy/dt) as:

$$v = F\,\partial_t\,y[t]$$

Then,

$$FD = 12\,F\,\eta\,\sqrt{\pi\,A}\,\partial_t\,y[t]$$

■ Summary

In summary the last three upward forces opposse the weight acting downwards. The resultant force is given by

$$S\,A = \rho\,g\,(\pi\,ro^2\,b + Q\,\tau) - \left(2\,\pi\,b\,\sigma LV + R\,4\,y\,\sigma LS + 12\,F\,\eta\,\sqrt{\pi\,A}\,\partial_t\,y[t]\right)$$

■ Lateral Forces

The following forces acting in the lateral direction at a cross-section in τ are considered:

■ Interfacial forces

The following forces due to liquid-vapor and liquid-solid intrfacial tensions act in a horizontal cross-section:

$$FH = 2\,\pi\,b\,\sigma LV + R\,4\,y\,\sigma LS$$

■ Viscous resistance to shrinkage

The shrinkage/extension of the bridge laterally is resisted by the following forces:

$$FV = 4\,y\,b\,3\,\eta\,\frac{1}{y[t]}\,\partial_t\,y[t]$$

■ Summary

The resulting lateral forces have a vertical component

$$S A = \frac{2 \pi b \, \sigma LV + R \, 4 \, y \, \sigma LS + 4 \, y \, b \, 3 \, \eta \, \frac{1}{y[t]} \, \partial_t \, y[t]}{2}$$

■ Bridge Detachment ODE

When bridge forming in a pre-wetted plates is considered the effect of solid liquid contact can be dropped:

$$S A = \rho \, g \, (\pi \, ro^2 \, b \, + \, Q \, \tau) \, - \, (2 \, \pi \, b \, \sigma LV)$$

$$S A = \frac{2 \pi b \, \sigma LV + 4 \, y \, b \, 3 \, \eta \, \frac{1}{y[t]} \, \partial_t \, y[t]}{2}$$

$$Eq1 = - \frac{2 \pi b \, \sigma LV + 4 \, y \, b \, 3 \, \eta \, \frac{1}{y} \, dydt}{2} == \rho \, g \, (\pi \, ro^2 \, b \, + \, Q \, \tau) \, - \, (2 \, \pi \, b \, \sigma LV) ;$$

$$Eq2 = \text{Solve}[Eq1, \, dydt] ;$$

$$Eq3 = Eq2[[1, \, 1, \, 2]]$$

$$- \frac{b \, g \, \pi \, ro^2 \, \rho \, - \, b \, \pi \, \sigma LV + g \, Q \, \rho \, \tau}{6 \, b \, \eta}$$

$$\partial_t \, y[t] = - \frac{b \, g \, \pi \, ro^2 \, \rho \, - \, b \, \pi \, \sigma LV + g \, Q \, \rho \, \tau}{6 \, b \, \eta}$$

■ Solution to Bridge Detachment ODE

General solution to Eq3 is given by,

$$Eq4 = \text{DSolve}\left[\partial_t \, y[t] == - \frac{b \, g \, \pi \, ro^2 \, \rho \, - \, b \, \pi \, \sigma LV + g \, Q \, \rho \, \tau}{6 \, b \, \eta}, \, y[t], \, t\right]$$

$$\left\{\left\{y[t] \rightarrow t \left(- \frac{g \, \pi \, ro^2 \, \rho}{6 \, \eta} + \frac{\pi \, \sigma LV}{6 \, \eta} - \frac{g \, Q \, \rho \, \tau}{6 \, b \, \eta}\right) + C[1]\right\}\right\}$$

Separate y(t) from Eq4

$$Y1 = Eq4[[1,1,2]];$$

Introducing the initial condition y[τ]=ro,

$$Eq5 = ro == Y1 /. t \rightarrow \tau$$

$$ro == \tau \left(- \frac{g \, \pi \, ro^2 \, \rho}{6 \, \eta} + \frac{\pi \, \sigma LV}{6 \, \eta} - \frac{g \, Q \, \rho \, \tau}{6 \, b \, \eta}\right) + C[1]$$

Solve Eq5 for constant C[1]

Eq6=Solve[Eq5,C[1]]

$$\left\{\left\{C[1] \to -\frac{-6\,b\,ro\,\eta - b\,g\,\pi\,ro^3\,\rho\,\tau + b\,\pi\,\sigma LV\,\tau - g\,Q\,\rho\,\tau^2}{6\,b\,\eta}\right\}\right\}$$

Separate C[1] from Eq6

K=Eq6[[1,1,2]];

Substitute K into Y1 and simplify

Y2=Simplify[Y1/.C[1]→K];

Detachment occurs at the first element that vanishes, Y2=0. The time at which detachment occurs is obtained by setting Y2=0 and solving for t

Eq7=Simplify[Solve[Y2==0,t]]

$$\left\{\left\{t \to \frac{g\,Q\,\rho\,\tau^2 + b\,(6\,ro\,\eta + g\,\pi\,ro^2\,\rho\,\tau - \pi\,\sigma LV\,\tau)}{b\,g\,\pi\,ro^2\,\rho - b\,\pi\,\sigma LV + g\,Q\,\rho\,\tau}\right\}\right\}$$

Separate t from Eq7

T1=Eq7[[1,1,2]];

The time of detachment also satisfies additional constraint of dt/dτ=0. Now, differentiating T1,

Eq8 = Simplify[∂_τ T1]

$$\frac{b^2\,\pi^2\,(-g\,ro^2\,\rho + \sigma LV)^2 + g^2\,Q^2\,\rho^2\,\tau^2 + 2\,b\,g\,Q\,\rho\,(-3\,ro\,\eta + g\,\pi\,ro^2\,\rho\,\tau - \pi\,\sigma LV\,\tau)}{(b\,\pi\,(g\,ro^2\,\rho - \sigma LV) + g\,Q\,\rho\,\tau)^2}$$

Setting Eq6 to zero and solving for the crtical τc,

Eq9=Simplify[Solve[Eq8==0,τ]]

$$\left\{\left\{\tau \to \frac{-\sqrt{6}\,\sqrt{b}\,\sqrt{g}\,\sqrt{Q}\,\sqrt{ro}\,\sqrt{\eta}\,\sqrt{\rho} + b\,\pi\,(-g\,ro^2\,\rho + \sigma LV)}{g\,Q\,\rho}\right\},\right.$$

$$\left.\left\{\tau \to \frac{\sqrt{6}\,\sqrt{b}\,\sqrt{g}\,\sqrt{Q}\,\sqrt{ro}\,\sqrt{\eta}\,\sqrt{\rho} + b\,\pi\,(-g\,ro^2\,\rho + \sigma LV)}{g\,Q\,\rho}\right\}\right\}$$

τ1=Eq9[[1,1,2]]
τ2=Eq9[[2,1,2]]

$$\frac{-\sqrt{6}\,\sqrt{b}\,\sqrt{g}\,\sqrt{Q}\,\sqrt{ro}\,\sqrt{\eta}\,\sqrt{\rho} + b\,\pi\,(-g\,ro^2\,\rho + \sigma LV)}{g\,Q\,\rho}$$

$$\frac{\sqrt{6}\,\sqrt{b}\,\sqrt{g}\,\sqrt{Q}\,\sqrt{ro}\,\sqrt{\eta}\,\sqrt{\rho} + b\,\pi\,(-g\,ro^2\,\rho + \sigma LV)}{g\,Q\,\rho}$$

The solution that provides positive detachment values is:

$$\frac{\sqrt{6}\,\sqrt{b}\,\sqrt{g}\,\sqrt{Q}\,\sqrt{ro}\,\sqrt{\eta}\,\sqrt{\rho} + b\,\pi\,(-g\,ro^2\,\rho + \sigma LV)}{g\,Q\,\rho}$$

Appendix J (b)

Intermittent Flux by summation of independent bridge detachment periods

INPUTS

1. Time Averaging Parameters

Total Time of observation $\quad Tf := 3600$

Averaging period $\quad\quad\quad \Delta T := 1$

2. Independent Components

Number of different asperities present

$NC := 5$

The event period (Δt) and event volume (v) of each component are entered as arrays numbered 1 through NC.

$\Delta t_1 := 20.127 \quad v_1 := 140.91$

$\Delta t_2 := 11.53 \quad v_2 := 80.71$

$\Delta t_3 := 7.711 \quad v_3 := 53.97$

$\Delta t_4 := 6.28 \quad v_4 := 43.96$

$\Delta t_5 := 4.985 \quad v_5 := 34.91$

b [mm]	t [sec]	vol [mm3]
0.2	20.127	140.91
0.4	11.53	80.71
0.6	7.711	53.97
0.8	6.28	43.96
1.8	4.985	34.91

3. Calculations

Time counter and array $\quad NT := \dfrac{Tf}{\Delta T} - \dfrac{mod(Tf, \Delta T)}{\Delta T} \quad i := 1 .. NT \quad\quad T_i := i \cdot \Delta T$

Component counter $\quad j := 1 .. NC$

Cumulative events $\quad N_{0,j} := 0 \quad\quad\quad\quad N_{i,j} := \dfrac{T_i}{\Delta t_j} - \dfrac{mod\left(T_i, \Delta t_j\right)}{\Delta t_j}$

Events per interval $\quad n_{i,j} := N_{i,j} - N_{i-1,j} \quad\quad \Sigma n_i := \displaystyle\sum_{j=1}^{NC} n_{i,j}$

Volume per interval $\quad V_i := \displaystyle\sum_{j=1}^{NC} n_{i,j} \cdot v_j \quad\quad$ Flux $\quad q_i := \dfrac{V_i}{\Delta T}$

Tabulated Results $\quad TABLE_{i,0} := T_i \quad\quad TABLE_{i,1} := V_i$

Interval $\Delta T = 1$
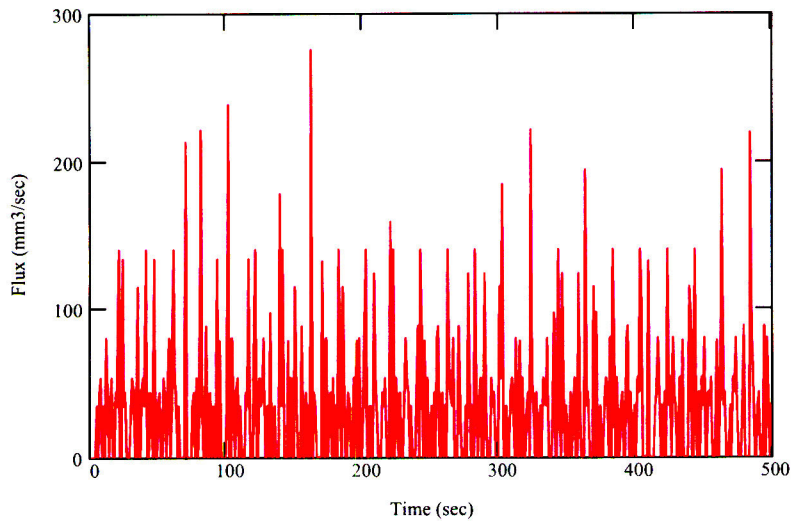
Appendix J (c)

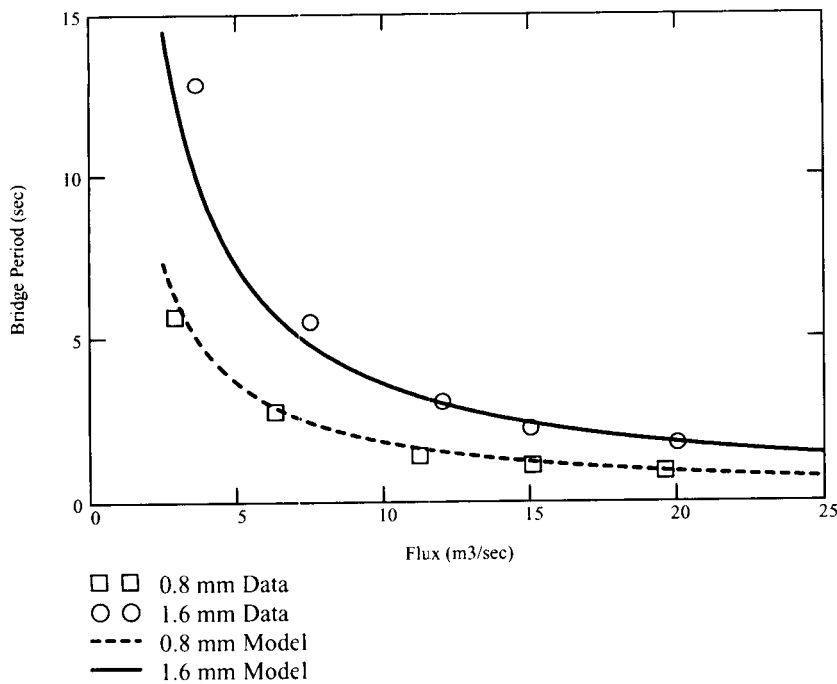## Growth and Detachment of Liquid Bridges

Physical Constants

$$\rho := 998 \qquad \eta := 0.1307 \cdot 10^{-2} \qquad \sigma_{LS} := 2 \cdot 7.29 \cdot 10^{-2} \qquad TOL := 10^{-4}$$

$$g := 9.8 \qquad \sigma := 7.29 \cdot 10^{-2} \qquad \sigma_{LV} := 7.29 \cdot 10^{-2} \qquad b := 0.4 \cdot 10^{-3} \qquad R := 1$$

- **1D Elongation and Detachment of Liquid Bridge from Appendix J (a),**

$$\tau b(Q, ro, R, b) := \frac{6 \cdot \eta \cdot b \cdot ro \cdot \rho \cdot g \cdot Q + -g \cdot ro^2 \cdot \rho + \sigma_{LV} \cdot b \cdot \pi}{g \cdot Q \cdot \rho}$$

$$c1 := 0.4 \cdot 10^{-3} \quad FLUX1 := \begin{bmatrix} 0.00290 \cdot 10^{-6} \\ 0.00632 \cdot 10^{-6} \\ 0.01122 \cdot 10^{-6} \\ 0.01506 \cdot 10^{-6} \\ 0.01958 \cdot 10^{-6} \end{bmatrix} \quad PERIOD1 := \begin{bmatrix} 5.688 \\ 2.778 \\ 1.411 \\ 1.111 \\ 0.931 \end{bmatrix} \quad c2 := 0.5 \cdot 10^{-3} \quad FLUX2 := \begin{bmatrix} 0.003627 \cdot 10^{-6} \\ 0.0075 \cdot 10^{-6} \\ 0.012 \cdot 10^{-6} \\ 0.015 \cdot 10^{-6} \\ 0.02 \cdot 10^{-6} \\ 0.033 \cdot 10^{-6} \end{bmatrix} \quad PERIOD2 := \begin{bmatrix} 12.84 \\ 5.5294 \\ 3.0742 \\ 2.2408 \\ 1.785856 \\ 1.112 \end{bmatrix}$$

$$q := 2.5 \cdot 10^{-9}, 2.6 \cdot 10^{-9} .. 3.5 \cdot 10^{-8}$$

Flux (m3/sec)

□ □ 0.8 mm Data
○ ○ 1.6 mm Data
---- 0.8 mm Model
—— 1.6 mm Model

ADDITIONAL INFORMATION FOR SCIENTIFIC NOTEBOOK #: 354E

Document Date:	06/30/1999
Availability:	Southwest Research Institute® Center for Nuclear Waste Regulatory Analyses 6220 Culebra Road San Antonio, Texas 78228
Contact:	Southwest Research Institute® Center for Nuclear Waste Regulatory Analyses 6220 Culebra Road San Antonio, TX 78228-5166 Attn.: Director of Administration 210.522.5054
Data Sensitivity:	■"Non-Sensitive" □ Sensitive □"Non-Sensitive - Copyright" □ Sensitive - Copyright
Date Generated:	10/02/2001
Operating System: (including version number)	Windows
Application Used: (including version number)	Microsoft Word 8.0; Microsoft Excel
Media Type: (CDs, 3 1/2, 5 1/4 disks, etc.)	2 zip drives
File Types: (.exe, .bat, .zip, etc.)	doc, xls, txt, pdf
Remarks: (computer runs, etc.)	Media contains: Flow in unsaturated fractured porous media-hydraulic conductivity of rough surfaces; Excel files, Fortran code and executable files, mathematic scripts, input/output examples.